Experimental and micromagnetic study of magnetisation behaviour in isolated ferromagnetic nanowires

MUSAAB SALMAN SULTAN

How to cite:

SULTAN, MUSAAB SALMAN (2013) Experimental and micromagnetic study of magnetisation behaviour in isolated ferromagnetic nanowires. Doctoral thesis, Durham University.

Experimental and micromagnetic study of magnetisation behaviour in isolated ferromagnetic nanowires

Musaab Salman Sultan

A thesis submitted in partial fulfilment of the requirements for the degree of
Doctor of Philosophy

University of Durham
2013

Contents

Chapter one

Introduction

Chapter two

Ferromagnetism and theory of magnetisation reversal

Chapter three

Magnetic, magnetisation reversal behaviour and alignment of ferromagnetic nanowires

Chapter four

Experimental methods: Fabrication of thin films and nanowires

Chapter five

Experimental methods: Investigative techniques for analysis of thin films and nanowires

Chapter six

Results: Composition, morphology and statistical distribution of ferromagnetic thin films and template released nanowires

Chapter seven

Results: Magnetic field alignment of template released ferromagnetic nanowires

Chapter eight

Results: Magnetic and electrical transport behaviour of template released isolated nanowires

Chapter nine

Results: Magnetic and magnetisation reversal behaviour of individual cylindrical and planar nanowires investigated by micromagnetic simulations

Chapter ten

Conclusions and suggestions for further work

Abstract

A full understanding of the magnetism of isolated ferromagnetic nanowires is still an unresolved issue and presents a research challenge for researchers. Understanding the intrinsic magnetic properties of such nanowires is significant from a scientific point of view and will be an issue for potential applications. Therefore, the aim of the work presented here is to investigate the magnetic and magnetisation reversal behaviour of electrodeposited template released isolated ferromagnetic nanowires complemented by detailed micromagnetic simulations.

To understand the fabrication techniques, characterisation systems and the materials used to fabricate the nanowires, the elemental composition, surface topography and magnetic properties of a range of electrodeposited thin films were investigated first.

In order to emphasis the reasons behind studying the magnetic behaviour of such isolated nanowires, the statistical distribution of template pore size and spacing, nanowire dimension distributions, and the morphology of such nanowires have been measured using *high resolution scanning electron microscope* analysis. To determine the crystal structure and the crystallite sizes within these nanowires, which might have a great influence on their magnetic properties, both the template deposited and selected areas of individual nanowires have been studied using a combination of *X-ray diffraction* and *high resolution transmission electron microscopy* incorporating with *electron diffraction*, respectively.

To align the template released nanowires with respect to the prefabricated micromarkers and electrical contact pads, *magnetic field assisted alignment* was developed. The effect of field strength, nanowire composition and aspect ratio on the percentage of aligned nanowires have been statistically analysed and the results explained.

The surface and bulk magnetisation reversal behaviour of isolated individual, small bundles and clusters of nanowires is technically challenging but have been successfully measured here using *magneto-optical Kerr effect magnetometry* and *magnetoresistance*, respectively. The magnetic switching behaviour obtained from these techniques is compared with each other, the literature and analytical models.

In addition, detailed *micromagnetic simulations* have been utilised to determine the magnetic behaviour of two wire geometries: cylindrical and planar $Ni_{81}Fe_{19}$ nanowires with a range of diameters and thicknesses, respectively. For both geometries, the effect of nanowire diameter and thickness on the magnetic properties such as switching fields, remanent magnetisation and magnetic state before and during the switching behaviour, have been analysed and compared. The switching field of the simulated nanowires are compared with their counterparts results obtained from both MOKE and MR measurements. The magnetisation reversal behaviour of these wires geometries was also investigated and compared with the classical analytical *curling* model of magnetisation reversal.

Declaration

I hereby declare that the work contained in this thesis is my own and has not been submitted for examination for any other degree at any University. The work of collaborators is acknowledged as appropriate. Fabrication process of electrodeposited thin films and nanowires presented in this thesis were done by *Bipul Das*, *Jenny King* and *Del Atkinson* in S. N. Bose scientific centre at Kolkata, India.

Acknowledgments

I would like to take this opportunity to thank the elected Iraqi government for their financial support and the staff of the Iraqi Embassy in London for their help and support.

I wish to express my deep sense of appreciation and many thanks to my supervisor *Dr. Del Atkinson* for his continued guidance throughout my PhD. I am extremely grateful for his friendship, supervision and advice. Without you, *Del*, I would not have been able to finish this work at all. I am also grateful to *Dr. Brian Tanner* for his supervision.

I wish to show my gratitude to the people in room 12 for their support and help, especially *Helen Armstrong*, who was always willing to help and showed great kindness to me. Big thanks are due to *Jenny King* and *David Eastwood*, as well as *Erhan Arac*, *David Burn*, *Alex Webb*, and *Sarah Dempsey* for their valuable assistance throughout this work.

I would like to express my deep thanks to *Jennifer King and Del Atkinson* who provide me with electrodeposited thin films and nanowires.

Many thanks are due to *Bipul Das*, who provide me with electrodeposited thin films and nanowires, as well as the raw XRD data of templated nanowires.

Sincere thanks go to *Budhika Mendis*, who helped me to measure the crystalline structure of isolated nanowires by HRTEM. The same thanks go to *Leon Bowen*, who supported me in measuring the composition of sputtered and electrodeposited thin films.

Throughout, *John Dobson* has given invaluable technical help and I thank him greatly for fixing the X-ray machine and sputtering system whenever a problem arose.

I would like to express my deep thanks to my family here, especially my wife, *Jowan*, for her help and continuous encouragement over the past four years. Many thanks to my lovely children, *Ahmed*, *Lana* and *Aya* for their long wait. Thanks to my father and mother for their patience over the long wait for us to return back and take care of them.

Finally, I would like to thank everyone who has contributed in any way to the culmination of this work.

Musaab Salman Sultan
2013

List of Publications

Chapter six and *chapter eight* contains work partially summarized in the following journal article:

"Template released ferromagnetic nanowires: Morphology and magnetic properties"

M. S. Sultan, B. Das, P. Sen, K. Mandal & D. Atkinson

***Journal of Spintronics and Magnetic Nanomaterials,* 1, 2, 2012.**

Chapter seven is entirely published in the following journal article:

"Magnetic alignment of template released ferromagnetic nanowires"

Musaab S. Sultan, Bipul Das, Kalyan Mandal & Del Atkinson

***Journal of Applied Physics*, 112, 1, 013910, 2012.**

The following papers are under preparation:

"Surface and bulk magnetisation behaviour of template released isolated ferromagnetic nanowires"

Musaab S. Sultan, Kalyan Mandal, Bipul Das & Del Atkinson

"Magnetisation behaviour in cylindrical and planar $Ni_{81}Fe_{19}$ nanowires investigated by micromagnetic simulations"

Musaab S. Sultan, David Burn & Del Atkinson

Chapter one
Introduction

1-1 Introduction

Ferromagnetic nanowires, *nanorods*, *nanoribbons* and *nanopillars* are closely related terms that can be defined as structures that have a thickness or diameter of nanometer scale and unconstrained length. Typical ferromagnetic nanowires exhibit high aspect ratios (length to diameter), and they have often been approximated as one-dimensional structures. These nanowires have many interesting features that are not seen in bulk or three-dimensional materials and therefore the fabrication, physical characterisation and analysis of the behaviour of these structures presents interest for both fundamental science and industrial applications [1-10]. As an example, they have been proposed for roles in future applications of various magnetic technology including spintronics, magneto-optical devices, sensors, logic circuits and ultra-high density magnetic storage media in hard-disk drives and non-volatile magneto-resistive random access memory (MRAM). These applications may lead to devices that are smaller, more compact and portable. In addition, they have numerous potential applications in various other fields, such as chemistry and biosciences.

There are two main approaches for fabricating these types of structures, the first is *lithographic patterning* of *vapour phase* deposited thin-films and multi-layers (typically thermal evaporation or sputtering techniques) by *electron beam lithography* and/or *focused ion beam milling*, to create planar nanowires with ultra-thin rectangular cross sections, where the thickness is of the order of ten nanometers and the width is in the range of 150-1000 nm [11-15]. These planar nanowires have been the focus of studies of magnetisation behaviour of individual nanowires and are most readily compatible with the production processes needed for device applications. The other important technique that has been widely used to create nanowires is the *electrochemical* deposition of ferromagnetic materials from solution into nanoscale porous templates, often made from alumina, mica, silica or track etched polycarbonate [16-23]. In contrast to lithographic patterning, this later technique produces circular cross-section nanowires with diameters from ~5 nm up to hundreds of nanometers. By controlling the electrodeposition conditions or template parameters, this technique can also produce nanotube structures [24-26]. This technique is powerful, as it can produce large numbers of nanowires relatively quickly and at a low cost, and while, for lithographic patterning, the nanowires lie parallel to the substrate plane, template deposited nanowires are orientated orthogonal to the substrate and attached to a conducting base layer, typically made of gold or copper. With this technique, single element [16-18], alloyed [19,20] or compositionally modulated multi-layered [21,22] nanowires can be prepared.

The magnetic and magnetisation reversal behaviour of as-deposited arrays of templated ferromagnetic nanowires have been investigated extensively over the last couple of decades using different techniques including *vibrating sample magnetometry (VSM)* [27,28], *superconducting quantum interference device (SQUID)* [29,30], *torque magnetometry* [31] and *magnetoresistance (MR)* [32-34]. These studies have produced significant insights into the physical behaviour of two-dimensional arrays of nanowires. These results are obtained as averages over many hundreds or thousands of nanowires, in which the dipolar or magnetostatic interaction between neighbouring wires complicates the situation regarding intrinsic magnetisation behaviour. Understanding the intrinsic magnetic properties and the magnetisation reversal processes in isolated individuals and small bundles of nanowires is significant and crucial from the scientific point of view and is a demanding issue for potential applications. Indeed, a full understanding of the magnetism of template released ferromagnetic nanowires is still unresolved issue and presents a significant challenge for researchers.

In order to understand the magnetic behaviour of such isolated nanowires, wire behaviour has been analysed by different groups using templates with a low density of nanopores. These studies however, cannot provide precise information and the interpretation of the data is limited, as will be shown later, due to variations of morphologies, orientations, dimensions, circularity and separation distances among these wires, where the wires are distributed randomly in a disordered fashion and the magnetostatic interaction between neighbouring wires again complicates the situation.

Therefore, researchers have attempted to investigate isolated nanowires by releasing them from the templates using suitable chemical solutions to dissolve the template without damaging the wires [35-38]. The focus of these studies has been nanowires of the smallest diameters that are likely to display single domain states and simpler magnetic behaviour compared to larger diameter nanowires, which support more complex domain structures. Most of these studies, however, involve primarily *electrical-transport measurements* and few measurements by *micro-SQUID*. Much less work has focused upon thicker isolated magnetic nanowires [39-42], where the magnetic processes are likely to be more complex. Indeed, as described later the contrast between transport measurements and magneto-optical magnetometry suggests that a combination of techniques is needed to understand the magnetisation behaviour of larger diameter nanowires. Thus, the main purpose of the research presented here is to investigate the magnetic state and magnetisation reversal behaviour of isolated template released ferromagnetic nanowires using both *magneto-optical Kerr effect (MOKE) magnetometry* and *magnetoresistance measurements*.

In this research, nickel (Ni), NiFe (nominal composition $Ni_{80}Fe_{20}$ (permalloy)) and cobalt (Co) nanowires and thin films were grown by an electrodeposition technique in alumina templates and on $Au/Cr/Si/SiO_2$ substrates, respectively. The nanowires were released from their templates, placed into a dilute suspension and then dispersed on oxidised silicon substrates for magnetic and electrical transport measurements. The results of these studies are discussed and interpreted in comparison with micromagnetic simulations of cylindrical and planar nanowires.

To perform these measurements, the isolated nanowires were aligned with respect to the prefabricated gold micromarkers and electrical contact pads using magnetic field assisted alignment. To better understand and interpret the magnetisation behaviour, the crystalline structure and the grain sizes within these nanowires was investigated using both *X-ray diffraction (XRD)* and *high resolution transmission electron microscopy HRTEM* incorporated with *selected area electron diffraction (SAED).*

Electrodeposited thin films were investigated here to gain an insight into the elemental composition, morphology and magnetic properties of the basic materials that form templated nanowires. The elemental composition was investigated using both *energy & wavelength dispersive X-ray (EDS & WDS)* analysis, whereas the topography of these films was studied using *grazing incidence X-ray reflectivity (GIXR)* measurements.

1-2 Thesis outline

In this thesis, *chapter two* presents some of the important theory of ferromagnetism to provide a relevant background framework that includes significant concepts and principles of magnetism, micromagnetic and magnetisation reversal processes needed to put this work into context. *Chapter three* presents a focused literature survey covering the relevant magnetic, magnetisation reversal behaviour and alignment of ferromagnetic nanowires. A review of material preparation and crystalline structure, as well as the effect of growth conditions, wire dimensions, magnetostatic interactions and filling factor on the magnetic and magnetisation reversal process in two-dimensional arrays and isolated ferromagnetic nanowires. Furthermore, a survey of the magnetic alignment of template released ferromagnetic nanowires is covered in this chapter. *Chapter four* deals with the experimental techniques used to fabricate thin-films, nanowires, micromarkers and contact pads as well as the electrical connection of the isolated nanowires with the contact pads and the external circuitry giving a theoretical background for each technique first. The methods used to release and deposit templated nanowires onto substrates are also described. Moreover, the technical difficulties associated with the electrical connection of these nanowires with the contact pads are also discussed along with some examples. Brief theoretical and experimental descriptions of the investigative techniques including scanning electron microscopy (SEM), grazing incidence X-ray reflectivity, magneto-optical Kerr effect magnetometry, magnetoresistance, and micromagnetic modelling employed in this research are presented in *chapter five*. Results and discussion of the chemical composition, roughness and thickness of a range of electrodeposited ferromagnetic thin films are presented in *chapter six*. The statistical distribution of template pore diameter, spacing and wire diameter, as well as length, morphology and crystal structure of the nanowires are also investigated in *chapter six*. The results presented in *chapter seven* provide a quantitative analysis of the magnetic field assisted alignment of a range of template released ferromagnetic nanowires. Specifically, this *chapter* investigates the alignment of nanowires deposited onto substrates as a function of magnetic field strength, composition (saturation magnetisation) and the aspect ratio of the nanowires. This *chapter* also reports some further observations resulting from the magnetic alignment experiments along with the most important potential applications of magnetically aligned ferromagnetic nanowires in various fields. *Chapter eight* investigates the results of magnetic, magnetisation reversal and electrical-transport behaviour of a range of template released isolated ferromagnetic nanowires using MOKE and MR measurements, respectively. A comparison between these results is investigated. The technical difficulties associated with the MR measurements are also discussed. To understand deeply the magnetic properties of such isolated nanowires, a range of electrodeposited thin films are investigated first. *Chapter nine* is a theoretical study of the magnetic and magnetisation reversal behaviour of cylindrical and planar cross-section $Ni_{81}Fe_{19}$ nanowires with a range of diameters and thicknesses/widths and all with the same length using the object oriented micromagnetic framework (OOMMF) software. A comparison between the simulation and the experimental results is presented in this chapter. Finally, *chapter ten* presents the conclusions of this work and suggestions for further work.

1-3 Definitions and magnetic units

The most significant terms used in the description of the magnetic phenomena in this work are defined here, including their units and conversions. In magnetism, unit systems are still complex as some use *system international (SI)* units and others the *centimetre gram second (cgs)* system. Each one, however, has certain advantages and disadvantages. Both are discussed here.

1-3.1 Magnetic field

Magnetic field is denoted by H and it appears in volume space whenever there is an electrical charge in motion. It also appears in a permanent magnet, as a result of electrons in orbital motions and the intrinsic spin of electrons. The unit of magnetic field strength is expressed by *ampere/metre (A/m)* or *orested (Oe)* in SI and cgs units, respectively [43,44].

1-3.2 Magnetic induction

The *magnetic induction* or *magnetic flux density*, B, is defined by the magnetic field and the magnetic characteristics of the media within the magnetic field. Its unit is given by *tesla* (or *weber per square meter* (W/m^2)) or *gauss*, G, in SI and cgs units, respectively. In free space the relation between magnetic induction and the magnetic field is given by [43]:

$$B = \mu_o H \qquad 1\text{-}1$$

Where, μ_o is a universal constant and known as the *permeability of free space*. In SI units, μ_o is equal to $4\pi \times 10^{-7}$ *Henry per meter* (*H/m*), whilst it is *one* in cgs units [43].

1-3.3 Magnetic moment

Magnetic moment, m, is a significant and basic quantity in magnetism. It is applicable for both bar magnet and electronic magnets. Its unit is generally referred to as, *emu,* because it is an electromagnet unit. Its unit is $A.m^2$ or *weber.m* in SI unit and *erg/oersted* in cgs system [44].

1-3.4 Intensity of magnetisation

Intensity of magnetisation or simply *magnetisation*, M, is a quantity used in magnetism to describe the degree of magnetisation in the magnetic materials. It is the *magnetic moment per unit volume*, V, $(M = m/V)$. Its unit is given by *erg/oersted cm*^{3} or *emu/*cm^3 [44].

1-3.5 Magnetic susceptibility and permeability

These two quantities represent the magnetic material response to the magnetic field where $\mu = \frac{B}{H}$ and $\chi = \frac{M}{H}$, where; μ and χ are the *permeability* and *susceptibility* of a specimen, respectively [44].

1-3.6 Basic units in magnetism and their conversions

The following table summarise the most important quantities used in magnetism and their conversions [43].

Quantity	**Symbol**	**SI units**	**CGS units**	**Conversions**
Magnetic field	H	A/m	Oresteds	1 oersted = (1000/4π) A m^{-1} = 79.58 A m^{-1}
Magnetic induction	B	Tesla	Gauss	1 gauss = 10^{-4} tesla
Magnetisation	M	A/m	emu cm^{-3}	1 emu/cm^3 = 1000 A m^{-1}
Magnetic moment	m	A m^2	Emu	1 emu = 10^{-3} Am^2

Table 1.1 Important units in SI and CGS systems currently used in magnetism and their conversions.

1-4 Chapter reference

1. Dao, N., Homer, S. R. & Whittenburg, S. L. "Micromagnetics simulation of nanoshaped iron elements: Comparison with experiment" *J. Appl. Phys.*, 86(6), 3262, 1999.
2. Lee, S.-W., Jeong, M.-C., Myoung, J.-M., Chae, G.-S. & Chung, I.-J. "Magnetic alignment of ZnO nanowires for optoelectronic device applications" *Appl. Phys. Lett.*, 90(13), 133115, 2007.
3. Coey, J. M. D. & Hinds, G. "Magnetic electrodeposition" *J. Alloys and Compounds*, 326(1-2), 238, 2001.
4. Sellmyer, D. J., Zheng, M. & Skomski, R. "Magnetism of Fe, Co and Ni nanowires in self-assembled arrays" *J. Phys.: Condens. Matter*, 13, R433, 2001.
5. Nielsch K. & Stadler, B. J. H. "Handbook of magnetism and advanced magnetic materials: Template-based synthesis and characterization of high-density ferromagnetic nanowire arrays" Edited by Helmut Kronmuller and Stuart Parkin, Volume 4: Novel Materials, John Wiley & Sons, Ltd., 2007.

6. Kunz, A., Reiff, S. C., Priem, J. D. & Rentsch, E. W. "Controlling individual domain walls in ferromagnetic nanowires for memory and sensor applications" *International Conference on Electromagnetics in Advanced Applications*, 248, 2010.
7. Hultgren, A., Tanase, M., Chen, C. S., Meyer, G. J. & Reich, D. H. "Cell manipulation using magnetic nanowires" *J. Appl. Phys.*, 93(10), 7554, 2003.
8. Daub, M., Enculescu, I., Neumann, R. & Spohr, R. "Ni nanowires electrodeposited in single ion track templates" *J. Optoelectronics and Advanced Materials*, 7(2), 865, 2005.
9. Andra, W., Hafeli, Urs, Hergt, R. & Misri, R. "Handbook of magnetism and advanced magnetic materials: *Application of magnetic particles in medicine and biology* " Edited by Helmut Kronmuller and Stuart Parkin, Volume 4: Novel Materials, John Wiley & Sons, Ltd., 2007.
10. Sun L., Hao Y., Chien C. L. & Searson P. C. "Tuning the properties of magnetic nanowires" *IBM J. RES. & DEV.*, 49(1),79, 2005.
11. Atkinson, D., Eastwood, D. S. & Bogart, L. K. "Controlling domain wall pinning in planar nanowires by selecting domain wall type and its application in a memory concept" *Appl. Phys. Lett.*, 92(2), 022510, 2008.
12. Bryan, M. T., Atkinson, D. & Allwood, D. A. "Multimode switching induced by a transverse field in planar magnetic nanowires" *Appl. Phys. Lett.*, 88(3), 032505, 2006.
13. Dumpich, G., Krome, T. P. & Hausmanns, B. "Magnetoresistance of single Co nanowires" *J. Mag. Mag. Mat.*, 248(2), 241, 2002.
14. Allwood, D. A, Xiong, G., Cooke, M. D. & Cowburn, R. P. "Magneto-optical Kerr effect analysis of magnetic nanostructures" *J. Phys. D: Appl. Phys.*, 36(18), 2175, 2003.
15. Lodder, J. C. "Methods for preparing patterned media for high-density recording" *J. Mag. Mag. Mat.*, 272-276, 1692, 2004.
16. Yin, A. J., Li, J., Jian, W., Bennett, A. J. & Xu, J. M. "Fabrication of highly ordered metallic nanowire arrays by electrodeposition" *Appl. Phys. Lett.*, 79(7), 1039, 2001.
17. Qin, J., Nogue, J., Mikhaylova, M., Roig, A. & Mun, J. S. "Differences in the magnetic properties of Co, Fe and Ni 250-300 nm wide nanowires electrodeposited in amorphous anodized alumina templates" *Chem. Mater.*, 17,1829, 2005.
18. Narayanan, T. N., Shaijumon, M. M., Ci, L., Ajayan, P. M. & Anantharaman, M. R. "On the growth mechanism of nickel and cobalt nanowires and comparison of their magnetic properties" *Nano. Res.*, 1(6), 465, 2008.
19. Khan, H. R. & Petrikowski, K. "Magnetic and structural properties of the electrochemically deposited arrays of Co and CoFe nanowires" *J. Mag. Mag. Mat.*, 249(3), 458, 2002.
20. Bai, A. & Hu, C.-C. "Iron–cobalt and iron–cobalt–nickel nanowires deposited by means of cyclic voltammetry and pulse-reverse electroplating" *Elec. Comm.*, 5(1), 78, 2003.
21. Ohgai, T., Hjort, K., Spohr, R. & Neumann, R. "Electrodeposition of cobalt based ferromagnetic metal nanowires in polycarbonate films with cylindrical nanochannels fabricated by heavy-ion-track etching" *J. Appl. Elec.*, 38(5), 713, 2008.
22. Tang, X.-T., Wang, G.-C. & Shima, M. "Magnetic layer thickness dependence of magnetization reversal in electrodeposited CoNi/Cu multilayer nanowires" *J. Mag. Mag. Mat.*, 309(2), 188, 2007.

23. Possin, E. George "A method for forming very small diameter wires" *Rev. Sci. Ins.*, 41, 772, 1970.
24. Davis, D. M., Moldovan, M., Young, D. P., Henk, M., Xie, X. & Podlaha, E. J. "Magnetoresistance in electrodeposited CoNiFe/Cu multilayered nanotubes" *Ele. Solid State Lett.*, 9(9), C153, 2006.
25. Han, X.-F., Shamaila, S., Sharif, R., Chen, J.-Y., Liu, H.-R. & Liu, D.-P. "Structural and magnetic properties of various ferromagnetic nanotubes" *Adv. Mat.*, 21(45), 4619, 2009.
26. Li, X. Wang, Y., Song, G., Peng, Z., Yu, Y., She, X. & Li, J. "Synthesis and growth mechanism of Ni nanotubes and nanowires" *Nano. Res. Lett.*, 4(9), 1015, 2009.
27. Chen, W., Tang, S., Lu, M. & Du, Y. "The magnetic properties and reversal of Fe–Co nanowire arrays" *J. Phys.: Condense Matter*, 15(26), 4623, 2003.
28. Vázquez, M. Pirota, K., Hernandez-Velez, M., Prida, V. M., Navas, D., Sanz, R. & Batallan F. "Magnetic properties of densely packed arrays of Ni nanowires as a function of their diameter and lattice parameter" *J. Appl. Phys*., 95(11), 6642, 2004.
29. Aravamudhan, S., Singleton, J., Goddard, P. A. & Bhansali, S. "Magnetic properties of Ni–Fe nanowire arrays: Effect of template material and deposition conditions" *J. Phys. D: Appl. Phys.*, 42(11), 115008, 2009.
30. Vázquez, M., Hernández-Vélez, M., Pirota, K., Asenjo, A., Navas, D., Velázquez, J., Vargas, P. & Ramos C. "Arrays of Ni nanowires in alumina membranes: magnetic properties and spatial ordering" *The European Physical Journal B*, 40(4), 489, 2004.
31. Dumpich, G., Krome, T. P. & Hausmanns, B. "Magnetoresistance of single Co nanowires" *J. Mag. Mag. Mat.*, 248(2), 241, 2002.
32. Ferré, R., Ounadjela, K., George, J., Piraux, L. & Dubois, S. "Magnetization processes in nickel and cobalt electrodeposited nanowires" *Phys. Rev. B*, 56(21), 14066, 1997
33. Fert, A. & Piraux, L. "Magnetic nanowires" *J. Mag. Mag. Mat.*, 200, 338, 1999.
34. Pignard, S., Goglio, G., Radulescu, A., Piraux, L., Dubois, S., Declémy, A. & Duvail, J. L. "Study of the magnetization reversal in individual nickel nanowires" *J. Appl. Phys.*, 87(2), 824, 2000.
35. Wernsdorfer, W., Doudin, B., Mailly, D., Hasselbach, K., Benoit, A, Meier, J., Ansermet, J.-Ph. & Barbara B. "Nucleation of magnetization reversal in individual nanosized nickel wires" *Phys. Rev. Lett.*, 77(9), 1873, 1996.
36. Yoo, B., Rheem, Y., Beyermann, W. P. & Myung, N. V. "Magnetically assembled 30 nm diameter nickel nanowire with ferromagnetic electrodes" *Nanotech.*, 17(10), 2512, 2006.
37. Vila, L., Piraux, L., George, J. M. & Faini, G. "Multiprobe magnetoresistance measurements on isolated magnetic nanowires" *Appl. Phys. Lett.*, 80(20), 3805, 2002.
38. Vila L., George J. M., Faini G., Popa A., Ebels U., Ounadjela K. & Piraux L. "Transport and magnetic properties of isolated cobalt nanowires" *IEEE Trans. Mag.*, 38(5), 2577, 2002.
39. Lupu, N., Lostun, M. & Chiriac, H. "Surface magnetization processes in soft magnetic nanowires" *J. Appl. Phys.*, 107(9), 09E315, 2010.
40. Rheem Y., Yoo, B.-Y., Beyermann W. P. & Myung N. V. "Magneto-transport studies of single ferromagnetic nanowire" *Phys. Stat. Sol. (a)*, 204(12), 4004, 2007.
41. Rheem Y., Yoo B.-Y., Beyermann W. P. & Myung N. V. "Electro-and magneto-transport properties of a single CoNi nanowire" *Nanotech.*, 18(12), 125204, 2007.

42. Rheem Y., Yoo B.-Y., Koo B. K., Beyermann W. P. & Myung N. V. "Synthesis and magnetotransport studies of single nickel-rich NiFe nanowire" *J. Phys. D: Appl. Phys.*, 40(23), 7267, 2007.
43. Jiles D. "Introduction to magnetism and magnetic materials" 2nd edition, Chapman and Hall/CRC New York, 1998.
44. Cullity, B. D. & Graham, C.D. "Introduction to magnetic materials" 2nd edition, John Wiley and Sons Inc., Hoboken, New Jersey, 2009.

Chapter two

Ferromagnetism and theory of magnetisation reversal

2.1 Introduction

This chapter discusses the key physics associated with ferromagnetism that is relevant to understanding the results presented and discussed later. The chapter starts with a brief introduction to the *microscopic origin of magnetisation* within magnetic materials, their classifications and the difference between demagnetised states and saturated ferromagnetic materials. The anisotropies that contribute to the magnetisation behaviour of ferromagnetic materials and the concepts behind *domains*, *domain walls* and *magnetisation reversal mechanisms* are also covered in this chapter along with a brief description of the theory of *micromagnetism*.

2-2 Microscopic origin of magnetism

In a simplified view, the clouds of electrons surrounding atoms may be visualised as rotating in circular orbits around the nucleus, as shown in Figure 2.1(a). These electrons (charge of, e, and mass of, m_e) rotate around the nucleus at a radius, r, with a velocity, υ [1-3].

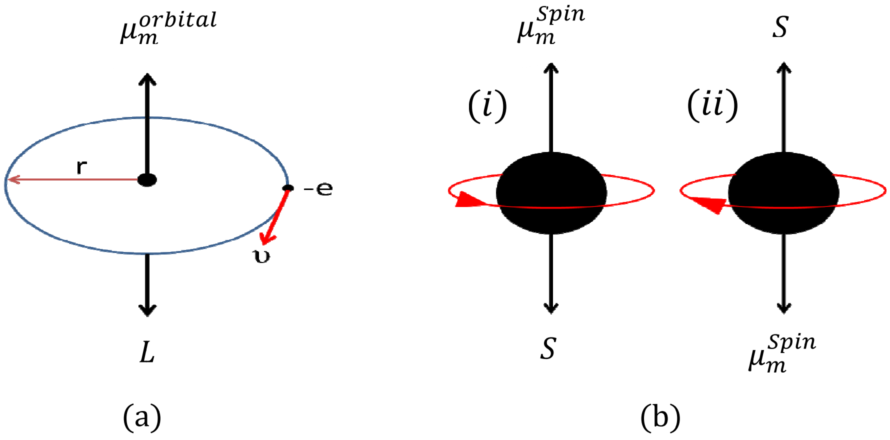

Figure 2.1 Schematic representation of the electron motion in an atom (a) orbital motion around the nucleus[4] produce a *magnetic moment*, $\mu_m^{orbital}$, and (b) spin motion around its own axis produce a *spin magnetic moment*, μ_m^{spin}. The two orientations of electron spin are shown as (i) clockwise and (ii) counter-clockwise. Modified from [5].

The rotation of electrons can be considered as an electric current flowing in a circular loop with zero resistance which gives rise to a *magnetic moment*, $\mu_m^{orbital}$, that appears perpendicular to the plane of the electron motion, as illustrated in Figure 2.1(a), associated with this moment is an *orbital angular momentum*, *L*, directed opposite to the orbital magnetic moment [4,5].

Very crudely, the electrons can also be thought to rotate about their own axis in a spin-like motion. This spin motion is used to describe a purely quantum mechanical concept which has no classical analogy. The spin can be in one of two quantum mechanical orientations namely: *spin up* and *spin down*. Therefore, the associated magnetic moments can take only one of these two directions. To understand the concept of electron spin, the electrons were assumed classically as a solid sphere and the charges are distributed over their surface, as shown in Figure 2.1(b) [5]. This representation is only an aid of visualisation with no quantitative importance [5]. The rotation of these charges produce current loops which all sum together to give rise to a *spin magnetic moment*, μ_m^{spin}, oriented along the rotation axis. As a result there will be a *spin angular momentum*, *S*, in an opposite direction to the spin magnetic moment [5].

The *total angular momentum*, J, of the electrons in an atom is given by the vector sum of the orbital and spin angular momentum as follows [1,3]:

$$J = L + S \qquad 2\text{-}1$$

while, the *total magnetic moment*, μ_m^{Total}, is given by [3]:

$$\mu_m^{Total} = -\frac{g\mu_B}{\hbar}J \qquad 2\text{-}2$$

Where, $\hbar$ is the reduced *Planck constant*, g is the *Landé factor* (dimensionless), and μ_B is the *Bohr magneton* given in SI units as [3]:

$$\mu_B = \frac{e\,\hbar}{2m_e} \qquad 2\text{-}3$$

The *Landé factor* can be given by [4]:

$$g = 1 + \frac{J\,(J+1) + S\,(S+1) - L\,(L+1)}{2\,J\,(J+1)} \qquad 2\text{-}4$$

The, g, factor can take values between 1 and 2, where it takes 1 for orbital motion and 2 for spin motion only. When *1 <* g *< 2* indicates that both effects are involved. The g factor can be measured from the frequency of an electron orbital motion, which is known as *gyromagnetic ratio*, γ [6]. This factor is significant in *micromagnetic theory* and it is defined as the ratio of the angular momentum to the magnetic moment and given by [6]:

$$\gamma = -\frac{\mathrm{e}\,g}{2\,m_e} = -\frac{g\,\mu_B}{\hbar} \qquad 2\text{-}5$$

The value of the *gyromagnetic ratio* confirms that the largest contribution to the intrinsic magnetic moments within ferromagnetic materials arises from the electron spin motion rather than electron orbital motion around the nucleus [6].

2-3 Classification of magnetic materials

It is clear from the previous section that the origin of the magnetisation within magnetic materials arises from electron orbital and spins contributions. Therefore, magnetic materials according to their response to an applied magnetic field can be classified into three main categories [5,7,8]. The first category is *diamagnetic* materials which have no net magnetisation because the electronic shells are completely filled. The induced magnetic moments in these materials opposes the external applied magnetic field and so they have a small and negative susceptibility (around -10^{-5} dimensionless in SI units) [7,8]. Diamagnetic susceptibilities are significantly independent of temperature. Examples of these materials are copper, silver, carbon, gold, bismuth and beryllium [7]. The second category is *paramagnetic* materials in which the atoms and molecules have an odd number of electrons in unfilled shells, so there is an unpaired electron spin, giving rise to a net magnetisation in response to an applied field. This magnetisation does not exhibit long-range order such as found in ferromagnetic materials, therefore the susceptibility is small and positive (typically 10^{-3}-10^{-5}) [7,8]. In fact, the atomic magnetic moments are randomly oriented when there is no applied magnetic field due to the *thermal* or *Boltzmann energy*. The magnetisation in these materials is weak and could be aligned parallel to the direction of the applied magnetic field. The susceptibility in most paramagnetic materials are inversely proportional to the temperature and this correlation is known as the *Curie law* [5,7]. Examples of these materials include aluminium, platinum, and copper sulphate. The third group is the *ferromagnetic* materials, which are the most significant group due to their extensive use in many applications and are the most relevant here. The susceptibility of these materials is positive, much greater than 1 and can have values ranging up to 10^4 [7].

2-4 Ferromagnetic materials

Ferromagnetic materials can be defined as materials that have a *spontaneous magnetisation* even when there is no external applied magnetic field [5,7]. Examples of these materials are: iron, cobalt, nickel, some rare earth elements (e.g. scandium, yttrium gadolinium, neodymium, and samarium) and their alloys. With these materials, maximum and minimum spontaneous magnetisation can be obtained at 0K and the *Curie temperature*, respectively, whilst above the *Curie temperature* ferromagnetic materials show paramagnetic properties in which the magnetic moments are randomly distributed with no field [7].

Different types of spontaneous magnetic materials exist and the moment depends on the relative orientation and magnitude of the magnetic moments (electron spins) with respect to each other. These materials are *ferrimagnets*, *antiferromagnets*, *helimagnets*, and *supermagnets* [7,8]. Figure 2.2 show schematic diagrams for the magnetic moment arrangement in ferromagnetic, antiferromagnetic and ferrimagnetic materials. In ferromagnetic materials, the nearest neighbour magnetic moments are aligned parallel in some regions, as schematically shown in Figure 2.2(a). The magnetic moments in anti-ferromagnetic materials are aligned anti-parallel, as shown in Figure 2.2(b). Examples of

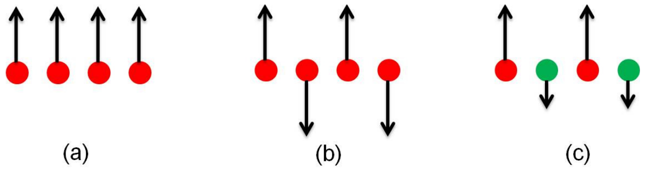

Figure 2.2 Schematic diagrams showing the alignment of magnetic moments in different magnetic materials [7]: (a) Ferromagnetic, (b) antiferromagnetic, and (c) ferrimagnetic alignments.

antiferromagnetic materials include chromium, manganese and the transition metal oxides such as FeO, CoO, NiO and MnO. Ferrimagnetism is a special case of antiferromagtism and these materials are usually referred to *ferrites* in which the magnetic moments on different lattice sites are aligned in opposite directions and with different magnitudes such that a net moment exist, as illustrated in Figure 2.2(c). It was first suggested by *Néel* in 1948 [9]. The archetypal ferrimagnetic material is Fe_3O_4 [9].

The alignments of the magnetic moments in small regions within these materials are known as magnetic *domains*, these will be discussed in further detail later. In the demagnetised state, the orientation of magnetic moments varies from domain to domain and the net magnetisation is zero, $\sum m=0$ [7,10], as shown in Figure 2.3. When an external magnetic field is applied, the domains that aligned in the opposite direction to the field are reduced and eventually with increasing the field all the magnetic moments are directed towards the field direction resulting in a single domain specimen [7] and the material reaches saturation magnetization, $\sum m= M_s$, as shown in Figure 2.3. Nevertheless, the alignment of the neighbouring electron spins within the domains is strongly dependent on the quantum mechanical *exchange interaction*, as will be seen in the following section.

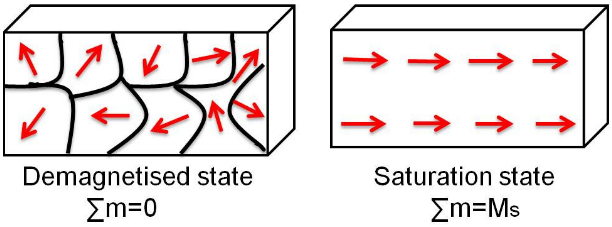

Figure 2.3 Alignment of magnetic moments within domains in ferromagnetic materials as a demagnetised state in which the magnetic moments varies from domain to domain, and saturated state in which all the magnetic moments are aligned parallel when a sufficient external magnetic field is applied [7].

2-5 Exchange interaction

The alignment of the magnetic moments within ferromagnetic materials is due to the quantum mechanical *exchange interaction* which was explained by *Heisenberg* in 1928 [5,7]. This interaction is dependent on the relative orientation of the neighbouring electron spins. As it is well known from *Pauli Exclusion Principle* that any two electrons cannot occupy the same energy level if they have the same quantum numbers, whilst they can occupy the same energy level if they have different quantum numbers [5]. Therefore, an attractive or repulsive force appears when the electrons spins are antiparallel or parallel, respectively. Hence, there is an electrostatic force between the nearest neighbours modified by the spin orientation known as the *exchange force* or the *exchange energy*, E_{ex}, which is responsible for introducing magnetic ordering to the electronic spins [5]. The exchange energy is dependent upon the interatomic distances and is a short-range effect, decreasing rapidly with increasing separation [5]. This energy can be given as a summation over adjacent interacting spins as follows [5-7]:

$$E_{ex} = -2\sum J_{ij}\, S_{ij}^{2} cos\theta_{ij} \qquad 2\text{-}6$$

Where, J_{ij} is the exchange integral, S_{ij} are the spin momenta associated with each adjacent spin, and θ_{ij} is the angle between the neighbouring spins. If the exchange integral is positive, the minimum (maximum) energy is obtained when the spins are parallel (antiparallel) to each other. If the exchange integral is negative, the minimum energy state is achieved when the spins are antiparallel to each other. Parallel (antiparallel) spin alignment leads to ferromagnetic (antiferromagnetic) order [9]. If the magnitude of the spins is equal and the angle between neighbouring spins is small, then the variation in the exchange energy, ΔE_{ex} can be written as [11]:

$$\Delta E_{ex} = -2J_{ij}S^{2}\theta^{2} \qquad 2\text{-}7$$

The *exchange stiffness constant* or simply *exchange constant*, A, is a measure of the force which acts to maintain the electron spin alignment. It can be expressed as [11]:

$$A = J\,S^2 n/a \qquad 2\text{-}8$$

where, S is the value of the individual spins, a is the lattice parameter, and n is the number of atoms in the unit cell [5]. For *simple cubic structure (SC)* $n=1$, for a *body centred cubic (BCC)* $n=2$, for a *face centred cubic (FCC)* $n=4$ and for a *hexagonal close packed (HCP)* structure $n = 2\sqrt{2}$ [5,11]. In most ferromagnetic materials, the exchange stiffness constant is around *1-2* $\times 10^{-6}$ *erg/cm* in *cgs units* and *1-2 x* 10^{-11} *J/m* in *SI units* [11]. As will be seen in later chapters this value is relevant to understanding the angular dependence data from the experimental work with the *curling model* of magnetisation reversal and is needed in simulation studies.

The exchange energy gives rise to long-range order, but it is not the only energy responsible for the overall magnetisation behaviour of ferromagnetic materials. There are various contributions termed magnetic anisotropy energies arising from different origins compete to give the overall magnetisation behaviour within the ferromagnetic materials.

2-6 Magnetic anisotropy

The magnetic moments within ferromagnetic materials prefer to align in a certain direction. This phenomenon is known as *magnetic anisotropy* [12,13]. There are two main sources of magnetic anisotropy in ferromagnetic materials depending on their origin. The first is of internal origin due to spin-orbit coupling and include both *magnetocrystalline anisotropy* and *magnetoelastic anisotropy* [12,13]. The second category is termed *magnetostatic* or *shape anisotropy, which is the most significant anisotropy in measuring nanowires and its origin* is related to the dipole-dipole interactions. These anisotropies strongly influence the overall magnetisation behaviour of the ferromagnetic nanomaterials and the shape of the hysteresis loops obtained.

2-6.1 Magnetocrystalline anisotropy

In ferromagnetic materials, the magnetic moments are usually oriented along a certain crystallographic axis known as the *easy axis of magnetisation*. In contrast, the direction along which it is difficult to align the magnetic moments is referred to as *hard axis of magnetisation*. This phenomenon is known as *magnetocrystalline anisotropy.* This anisotropy is due to the fact that the spin of the electrons in the orbit is strongly coupled to the lattice via a mechanism called *spin-orbit coupling* [12,13]. As an example, the magnetisation curves at room temperature of Fe, Ni and Co materials measured along all the crystallographic axes are shown in Figure 2.4 [5,6]. Fe and Ni have BCC and FCC crystal structure, respectively [5,6]. It is easier to magnetise Fe to saturation along the [100] axis than the [111]. Therefore, the [100] axis is the easy axis of magnetisation for Fe. In contrast, the [111] axis for Ni is the easy axis of magnetisation and the [100] axis is the hard direction of magnetisation. On the other hand, Co has a HCP structure and the *c* axis is the easy axis of magnetisation, whilst all the axes of the basal plane are hard to magnetise[5].

In order to rotate the magnetic moments in a ferromagnetic material away from an easy axis of magnetisation, energy is required to overcome the spin-orbit coupling. This energy is known as *magnetocrystalline anisotropy energy* [5]. In a cubic structure such as Fe and Ni, the *magnetocrystalline anisotropy energy*, E_{ca}, is given by a series expansion in terms of the angles between the direction of magnetisation and the cubic axis as follows [6,7]:

$$E_{ca} = K_0 + K_1(cos^2\theta_1 cos^2\theta_2 + cos^2\theta_2 cos^2\theta_3 + cos^2\theta_3 cos^2\theta_1)$$

$$+K_2 cos^2\theta_1 cos^2\theta_2 cos^2\theta_3 + \cdots\cdots\cdots\cdots\cdots\cdots \qquad 2\text{-}9$$

Where, K_0, K_1, K_2 .... are known as *magnetocrystalline anisotropy constants* for a particular material and θ_1, θ_2, and θ_3 are the angles between the magnetisation direction and the three crystal axes, respectively.

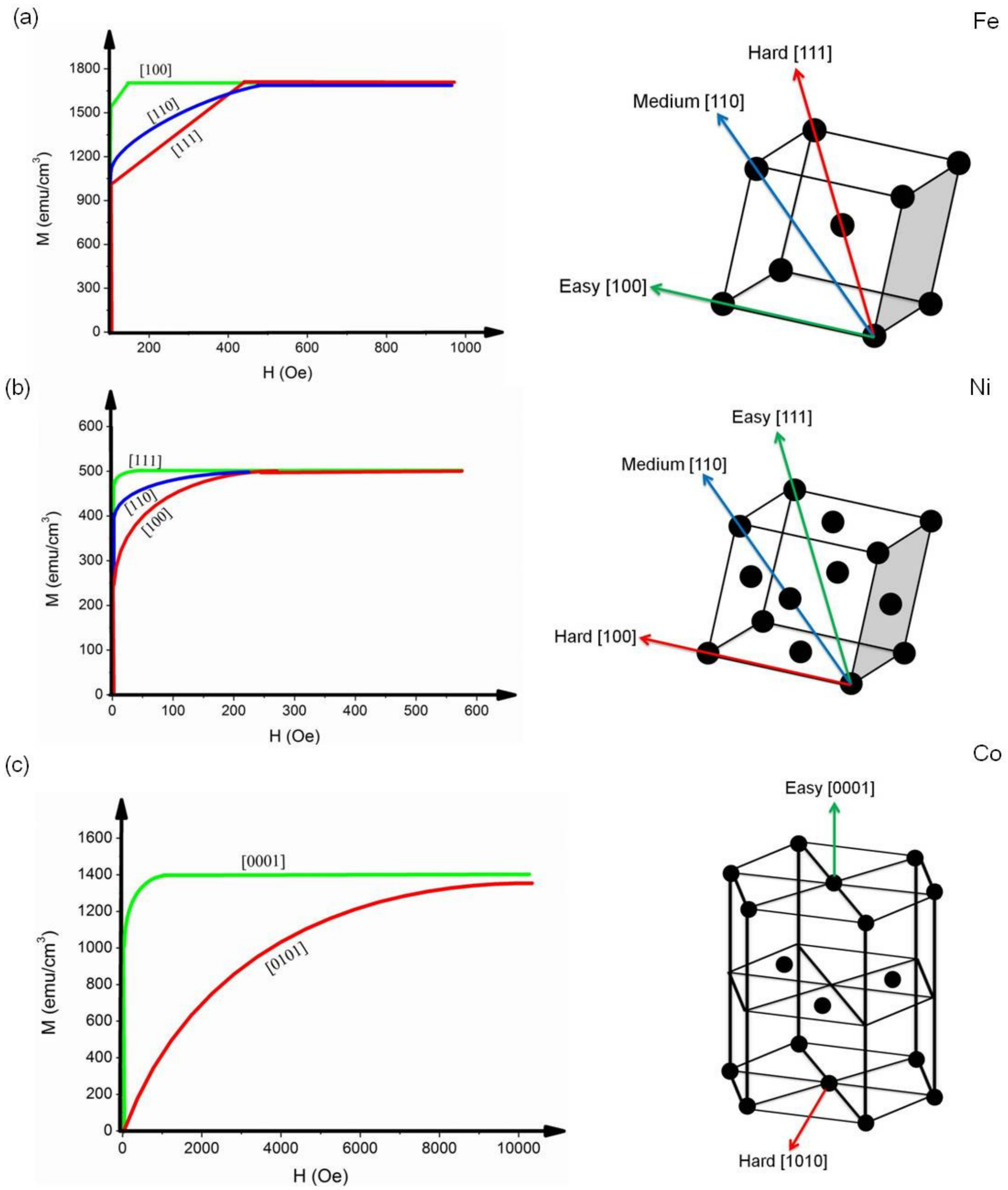

Figure 2.4 Magnetisation hysteresis curves for three different structures of single crystal (a) BCC (Fe), (b) FCC (Ni), and (c) HCP (Co). Reproduced from [5,6].

The magnetocrystalline anisotropy constants, K_0 and K_2 can be neglected because K_0 is independent of the direction of magnetisation and K_2 has very small value compared to K_1 [11]. For example, K_1 and K_2, for nickel are $-5.7\times10^3\ J/m^3$ and $-2.3\times10^3\ J/m^3$, respectively [13], whilst for Ni-Fe alloys, K_1 is dependent on the Ni content. K_1 is found to be around zero when the Ni content is between 75% and 80% [11,14]. The magnetocrystalline anisotropy energy of HCP structure such as Co is given by [5,13]:

$$E_{ca} = K_0 + K_1 sin^2\theta + K_2 sin^4\theta \qquad 2\text{-}10$$

where, θ is the angle between the easy axis, *c*, and the magnetisation direction. The uniaxial anisotropy constants, K_1 and K_2, for cobalt are $4.1\times10^5\ J/m^3$ and $1.2\times10^5\ J/m^3$, respectively[6].

The magnetocrystalline anisotropy can have a significant effect on the magnetic properties and magnetisation reversal process of ferromagnetic nanostructures, as well as the magnetic alignment of nanowires, as will be seen in the later chapters.

2-6.2 Magnetoelastic anisotropy

Magnetoelastic anisotropy is associated with *magnetostriction* which is the change in the dimensions of a ferromagnetic material under the application of an external magnetic field [7]. This effect was first discovered by *Joule* in 1842 and it is sometimes called as *Joule effect*. There are two types of magnetostriction [7]. The first one is known as *spontaneous magnetostriction* and it appears as a result of ordering the magnetic moments into domains when cooling through the Curie temperature [7]. The other type is known as *field induced magnetostriction* which appears as a result of applying a magnetic field to a ferromagnetic material [5,7]. In both cases, magnetostriction, λ, is defined as the fractional change, $(\frac{\Delta l}{l})$, in a material length, *l*, as a result of magnetising the material into its saturation state. Figure 2.5 shows a schematic representation of the change in the material length as a result of applying magnetic field.

The fractional change in the length is small and in the range of 10^{-5}-10^{-6}. For example, the magnetostrictive strain (at room temperature) of Ni along the <100> direction (λ_{100}) is

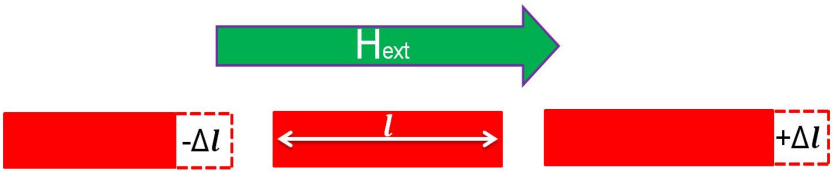

Figure 2.5 Schematic diagram demonstrating the change in the material length Δl as a result of applying a magnetic field H_{ext} for positive $+\Delta l$ and negative $-\Delta l$ magnetostrictive effects.

-45.9×10^{-6} and in the <111> direction (λ_{111}) is -24.3×10^{-6} [6,13]. For Fe λ_{100} is 20.7×10^{-6} and $\lambda_{111} = -21.2\times10^{-6}$ [6,13]. For $Ni_{81}Fe_{19}$, λ_{111} and λ_{100} are extremely small [13]. The positive (negative) signs in the values of magnetostriction indicate that the magnetisation of the material expands (shrinks) as a result of changing from the demagnetised to saturated state [9].

A further effect of magnetostriction is the converse effect where applying tension or compression to a ferromagnetic material can change it is magnetisation behaviour and easy axis. This effect is referred to as the *inverse-magnetostriction effect* [5]. The induced magnetoelastic anisotropy energy, E_{me}, for cubic structures can then be written as [14]:

$$E_{me} = \frac{3}{2}(\lambda_s\, \sigma\, sin^2\theta) \qquad 2\text{-}11$$

where, λ_s, is the average change in the length along the two directions (λ_{100} and λ_{111}), σ is the longitudinal stress (N/m^2) applied on the material and θ is the angle between the measured change in the length and saturation magnetisation.

2-6.3 Shape and magnetostatic anisotropy

It is equally easy to magnetise a sphere of a magnetic material along any direction in the absence of magnetocrystalline anisotropy, whilst non-spherical shapes are more easily magnetised along their longer axis than their short axis [5]. This phenomenon is known as *shape anisotropy*. The shape anisotropy arises from the magnetic dipolar interaction and will be discussed briefly in the following example.

Now consider a uniformly magnetised magnet as shown in Figure 2.6, the magnetic flux density, *B*, is continuous and the material discontinuity leads to the formation of free poles. The poles create a magnetic field, *H*, outside and inside the bar magnet [5]. The magnetic field inside the magnet acts in the opposite direction to the magnetic moments and therefore acts to *demagnetise* the magnet. This *self-demagnetising field* is very important, as it affects both the effective magnetic field and influences the magnetisation behaviour of the magnetic materials.

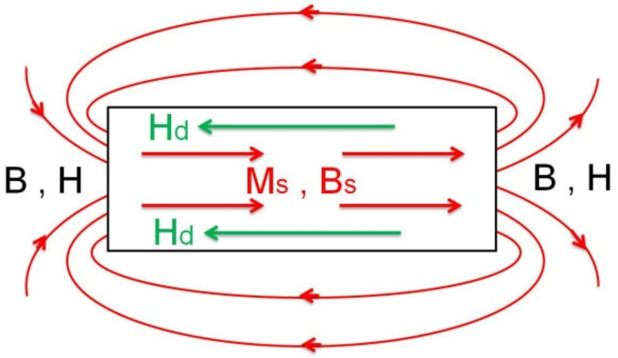

Figure 2.6 Schematic representation of a uniform magnet showing the demagnetising field H_d created by the magnetic moments.

The demagnetising field, H_d, is proportional to the material magnetisation and is given by [7,11]:

$$H_d = -N_d M \tag{2-12}$$

Where, N_d is known as the *demagnetising factor* or *demagnetising coefficient* and is strongly dependent upon the shape of the material and the axis along which the magnetisation lies. For a sphere, the three demagnetising factors are equal to each other [11], whilst for non-spherical shapes, the demagnetising factor is found to be larger along the short axis and hence a large magnetic field is required to saturate the magnetisation, M_s, along that direction. The magnetostatic energy, E_{mag}, for a given magnetisation direction can be expressed in cgs units as [11]:

$$E_{mag} = \frac{1}{2} N_d M_s^2 \tag{2-13}$$

2-6.3.1 Single domain structures

Single domain structures occur when all the magnetic moments within a ferromagnetic material are aligned parallel to each other [5]. It occurs when the size of the structure or particle is smaller than a critical size. It is found that the critical size is independent of the elongation of the particle and magnetocrstalline anisotropy [9], whereas it is dependent on the balance between exchange energy and magnetostatic energy. When the particle exceeds this size, a multi-domain structure is expected to occur.

The demagnetisation factors in a single domain nanostructure can only be calculated exactly for an ellipsoidal shaped object [11]. This is because the magnetisation in this shape is uniform throughout the structure and single valued. The sum of these factors along the three perpendicular axes is constant and related to each other by $N_a + N_b + N_c = 4\pi$ in *cgs units* and equal to *1* in *SI units* [11]. Where, N_a, N_b, and N_c are the demagnetisation factors along the minor, *a*, semi minor, *b*, and major axis, *c*, of the spheroid (see Figure 2.7) [11]. Three types of ellipsoids are available for studying single domain structures. The *prolate spheroid (ellipsoid of revolution)* shown in Figure 2.7 is the most relevant here because it can be used as an approximation for a single domain nanowire [11]. Its semi axis is $c > a = b$ and the aspect ratio, *m*, is defined as $m = c/a$. Therefore, the critical size, r_{sd}, for a prolate spheroid nanowire can be given by [5,11]:

$$r_{sd} = \sqrt{\frac{6A}{N_c M_S^2}\left[\ln\left(\frac{2r_{sd}}{a} - 1\right)\right]} \qquad 2\text{-}14$$

Using equation 2-14, the calculated critical size for Ni and Co nanowires as an example with an aspect ratio around 10 is found to be 300 nm and 70 nm, respectively [11]. Therefore, single domain particles are expected to occur for a radius less than 300 nm for Ni and 70 nm for Co nanowires [11].

2.6.3.2 Principles of domain formation in ferromagnetic materials

The first satisfactory explanation of the idea behind domain formation within ferromagnetic materials was produced by *Landau and Lifshitz* in 1935 [6]. This idea can be understood by considering the magnetic bars presented in Figure 2.8 [5,7].

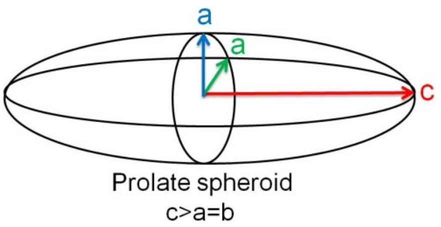

Figure 2.7 Schematic representation of a prolate spheroid (ellipsoid of revelation) which is often used to represents a single domain nanowire. Reproduced from [11].

The illustrations in Figure 2.8(a-c) are cross sections throughout a uniaxial single crystal ferromagnetic material. Figure 2.8(a) shows a single domain structure with high magnetostatic energy as a consequence of the magnetic poles formed on the end surfaces of the bar. Reducing the magnetostatic energy and hence the demagnetising field to nearly half its value is achieved by creating two domains separated by a domain wall, as shown in Figure 2.8(b) [5-7]. Further reduction in the magnetostatic energy to approximately a quarter of its value occurs by creating further domain and domain walls, as shown in figure 2.8(c). A further reduction in magnetostatic energy can be achieved in cubic systems by creating additional domains and 90^{o} walls, as shown in Figure 2.8(d), these closure domains reduce the magnetostatic energy to zero. This configuration completely removes the demagnetising field. Thus, the system can reach an equilibrium domain size in which the energy required to form further domain walls is much greater than the reduction in the magnetostatic energy.

In reality, the formation of domains in ferromagnetic materials is more complicated than those considered in this example, but it gives the principle behind the formation of domains by lowering the energy of the system from a saturated state with high magnetostatic energy to a closure system with lower demagnetisation energy. The addition of domain walls adds energy each time.

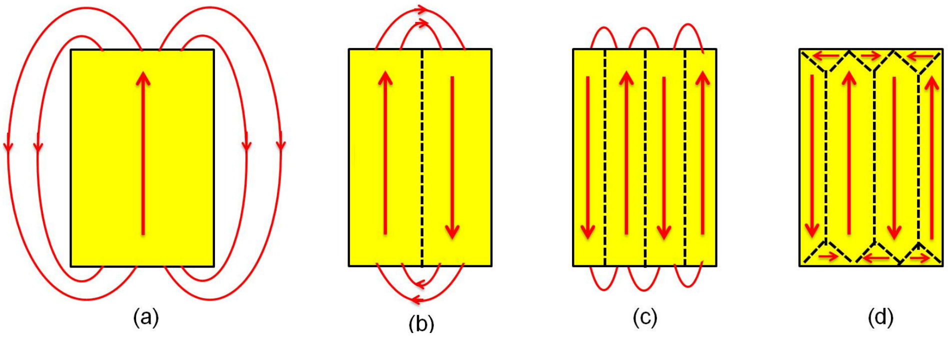

Figure 2.8 Schematic diagrams showing the idea behind domain formation in a perfect uniaxial crystal of a bar magnet. The domain formation lowers the magnetostatic energy of a system by going from a saturated condition shown in (a) with a high demagnetisation field to a flux closure system shown in (d). Reproduced from [7].

2-7 Zeeman energy

The *Zeeman energy*, E_H, is a result of the interaction of an externally applied magnetic field with the magnetisation of a ferromagnetic material. This energy is minimised (maximised) when the magnetic moments are aligned parallel (anti-parallel) to the applied magnetic field and is given by [11]:

$$E_H = -M.H \qquad 2\text{-}15$$

2-8 Total free energy of ferromagnetic materials

The *total free energy density*, E_ρ, of a ferromagnetic material is the sum of the contributions of the magnetic anisotropy energies, the exchange and the Zeeman terms described in the previous sections. It can be expressed as [11]:

$$E_\rho = E_{ex} + E_{ca} + E_{me} + E_{mag} + E_H \qquad 2\text{-}16$$

It will be seen later in the theory of magnetisation reversal that the competitions between these anisotropies in ferromagnetic nanowires under different conditions are responsible for the overall magnetisation behaviour of a ferromagnetic system.

2.9 Ferromagnetism and the theory of domains

As mentioned earlier, the magnetic moments in the ferromagnetic materials are aligned uniformly in volumes called *magnetic domains*. The boundaries between these domains are known as *domain walls*. The domains and the associated domain walls appear as a result of energy minimisation of the system [7]. Domain walls were first suggested by *Bloch* in 1932 [5]. Domain walls are transition regions between adjacent domains where the magnetic moments realigns over many atomic planes and not in one discontinuous jump across a single atomic plane. The total angular displacement of the magnetic moments across the wall is often 90^o or 180^o [5,7]. Depending on the material thickness, two types of domain walls may occur, known as *Bloch* and *Néel domain walls*, as illustrated schematically in Figure 2.9 [7]. The change in the magnetic moments within the *Bloch wall* is out of the plane.

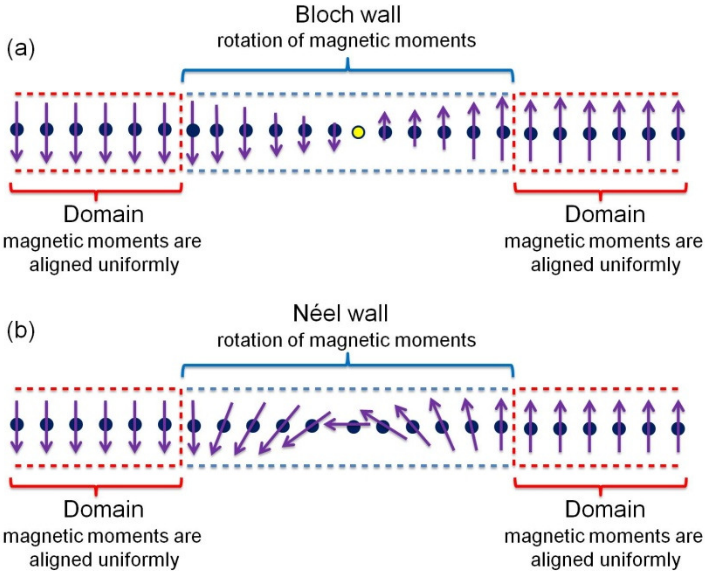

Figure 2.9 Schematic diagrams showing the localised spin moments in the domains and domain walls in a ferromagnetic material. Two types of domain walls are available (a) Bloch wall, and (b) Néel wall depending on the thickness of the ferromagnetic material. Modified from [7].

Its width can be calculated using micromagnetic simulations by minimising the total energy of the wall with respect to its width using the exchange energy and anisotropy energy [5]. The contribution of magnetostatic energy is neglected, because the *Bloch wall* is usually far from the surface of the ferromagnetic material where the uncompensated poles are located. Thus, the *Bloch wall* thickness is strongly dependent on the competition between the exchange energy (which tries to make the wall as wide as possible) and magnetocrystalline anisotropy (which tries to make the wall as thin as possible to reduce the number of spins oriented away from easy axis). The width of *Bloch wall*, δ_{DW}^{Bloch}, is given by [5]:

$$\delta_{DW}^{Bloch} \approx \pi\sqrt{\frac{A}{K_1}} \qquad 2\text{-}17$$

The associated domain wall energies for both 90° and 180° cubic structures can be given by [5]:

$$E_{cubic}^{90} = 2\sqrt{AK_1} \qquad and \qquad E_{cubic}^{180} = 4\sqrt{AK_1} \qquad 2\text{-}18$$

The energy of the domain wall in most ferromagnetic materials is around few erg/cm^2 which is also dependent on the wall orientation in the crystal. For example using equation

2-17, the calculated 90^o and 180^o domain wall thickness for iron was found to be approximately 40 nm and 85 nm, respectively [5].

In contrast, *Néel walls* shown schematically in Figure 2.9(b), appear in ferromagnetic materials where their thickness becomes equivalent to the thickness of *Bloch walls*. As the thickness of the ferromagnetic material becomes very thin, the magnetostatic anisotropy energy cannot be ignored in this case due to the formation of free poles on the wall [5,7]. Therefore, the rotation of the magnetic moments in a *Néel wall* is in the plane of the sample [5,7].

2-10 Magnetic hysteresis and magnetic properties

Magnetic hysteresis has been widely used to characterise the behaviour of ferromagnetic thin films and nanostructures by plotting the *magnetic induction*, *B*, or *magnetisation*, *M*, as a function of an external applied *magnetic field*, *H* [15]. A typical hysteresis loop is shown in Figure 2.10 obtained from measuring a $Ni_{60}Fe_{40}$ thin film. The inset figures are schematic representations of the magnetic moment orientations within the sample at saturation and remanence states.

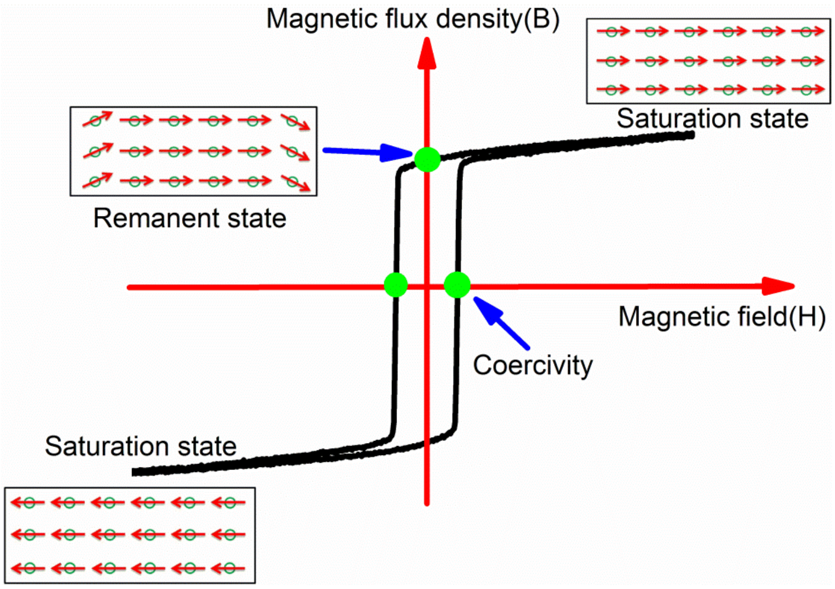

Figure 2.10 A typical hysteresis loop obtained from measuring ferromagnetic NiFe thin film showing the saturation state, remanent state, and coercivity. The insets are schematic diagrams showing the magnetic moment orientations at saturation and remnant states.

The ratio of the *remanent magnetisation*, M_R, to the *saturation magnetisation*, M_S, is referred to as the *squareness ratio*, $S=M_R/M_S$ [11], this is widely used in describing hysteresis loops. The squareness ratio is an indication of the fraction of magnetisation along the measurement axis at zero fields, hence informing on the anisotropy. In order to reduce the remanent magnetisation or saturation magnetisation to zero, an extra reversed applied magnetic field is required. This field is known as the *coercive field* or *coercivity*, H_c, respectively [7]. The coercivity is strongly dependent on the composition, geometry, dimensions, magnetic history and the crystalline structure of the material under investigation as well the angle of applied field with respect to the sample long axis [11]. Other significant terms that are commonly used in describing the magnetisation reversal in nano-materials are the *switching field*, H_{sw}, and *nucleation field*, H_n [5,11]. The switching field is the field required to make the slope of the hysteresis loop a maximum, $\frac{d^2M}{dH^2}=0$ (i.e. an abrupt change in the magnetisation) [11]. The nucleation field is a theoretical concept used for describing the change in the magnetisation when just it begins in a single domain state.

Several techniques can be used to measure magnetic hysteresis loops to derive significant information about the ferromagnetic materials including thin films and arrays of ferromagnetic nanostructures. These include *vibrating sample magnetometers (VSM)* [16-18], *superconducting quantum interference devices (SQUID)* [19-20] and *alternating gradient magnetometers (AGM)* [21-22]. In addition, the *magneto-optical Kerr effect (MOKE) magnetometry* can be used to study these properties in thin films [23], planar [24-25] and more recently cylindrical nanowires [26-28]. The principles of MOKE magnetometry are described in some detail in chapter five.

2.11 Micromagnetic theory

Micromagnetic theory was first introduced by *William Fuller Brown, Jr.* in 1963 [29]. It is defined as the science that deals with the electron spin interactions in ferromagnetic materials on sub-micrometre length scales between atoms and domains. It deals with the local directions of magnetisation as a function of position considering their magnitude as constant [29,30]. Thus, micromagnetic theory does not require the need for domains and domain walls and can be used to find the *distribution of magnetisation vectors* within ferromagnetic materials which in turn can lead to the appearance of domains and domain walls. This can be achieved by finding the *lowest energy* for the sum of all the energy contribution terms in equation 2-16. For simplification in micromagnetic analysis some of these terms can be ignored depending upon the magnetic system in use. As an example, the magnetostriction and magnetocrystalline anisotropy energies in $Ni_{81}Fe_{19}$ nanomaterials are extremely small and close to zero [13], therefore they can be ignored in micromagnetic modelling.

Due to the contributions of all the energy terms on the distribution of the magnetic moments, for a given applied magnetic field there is an *effective field*, H_{eff}, that can drive the motion of the magnetic moments given by [31]:

$$H_{eff} = -\frac{1}{\mu_0}\frac{\partial E_{Total}}{\partial M} \qquad 2\text{-}19$$

Where, E_{Total} is the total free energy given in equation 2-16, M is the magnetisation and μ_0 is the permeability of free space. The effective field exerts a torque on the magnetisation within the sample to drive its orientation until the torque is negligible at thermodynamic equilibrium [30]. To reach thermodynamic equilibrium a *dissipative process* is required, as schematically shown in Figure 2.11(a). The precessional motion of the magnetic moments in an effective field was first described by *Landau and Lifshitz* in 1935 and is given by:

$$\frac{\partial \mathrm{M}}{\partial \mathrm{t}} = -|\gamma|\mathrm{M} \times H_{eff} \qquad 2\text{-}20$$

However, in all materials there is a natural decay of the magnetisation precession over time [32] due to the existence of different factors such as defects in the material, magnon-

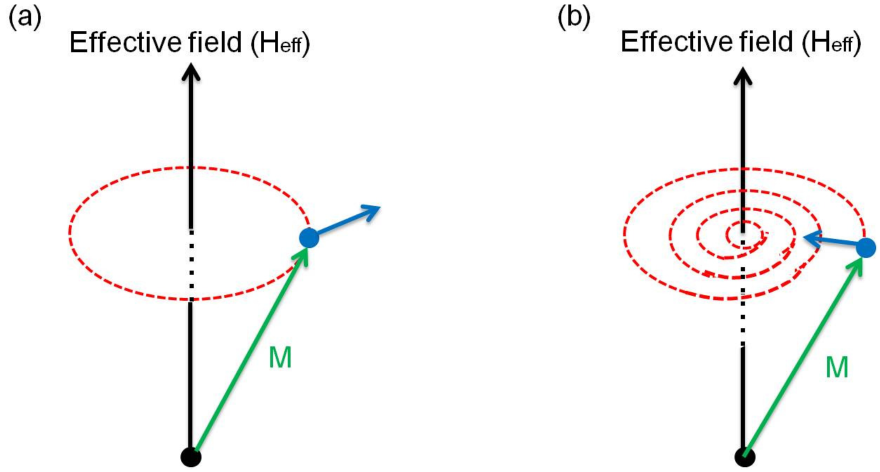

Figure 2.11 Schematic representation of the effect of torque exerted on the magnetisation vector which induces (a) Precessional motion, and (b) damped precision leading the magnetisation aligning in the direction of the effective field. Reproduced from [30].

magnon scattering, and eddy currents as illustrated in the schematic diagram shown in Figure 2.11(b) [30].

In 1955 *Gilbert* introduced the idea of a *phenomelogical damping parameter*, α, to represent these factors into equation 2-20 to give the following equation [33]:

$$\frac{\partial M}{\partial t} = -|\gamma| M \times H_{eff} + \alpha \frac{M}{M_s} \times \frac{\partial M}{\partial t} \qquad 2\text{-}21$$

Where, α is not constant for common ferromagnetic materials and it is nonlinearly dependent on the magnetisation [30]. In micromagnetic simulations, the damping parameter is often set to a value between 0.1 and 1. Using these higher values results in a reduced computation time as it governs the rate to reach equilibrium. In reality, the damping parameter is usually smaller, e.g. 0.01 for permalloy.

The *Landau-Lifshitz-Gilbert* (*LLG*) equation is used to solve the time-dependent micromagnetic problems in two and three dimensional ferromagnetic structures using code such as the *object oriented micromagnetic framework (OOMMF) software* available at the *national institute of standard technology (NIST)* website [34]. Further discussion on this software is given in chapter five.

2.12 Magnetisation reversal in ferromagnetic nanowires

M*agnetisation reversal* can be defined as the change in the magnetisation from an energy minima state to a different state. According to theoretical analysis and micromagnetic calculations there are various distinct mechanisms that are able to describe the magnetisation reversal processes in single domain nanoparticles and nanowires. Models considered here are *coherent rotation of Stoner-Wohlfarth* and *incoherent rotation* including *curling*, *buckling* and *fanning model*s. Brief theoretical descriptions of these models are presented in the following subsections. Their applicability to a system as will be seen later depends upon various parameters.

2-12.1 Magnetisation reversal via coherent rotation (Stoner-Wohlfarth model)

The simplest model of reversal was investigated classically by *Stoner and Wohlfarth* (*S-W*) in 1948 [35]. This model describes the magnetisation reversal process in a single domain ferromagnetic nanostructure. In which the spins of all atoms rotate simultaneously and uniformly in-phase with each other during the application of an external magnetic field at an angle with respect to the anisotropy axis (easy axis of magnetisation), as shown schematically in Figure 2.12. Figure 2.12 (a) represents the distribution of magnetic moments within the nanoparticle during the application of magnetic field at an angle, θ_o, with respect to the anisotropy axis, and (b) the coordinate system (ellipsoid of revolution) used here for the theoretical analysis in this model.

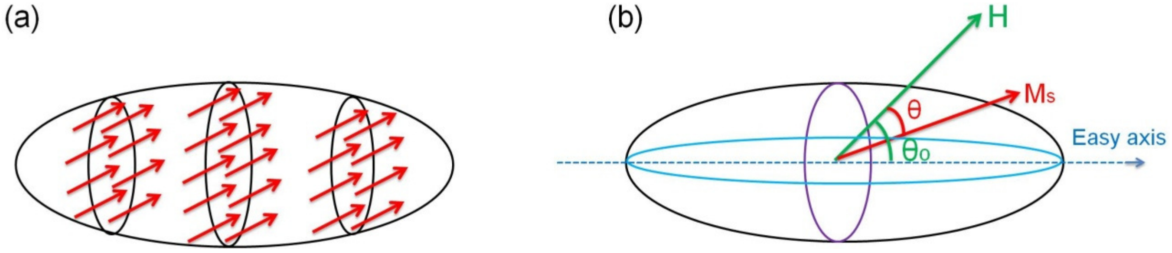

Figure 2.12 (a) Schematic representation of the distribution of magnetic moments within the particle of Stoner-Wohlfarth in which the magnetic moments rotate simultaneously and coherently during the reversal, and (b) the coordinate system used for the theoretical analysis. Reproduced from [11].

For simplicity in this model, different assumptions have been used. For instance, the magnetocrystalline anisotropy energy was neglected from the calculations as it has a small effect compared with the magnetostatic anisotropy energy [35]. The magnetoelastic anisotropy was also ignored from the calculations. The particle is assumed to be uniform and free from imperfections and its shape is approximated to an ellipsoid of revolution [6,11]. Thus, the total *free* energy, E_{Total}, in this model can be written as a function of demagnetising energy (magnetostatic energy, E_{mag}) and *Zeeman energy,* E_H as follows [11]:

$$E_{Total} = E_{mag} + E_H \qquad 2\text{-}22$$

The magnetostatic energy of the particle is given by [11]:

$$E_{mag} = K_u \, sin^2(\theta - \theta_o) \qquad 2\text{-}23$$

where, θ is the angle between the magnetic field and the magnetisation component, M_s, as shown in Figure 2.12(b). K_u is the uniaxial magnetostatic anisotropy constant. For a prolate spheroid particle with high aspect ratio, the demagnetisation factor along the hard axis is 2π and along the easy axis is 0 in cgs units [35]. Therefore, the difference in the demagnetisation factors is 2π and hence:

$$K_u = \pi M_s^2 \qquad 2\text{-}24$$

Using equations 2-15 and 2-23, the total energy can be expressed as [11]:

$$E_{Total} = K_u \, sin^2\,(\theta - \theta_o) - H\,.M \qquad 2\text{-}25$$

The magnetisation component, M, along the field axis is:

$$M = M_s \, cos\theta \qquad 2\text{-}26$$

Therefore, equation 2-25 can be written as [11]:

$$E_{Total} = K_u \, sin^2\,(\theta - \theta_o) - H\,.M_s \, cos\theta \qquad 2\text{-}27$$

When, $\frac{dE}{d\theta} = 0$, the total energy is minimised, therefore equation 2-27 at equilibrium position of M_s is [11]:

$$2K_u sin(\theta - \theta_o) cos(\theta - \theta_o) + H \,.\, M_s \; sin\,\theta \; = 0 \qquad 2\text{-}28$$

Let,

$$h \; = \; H \,/\, (2K_u / M_s) \qquad 2\text{-}29$$

and

$$m \; = \; M / M_s \qquad 2\text{-}30$$

Then,

$$sin\,[2(\theta - \theta_o)] = -2h \sin\theta \qquad 2\text{-}31$$

where, h and m are referred to as *reduced field* and *reduced magnetisation*, respectively. Solving equation 2-28 using trigonometric relations, reduced field and reduced magnetisation yields the general solution of the magnetisation, m, with respect to, h, at a definite angle, θ_o as follows [11]:

$$2m(1 - m^2)^{1/2} cos2\theta_o + (1 - 2m^2) sin2\theta_o$$
$$= \pm 2h(1 - m^2)^{1/2} \qquad 2\text{-}32$$

The hysteresis loops can be obtained by solving equation 2-32. When $\partial h / \partial m = 0$ and $\partial^2 E / \partial \theta^2 > 0$, the reduced switching field, h_{sw}, and reduced coercivity, h_c, can be obtained as follows [11,36]:

$$h_{sw} \; = \; (cos^{2/3}\theta_o + sin^{2/3}\,\theta_o)^{-3/2} \qquad 2\text{-}33$$

$$h_c \; = \; sin\theta_o \, cos\,\theta_o \qquad 2\text{-}34$$

where, $h_{sw} \; = \; H_{sw} \,/\, (2K_u \,/\, M_s)$ and $h_c \; = \; H_c \,/\, (2K_u \,/\, M_s)$

Solving equation 2-32 for various angles θ_o, the hysteresis loops can be obtained with two identified regimes. When the magnetic field is applied between *0°* and *45°* (i.e. close to easy axis of magnetisation), relatively rectangular hysteresis loops are obtained and the coercivity is equal to the switching field, whilst when the field is applied above *45°* (i.e.

approaching the hard axis of magnetisation), sheared hysteresis loops are obtained and the coercivity in this case is not equal to the switching field. Thus, the change in the orientation of the magnetic moments within this model may occur suddenly via switching or smoothly via rotation. Figure 2.13 show examples of the hysteresis loops obtained from solving equation 2-32 when the field is applied at four different angles 0^o, 30^o, 60^o and 90^o to the anisotropy axis.

The angular dependence of the reduced switching field and reduced coercivity from solving equations 2-33 and 2-34 are shown in Figure 2.14. These figures demonstrate that $h_{sw} = h_c$ when $0^o<\theta_0<45^o$ and $h_{sw} \neq h_c$ when $45^o<\theta_0<90^o$ [11]. Importantly, the switching field and coercivity in the *S-W* model are independent of the size of the nanomaterial, due to the rapid increase of the magnetostatic energy with nanoparticle size [5].

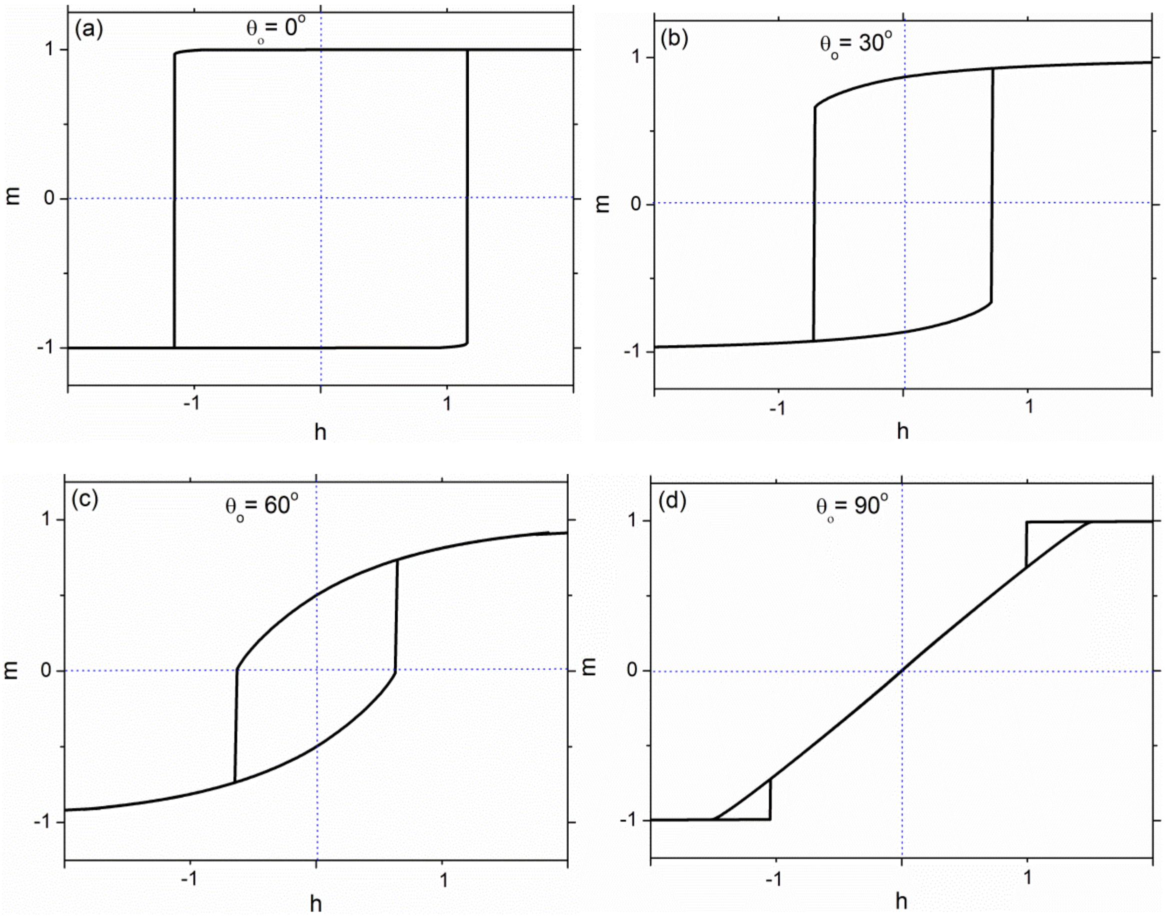

Figure 2.13 Hysteresis loops obtained from solving equation 2-32 of Stoner-Wohlfarth model assuming an applied field at four different angles (a) 0^o, (b) 30^o, (c) 60^o and (d) 90^o with respect to the easy axis of magnetisation. Reproduced from [11].

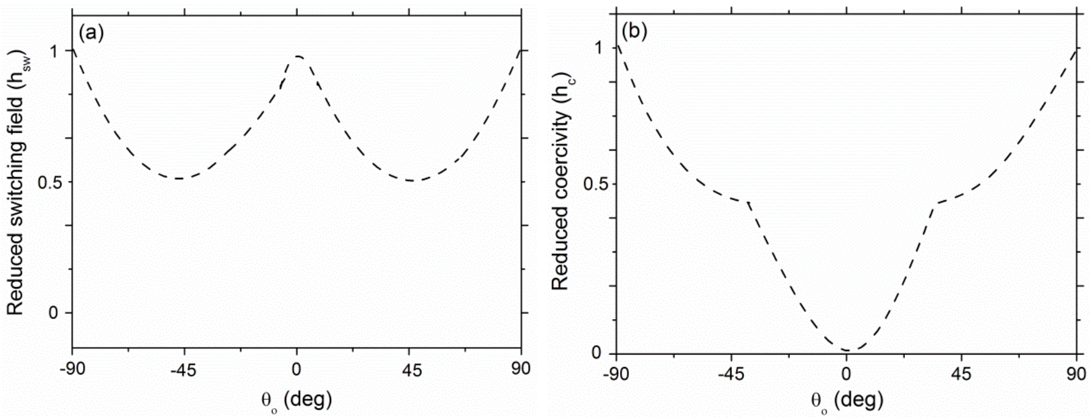

Figure 2.14 Angular dependence of (a) reduced switching field, h_{sw}, and (b) reduced coercivity, h_c, calculated using equations 2-33 and 2-34 of S-W model. The reduced coercivity and switching fields are normalised by $2K_u/M_s$. Reproduced from [11].

The *Stoner-Wohlfarth model* has several limitations due to the usage of several assumptions [37]. As stated earlier, the model assumes that the particle is a single domain structure despite the fact that most ferromagnetic materials are multidomain structures. This model neglects the imperfections, roughness and dimension variations which may have a great influence on magnetisation reversal process. Moreover, the calculations have been performed on the particles that have a simple uniaxial anisotropy such as Co particles, whereas other compositions such as Fe and Ni have cubic anisotropy which complicates the situation [37]. Furthermore, it has been found experimentally as will be seen in chapter three that the measured coercivity of arrays of particles are much lower than the predicted by this model [38]. In spite of all these limitations, this model of reversal can give a useful picture of uniformly magnetised nano-materials. This model is dominated by uniaxial shape anisotropy.

2-12.2 Magnetisation reversal via incoherent rotation

Since 1950 researchers have tried to study magnetisation reversal in magnetic recording particles and very thin elongated particles [5,39,40]. They found that these particles have much lower values of nucleation fields than predicted by the *S-W model* [5,40]. This led the researchers to find other possible models of magnetisation reversal. Therefore, incoherent rotational processes such as *curling* [41-43], *buckling* [44-48] and *fanning* [5,49-52] have been considered to describe the magnetisation reversal in ferromagnetic nanostructures. The following subsections briefly describe these models.

2-12.2.1 Curling rotation model

Curling rotation is theoretically discussed using micromagnetic calculations [5,6,11]. This model of reversal is expected to occur when the particle size is still in a single domain regime but larger than a critical size known as *exchange length*. It assumes that the magnetic moments within infinitely long particles rotate in a plane perpendicular to the anisotropy axis and they are not parallel to each other during reversal, as shown schematically in Figure 2.15, reducing the longitudinal component of the magnetisation and hence the magnitude of the switching field [11]. The distribution of the magnetic moments in such configuration eliminates the formation of free poles and hence the magnetostatic energy [5]. Therefore, this model of reversal is entirely dominated by the exchange energy. In contrast, decreasing the aspect ratio of the particles, magnetostatic energy will be generated because the magnetic moments within the ellipsoid will no longer be parallel to its surface and the *S-W model* [5] will dominate.

The switching field, H_{sw}, of the curling model for an infinite cylinder is given by [53]:

$$H_{sw} = \frac{M_s}{2} \frac{a(1+a)}{\sqrt{a^2+(1+2a)cos^2\theta_o}} \qquad \text{2-35}$$

The reduced switching field is $h_{sw} = H_{sw}/2\pi M_s$ and:

$$a = -1.08(\frac{r_0}{r})^2 \qquad \text{2-36}$$

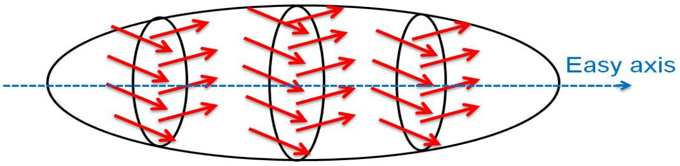

Figure 2.15 Schematic representations showing the distribution of magnetic moments in curling model in a prolate spheroid particle. It assumes the magnetic moments rotate in a plane perpendicular to the anisotropy (easy) axis of the nanowire. Reproduced from [6,11].

where, r and r_o are the *particle radius* and *exchange length*, respectively. The ratio, $\frac{r_0}{r}$, is known as *reduced radius*, S. The exchange length is a parameter that defines the transition from uniform rotation to the curling model. When the diameter of the particle is in the single domain regime but larger than the exchange length, the curling model is expected to occur, whereas for diameters less than the exchange length, *Stoner-Wohlfarth* switching is expected [5,11]. For example, when the diameter of ferromagnetic Ni nanowire is greater than 50 nm, curling model was found to be the dominating mechanism, whereas for wires with diameters less than 30 nm, the magnetisation reversal mechanism switched to S-W coherent rotation.

The exchange length is dependent upon the critical size, r_{sd}, and independent of the actual size and the shape of the particle. It is given by [36]:

$$r_o = A^{1/2}/M_s \qquad 2\text{-}37$$

In curling reversal model the change in the magnetisation is an abrupt process and the switching field is very close to the nucleation field and the coercivity is equal to the switching field in all angles of applied field [11,54]. The angular dependence of the switching field can be obtained by solving equation 2-35 for different angles. As an example, Figure 2.16 shows the angular dependence of the reduced coercivity for particles with (a) three different aspect ratios (5,10 and 50) having the same reduced radius (S = 3), and (b) three different reduced radii (2, 3 and 5) with the same aspect ratio (10). In general, the coercivity is found to increase slowly at low angles and increases rapidly at higher angles of applied magnetic field with respect to the long axis of the nanoparticle. The coercivity is dependent on the aspect ratio, size and shape of the particle [5,47]. With increasing aspect ratio the coercivity increases due to a reduction of the magnetostatic energy and the exchange energy dominates the behaviour. The coercivity also decreases as the particle diameter increases because the exchange energy per unit volume decreases with increasing particle size [47].

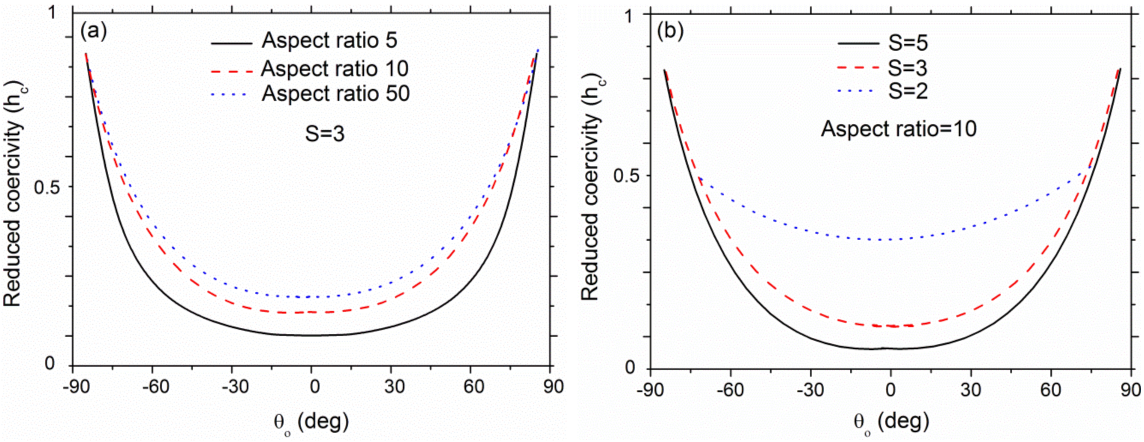

Figure 2.16 Reduced coercivity as a function of prolate spheroid axial angle for the curling model calculated by solving equation 2-35 for three different (a) aspect ratios with $S = 3$, and (b) reduced radius with aspect ratio =10 [11].

2-12.2.2 Buckling rotation model

The *Buckling model* is another incoherent rotation of magnetisation reversal mechanism that occurs in single domain ferromagnetic nanoparticles. It was first described in 1957 by Frei et. al. [39]. This model of reversal is similar to the coherent rotation of the *Stoner-Wohlfarth* model, but the nucleation field obtained with this model is lower than that obtained by coherent rotation or the curling model over a very narrow range of reduced radius (near unity) [39]. In this model, the magnetic moments are uniform in any plane perpendicular to the easy axis with the magnetisation distribution varying periodicity along the easy axis in a wave-like pattern [11,47]. This is illustrated schematically in Figure 2.17 [11].

The buckling model has been investigated theoretically using different shapes of particles [39,40]. It has been proved that this model can never take place in shapes ranging from oblate spheroids up to spheres [40] and also in prolate spheroids with small aspect ratio. However, it is found difficult to completely rule out the possibility of this model in more elongated prolate spheroids. In this model square hysteresis loops have been obtained in infinite circular cylinders [40] when the field was applied parallel to their long axis. In this case the nucleation field is equal to the coercive field [47].

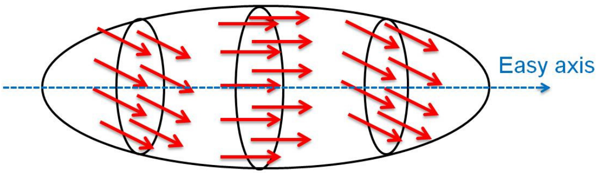

Figure 2.17 Schematic representations showing the distribution of magnetic moments in buckling model of reversal. The magnetic moments are uniform in any plane perpendicular to the particle axis with the existence of periodicity of the magnetisation distribution along the particle long axis. Reproduced from [11].

2-12.2.3 Fanning rotation model

The *fanning rotation* model of magnetisation reversal was first introduced by *Jacob and Bean* in 1955 [5]. This model of reversal was suggested by the shape of the iron particles grown by electrodeposition which has a *peanut shape* with periodic bulges rather than smooth sides. Therefore, these particles were approximated as a *chain of spheres* with the same diameter [5,6,49]. Usually, the angle of the magnetic moments along the axis of the chain is constant and therefore called *symmetric fanning*. A schematic diagram of this model is shown in Figure 2.18 [5,6].

The spheres are assumed to be single domain structures without anisotropy of their own and without exchange interaction between the adjacent spheres due to the assumption of minimal contact [5]. If the contact area is considered to be high, the magnetic moments favour coherent reversal according to the *S-W model*. Under the application of an external magnetic field on the chain of spheres, the magnetic moments in each sphere fans out coherently by rotating in alternate directions in the different sphere.

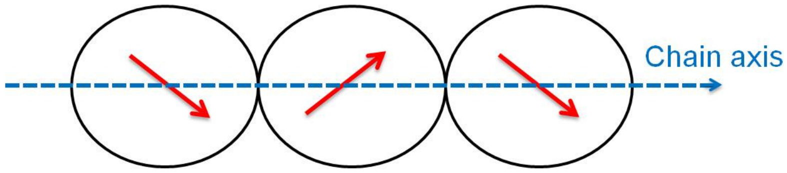

Figure 2.18 Schematic diagram showing the orientation of magnetic moments in the fanning model. It approximates the particle as a chain of spheres according to their shape. The angle of the magnetic moments in the fanning model is constant along the long axis of the chain and hence it is called symmetric fanning [5,6].

This is in contrast to the *S-W model* where the magnetic moments rotate at the same polar angle. In this way the hysteresis loop is characterised by a square shape. The coercivity in this model is independent of the particle size as in the S-W model [5]. The predictions of this theory were found to be in a good agreement with the experimental results on elongated iron nanoparticles [5].

2-13 Chapter references

1. Kittel, C. "Introduction to solid state physics" 2nd edition, John Wiley & Sons, Inc., 2000.
2. Rosenberg, H. M. "The solid state: An introduction to the physics of crystals for students of physics, materials science and engineering" 2nd edition, Oxford University Press Inc., New York, 1978.
3. Turton, Richard "The physics of solids" Oxford University Press Inc., New York, 2000.
4. Omar, M. A. "Elementary solid state physics: Principles and applications" Addison-Wesley Publishing Com. Inc., 1975.
5. Cullity, B. D. & Graham, C. D."Introduction to magnetic materials" 2nd edition, John Wiley & Sons, Inc., USA, 2009.
6. Carey, R. & Isaac, E. D. "Magnetic domains and techniques for their observations" The English Universities Press Ltd., UK, 1966.
7. Jiles, D. "Introduction to magnetism and magnetic materials" 2nd edition, Chapman and Hall/CRC, New York, 1998.
8. Philipe, Robert "Electrical and magnetic properties of materials" Artech House Inc., 1988.
9. Aharoni, Amikam "Introduction to the theory of ferromagnetism" Clarendon Press Inc., Oxford, 1998.
10. Tebble, R. S. "Magnetic Domains" Butler and Tanner Ltd., France & London, 1969.
11. Sun L., Hao Y., Chien C. L. & Searson P. C. "Tuning the properties of magnetic nanowires" *IBM J. RES. & DEV.*, 49(1),79, 2005.
12. Skomski, R. "Topical review: Nanomagnetics" *J. Phys.: Condens. Matter*, 15, R 841, 2003.
13. Chikazumi, Soshin "Physics of ferromagnetism" 2nd edition, Clarendon Press, Oxford, 1997.
14. Bozorth, R. M. "Ferromagnetism" John Wiley & Sons Inc., Hoboken, New Jersey, 1951.
15. Fishbane, M. Paul, Gasiorowicz, G. Stephen & Thornton, T. Stephen "Physics for scientists and engineers with modern physics" 3rd edition, Pearson Education Inc., New Jersey, USA, 2005.
16. Garcıa, J. M., Asenjo A., Velazquez J., Garcıa D., Vazquez M., Aranda P. & Ruiz-Hitzky E. "Magnetic behaviour of an array of cobalt nanowires" *J. Appl. Phys.*, 85(8), 5480, 1999.
17. Ren Y., Liu, Q. F., Li, S. L., Wang, J. B. & Han, X. H. "The effect of structure on magnetic properties of Co nanowire arrays" *J. Mag. Mag. Mat.*, 321(3), 226, 2009.
18. Cheng, S. F., Lubitz, P., Zheng Y. & Edelstein, A. S. "Effects of spacer layer on

growth, stress and magnetic properties of sputtered permalloy film" *J. Mag. Mag. Mat.*, 282,114, 2004.

19. Shamaila S., Sharif R., Riaz S., Ma M., Khaleeq-ur-Rahman M. & Han, X. F. "Magnetic and magnetization properties of electrodeposited fcc CoPt nanowire arrays" *J. Mag. Mag. Mat.*, 320(12), 1803, 2008.
20. Encinas-Oropesa, A., Demand M., Piraux, L., Huynen I. & Ebels, U. "Dipolar interactions in arrays of nickel nanowires studied by ferromagnetic resonance" *Phys. Rev. B*, 63(10), 104415, 2001.
21. Yuan J., Pei W., Hasagawa T., Washiya T., Saito H., Ishio S., Oshima H. & Ken-ichi Itoh "Study on magnetization reversal of cobalt nanowire arrays by magnetic force microscopy" *J. Mag. Mag. Mat.*, 320(5), 736, 2008.
22. Chen X., Qiu H., Qian H., Wu P., Wang F., Pan L. & Tian Y. "Characteristics of Ni_xFe_{100-x} films deposited on SiO_2/Si(100) by DC magnetron co-sputtering" *Vacuum*, 75(3), 217, 2004.
23. Bergenti I., Riminucci A., Arisi E., Murgia M., Cavallini M., Solzi M., Casoli F. & Dediu V. "Magnetic properties of cobalt thin films deposited on soft organic layers" *J. Mag. Mag. Mat.*, 316(2), e987, 2007.
24. Adeyeye, A. O., Bland, J. A. C., Daboo C., Lee J., Ebels U. & Ahmed H. "Size dependence of the magnetoresistance in submicron FeNi wires" *J. Appl. Phys.*, 79(8), 6120, 1996.
25. Atkinson D., Allwood D., Xiong G., Cooke, M. D., Faulkner C. C. & Cowburn R. P. "Magnetic domain-wall dynamics in a submicrometre ferromagnetic structure" *Nat. Mat.*, 2(2), 85, 2003.
26. Lupu N., Lostun M. & Chiriac H. "Surface magnetization processes in soft magnetic nanowires" *J. Appl. Phys.*, 107(9), 09E315, 2010.
27. Sharma S., Barman A., Sharma M., Shelford, L. R., Kruglyak, V. V. & Hicken, R. J. "Structural and magnetic properties of electrodeposited cobalt nanowire arrays" *Sol. St. Comm.*, 149, 1650, 2009.
28. Sultan, M. S., Das B., Sen P., Mandal K. & Atkinson D. "Template released ferromagnetic nanowires: Morphology and magnetic properties" *J. Spintron. Magn. Nanomater.*, 1, 1, 2012.
29. Brown, William Fuller Jr. "Micromagnetics" John Wiley & Sons Inc., USA, 1963.
30. Fidler Josef & Schrefl Thomas "Topical Review: Micromagnetic modelling: The current state of art" *J. Phys. D: Appl. Phys*., 33, R135, 2000.
31. Han N., Guo G., Zhang L., Zhang G. & Song W."Magnetization reversal for Ni nanowires studied by micromagnetic simulations" *J. Mater. Sci. Technol.*, 25(2), 151, 2009.
32. Brown, William Fuller Jr. "Magnetostatic principles in ferromagnetism" North Holland Publishing Co., Amsterdam, Volume 1, 1962.
33. Gilbert, T. L. "A Lagrangian formulation of the gyromagnetic equation of the magnetisation field" *Phys. Rev*., 100, 1243, 1955.
34. "http://math.nist.gov/oommf/software.html" accessed on 15th July 2012.
35. Stoner, E. C. & Wohlfarth, E. P. "A mechanism of magnetic hysteresis in heterogeneous alloys" *Phil. Trans. R. Soc. Lond. A*, 240(826), 599, 1948.
36. Rheem, Y., Yoo, B., Beyermann, W. P. & Myung, N. V. "Electro-and magneto-transport properties of a single CoNi nanowire" *Nanotech.*, 18(12),125204, 2007.

37. Tannous C. & Gieraltowski J. "The Stoner–Wohlfarth model of ferromagnetism" *Eur. J. Phys.*, 29(3), 475, 2008.
38. Ferré R., Ounadjela K., George J., Piraux L. & Dubois S. "Magnetization processes in nickel and cobalt electrodeposited nanowires" *Phys. Rev. B*, 56(21), 14066,1997.
39. Frei, E. H., Shtrikman, S. & Treves, D. "Critical size and nucleation field of ideal ferromagnetic particles" *Phys. Rev.*,106, 1957.
40. Aharoni, A. & Shtrikman, S. "Magnetization curve of the infinite cylinder" *Phys. Rev.*, 109(5), 1522, 1958.
41. Aharoni, A. "Curling reversal mode in nonellipsoidal ferromagnetic particles" *J. Appl. Phys.*, 86(2), 1041, 1999.
42. Skomski R., Zeng H., Zheng M. & Sellmyer D. "Magnetic localization in transition-metal nanowires" *Phys. Rev. B*, 62(6), 3900, 2000.
43. Goolaup S., Singh N., Adeyeye A. O., Ng V. & Jalil M. B. A. "Transition from coherent rotation to curling mode reversal process in ferromagnetic nanowires" *Eur. Phys. J. B*, 44, 259, 2005.
44. Aharoni, A. "Magnetization buckling in a prolate spheroid" *J. Appl. Phys.*, 60(3), 1118, 1986.
45. Oliveira, A. B. De, Silva, G. L. D., Rezende, S. M. & Azevedo, A. "Magnetization reversal in single ferromagnetic rectangular nanowires" *J. Phys.: Conf. Series*, 200(7), 072023, 2010.
46. Moon K., Lee J., Jung M., Shin K. & Choe S. "Incoherent domain configuration along wire width in permalloy nanowires" *IEEE Trans. Mag.*, 45(6), 2485, 2009.
47. Gao, J.-H., Sun, D.-L., Zhan, Q.-F., He, W. & Cheng, Z.-H. "Magnetization reversal process and magnetic relaxation of self-assembled Fe_3Pt nanowire array with different diameters: Experiment and micromagnetic simulations" *Phys. Rev. B*, 75(6), 1, 2007.
48. Pignard S., Goglio G., Radulescu A. & Piraux L. "Study of the magnetization reversal in individual nickel nanowires" *J. Appl. Phys.*, 87(2), 824, 2000.
49. Milne, G. A. & Dunlop, D. J. "Angular variation of the magnetic properties and reversal mode of aligned single-domain iron nanoparticles" *J. Geophys. Res.*, 111(B12S08), 1, 2006.
50. Tang X., Wang G. & Shima M. "Magnetic layer thickness dependence of magnetization reversal in electrodeposited CoNi/Cu multilayer nanowires" *J. Mag. Mag. Mat.*, 309, 188, 2007.
51. Han, G. C., Zong, B. Y., Luo, P. & Wu, Y. H. "Angular dependence of the coercivity and remanence of ferromagnetic nanowire arrays" *J. Appl. Phys.*, 93(11), 9202, 2003.
52. Gao, J.-H., Zhan, Q.-F., He, W., Sun, D.-L. & Cheng, Z.-H. "Thermally activated magnetization reversal process of self-assembled $Fe_{55}Co_{45}$ nanowire arrays" *J. Mag. Mag. Mat.*, 305(2), 365, 2006.
53. Rheem, Y., Yoo, B., Beyermann, W. P. & Myung, N. V. "Magnetotransport studies of a single nickel nanowire" *Nanotech.*, 18, 1, 2007.
54. Ghaddar A, Gloaguen F. & Gieraltowski J. "Magnetic properties of ferromagnetic nanowire arrays: Theory and experiment" *J. Phys.: Conf. Series*, 200(7), 072032, 2010.

Chapter three

Magnetic, magnetisation reversal behaviour and alignment of ferromagnetic nanowires

3-1 Introduction

This chapter presents a review of the magnetic and magnetisation reversal behaviour of ferromagnetic nanowires prepared by electrodeposition and in addition, a review of previous work on the alignment of template released nanowires that related to the main work in this thesis. Most of the studies described were performed on nanowires of a single element or alloys of a range of compositions with diameters that ranging from 5-500 nm and lengths of several micrometers. Many studies were carried out on nanowires embedded in their original templates, due to the simplicity of these measurements and the opportunity to use a wide range of investigative techniques owing to their large net magnetisation and associated high signal, as well as the fact that these wires are more protected against oxidation. The preparation and the crystalline structure of a range of ferromagnetic nanowires are first discussed. Then, the effects of nanowire growth conditions, temperature, diameter, length, magnetostatic interactions and filling factor on their magnetic behaviour is summarised and discussed with some examples. The magnetisation reversal processes in two dimensional arrays and isolated wires are then briefly described. Finally, the magnetic field assisted alignment of template released ferromagnetic nanowires is reviewed.

3-2 Preparation of ferromagnetic nanowires

Different approaches have been utilised to prepare ferromagnetic nanowires. The first approach is using *lithographic patterning* (typically *electron beam lithography* or *ion beam milling)* [1-3]. The second approach is using *ion or electron beam induced deposition* which is also known as: *local chemical vapour deposition (LCVD)* [4-6]. These techniques are investigated in some detail in chapter four. *Atomic force microscopy (AFM)* has also been employed to create $Ni_{81}Fe_{19}$ nanowires [7,8]. These techniques however are expensive, complicated and time consuming as well as creating planar (rectangular) nanowires that lie parallel and fixed to an underlying substrate plane. In contrast, *electrochemical deposition*, or more commonly *electrodeposition* has been widely used to create cylindrical nanostructures oriented perpendicular to the substrate plane. Among these techniques, the most important and widely used method is electrodeposition due to its ease of use, short preparation time and relatively low cost. Moreover, it can be easily scaled up for industrial processing to produce single element [9-11], alloys [12,13], and compositionally modulated layers [14,15] of electrically conducting materials as thin films, nanowires [9-15], nanodots [16,17] and nanotubes [18-20].

Although, this technique has been known for a considerable time, it was first introduced to create metallic nanowires in two dimensional mica template with diameters as small as 40 nm by *George Possin* in 1970 [21]. These templates had arrays of channels (pores) backed with a good conducting layer to serve as a working electrode (cathode) in an electrochemical cell to direct the growth of the desired composition of nanostructures inside these pores. A detailed discussion of electrodeposition technique is given in chapter four.

With this technique, different templates have been utilised to synthesis ferromagnetic nanowires including nanoporous polymeric (e.g., polycarbonate), inorganic (e.g., mica) insulating films, silica and alumina membranes. These templates are available commercially with a wide range of pore diameters, spacing and thicknesses. The typical size of these templates is in the range of a few cm^2 [22]. Examples of scanning electron micrographs showing the top and side view of alumina templates are shown in Figure 3.1(a,b).

The pores in polycarbonate or mica insulating films are prepared by etching the damage tracks created by highly energetic particles [14,24-26]. The thickness of these templates is in the range of 5 to 50 μm. The pores within these templates are randomly distributed with diameters ranged from 5 nm to 3 μm depending on the chemical treatment [19]. On the other hand, the pores in the alumina membranes are produced by anodic oxidation of pure

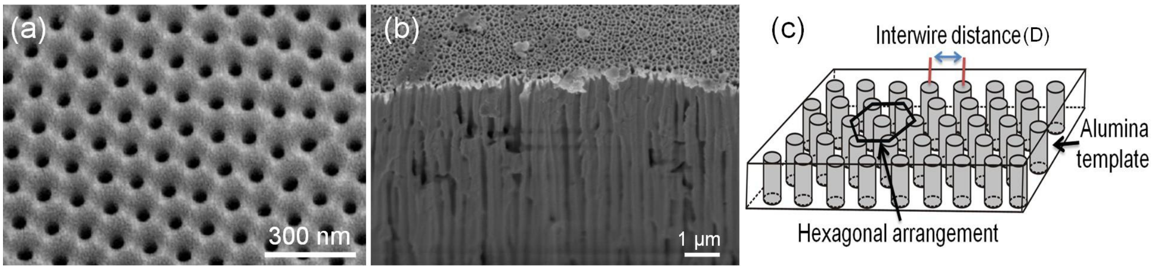

Figure 3.1 Examples of scanning electron micrographs showing alumina template as a: (a) top view with 50 nm pores diameter [23], (b) side view, and (c) schematic illustration of hexagonal arrangement of the nonporous in this template.

aluminium foil in acidic solution [18]. The pore density in alumina membranes is much higher than for polycarbonate templates where they range from 10^9 to 10^{11} cm^{-2} for alumina templates [18,26] and 10^7 to 10^9 cm^{-2} for polycarbonate membranes [26]. The thickness of alumina templates may be up to 200 μm with typical pores diameter of 5 to 500 nm.

Figure 3.1(c) shows a schematic diagram of two dimensional arrays of nanopores in an alumina template. The spacing between the centres of pores is known as *interwire or interpore distance.* The distance between any two neighbouring pores is known as *pore wall thickness*. The ratio of pore diameter, *d*, to the interpore distance, *D*, is referred to as *filling factor*, *d/D*. The filling factor in alumina templates are strongly dependent on the anodisation conditions and the electrolyte used for anodisation [27,28]. With careful preparation hexagonally ordered pores in alumina templates can be achieved [27].

To study the magnetic properties of such nanowires, alumina templates are preferred over other type of templates because it is easy to control the density of pores, their distribution is more uniform and their diameter is controllable [9,23]. Furthermore, the pores are typically parallel to each other and perpendicular to the membrane surface. Nonetheless, the crystalline structure of the nanowires created in such a technique is strongly dependent on the growth conditions and wire dimensions, which in turn affect their magnetic properties. Thus, the following sections briefly outline the effect of some of these parameters upon their crystal structure and magnetic properties.

3-3 Structural characterisation of ferromagnetic nanowires

Different techniques have been adopted to study the crystalline structure of ferromagnetic nanowires. These include *transmission electron microscopy (TEM)* with *selected area electron diffraction (SAED)* and *X-ray diffraction (XRD)* [23,27-36]. These studies reveal that these wires are polycrystalline in nature having crystallites with a large variation in size and preferred orientation depending upon various parameters including nanowire composition, dimensions and the growth conditions.

For example, Ni nanowires have a faced centred cubic structure [29]. The crystallite size was found to be 29 nm for wire diameter of 200 nm and 22 nm for wire diameters of 30 nm [29]. The crystallites in nanowires with diameter of 200 nm were found to have a preferred orientation, whereas the crystallites are oriented randomly in wires with diameter of 30 nm. The variations in the grain size were attributed to the preparation conditions and the diameter variations [29]. In contrast, Co nanowires were found to have a mixture of two different phases: FCC and HCP [12,31-33]. The later HCP structure was found in thin nanowires, whilst a mixture of FCC and HCP structures was found in thicker nanowires [31]. Thinner Co nanowires have a highly textured HCP phase, whilst thicker nanowires have a mixture of textured HCP and FCC phases. The FCC phase was found to be the main phase. HCP was observed to be the major phase when the wire diameter was small, which suggests a transition from FCC to HCP with decreasing nanowire diameter [31]. Again, the size of crystallites and their orientation was found to depend on the growth conditions. However, the grain sizes estimated were extremely small up to a few tens of nanometers. The crystal structure of a range of electrodeposited alloys such as $Co_{23}Ni_{77}$ [34,35] and $Ni_{85}Fe_{15}$ [34,36] nanowires with 200 nm diameters demonstrate that these nanowires have FCC structure with the existence of preferred orientations and the average grain sizes are 15 nm and 11 nm, respectively [34-36].

As will be seen in the following sections, these variations in the crystalline structure have a significant influence on the magnetic behaviour and magnetisation reversal state in such nanowires.

3-4 Magnetic behaviour in two dimensional arrays of ferromagnetic nanowires

During the past few decades, the magnetic properties of two dimensional arrays of ferromagnetic nanowires have been extensively investigated using a range of investigative techniques. As an example, Figure 3.2(a,b) shows typical hysteresis loops obtained from VSM measurements of an array of Ni nanowires synthesised in an alumina template with nominally 60 nm diameter and a few microns length. The magnetic field was applied parallel and perpendicular to the nanowire long axis, respectively [23].

In general, the preferred magnetisation orientation (i.e. easy axis of magnetisation) was found to be parallel to the nanowire long axis when the external magnetic field was applied parallel to the long axis (perpendicular to the template plane). The hysteresis loops were found to exhibit a large coercivity with a high remanent magnetisation. This behaviour indicates that the shape anisotropy dominates the magnetic anisotropies owing to the large aspect ratio (length to diameter).

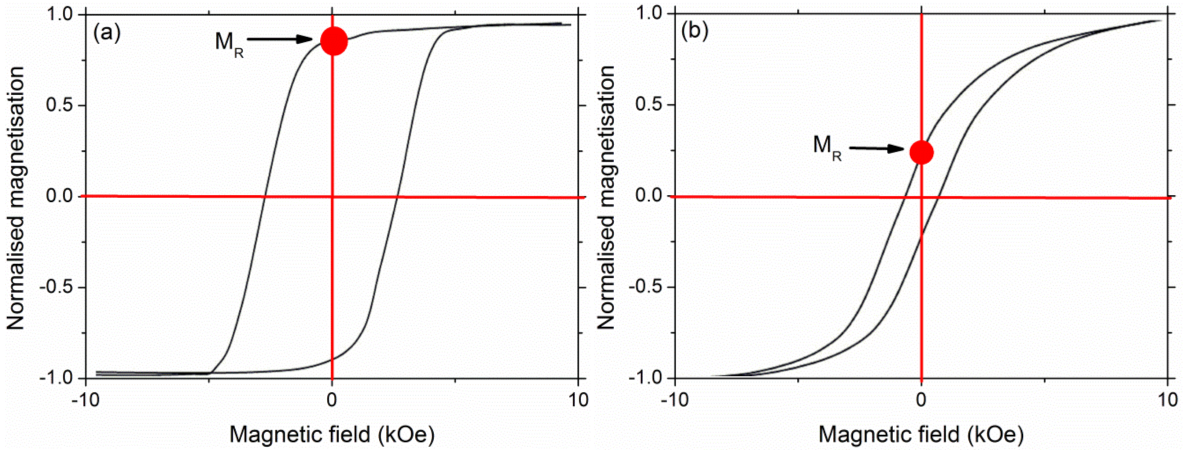

Figure 3.2 Typical hysteresis loops of an array of Ni nanowires with 60 nm diameter and few micron lengths obtained from VSM measurements when the field was applied (a) parallel, and (b) perpendicular to the nanowires long axis. Reproduced from [23].

In contrast, these properties become insignificant when the magnetic field was applied perpendicular to the nanowires long axis (i.e. parallel to the template plane) as shown in Figure 3.2(b).

In most work, the loops were found to be slightly sheared in field, despite the large shape anisotropy of these wires and the remanence ratio was found to be below than 1.0 when the magnetic field was applied parallel to the nanowires long axis. Various reasons have been proposed. The most significant one is the dipolar or magnetostatic interactions between the neighbouring wires (discussed later in section 3-4.5). Another explanation is that the wires are not perfectly aligned with each other. The magnetocrystalline anisotropy is another significant reason, because if the magnetocrystalline anisotropy is strong and the easy axis is not aligned along the wire long axis, a competition between the magnetocrystalline anisotropy and shape anisotropy occurs and hence there may be a reduction in the remanence ratio along that direction. For instance, the magnetocrystalline anisotropy of $Ni_{81}Fe_{19}$ and Ni nanowires is zero or extremely small compared with the shape anisotropy and hence the magnetisation lies along the wire long axis giving rise to high remanence ratio. In contrast, the strong magnetocrystalline anisotropy of HCP-Co nanowires and the orientation of the crystal easy axis nearly perpendicular to the wire long axis allows for the appearance of a multi-domain magnetisation configuration where domains are oriented partially along the normal to the wire long axis resulting in a reduction of remanent magnetisation [37,38].

The following subsections briefly describe how the growth conditions, temperatures, diameter and length of these nanowires, as well as the magnetostatic interaction and filling factor have a significant role in determining their final magnetisation configuration.

3-4.1 Magnetisation dependence upon growth conditions

The magnetic properties of ferromagnetic nanowires are strongly dependent on the parameters or the conditions under which they are prepared. For example, the effect of using different *electrolyte temperature* during the electrodeposition growth has been investigated [39-42]. Different temperatures were found to change the size and the preferred orientation of the crystallites within Ni wires (20-200 nm diameters) which in turn affects their magnetic behaviour. Ni nanowires prepared using an electrolyte temperature of 40^oC were found to have a higher coercivity (70-150 Oe) and remanent magnetisation than nanowires prepared under same conditions but an electrolyte temperature of 60^oC (coercivity 50-100 Oe). This was attributed to the formation of larger grain sizes compared with the nanowires diameter at low temperatures, which leads to the formation of single domain structures and enhances the coercivity [39,40].

pH is a measure of the concentration of hydrogen ions in the solution. The *pH of the electrolyte* in the electrochemical cell was also found to have a strong influence on the crystalline structure of a range of ferromagnetic nanowires with various dimensions [26,39-42]. For instance, with an electrolyte pH of 4 during the preparation of Co nanowires with 50 nm diameters and 0.8-3 μm lengths, the microstructure was found to be HCP with c-axis oriented perpendicular to the wire axis [41]. Increasing the pH of the electrolyte to greater than 4 led to the orientation of c-axis becoming predominantly parallel to the nanowire long axis. Using lower pH (< 2), only FCC crystallites were found. This variation in the crystalline structure was found to affect the magnetic behaviour of such wires [41].

The effect of using different electric potentials (-0.9 to -1.46 V) during the electrodeposition growth of alloys of Ni-Zn nanowires with 60 nm diameter and 40 μm lengths on the magnetic behaviour was also investigated [43]. Using higher deposition potential, the elemental composition of the alloys was not only changed, but the crystalline structure of these wires was also changed and this affects the magnetisation [43].

The effect of *annealing condition* for arrays of ferromagnetic nanowires under vacuum or argon atmosphere was found to have a great influence on their magnetic properties [44-46]. Under certain temperatures, annealing was found to enhance the coercivity. As an example, annealing the Fe nanowires under vacuum for about 6 hours at temperatures between 100 and 400°C was found to enhance the coercivity. The highest coercivity was obtained at an annealing temperature of 300°C. Annealing the samples above 400°C sharply degrading the coercivity, suggesting that the nanowires were damaged or oxidised. Again, the enhancement of the coercivity with annealing was attributed to the change in the crystalline structure [44].

The effect of *applying a magnetic field* parallel to the template nanopores during the electrodeposition growth of nanowires has also been thoroughly investigated [47-51]. The results show that the magnetic properties of such nanowires are sharply improved. As an example, Figure 3.3 shows the coercivity and squareness ratio as a function of the magnetic field applied perpendicular to the template surface during the growth of $Ni_{84}Fe_{15}$ nanowires [47]. When there is no magnetic field applied during the growth of nanowires, the coercivity was found to be ~378 Oe and the squareness ratio is 0.46, whereas they increased linearly to 530 Oe and 0.77, respectively when an ~1000 Oe external magnetic field was applied during the electrodeposition growth [47]. The application of magnetic field during electrodeposition process was found to enhance the textures and improve the magnetocrystalline anisotropy of these wires [47].

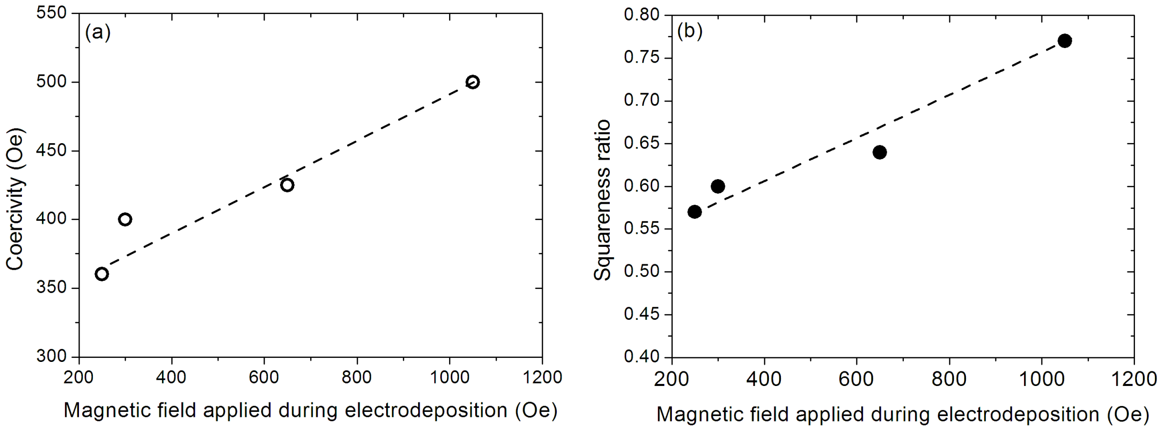

Figure 3.3 (a) Coercivity, and (b) squareness ratio as a function of magnetic field applied along the nanoporous axis during the electrodeposition growth of $Ni_{84}Fe_{15}$ nanowires. The dashed lines provide a guide to the eye. Data analysed from [47].

Micromagnetic models are in agreement with the previous experimental results indicating that the magnetism of such nanowires is strongly affected by the grains in the nanowires, specifically the size, orientation, and their interactions are the origin of the differences in the magnetic properties of such nanowires [48].

3-4.2 Magnetisation dependence upon temperature

The effect of using *different temperatures* during the measurements on the saturation magnetisation, remanent magnetisation and coercivity of a range of electrodeposited ferromagnetic nanowires embedded in their templates has been investigated widely [11,52-55]. As an example, Figure 3.4 summarise the effect of temperature change on the coercivity [52] and saturation magnetisation [53] of arrays of Ni, Co and Fe nanowires with aspect ratio greater than 50 when the magnetic field was applied parallel to the nanowire long axis .

In general, there is a reduction in these properties with increasing temperature from liquid helium to room temperature (10-300 K) in both orientations of measurements (i.e. when the field was applied parallel and perpendicular to the nanowires long axis). This reduction was attributed to the reduction of the magnetocrystalline anisotropy energy with increasing temperature [54], thermal fluctuations which were found to be stronger for

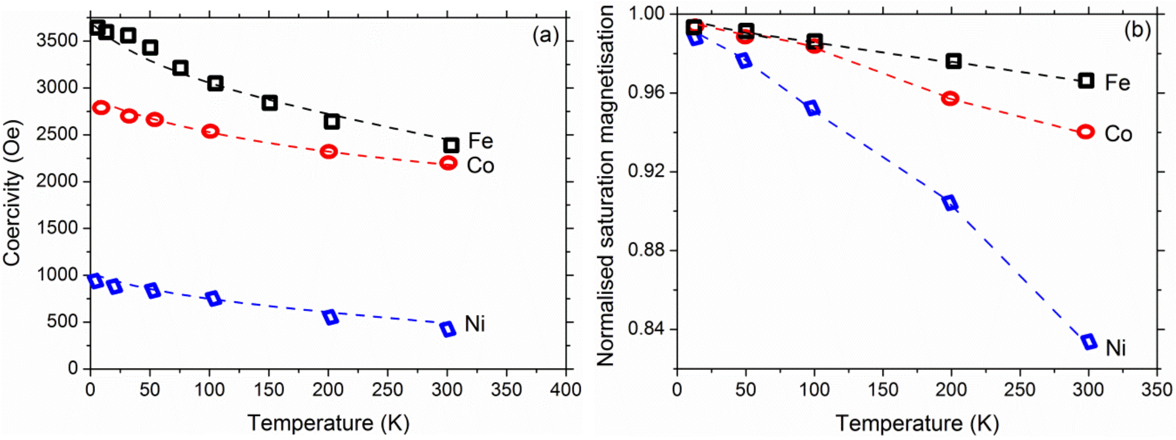

Figure 3.4 Effect of temperature change on the (a) coercivity [52], and (b) normalised saturation magnetisation [53] of arrays of electrodeposited Ni, Co, and Fe nanowires with aspect ratio greater than 50 when the field was applied parallel to the nanowires long axis. The dashed lines provide a guide to the eye.

thinner wires [53], as well as changes in the magnetoelastic effects. The magnetoelastic effects were attributed to the large difference between thermal expansion coefficients of the wires and their templates. Moreover, the reduction in the coercivity was found to depend on the wire diameter (not shown in Figure 3.4) and composition. The variation with different compositions is attributed to the difference in the *Curie temperature* of these materials [53].

3-4.3 Magnetisation dependence upon nanowires diameter

The effect of *nanowire diameter* on the magnetic properties of arrays and individual ferromagnetic nanowires has extensively been studied [31,38,52-65]. These investigations demonstrate that there is an increase in the coercivity and the remanent magnetisation with increasing nanowire diameter up to 13-18 nm and which has been attributed to the reduced effect of thermal fluctuations [52,56]. Increasing the wire diameter greater than 18 nm leads to a reduction in the coercivity and the remanent magnetisation. Figure 3.5 shows an example of the coercive field and squareness ratio of Ni nanowires as a function of nanowire diameter when the external magnetic field was applied along the nanowires long axis [57]. The measured coercivity along the parallel axis for 40 nm diameter wires was found to be ~800 Oe falling to ~200 Oe for 200 nm diameter wires.

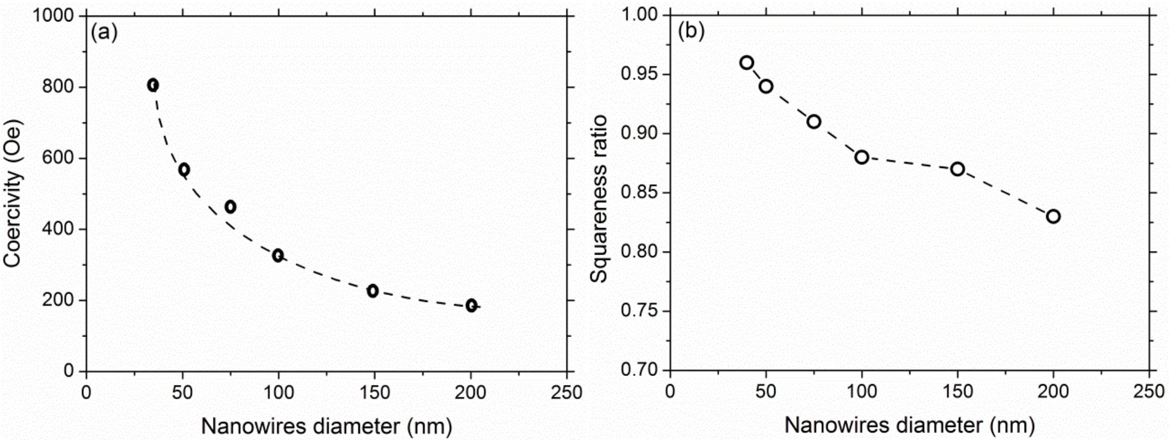

Figure 3.5 (a) Coercivity, and (b) squareness ratio as a function of nanowire diameter for arrays of Ni nanowires obtained when the magnetic field was applied parallel to the nanowires long axis. The dashed lines provide a guide to the eye. Reproduced from [57].

Micromagnetic simulations of individual ferromagnetic nanowires are in good agreement with the above experimental results [60].

The interpretations of these results are quite complex for several reasons. One of the most important reasons is the tendency of these wires to form single domain structures as their diameter gets smaller [38,58]. Decreasing the wire's diameter, increases the shape anisotropy and the relative contribution of any magnetocrystalline anisotropy becomes less important [59]. Moreover, it is difficult to explain these results without taking into account the magnetostatic interactions between neighbouring wires (discussed in section 3-4.5) which affect the overall magnetisation behaviour of such wires [38,53].

3-4.4 Magnetisation dependence upon nanowires length

The effect of *nanowire length* on the magnetic properties has been experimentally and theoretically investigated on a wide range of wires [47,49,52,54,61,62,66]. These studies demonstrate that the nanowire lengths have a great influence on their magnetic properties. Two different behaviours have been noticed in these researches. For example, the coercivity and remanence ratio was found to increase rapidly with increasing the length of Co nanowires and then approaches saturation when the aspect ratio exceeds 5, as demonstrated in Figure 3.6(a) [52,66].

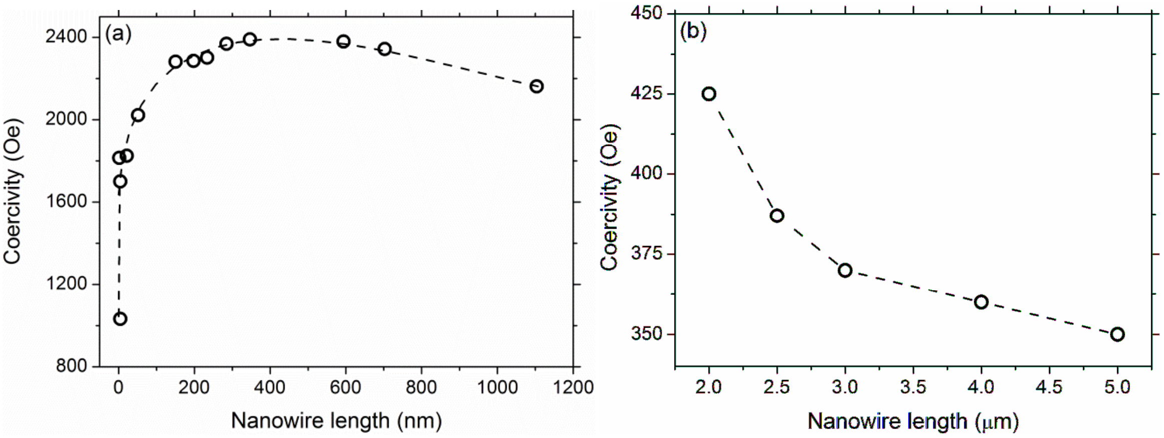

Figure 3.6 Coercivity of two dimensional arrays of nanowires as a function of their length for (a) Co nanowires [52,66], and (b) $Ni_{84}Fe_{15}$ nanowires [47]. The dashed lines provide a guide to the eye. Note the change of scale on x-axis.

This behaviour can be attributed to the enhancement of the shape anisotropy with increasing the nanowires length according to the infinite long magnetic cylinder model.

In contrast, a reduction in the coercivity and remanence ratio was noticed with increasing the nanowire lengths for longer wires of other compositions [47,49]. As an example, Figure 3.6(b) shows the coercivity of $Ni_{84}Fe_{15}$ nanowires with 200 nm diameter embedded in their templates as a function of their lengths [47]. Clearly, there is a reduction in the coercivity with increasing nanowire length which has been attributed to the strong dipolar interactions which increases with increasing the wire length or the different strength of the magnetostatic interactions among these wires [61,57]. Thus, it can be concluded that there is a transition region in the magnetisation behaviour of such wires depending on their lengths.

3-4.5 Magnetisation dependence upon magnetostatic interactions

When the *interwire spacing* in an array of ferromagnetic nanowires is smaller or comparable to the nanowire diameter or length, *magnetostatic interactions* are expected to occur between the neighbouring wires [62]. This interaction is often defined as a long range interaction. The interaction creates an *internal effective field* which strongly affects the magnetic properties of such wires [68]. Most of the experimental studies of these nanowires correlate the variations in the magnetic behaviour to this effect [22,61,62,67-75].

Recently, micromagnetic modelling confirms that the magnetostatic interactions among a small number of ferromagnetic nanowires have a significant influence on their magnetisation state [69-71]. For example, the results of studying an array of 16 hexagonal closely packed Ni nanowires with 40 nm diameter and 100 nm spacing on the coercivity and remanence when the field was applied parallel to the nanowires long axis are summarised in Figure 3.7 [69]. The inset figure shows a schematic diagram of the arrangement of simulated nanowires. Obviously, there is a reduction in the coercivity and the remanent magnetisation with increasing the number of interacting nanowires.

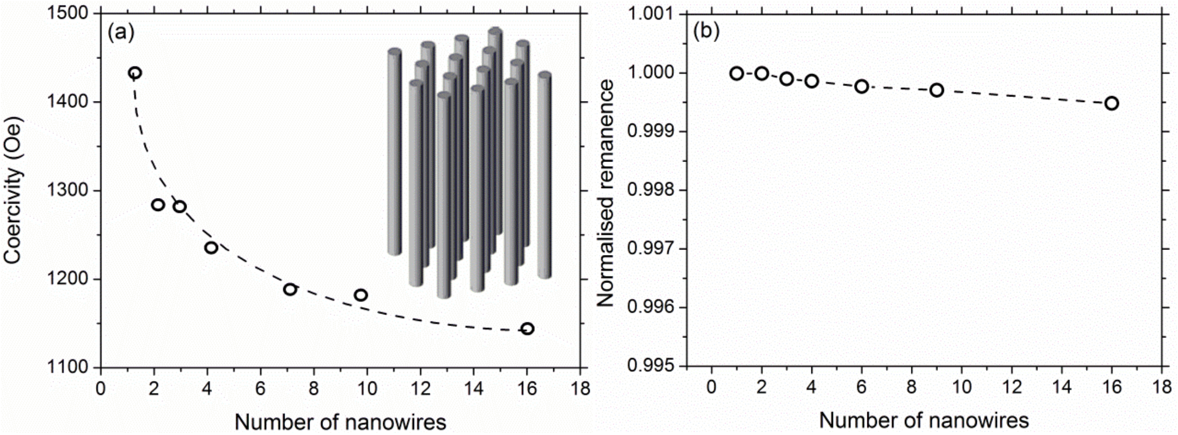

Figure 3.7 (a) Coercivity, and (b) normalised remanence as a function of number of Ni nanowires obtained from micromagnetic modelling. The figure inset is a schematic diagram showing the simulated nanowires. The dashed lines provide a guide to the eye. Data analysed from [69].

The effect of magnetostatic interaction on the remanent magnetisation is very small and correlated to the small number of wires [69]. Similar trends were obtained with lower values when the external magnetic field was applied perpendicular to the nanowires long axis [69]. This is because the loop is already narrow at that direction. Thus, increasing the number of interacting wires will aid to increase the internal effective field which in turn reduce the field required to reverse the magnetic state of such wires.

3-4.6 Magnetisation dependence upon filling factor

The magnetic properties of two dimensional arrays of ferromagnetic nanowires are strongly dependent on the *filling factor*, *d/D*, defined earlier [62,75,76]. For example, Figure 3.8(a) summarises the effect of filling factor on the coercivity of Ni nanowires with two different diameters (30 and 50 nm) and four different lengths (3, 6, 9 and 12 μm) [62]. This study was performed both experimentally and theoretically using simple models to calculate the coercivity as a function of nanowire geometry. When d*/D=1* this means that the wires are in contact, whilst when *d/D=0* the wires are infinitely separated [62]. Clearly, there is a reduction in the coercivity with increasing nanowire diameter and decreasing its length. On the other hand, for the same diameter or length the coercivity decreases with increasing the ratio of *d/D*.

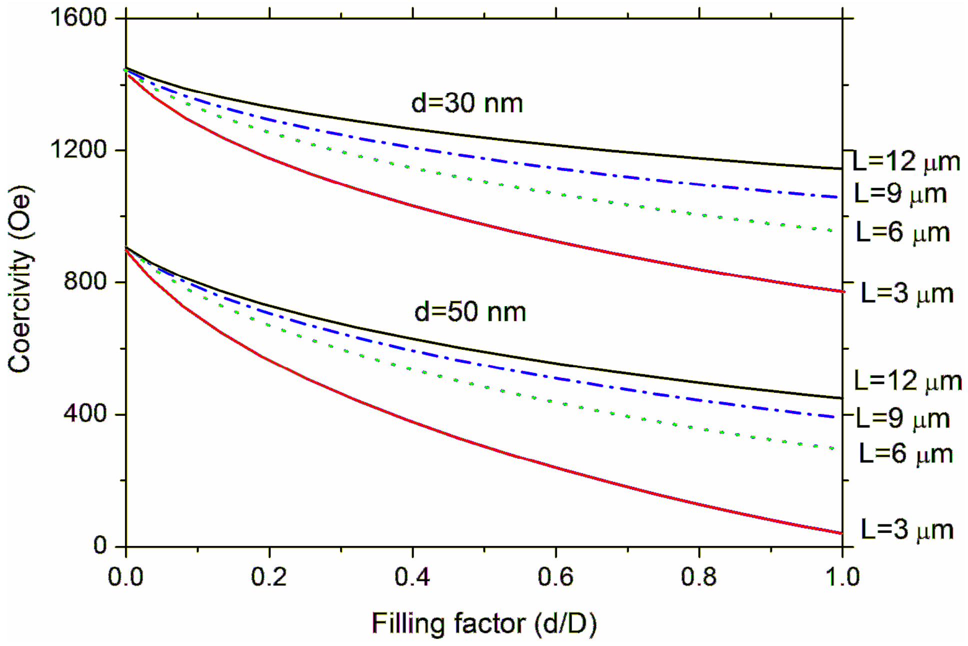

Figure 3.8 Effect of filling factor *(d/D)* on the coercivity of arrays of Ni nanowires with two different diameters (30 and 50 nm) and four different lengths (3, 6, 9 and 12 μm). Reproduced from [62].

Thus, the interwire spacing, diameter and length of such systems play a significant role in their final magnetisation behaviour of arrays of nanowires.

As another example, *MOKE magnetometry* has been used during the course of this research to investigate the surface magnetisation behaviour of isolated small clusters of $Ni_{80}Fe_{20}$ nanowires and other alloys and multilayer nanowires with diameters ranged from 35 nm to 300 nm [77]. The results of this study demonstrate that the magnetisation of these wires is strongly dependent on the wires diameter, composition and the number of the wires in the cluster. The switching field was initially found to decrease with increasing wire diameter and then increases for larger diameter. This was attributed to the difference in the penetration depth of the laser spot and the demagnetisation effect. The effect of magnetostatic interactions was also evident from this study where the switching field was found to increase with increasing the number of wires up to 3 and then it decreases for 4 wires. This behaviour was attributed to the complicated magnetic field distribution in the cluster as a result of the magnetostatic interactions [77].

3-5 Magnetisation reversal processes in ferromagnetic nanowires

As stated in the previous chapter, there are various theoretical models describing the magnetisation reversal processes in ferromagnetic nanowires. Their applicability depends on different parameters. The most important and widely used method to study the magnetisation reversal process is applying an external magnetic field at different angles with respect to the nanowires long axis. Then, by extracting the coercivity from the hysteresis loops and plotting against the nanowire angle, the *angular variation of the coercivity* can be obtained. Thus, the following subsections review the most important results obtained from studying the magnetisation reversal processes in nanowires synthesised in their templates and then discussing these properties on an individual nanowires.

3-5.1 Magnetisation reversal in arrays of nanowires

Magnetisation reversal processes in arrays of planar [5,78,82] and cylindrical [10,37,38,55,83-88] nanowires are extensively investigated experimentally and theoretically using a range of investigative techniques. These studies demonstrate that the magnetisation reversal is strongly dependent on the competition between various magnetic anisotropy energies. The magnetic anisotropy energy in turn depends on the physical properties of the system under investigation such as crystalline structure, composition, diameter and temperature during measurements, as mentioned earlier. Moreover, both the experimental measurements and micromagnetic simulations confirms that the magnetostatic or dipolar interactions between the neighbouring nanowires significantly reduce the coercivity and the remanence ratio, in addition to changing the magnetisation reversal from one mode to another.

As an example, studying the magnetisation reversal of Ni, Co and Fe nanowires embedded in an alumina templates with diameters ranged from 6 to 50 nm at 5K indicates that the coercivity of Ni and Fe are significantly lower than the predicted for the uniform rotation of the *Stoner–Wohlfarth* model [37]. The magnetisation reversal was attributed to the domain nucleation and domain wall propagation through the entire wires. In contrast, Co nanowires show different behaviour attributed to the competition between shape and magnetocrystalline anisotropies [37]. Using the same compositions of wires with diameters in the range of 250-300 nm and lengths in the range of 3-8 μm shows that curling modes occur for Co and Fe nanowires with fields applied at angles less than 70^o to75^o and that the coercivity drops almost to zero at angles larger than 75^o, as shown in Figure 3.9(a) [10]. In contrast, the coercivity of Ni nanowires was roughly constant up to 60^o before decreasing to zero at 90^o as shown in Figure 3.9(b) [10]. The difference in the magnetisation behaviour was ascribed to the competition between shape anisotropy and magnetostatic interactions among the interacting wires.

In order to gain a better understanding of the magnetisation and magnetisation reversal process of isolated nanowires, researchers have reduced the number of nanowires using templates such as polycarbonate with low density of nanopores. The discussions in these researches remain intriguing and controversial and there is still no common agreement about the reversal process in such arrays of ferromagnetic wires due to the variation of morphologies, wire diameter and the separation distances among these wires in addition to the existence of surface features, as will be seen in chapter six.

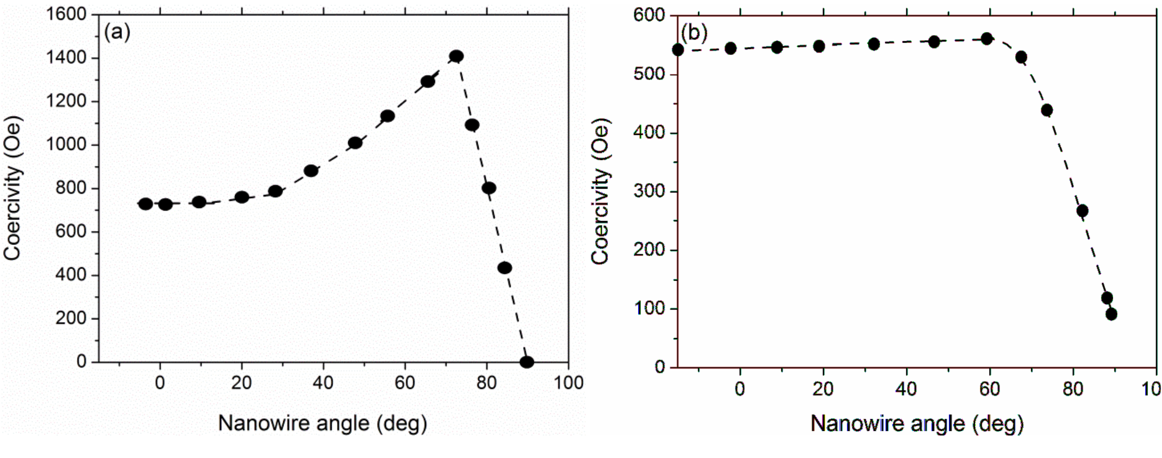

Figure 3.9 Angular dependent of coercivity for (a) Co, and (b) Ni nanowires with diameters of 200-300 nm embedded in alumina templates. Reproduced from [10].

Furthermore, the dipolar or magnetostatic interactions between neighbouring wires again complicate the situation and can give inaccurate explanations of individual wires. Thus, studying the magnetic properties and magnetisation reversal in two dimensional arrays of wires cannot always provide precise information about individual wires and the interpretation of the data is limited.

3-5.2 Magnetisation reversal in isolated nanowires

Studying the magnetic and magnetisation reversal behaviour of isolated nanowires experimentally is complicated and represents a real challenge because the magnetisation of such small wires is of the order of 10^{-11} *emu* ($10^{-14} Am^2$) [89,90], which cannot be measured with conventional magnetometry. Recently, due to development in the fabrication and characterisation techniques it has become possible to measure these properties on isolated ferromagnetic nanowires. This was achieved by creating arrays or individual planar nanowires on the semiconductor chips using *EBL, ion beam milling* [3,78,91], *ion/electron beam induced deposition* [4-6] and *atomic force microscopy* [7,8]. The thicknesses of these wires however ranged from 5 nm to 50 nm and the widths ranged from 150 nm up to a few microns. These planar wires however do not represent the cylindrical nanowires owing to the large variations in the shape and dimensions. Therefore, researchers have attempted to investigate isolated cylindrical nanowires by creating individual nanowires within the templates [24,38,92,93] or removing the templates and releasing the nanowires in a dilute suspension using a suitable chemical solution without damaging them [34-36,40,93-95]. Then, micro-*superconducting quantum interference device* at low temperatures or *magnetic force microscopy (MFM)* measurements at room temperature have been used to study the magnetisation reversal in such wires. However, the focus of these studies has been on nanowires of the smallest diameters that are likely to display single domain states with simpler magnetic behaviour compared to larger diameter nanowires that can support more complex and interesting domain structure.

As an example, the first experimental report which investigated the magnetisation reversal process of a single isolated Ni nanowires with a range of diameters (40-100 nm) was carried out in 1996 by *Wernsdorfer et. al.* using micro-SQUID magnetometer by applying the magnetic field at different angles with respect to the nanowire long axis [95]. The results showed that the magnetisation reversal started by distortion of the magnetisation followed by a nucleation and propagation through the entire wire length. The nucleation value was close to the curling instability for wires greater than 50 nm in diameter, whilst for wires having diameters less than 30 nm, the *Stoner-Wohlfarth* model was relevant.

Magnetoresistance measurements have also been utilised to investigate the magnetisation reversal in such isolated wires using the *anisotropic magnetoresistance effect* as this technique is sensitive to the orientation of the magnetic moments within these wires [34-36,92-94]. These studies were carried out by dispersing the nanowire suspension onto prefabricated metallic electrodes and then magneto-transport measurements were performed after electrically connecting these wires with the electrodes. Two significant approaches have been used to electrically connect these wires. The first approach is using *lithographic patterning* which will be described in details in chapter four. For example, *Vila et. al.* adopted this approach to electrically connect single Co nanowire with 60 nm diameter and 20 μm length at different locations on the same wire as shown in Figure 3.10 [33,89]. With this connection, they were able to measure the magnetic properties of small parts (500 nm) on the same wire.

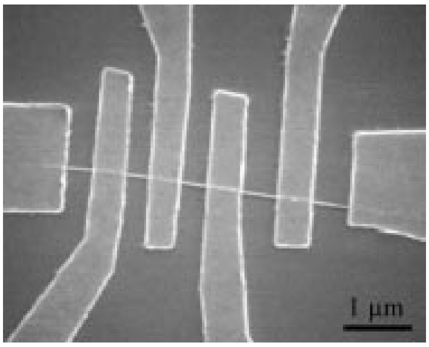

Figure 3.10 Scanning election micrograph showing an individual Co nanowire with 60 nm diameter and 20 μm length electrically connected at different locations using EBL. Reproduced from [33,89].

From these measurements, different magnetisation reversal was observed at different locations on the same wire, indicating the local in-homogeneity of the magnetisation reversal process. This was attributed to the change in the orientation of the magnetocrystalline anisotropy (c axis) to be either along or perpendicular to the wire long axis [89].

More recently, researchers have been used another approach to electrically connect the individual ferromagnetic nanowires to the prefabricated metallic or ferromagnetic contacts patterns using *magnetic field assisted alignment* during the dispersion of nanowire suspensions onto the substrates to allow them to bridge on these patterns (see section 3-6 for further details) [29,34-36]. In this approach, the contact resistance was found to be very high, in the range of 10 MΩ, due to the existence of surface oxide or hydroxide layer or other residue remaining on the wires after removing the templates. Annealing the samples in 5% H_2 + 95% N_2 ambient at a temperature of ~300^{o}C for 30 minutes was found to reduce the contact resistance dramatically. With this technique the magnetisation reversal behaviour of a range of individual ferromagnetic nanowires was investigated [29,34-36]. For instance, the angular dependence of the switching field obtained from the jumps in the magneto-transport profiles of individual $Ni_{85}Fe_{15}$ [36] at room temperature and Ni nanowires [29,34] at 10K with 200 nm diameters and more than 5 μm lengths was found to be consistent with the curling model of reversal as shown in Figure 3.11. According to their calculations, the size of the nucleation was found to be smaller than the nanowire diameter indicating that the reversal begins in a small area. In contrast, the magnetisation reversal of an individual $Co_{20}Ni_{80}$ nanowire also 200 nm in diameter and measured with the same technique showed that the reversal was more likely to follow the curling model at low angles (< 75^o) and *S-W model* at higher angles (> 75^o) [35].

With the recent developments in the computer systems and memory, it has become possible to use micromagnetic simulation to study the magnetic properties of a range of

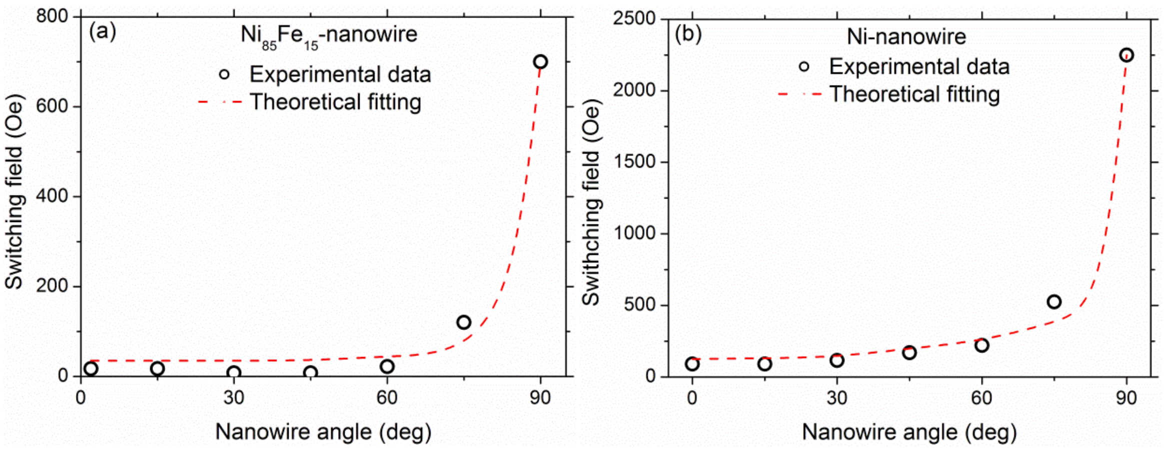

Figure 3.11 Angular dependent of the switching field obtained from magneto-transport measurements of an individual (a) $Ni_{85}Fe_{15}$ [36], and (b) Ni [29] nanowires with 200 nm diameter and more than 5 µm length. The dashed line is the theoretical fitting using curling model of reversal.

nanostructures including nanowires and nanotubes [38,60,69,71,96-98]. Therefore, *micromagnetic simulations* on a range of isolated cylindrical soft ferromagnetic nanowires have shown that the magnetisation reversal can occur via two different mechanisms, known as the *transverse wall mode* and *vortex wall mode* [38,60,71,96-98]. In the absence of magnetocrystalline anisotropy the competition between the demagnetisation and exchange energies determine the domain wall structure [97]. The main difference between these two modes is in the configuration of the magnetic moments within the plane of the domain wall. The distribution of the magnetic moments in these modes is shown in Figure 3.12 together with their schematic diagrams. These configurations have been obtained from micromagnetic simulations of $Ni_{81}Fe_{19}$ planar nanowires. During the application of an external magnetic field a reversed domain can nucleate at each end of the nanowire, or at defects [97] or imperfections [37] separated from the original domain by a newly formed domain wall. Subsequent propagation of the domain walls throughout the entire wire leads to the wire switching from one magnetisation state to another and reduces the total magnetostatic energy. The occurrence of nucleation at the ends of the wires is due to the large demagnetisation field at the end of the wire [97].

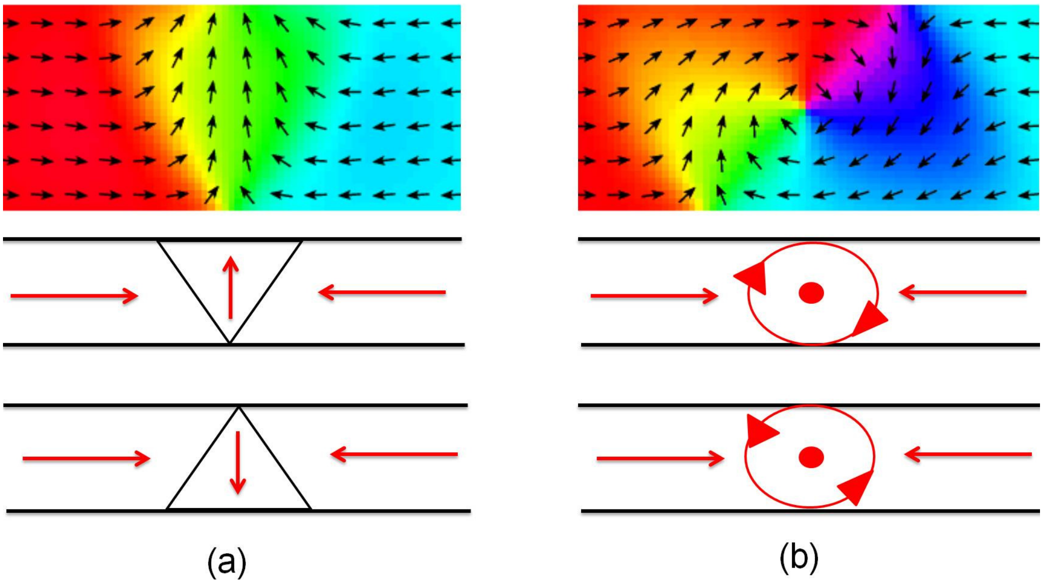

Figure 3.12 Distribution of magnetic moments in (a) transverse, and (b) vortex domain wall modes together with their schematic diagrams. These configurations were obtained from micromagnetic simulations of $Ni_{81}Fe_{19}$ planar nanowires [99].

During magnetisation reversal, the magnetic moments precede in a spiral motion as the wall propagates along the axial direction of the wire as a result of the torque exerted on spin. Vortex domain walls have been found to move faster than transverse domain wall [96,98].

The transition between these modes was found to depend on the diameter, the composition of the nanowire under investigation and the initial field applied [98]. In small diameters, the reversal was found to occur by transverse walls, whilst in thick wires the reversal occurred by vortex walls. For instance, the critical diameter for the transition of Ni and Fe nanowires was found to be 40 nm and 20 nm, respectively as measured using micromagnetic simulations on cone shaped Ni and Fe nanowires [97]. However, the value of the critical diameter of Ni nanowires (40 nm) is very close to that which has been reported for the transition between coherent and curling rotation modes (41 nm).

Nonetheless, the magnetic behaviour and magnetisation reversal of template released isolated individual and small bundles of ferromagnetic nanowires is still ambiguous and need further investigations which is the main purpose of this research and presented in chapter eight.

3-6 Magnetic alignment of template released ferromagnetic nanowires

For scientific study and also for potential applications of metallic nanowires, the manipulation and alignment of the wires is a significant and demanding issue in different fields. Therefore, a variety of techniques have been used to manipulate and control a wide range of electrodeposited nanowires including *thermocapillary motion* of nanowire suspensions in micro-channels [100,101], *electrostatics* [101-104], *electric field* [101,104,105], and *magnetic field assisted alignment* [106-119]. Specifically, this section investigates briefly the alignment of template released metallic nanowires using magnetic fields during dispersion of these nanowires from a dilute suspension onto substrates.

Magnetic field assisted alignment is an attractive, inexpensive and straightforward technique for aligning ferromagnetic nanowires. This technique has been utilized by several researchers to control assembly and alignment of carbon nanotubes [101,115], semiconductor [101], conductive [117], copper-tin [116], Pt [118], and ZnO [113] nanowires capped with ferromagnetic ends and ferromagnetic [106-110] nanowires in their suspension or by manually drop casting the suspension containing these nanowires between two metallic (ferromagnetic or gold) electrodes using two permanent magnets. These studies have been performed to investigate and analyse the motion of these wires in the suspension under the influence of an applied magnetic field, and the effects of viscosity of the solvents on the motion [57,108,110]. In addition, recent work has demonstrated the use of magnetic alignment of ferromagnetic nanowires to create hierarchical structures [109]. Again, permanent magnets were used, this time for sequential alignment of the nanowires onto either un-patterned or pre-patterned metallic electrodes on substrates. A schematic diagram showing this process is presented in Figure 3.13(a). An example of an SEM image of ferromagnetic nanowire aligned between two metallic electrodes using this method is shown in Figure 3.13(b) [106]. The effects of shape [114], separation distances and dimensions [119] of the prefabricated ferromagnetic electrodes and the local magnetic field on the alignment process were also examined.

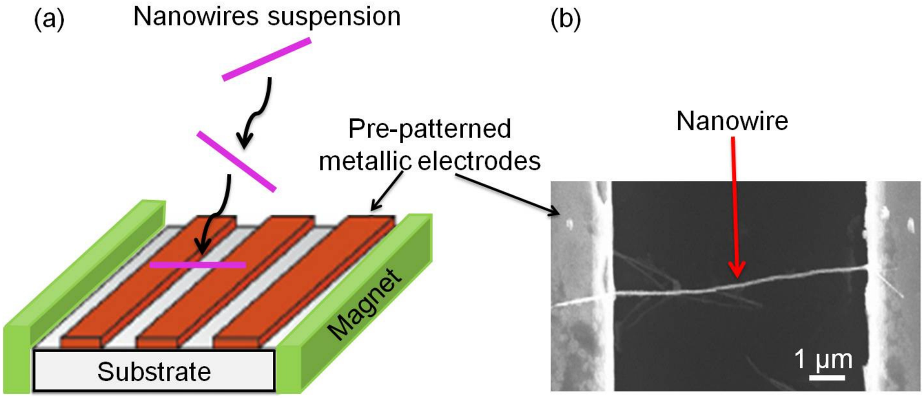

Figure 3.13 (a) Schematic representation of the magnetic field alignment of ferromagnetic nanowires in which the nanowires suspension was spilled onto a pre-patterned substrate with Ni or Au electrodes and placed between two permanent magnets. (b) Scanning electron micrograph showing individual Ni nanowire bridged on the electrodes [106].

In the absence of magnetic field, various forces affect the directionality of the nanowires in the droplet of a dilute suspension on a specimen including *drag*, *weight* of the nanowires, and *buoyancy forces* [109]. In addition, the *concentration* of nanowires, the *distance* between nanowires, the *density of the wires and the suspension*, as well as the *contact angle* of the solvent with the substrate have a significant influence on the directionality of these wires. Therefore, the net force exerted on the nanowires, F_n, has been summarised by [109]:

$$F_n = F_w + F_d + F_b \qquad 3\text{-}1$$

Where, F_w, F_d, and F_b are the *weight* of the nanowires, *drag force*, and *buoyancy force*, respectively. The weight of the nanowires can be neglected due to their small sizes. The drag force is given by *Stokes formula* as [109]:

$$F_d = 6\pi\mu r v \qquad 3\text{-}2$$

Where, μ is the *viscosity* of the suspension, v is the *velocity* of the nanowires and r is the *equivalent radius* of nanowires. The buoyancy force can be given by the density of the suspension, ρ_{sus}, and the density of the nanowires, ρ_n, as well as nanowires length, l, and diameter, d, as [109]:

$$F_b = (\rho_n - \rho_{sus}) l\pi (\tfrac{d}{2})^2 g \qquad 3\text{-}3$$

Where, g is the acceleration due to *gravity*. Although, the gravitation might cause some preferential orientation to the dispersed nanowires, it can be ignored because its direction is opposite to the buoyancy force [109]. Thus, the dominant force on such wires is the *viscous drag* which is responsible for their orientations and make them distributed randomly on the substrate.

The situation is quite different with applying a uniform magnetic field in the direction of the substrate plane during the dispersion of these wires. In this case, the magnetic field exerts a *torque force* on the nanowires, as shown schematically in Figure 3.14 considering these nanowires having a prolate spheroid shape. This torque, $\underline{\tau}$, is determined by the vector product of the magnetic moment, $\underline{m}$, and the applied field, $\underline{H}$ as follows [100,109]:

$$\underline{\tau} = \underline{m} \times \underline{H} \qquad 3\text{-}4$$

The magnetic moment depends upon the magnetisation, M, length and cross-sectional area, A, of the nanowire. Therefore, the torque exerted on the nanowires can be given by the following expression [110].

$$\tau = VMH \sin\theta = l\,\pi\,(d/2)^2 MH \sin\theta \qquad 3\text{-}5$$

where, V is the volume of the nanowire and θ is the angle between the nanowire long axis and the direction of the applied magnetic field, as shown in Figure 3.14.

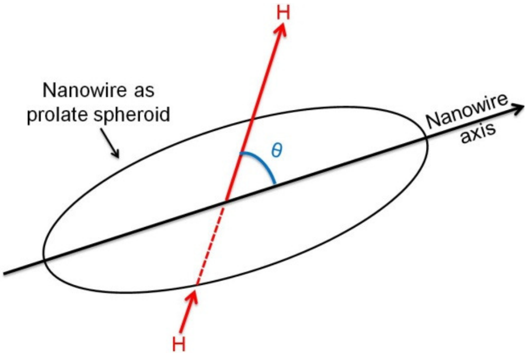

Figure 3.14 Schematic representation of the nanowire as a prolate spheroid with respect to the field applied, H, where θ is the initial angle between the applied magnetic field direction and the nanowire long axis.

Thus, application of a sufficient magnetic field during nanowires deposition induces movement of these nanowires to align themselves with the magnetic field lines due to the high aspect ratios and the dominant shape anisotropy on the behaviour. It is therefore reasonable to expect that the process of magnetic alignment will also depend upon the *strength of the magnetic field*, *saturation magnetisation* and the *aspect ratio* of nanowires. This forms a topic in this work investigated in chapter seven.

3-7 Chapter references

1. Atkinson, D., Eastwood, D. S. & Bogart, L. K. "Controlling domain wall pinning in planar nanowires by selecting domain wall type and its application in a memory concept" *Appl. Phys. Lett.*, 92(2), 022510, 2008.
2. Bryan, M. T., Atkinson, D. & Allwood, D. A. "Multimode switching induced by a transverse field in planar magnetic nanowires" *Appl. Phys. Lett.*, 88(3), 032505, 2006.
3. Dumpich, G., Krome, T. P. & Hausmanns, B. "Magnetoresistance of single Co nanowires" *J. Mag. Mag. Mat.*, 248(2), 241, 2002.
4. Nikulina, E., Idigoras, O., Vavassori, P., Chuvilin, A. & Berger, A. "Magneto-optical magnetometry of individual 30 nm cobalt nanowires grown by electron beam induced deposition" *Appl. Phys. Lett.*, 100, 142401, 2012.
5. Fernández-Pacheco, A., Teresa, De, Szkudlarek, A., Córdoba, R., Ibarra, M. R., Petit, D., O'Brien, L., Zeng, H. T., Lewis, E. R., Read, D. E. & Cowburn, R. P. "Magnetization reversal in individual cobalt micro-and nanowires grown by focused-electron-beam-induced-deposition" *Nanotech.*, 20(47), 475704, 2009.
6. Fernández-Pacheco, A., Teresa, De., Córdoba, R. & Ibarra, M. R. "Magnetotransport properties of high-quality cobalt nanowires grown by focused-electron-beam-induced deposition" *J. Phys. D: Appl. Phys.*, 42, 5, 2008.
7. Oliveira, A. B. De, Silva, G. L. Da, Rezende, S. M. & Azevedo, A. "Magnetization reversal in single ferromagnetic rectangular nanowires" *J. Phys.: Conf. Series*, 200(7), 072023, 2010.
8. Oliveira, A. B., Rezende, S. M. & Azevedo, A. "Magnetization reversal in permalloy ferromagnetic nanowires investigated with magnetoresistance measurements" *Phys. Rev. B*, 78(2), 024423, 2008.
9. Yin, A. J., Li, J., Jian, W., Bennett, A. J. & Xu, J. M. "Fabrication of highly ordered metallic nanowire arrays by electrodeposition" *Appl. Phys. Lett.*, 79(7), 1039, 2001.
10. Qin, J., Nogue, J., Mikhaylova, M., Roig, A. & Mun, J. S. "Differences in the magnetic properties of Co, Fe and Ni 250-300 nm wide nanowires electrodeposited in amorphous anodized alumina templates" *Chem. Mater.*, 17,1829, 2005.
11. Narayanan, T. N., Shaijumon, M. M., Ci, L., Ajayan, P. M. & Anantharaman, M. R. "On the growth mechanism of nickel and cobalt nanowires and comparison of their magnetic properties" *Nano. Res.*, 1(6), 465, 2008.

12. Khan, H. R. & Petrikowski, K. "Magnetic and structural properties of the electrochemically deposited arrays of Co and CoFe nanowires" *J. Mag. Mag. Mat.*, 249(3), 458, 2002.
13. Bai, A. & Hu, C.-C. "Iron–cobalt and iron–cobalt–nickel nanowires deposited by means of cyclic voltammetry and pulse-reverse electroplating" *Elec. Comm.*, 5(1), 78, 2003.
14. Ohgai, T., Hjort, K., Spohr, R. & Neumann, R. "Electrodeposition of cobalt based ferromagnetic metal nanowires in polycarbonate films with cylindrical nanochannels fabricated by heavy-ion-track etching" *J. Appl. Elec.*, 38(5), 713, 2008.
15. Tang, X.-T., Wang, G.-C. & Shima, M. "Magnetic layer thickness dependence of magnetization reversal in electrodeposited CoNi/Cu multilayer nanowires" *J. Mag. Mag. Mat.*, 309(2), 188, 2007.
16. Xiao, Z. L., Han, C. Y., Welp, U., Wang, H. H., Vlasko-Vlasov, V. K., Kwok, W. K., Miller, D. J., Hiller, J. M., Cook, R. E., Willing, G. A. & Crabtree, G. W. "Nickel antidot arrays on anodic alumina substrates" *Appl. Phys. Lett.*, 81(15), 2869, 2002.
17. Jung, J.-S., Malinski L., Lim, J.-H., Yu M., O'Coonnor, Lee H. O. & Kim E. M. "Fabrication and magnetic properties of Co nanostructures in AAO membranes" *Bull Korean Chem. Soc.*, 29(4), 2008.
18. Davis, D. M., Moldovan, M., Young, D. P., Henk, M., Xie, X. & Podlaha, E. J. "Magnetoresistance in electrodeposited CoNiFe/Cu multilayered nanotubes" *Ele. Solid State Lett.*, 9(9), C153, 2006.
19. Han, X.-F., Shamaila, S., Sharif, R., Chen, J.-Y., Liu, H.-R. & Liu, D.-P. "Structural and magnetic properties of various ferromagnetic nanotubes" *Adv. Mat.*, 21(45), 4619–4624, 2009.
20. Li, X. Wang, Y., Song, G., Peng, Z., Yu, Y., She, X. & Li, J. "Synthesis and growth mechanism of Ni nanotubes and nanowires" *Nano. Res. Lett.*, *4*(9), 1015, 2009.
21. Possin, E. George "A method for forming very small diameter wires" *Rev. Sci. Ins.*, 41**,** 772, 1970.
22. Vázquez, M., Hernández-Vélez, M., Pirota, K., Asenjo, A., Navas, D., Velázquez, J., Vargas, P. & Ramos C. "Arrays of Ni nanowires in alumina membranes: Magnetic properties and spatial ordering" *Eur. Phys. J. B*, 40(4), 489, 2004.
23. Jin, C. G., Liu, W. F., Jia C., Xiang, X. Q., Cai, W. L., Yao, L. Z. & Li, X. G. "High filling large area Ni nanowires arrays and the magnetic properties" *J. Cry. Gro.*, 258, 337, 2003.
24. Daub, M., Enculescu, I., Neumann, R. & Spohr, R. "Ni nanowires electrodeposited in single ion track templates" *J. Opt. Adv. Mat.*, 7(2), 865, 2005.
25. Ampere, A. Tseng "Nanofabrication fundamentals and applications" World scientific publishing Co. Pte. Ltd., USA, 2008.
26. Nasirpouri, F. "Template electrodeposition of magnetic nanowire arrays" *Trans world Res. Net.*, 661, 37, 2007.
27. Han, X., Shamaila, S. & Sharif, R. "Ferromagnetic nanowires and nanotubes" Edited by Nicoleta Lupu "Electrodeposited nanowires and their applications" *Intech.*, Olanjnic, India, 2010.
28. Shimizu, T., Aoki, K., Tanaka, Y., Terui, T. & Shingubara, S. "Preparation of ultrahigh-density magnetic nanowire arrays beyond 1 Terabit/Inch^2 on Si substrate using anodic aluminium oxide template" *Japanese J. Appl. Phys.*, 50(6), 06GE01, 2011.

29. Rheem, Y., Yoo, B. B.-Y., Beyermann, W. P. & Myung, N. V. "Magnetotransport studies of a single nickel nanowire" *Nanotech.*, 18, 015202, 2007.
30. Vieyra M., Meydan T. & Borza F. "X-ray diffraction analysis and magnetic behaviour of amorphous $Fe_{15}Co_{17}Ni_{58}B_{10}$ nanowires obtained by electrochemical deposition" *J. Appl. Phys.*, 101, 09N102, 2007.
31. Ye Z., Liu H., Luo Z., Lee H.-G., Wu W., Naugle D. G. & Lyuksyutov I. "Changes in the crystalline structure of electroplated Co nanowires induced by small template pore size" *J. Appl. Phys.*, 105(7), 07E126, 2009.
32. Huang X., Li L., Luo X., Zhu X. & Li G. "Orientation-controlled synthesis and ferromagnetism of single crystalline Co nanowire arrays" *J. Phys. Chem. C*, 112, 1468, 2008.
33. Vila L., George J. M., Faini G., Popa A., Ebels U., Ounadjela K. & Piraux L. "Transport and magnetic properties of isolated cobalt nanowires" *IEEE Trans. Mag.*, 38(5), 2577, 2002.
34. Rheem Y., Yoo, B.-Y., Beyermann W. P. & Myung N. V. "Magneto-transport studies of single ferromagnetic nanowire" *Phys. Stat. Sol. (a)*, 204(12), 4004, 2007.
35. Rheem Y., Yoo B.-Y., Beyermann W. P. & Myung N. V. "Electro-and magneto-transport properties of a single CoNi nanowire" *Nanotech.*, 18(12), 125204, 2007.
36. Rheem Y., Yoo B.-Y., Koo B. K., Beyermann W. P. & Myung N. V. "Synthesis and magnetotransport studies of single nickel-rich NiFe nanowire" *J. Phys. D: Appl. Phys.*, 40(23), 7267, 2007.
37. Paulus, P. M., Luis, F., Kro, M., Schmid, G., & Jongh, L. J. De. "Low-temperature study of the magnetization reversal and magnetic anisotropy of Fe, Ni and Co nanowires" *J. Mag. Mag. Mat.*, 224, 180, 2001.
38. Ferré, R., Ounadjela, K., George, J., Piraux, L., & Dubois, S. "Magnetization processes in nickel and cobalt electrodeposited nanowires" *Phys. Rev. B*, 56(21), 14066–14075 1997.
39. Kafil, M. Razzeb, Fernando, M. F. Rhen & Saibal Roy "Magnetic properties of nickel nanowires: Effect of deposition temperature" *J. App. Phys.*, 105, 083922, 2009.
40. Rahman, I. Z., Razeeb, K. M., Kamruzzaman, Md. & Serantoni M. "Characterisation of electrodeposited nickel nanowires using NCA template" J. *Mat. Proc. Tech.*, 153-154, 811, 2004.
41. Daimon, H. & Kitakami, O. "Magnetic and crystallographic study of Co electrodeposited alumite films" *J. Appl. Phys.*, 73(10), 5391, 1993.
42. Ren, Y., Liu, Q. F., Li, S. L., Wang, J. B. & Han, X. H. "The effect of structure on magnetic properties of Co nanowire arrays" *J. Mag. Mag. Mat.*, 321(3), 226, 2009.
43. Lihu Liu, Haitao Li, Shenghua Fan, Jianjun Gu, Yaopeng Li & Huiyuan Sun "Fabrication and magnetic properties of Ni-Zn nanowire arrays" *J. Mag. Mag. Mat.*, 321, 3511, 2009.
44. Qin, D. H., Wang, C. W., Sun, Q. Y. & Li, H. L. "The effect of annealing on the structure and magnetic properties of CoNi patterned nanowire arrays" *Appl. Phys.* A, 74, 761, 2002.
45. Koohbor, M., Soltanian, S., Najafi, M. & Servati, P. "Fabrication of CoZn alloy nanowire arrays: Significant improvement in magnetic properties by annealing process" *Mat. Chem. Phys.*, 131(3), 728, 2012.

46. Guo, Y., Qin, D.-H., Ding, J.-B. & Li, H.-L. "Annealing and morphology effects on the $Fe_{0.39}Co_{0.61}$ nanowire arrays" *Appl. Surf. Science*, 218(1-4), 107, 2003.
47. Aravamudhan S., Singleton J., Goddard, P. A. & Bhansali S. "Magnetic properties of Ni-Fe nanowire arrays: Effect of template material and deposition conditions" *J. Phys. D: Appl. Phys.*, 42, 115008, 2009.
48. Tian, F., Chen, J., Zhu, J. & Wei, D. "Magnetism of thin polycrystalline nickel nanowires" *J. Appl. Phys.*, 103, 013901, 2008.
49. Tian F., Zhu J., Wei D. & Shen Y. T. "Magnetic field assisting DC electrodeposition: General methods for high-performance Ni nanowire array fabrication" *J. Phys. Chem. B*, 109, 14852, 2005.
50. Coey, J. M. D. & Hinds, G. "Magnetic electrodeposition" *J. Alloys and Compounds*, 326(1-2), 238–245, 2001.
51. Sun, L. & Chen, Q. "Magnetic field effects on the formation and properties of nickel nanostructures" *Eur. J. Inorg. Chem.*, 435–440, 2009.
52. Sellmyer, D. J., Zheng. M. & Skomski, R. "Magnetism of Fe, Co and Ni nanowires in self-assembled arrays" *J. Phys.: Condens. Matter*, 13, 433, 2001.
53. Zeng, H., Skomski, R., Menon, L., Liu, Y., Bandyopadhyay, S. & Sellmyer, D. "Structure and magnetic properties of ferromagnetic nanowires in self-assembled arrays" *Phys. Rev. B*, 65(13), 134426, 2002.
54. Das, B., Mandal, K., Sen, P. & Bandopadhyay, S. K. "Effect of aspect ratio on the magnetic properties of nickel nanowires" *J. Appl. Phys*., 103, 013908, 2008.
55. Gao, T. R., Yin, L. F., Tian, C. S., Lu, M., Sang, H. & Zhou, S. M. "Magnetic properties of Co–Pt alloy nanowire arrays in anodic alumina templates" *J. Mag. Mag. Mat.*, 300(2), 471, 2006.
56. Zheng, M., Menon, L., Zeng, H., Liu, Y., Bandyopadhyay, S., Kirby, R. D. & Sellmyer, D. J. "Magnetic properties of Ni nanowires in self-assembled arrays" *Phys. Rev. B*, 62(18), 282, 2000.
57. Chien, C. L., Sun, L., Tanase, M., Bauer, L. A., Hultgren, A., Silevitch, D. M., Meyer, G. J., Searsonb, P. C. & Reich, D. H. "Electrodeposited magnetic nanowires: Arrays, field-induced assembly, and surface functionalization" *J. Mag. Mag. Mat.*, 249(1-2), 146, 2002.
58. Lin, S. W., Chang, S. C., Liu, R. S., Hu, S. F. & Jan, N. T. "Fabrication and magnetic properties of Ni nanowires" *J. Mag. Mag. Mat*., 282, 28, 2004.
59. Beck, G., Petrikowski, K. & Khan, H. R. "Magnetism in magnetic nanowire arrays" *Microstructure Analysis in Materials Science*, *Freiberg*, 15–17, 2005.
60. Han N., Guo G., Zhang L., Zhang G. & Song W. "Magnetization reversal for Ni nanowires studied by micromagnetic simulations" *J. Mater. Sci. Technol.*, 25(2), 151, 2009.
61. Vazquez M., Pirota, K., Torrejo, J., Navas, D. & Herna, M. "Magnetic behaviour of densely packed hexagonal arrays of Ni nanowires: Influence of geometric characteristics" *J. Mag. Mag. Mat.*, 294, 174, 2005.
62. Escrig, J., Lavín, R., Palma, J. L., Denardin, J. C., Altbir, D., Cortés, A & Gómez, H. "Geometry dependence of coercivity in Ni nanowire arrays" *Nanotech.*, 19(7), 075713, 2008.

63. Nielsch, K., Wehrspohn, R. B., Barthel, J., Kirschner, J., Go, U., Fischer, S. F. & Kronmu, H. "Hexagonally ordered 100 nm period nickel nanowire arrays" *Appl. Phys. Lett.*, 79(9), 1360, 2001.
64. Whitney, T. M., Jiang, J. S., Searson, P. C. & Chien L. C. "Fabrication and magnetic properties of arrays of metallic nanowires" *Science*, 261, 1316, 1993.
65. Kehua Zhong, Zhicheng Zhang, Baohua Shen, Meimei Lin, Qian Feng & Zhigo Huang "The size and temperature effects of coercivity for the magnetic nanowire: Monte Carlo Simulation" *Solid State Phenomena*, 121-123, 1081, 2007.
66. Zeng H., Zheng M., Skomski R., Sellmyer D. J., Liu Y., Menon L. & Bandyopadhyay, S. "Magnetic properties of self-assembled Co nanowires of varying length and diameter" *J. Appl. Phys.,* 87, 4718, 2000.
67. Yeh, W. J. & Yang Kun "Fabrication of uniform magnetic nanowire array" *J. Phys.: Conference Series*, 61, 1299, 2007.
68. Nielsch K. & Stadler, B. J. H. "Handbook of magnetism and advanced magnetic materials: Template-based synthesis and characterization of high-density ferromagnetic nanowire arrays" Edited by Helmut Kronmuller and Stuart Parkin, Volume 4: Novel Materials, John Wiley & Sons, Ltd., 2007.
69. Hertel R. "Micromagnetic simulations of magnetostatically coupled Nickel nanowires" *J. Appl. Phys.*, 90(11), 5752, 2001.
70. Sun, D.-L., Gao, J.-H., Zhang, X.-Q., Zhan, Q.-F., He, W., Sun, Y. & Cheng, Z.-H. "Contribution of magnetostatic interaction to magnetization reversal of Fe_3Pt nanowires arrays: A micromagnetic simulation" *J. Mag. Mag. Mat.*, 321(18), 2737, 2009.
71. Hertel R. "Computational micromagnetism of magnetization processes in nickel nanowires" *J. Mag. Mag. Mat.*, 249(1-2), 251, 2002.
72. Velazquez J., Garcıa C., Vazquez M. & Hernando A. "Dynamic magnetostatic interaction between amorphous ferromagnetic wires" *Phys. Rev. B*, 54(14), 9903, 1996.
73. Raposo V., Garcia, J. M., Gonza, J. M. & Va M. "Long-range magnetostatic interactions in arrays of nanowires" *J. Mag. Mag. Mat.*, 222, 227, 2000.
74. Lavín R., Denardin, J. C., Cortés, A., Gómez H., Cornejo M. & González G. "Magnetic properties of cobalt nanowire arrays" *Molecular Cry. Liq. Cry.*, 521(1), 293, 2010.
75. Rivas J., Mukenga, A. K., Zaragoza, G. & Blanco, M. C. "Preparation and magnetic behaviour of arrays of electrodeposited Co nanowires" *J. Mag. Mag. Mat.*, 249, 220, 2002.
76. Sorop, T. G., Nielsch, K., Göring, P., Kröll, M., Blau, W., Wehrspohn, R. B., Gösele, U. & de Jongh, L. J. "Study of the magnetic hysteresis in arrays of ferromagnetic Fe nanowires as a function of the template filling fraction" *J. Mag. Mag. Mat.*, 272-276, 1656, 2004.
77. Lupu, N., Lostun, M. & Chiriac, H. "Surface magnetization processes in soft magnetic nanowires" *J. Appl. Phys.*, 107(9), 09E315, 2010.
78. Adeyeye, A. O. & White R. L. "Magnetoresistance behaviour of single castellated $Ni_{80}Fe_{20}$ nanowires" *J. Appl. Phys.*, 95(4), 2025, 2004.
79. Bisero, D., Cremon, P., Madami, M., Tacchi, S., Gubbiotti, G., Carlotti, G. & Adeyeye, A. O. "Magnetization reversal of rectangular particles: Closure states and effect of dipolar coupling" *IEEE Trans. Mag.*, 48(4), 1593, 2012.

80. Beguivin, A., O'Brien, L. A., Jausovec, A. V., Petit, D. & Cowburn, R. P. "Magnetisation reversal in permalloy nanowires controlled by near-field charge interactions" *Appl. Phys. Lett.*, 99(14), 142506, 2011.
81. Volmer, M. & Neamtu, J. "Simulation of magnetisation curves in magnetic thin films using Stoner-Wohlfarth model" *Romanian Reports in Physics*, 56(3), 367, 2004.
82. Goolaup, S., Adeyeye, A. O. & Singh, N. "Magnetoresistance of closely packed $Ni_{80}Fe_{20}$ nanowires" *Thin Solid Films*, 505(1-2), 29, 2006.
83. Pal, S., Saha, S., Polley, D. & Barman, A. "Magnetization reversal dynamics in Co nanowires with competing magnetic anisotropies" *Solid State Communications*, 151(24), 1994, 2011.
84. Han, G. C., Zong, B. Y., Luo P. & Wu Y. H. "Angular dependence of the coercivity and remanence of ferromagnetic nanowire arrays" *J. Appl. Phys.*, 93(11), 9202, 2003.
85. Sharma, S., Barman, A., Sharma, M., Shelford, L. R., Kruglyak, V. V. & Hicken, R. J. "Structural and magnetic properties of electrodeposited cobalt nanowire arrays" *Solid State Communications*, 149(39-40), 1650, 2009.
86. Sorop, T., Untiedt, C., Luis, F., Kröll, M., Raşa, M. & De Jongh, L. "Magnetization reversal of ferromagnetic nanowires studied by magnetic force microscopy" *Phys. Rev. B*, 67(1), 014402, 2003.
87. Sorop, T., Untiedt, C., Luis F., & de Jongh, L."Magnetisation reversal of Fe nanowires in alumites studied by magnetic force microscopy" *J. Appl. Phys*., 93, 10, 2003.
88. Carignan, L., Massicotte, M., Caloz, C., Yelon, A., Fellow, L. & Ménard, D. "Magnetization reversal in arrays of Ni nanowires with different diameters" *IEEE Trans. Mag*., 45(10), 4070, 2009.
89. Vila, L., Piraux, L., George, J. M. & Faini, G. "Multiprobe magnetoresistance measurements on isolated magnetic nanowires" *Appl. Phys. Lett.*, 80(20), 3805, 2002.
90. Ounadjela k., Ferre R. & Louail L. "Magnetisation reversal in cobalt and nickel electrodeposited nanowires" *J. Appl. Phys*., 81, 8, 1997.
91. Hausmanns B., Krome, T. P., Dumpich, G., Wassermann, E. F., Hinzke, D., Nowak, U. & Usadel, K. D. "Magnetization reversal process in thin Co nanowires" *J. Mag. Mag. Mat.*, 240(2002), 297, 2009.
92. Fert, A. & Piraux, L. "Magnetic nanowires" *J. Mag. Mag. Mat.*, *200*, 338–358, 1999.
93. Pignard, S., Goglio, G., Radulescu, A., Piraux, L., Dubois, S., Declémy, A. & Duvail, J. L. "Study of the magnetization reversal in individual nickel nanowires" *J. Appl. Phys.*, 87(2), 824, 2000.
94. Liu, T., Wu, Y. H., Long, H. H., Liu, Z. J., Zheng, Y. K. & Adeyeye, A. O. "Transport properties and micromagnetic modelling of magnetic nanowires with multiple constrictions" *Thin Solid Films*, 505(1-2), 35, 2006.
95. Wernsdorfer, W., Doudin, B., Mailly, D., Hasselbach, K., Benoit, A, Meier, J., Ansermet, J.-Ph. & Barbara B. "Nucleation of magnetization reversal in individual nanosized nickel wires" *Phys. Rev. Lett.*, 77(9), 1873, 1996.
96. Hertel, R. & Kirschner, J. "Magnetization reversal dynamics in nickel nanowires" *Physica B: Condensed Matter*, 343(1-4), 206, 2004
97. Nian-mei, Han, Guang-hua, Guo, Guang-fu, Z., Wen-bing, S. & Gao-fu, Men "Domain wall structure transition during magnetization reversal process in magnetic nanowires" *Trans. Nonferrous Met. Soc. China*, 17(60571043), 1034, 2007.
98. Forster, H., Schrefl, T., Scholz, W., Suess, D., Tsiantos, V. & Fidler, J. "Micromagnetic

simulation of domain wall motion in magnetic nano-wires" *J. Mag. Mag. Mat.*, 249(1-2), 181, 2002.

99. Burn D. in private communication, 2013.
100. Salalha, W. & Zussman, E. "Investigation of fluidic assembly of nanowires using a droplet inside microchannels" *E., Phys. Flu.*, 17(6), 063301, 2005.
101. Wanekaya, A. K., Chen, W., Myung, N. V. & Mulchandani, A. "Nanowire based electrochemical biosensors" *Electroanalysis*, 18(6), 533, 2006.
102. Theron A., Zussman E. & Yarin A. L., "Electrostatic field –assisted alignment of electrospun nanofibers" *Nanotech.*, 12, 384, 2001.
103. Li, Q., Koo, S.-mo, Richter, C. A., Member, S., Edelstein, M. D., Bonevich, J. E., Kopanski, J. J., John, S. Suehle & Eric, M. Vogel. "Precise alignment of single nanowires and fabrication of nanoelectromechanical switch and other test structures" *IEEE Trans. Nanotech.*, 6(2), 256, 2007.
104. Smith, P. A., Nordquist, C. D., Jackson, T. N. & Mayer, T. S., "Electric field assisted assembly and alignment of metallic nanowires" *Appl. Phys. Lett.*, 77, 9, 2000.
105. Maijenburg, A. W., Maas, M. G., Rodijk, E. J. B., Ahmed, W., Kooij, E. S., Carlen, E. T., Blank, D. H. A. & Elshof, J. E.T. "Dielectrophoretic alignment of metal and metal oxide nanowires and nanotubes: A universal set of parameters for bridging pre-patterned microelectrodes" *J. Col. Inter. Sci.*, 355, 2, 486, 2011.
106. Yoo, B., Rheem, Y., Beyermann, W. P. & Myung, N. V. "Magnetically assembled 30nm diameter nickel nanowire with ferromagnetic electrodes" *Nanotech.*, 17(10), 2512, 2006.
107. Sun, L., Keshoju, K. & Xing, H., "Magnetic field mediated nanowire alignment in liquids for nanocomposite synthesis" *Nanotech.*, 19(40), 405603, 2008.
108. Tanase, M., Bauer, L. A., Hultgren, A., Silevitch, D. M., Sun, L., Reich, D. H., Searson, P. C. & Meyer, G. J., "Magnetic alignment of fluorescent nanowires" *Nano. Lett.*, 1(3), 155, 2001.
109. Hangarter, C. M., Rheem, Y., Yoo, B., Yang, E.-H. & Myung, N. V. "Hierarchical magnetic assembly of nanowires" *Nanotech.*, 18(20), 205305, 2007.
110. Zhang, L., Lu, Y., Dong, L., Pei, R., Lou, J., Kratochvil, B. E. & Nelson, B. J. "Noncontact manipulation of Ni nanowires using a rotating magnetic field" *9th Nanotech. Conf.: IEEE Nano*, 8, 586, 2009.
111. Bangar, M. A., Hangarter, C. M., Yoo, B., Rheem, Y., Chen, W. & Mulchandani, A."Magnetically assembled multisegmented nanowires and their applications" *Electroanalysis*, 21(1), 61, 2009.
112. Bellino, M. G., Calvo, E. J. & Gordillo, G. J. "Nanowire manipulation on surfaces through electrostatic self-assembly and magnetic interactions" *Phys. Stat. Sol. (RRL) - Rapid Research Letters*, 3(1), 1, 2009.
113. Lee, S.-W., Ham, M.-H., Kar, J. P., Lee, W. & Myoung, J.-M., "Selective alignment of a ZnO nanowire in a magnetic field for the fabrication of an air-gap field-effect transistor" *Micro. Eng.*, 87(1), 10, 2010.
114. Rheem, Y., Hangarter, C. M., Yang, E.-hyeok E. H., Member, S., Park, D.-yong, Myung, N. V. & Yoo, B. "Site-specific magnetic assembly of nanowires for sensor arrays fabrication" *IEEE Tran. Nanotech.*, 7(3), 251, 2008.
115. Horton, M., Hong, H., Li, C., Shi, B., Peterson, G. P. & Jin, S. "Magnetic alignment of Ni-coated single wall carbon nanotubes in heat transfer nanofluids" *J. Appl. Phys.*,

107(10), 104320, 2010.

116. Bentley, A. K., Trethewey, J. S., Ellis, A. B. & Crone, W. C. "Magnetic manipulation of copper-tin nanowires capped with nickel ends" *Nano. Lett.*, 4(3), 487, 2004.
117. Hangarter, C. M. & Myung, N. V. "Magnetic alignment of nanowires" *Chem. Mat.*, 17(6), 1320, 2005.
118. Tanase, M., Silevitch, D. M. & Hultgren, A. "Magnetic trapping and self-assembly of multicomponent nanowires" *J. Appl. Phys.*, 91(10), 8549, 2002.
119. Lee, S.-W., Jeong, M.-C., Myoung, J.-M., Chae, G.-S. & Chung, I.-J. "Magnetic alignment of ZnO nanowires for optoelectronic device applications" *Appl. Phys. Lett.*, 90(13), 133115, 2007.

Chapter four

Experimental methods: Fabrication of thin films and nanowires

4-1 Introduction

The experimental techniques used to fabricate ferromagnetic thin films, cylindrical nanowires, micromarkers and contact pads are described in this chapter following a brief discussion on the theory behind each technique. The technique used to create thin films and nanowires was *electrodeposition.* The methods used to release and deposit templated nanowires onto substrates are described. To allow the magnetic and electrical transport measurements to be performed on isolated ferromagnetic nanowires, gold micromarkers and contact pads were prepared using *physical vapour deposition (PVD)* methods combined with *electron beam lithography*. The PVD methods include *magnetron sputtering* and *thermal evaporation* techniques. To electrically connect the isolated nanowires with the contact pads, *electron beam lithography* and *local chemical vapour deposition* were used. The technical difficulties associated with the electrical connections of isolated nanowires to the contact pads are also discussed along with some examples. Finally, the *wire bonding* process used to electrically connect the contact pads with the chip carrier for external connections is also described.

4-2 Electrochemical deposition

Arrays of ferromagnetic cylindrical nanowires (and thin films) were grown by electrochemical deposition in alumina templates (on flat substrates) with different diameters (thicknesses) and compositions. The nanowires were released from their templates by dissolving the templates and then kept in a suitable dilute suspension. The suspension was dispensed onto substrates with prefabricated gold micro-patterns and electrical contact pads for magnetic and electrical transport investigations, respectively. Therefore, a theoretical background of this technique and the experimental procedure followed to fabricate these structures is presented in the following sub-sections. Release of the nanowires into a dilute suspension, and their deposition onto substrates (in the absence or presence of a magnetic field) are also described in detail.

4-2.1 Theoretical background of electrochemical deposition

Electrochemical deposition (*electrodeposition)* has been known for a long time and is commonly known as *electroplating* to describe its usage in covering various materials with different metals [1]. It can replicate the exact shape of the surface needing to be covered by selected metals depositing atom by atom. As mentioned in the previous chapter, this technique can be easily scaled up for industrial processing and it is possible to produce different types of nanostructures of single elements [2,3], alloys [4,5] and multilayers [6,7] of electrically conducting materials such as thin films, nanowires, nanodots and nanotubes.

Let us now consider the theoretical background of electrochemical deposition. If an electrode of solid material such as zinc is immersed in a container containing a polar solvent or an electrolyte solution, electrochemical reactions occur accompanied by charge transfer across the metal/solute interface until equilibrium is reached [8,9]. The zinc ions Zn^{2+}, move into solution leaving behind electrons in the Zn electrode. Due to electrostatic forces, the ions are distributed at the electrode surface, as shown schematically in Figure 4.1[10]. The surface of the Zn electrode thus becomes covered with negatively charged electrons and the solution in close proximity to the electrode will contain positively charged Zn^{2+}, forming an *electric double layer* at the metal/solution interface [8,9].

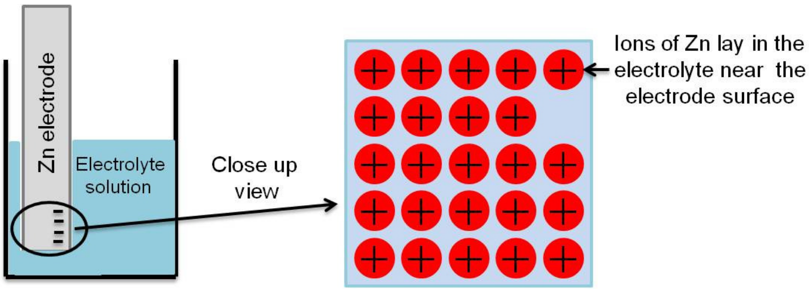

Figure 4.1 Schematic diagram showing charges across the solid/liquid interface when equilibrium is reached. Zinc ions transfer from the metal to the solution leaving behind electrons to build up on the metal surface creating an electric double layer. Modified from [10].

For a given size of electrode, the number of ions produced in the process depends on its composition [8,9]. As an example, magnesium produce more positive ions than copper or zinc [8]. This basically depends on the location of the element in the electrochemical series. Some of the ions get back their electrons and become neutral atoms sticking to that point of the electrode surface. After a period of time, a dynamic equilibrium will be established between the rate at which the ions leave the electrode surface and the rate at which they rejoin it, leading to a final potential difference at the double layer. This potential difference is known as the *electrode potential* for that particular electrode/solution interface [8,9]. Although, this potential is very small (around a few volts at most), the potential gradient is high due to the very small layer thickness [8]. It is very difficult to measure this potential directly using a voltmeter, because it is impossible to connect the voltmeter with the negatively charged electrode surface and the positively charged ionic layer of the solution. Therefore, relative potentials of the electrodes are measured with respect to a standard electrode known as a *standard hydrogen electrode* and assuming this electrode has zero potential [8,9]. Some elements such as Mg and Zn oxidise more easily than hydrogen, losing electrons and forming ions. In contrast, elements such as Cu, Ag and Au have a *lesser ability* to be oxidized than hydrogen which means that they reduce easily back to the neutral atoms. Accordingly, Zn and Cu electrodes have the standard potentials of –0.76 V and +0.34 V, respectively [11]. This means that the Zn electrode oxidizes easily (producing more electrons) than the hydrogen electrode, whilst the Cu electrode reduces more than the hydrogen electrode.

Let us now imagine two electrodes of different materials such as Zn and Cu immersed in suitable electrolyte solutions such as $ZnSO_4$ and $CuSO_4$, respectively separated by a porous membrane. The electrochemical reactions would produce their metal ions (Zn^{2+}, Cu^{2+}) at the respective metal/electrolyte interfaces. The Zn electrode will have more excess electrons than the Cu electrode on their surfaces until they reach their corresponding standard electrode potentials of –0.76 and +0.34 V, respectively [11]. The electrochemical reactions at the zinc/electrolyte and copper/electrolyte interfaces are given by $Zn \rightarrow Zn^{+2} + 2e^-$ and $Cu^{+2} + 2e^- \rightarrow Cu$, respectively. These equations indicate that, the Zn continuously dissolves into the solution due to its oxidation, whereas the reduction of Cu^{2+} ions results in the deposition of Cu onto the Cu electrode. This process will end only when a new equilibrium is reached.

The situation can be reversed by applying an external electric field to these electrodes using a constant voltage source. This process is known as *electrolysis* in which the electrical energy converts into chemical potential. The setup used for this process is referred to as an *electrochemical cell* and the electrode connected with the positive terminal of the external voltage source where the oxidation reaction took place is known as the *anode* or *counter electrode*. The electrode connected with the negative terminal of the external source, where reduction process occurs accompanied by material deposition, is termed the *cathode* or *working electrode* [8]. In a two-electrode system however, it is impossible to measure the exact potential difference between these electrodes. Therefore, three electrode systems have been developed. The third electrode is a standard electrode with a known potential and is referred to as the *reference electrode* [8]. A reference electrode composed of Ag/AgCl in saturated KCl solution is widely used in this technique [8]. It has a standard electrode potential of +0.197 V [8]. A schematic diagram of a three-electrode electrodeposition system is shown in Figure 4.2(a). Three electrode systems are recommended for exact measurements of the voltage between the working and counter electrodes during the synthesis of thin films and nanowires of desirable conducting materials. Therefore, a three-electrode system was used to produce ferromagnetic thin films and nanowires in this work. Figure 4.2(b) is a photograph showing the actual electrochemical cell used in this work. The green colour of the electrolyte is a $NiSO_4$ solution.

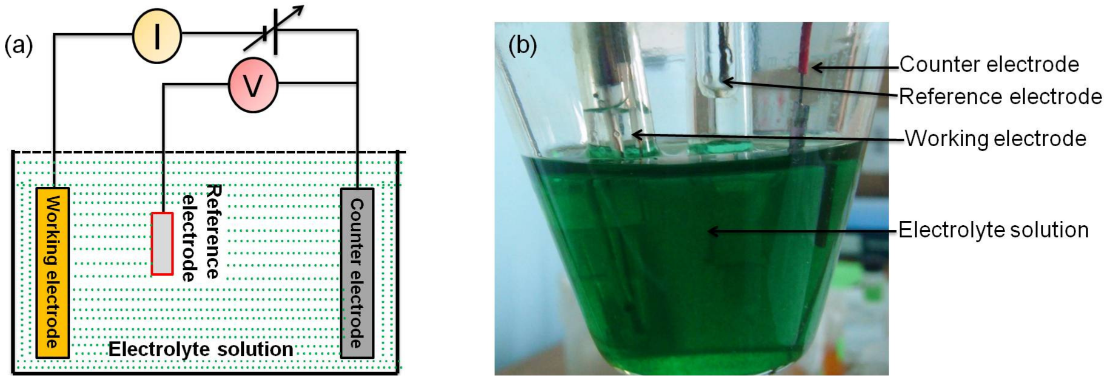

Figure 4.2(a) Schematic diagram showing the three electrode system in which a reference electrode is added in order to measure the exact voltage and hence to improve the deposited materials, and (b) photograph of the actual system used to fabricate ferromagnetic nanowires and thin films [12].

In order to create thin films of various materials, suitable substrates such as Si/SiO_2 were used as a working electrode, whilst to create nanowires, nanoporous (nano-channel) membranes are needed. As mentioned in chapter three (section 3.2) a wide range of templates have been developed, such as alumina and polycarbonate. These templates are widely used to create ferromagnetic nanowires [2-7], nanodots [13] and nanotubes [14,15]. As such membranes are insulators to electric current, a good electrically conducting layer needs to be deposited on one side of them to serve as a working electrode and to block the pores on one side. A platinum or gold wire of purity ~99.999% is often used as a counter electrode in the electrochemical cell. The membrane electrode is placed vertically in the electrolyte solution with the open end of the nanopores facing towards the counter electrode. By applying a suitable negative potential between the working and the counter electrodes, the desired materials such as Ni, Co and Fe and their alloys (such as $Ni_{80}Fe_{20}$) can be deposited onto the working electrode either in the form of continuous thin films or template structured nanowires depending on the substrate in use. To grow these materials, sulphate salts of the elemental metals such as; $NiSO_4$, $CoSO_4$ and $Fe_2(SO_4)_3$, respectively are used as the electrolyte solution. To deposit an alloy of the desired metals, a mixture of the corresponding sulphate salts can be used.

During the electrodeposition, the positively charged metal ions of the sulphate salts do not move alone towards the negatively charged working electrode under the potential difference between the working and counter electrodes. This is because the metal ions are surrounded with negatively charged hydroxyl ions, OH^{2-}. Therefore, these clusters of ions as a whole are moving towards the working electrode. Consequently, the pH value of the solution, that determines the hydrogen ion, H^+, concentration of a particular electrolyte solution, plays a crucial role in depositing the metal ions on the substrates. Depending on the pH value, the crystalline structure of the deposited materials may also change [7,16,17].

For a particular material deposition, a specific potential difference between the working and counter electrodes is desirable depending upon the position of the metals in electrochemical series [8,9]. Otherwise, the metal ions will not deposit at all on the working electrode substrate or will be contaminated by the deposition of other undesirable ions that are present in the electrolyte solution. *Linear sweep voltametry (LSV) measurements* were used to determine the desirable potential needed [8,9,17]. During this measurement, the working electrode potential is swept from zero to a negative value with respect to the counter electrode and the corresponding electrical current passing through the electrolyte recorded. As an example, Figure 4.3 shows a linear sweep voltametry result obtained from a particular electrolyte solution and working electrode [12]. When the applied potential difference is small, the corresponding cell current would be zero or very low because there is no deposition on the working electrode. As the potential difference increases, the current increases mainly due to the desired metal ion deposition, as the population of those ions are the highest in the solution and it should be linearly proportional to the potential difference. Any non-linear behaviour indicates the deposition of other undesired ions. In general, the desired deposition potential is selected as the first rapid increase in the current, as marked with a red circle in the Figure 4.3.

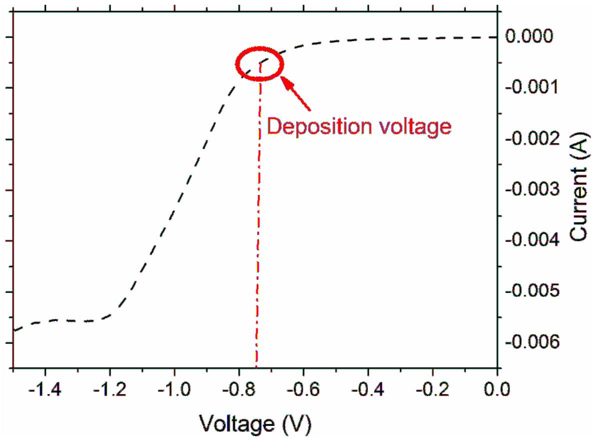

Figure 4.3 Linear sweep voltametry for a particular combination of electrolyte solution and working electrode. This measurement was performed during the preparation of Ni nanowires [12].

Thus, when a suitable negative potential is applied between the working and counter electrodes, the positively charged metallic ions within the electrolyte solution move towards the working electrode that is the gold thin film on one side of the membranes, through the nanochannels and are reduced to metallic atoms by capturing electrons from the gold electrode [16,17]. Using this technique thousands of metallic nanowires can be grown within the membrane with nanowire diameters the same as the nanopores and with maximum lengths same as of the thickness of the membranes. However, different deposition times lead to different lengths of the nanowires with a uniform length across the whole area of the membrane. Using a high quality template, one can achieve highly ordered two-dimensional arrays of parallel cylindrical nanowires with a specific inter-wire separation [17-19].

4-2.2 Fabrication of thin films and arrays of ferromagnetic nanowires

Nickel (Ni) and Permalloy ($Ni_{80}Fe_{20}$) thin films were deposited onto Si/SiO_2 substrates with different deposition times (different thicknesses) using electrochemical deposition. The area of these substrates was 2.5 mm × 20 mm. The same procedure was used to synthesise ferromagnetic nanowires in commercially available ~60 µm thick alumina templates purchased from Whatman Inc. with a nominal pore diameter of ~200 nm for preparing NiFe nanowires and ~300 nm diameter for growing Ni and Co nanowires. The fabrication process was carried out using an Autolab-30 potentiostat and a glass electrochemical cell of a capacity of 20 cm^3 with three-electrode arrangement (see Figure 4.2(b)). The reference electrode used was Ag/AgCl, whilst a platinum electrode was used as the counter electrode.

Prior to deposition, all the Si/SiO$_2$ substrates were first carefully cleaned using acetone and isopropanol (IPA), then dried very well using a nitrogen blower. A gold layer of purity 99.99% was deposited onto Si/SiO$_2$ substrates with a thickness of ~10 nm using thermal evaporation (explained in section 4-3.2). To enhance the adhesion of this layer to the substrates, 3 nm of Cr was deposited prior to Au deposition. On the other hand, a layer of Au with thickness of ~100 nm was deposited on one side of the alumina templates using the sputtering technique (explained in section 4-3.1). The samples were placed in the electrochemical cell and connected to the external circuit using copper wires attached to the sample by silver conductive paint. To prevent electrodeposition onto the backside surface of the substrate (gold surface) the surface was covered with a strip of insulating tape. The thin films and nanowires samples were produced by *B. Das* (SN Bose National Science Centre, Kolkata, India), *J. King* and *D. Atkinson* (Department of Physics, Durham University, U.K.) at SN Bose National Centre for Basic Science in Kolkata, India [12].

Ni and Co thin films and nanowires were grown using 0.57 M of NiSO$_4$ and CoSO$_4$, respectively with 31 g/l of H$_3$BO$_3$. Ni$_{80}$Fe$_{20}$ thin films and nanowires were prepared using an electrochemical bath consisting of 1.3 M of NiSO$_4$ and 0.151 M of FeSO$_4$ along with boric acid. The pH of the solution was maintained between 3.5 and 4 by adding few drops of dilute ammonia solution.

To obtain different thicknesses of thin films, deposition times of 10, 20, 30, 60, and 90 s were used. For nanowire deposition, the pores of the alumina templates were filled with nanowires of approximate length of 20 μm for a deposition time of ~180 minutes. After electrodeposition, the samples were washed very well in distilled water followed by acetone for a time of ~30 seconds followed by IPA for another ~30 seconds and blown with argon /nitrogen gas to dry completely.

4-2.3 Release of nanowires from their templates

Before the nanowires can be measured with magneto optic Kerr effect (MOKE) and magnetoresistance (MR) setups, they need to be separated from the membrane and cleaned. This was carried out by dissolution of the alumina membrane. The objective was to obtain clean nanowires distributed over prefabricated substrates with gold patterns and sufficiently isolated from each other to allow the electrical and magnetic measurements to be performed on isolated individual or small clusters of nanowires.

To dissolve the alumina templates, the nanowire filled templates were subdivided into small sections of approximate areas of 4 mm^2 and placed in 2 M sodium hydroxide (NaOH) for approximately 48 hours at room temperature. Sodium hydroxide dissolved the alumina template and formed a water soluble complex ion with hydroxide ions [20,21]. The nanowires were washed repeatedly with distilled water and then with IPA leaving the nanowires attached to the gold base layer. Figure 4.4 shows two example scanning electron micrographs of arrays of NiFe nanowires attached to the gold electrode layer after removal of the alumina templates. To release the nanowires from the gold layer, the suspension in IPA was placed in an ultrasonic bath for sonication. Different periods of sonication were used to investigate the effect of sonication time upon the nanowire lengths as presented in chapter six.

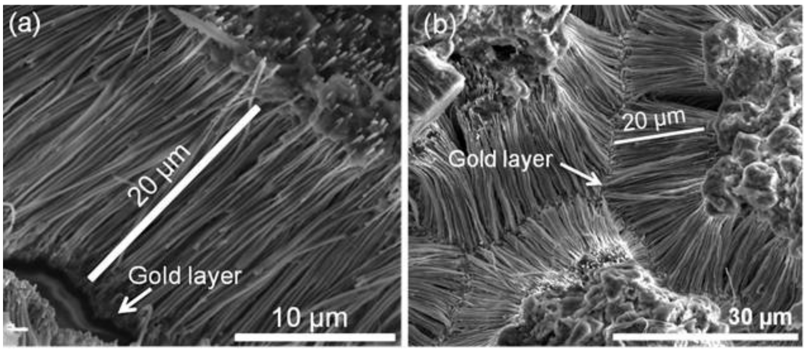

Figure 4.4 Scanning electron micrographs showing examples of arrays of electrodeposited NiFe nanowires attached to the gold layer after removal of the alumina templates using sodium hydroxide.

4-2.4 Deposition of released ferromagnetic nanowires on substrates

Once the nanowires were released to form a dilute suspension in IPA, single drops of the suspension were placed onto the centre of a clean Si/SiO_2 substrate. Two areas of substrates were used in this work. One set of substrates of approximate area of 8×10 mm^2, were used for studying the morphology, dimensions and for analysis of magnetic alignment presented in chapters six and seven, respectively. The other one is of approximately 4×4 mm^2 substrates with prefabricated gold patterns were used for the magnetic and electrical transport investigations presented in chapter eight.

For magnetic alignment analysis, the substrates were placed horizontally between the pole pieces of a small purpose made electromagnet as demonstrated in the schematic diagram shown in Figure 4.5. Low concentration nanowire suspensions were allowed to deposit the nanowires on the desired substrates using a pipette with a fixed volume of 15 μL by drop casting the dilute suspension into the substrate. The solvent evaporated at room temperature under normal laboratory atmospheric conditions, which typically took a few minutes. The deposited nanowires become fixed to the substrate probably due to the *van der Waals* or *electrostatic forces*. This is important because it enables all the characterisation measurements and the subsequent nanofabrication steps needed later.

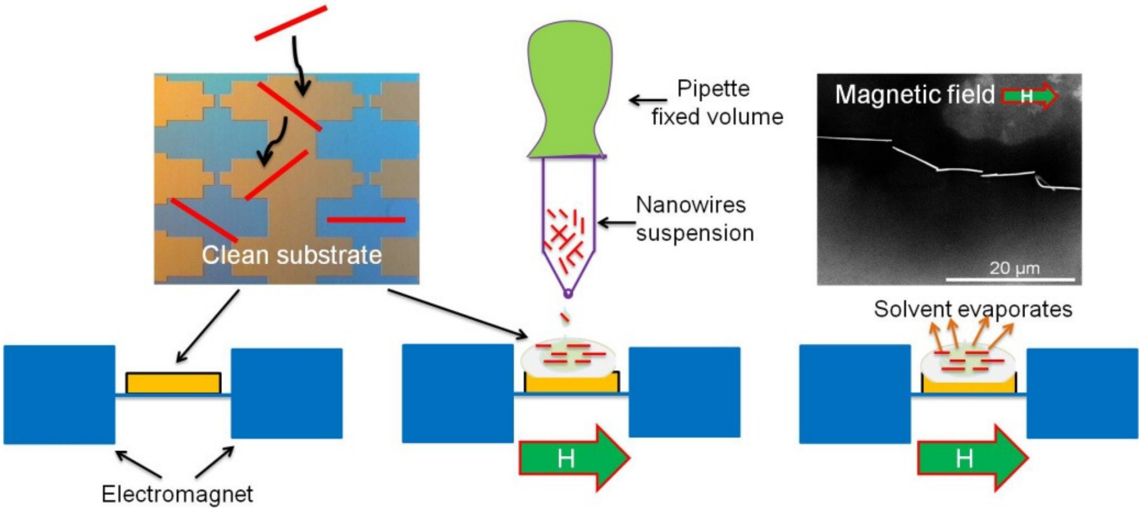

Figure 4.5 Schematic illustration of the deposition of nanowires onto a clean silicon substrate placed between the poles of an electromagnet.

4-3 Physical vapour deposition for thin films and nanostructures

Physical vapour deposition (PVD) is another method for preparing thin film materials. The atoms of the material need to be evaporated as in thermal evaporation and molecular beam epitaxy or ejected from a target as in sputtering by ion bombardment. The evaporated or sputtered atoms need to have a sufficient energy to transfer and be deposited on a substrate by condensation and relaxation. The following subsections investigate both magnetron sputtering and thermal evaporation techniques which were extensively used throughout this work.

4-3.1 Magnetron sputtering technique

Magnetron sputtering was mainly used here to fabricate contact pads, electrically connect the isolated wires with the contact pads after patterning and deposit gold layers on one side of the alumina templates to serve as a working electrode in the electrochemical cell. In this work a single source magnetron sputter system was constructed and built by the author with help from *D. Atkinson* and technical staff (Department of Physics, Durham University, U.K.). This section deals with the theoretical background of this technique followed by the experimental procedure employed to deposit these structures.

4-3.1.1 Theoretical consideration of magnetron sputtering technique

Sputtering in general can be defined as the removal of surface material when it is bombarded with highly energetic ions. It was first discovered in 1852 by *W. R. Grove* when he was working on the electrical conductivity of gases [22]. In a sputtering system, an electric field is applied between two metallic electrodes known as the *cathode* and *anode* that are sited in an evacuated chamber. The electrodes can be connected to a D.C. or R.F power supply [22]. A schematic description of a conventional sputtering system is shown in Figure 4.6(a). The target material is usually placed on the surface of the cathode. The chamber is filled with a low pressure inert gas such as argon, xenon, or krypton. This gas becomes positively ionised upon applying a sufficient electric field to strike the glow disch-

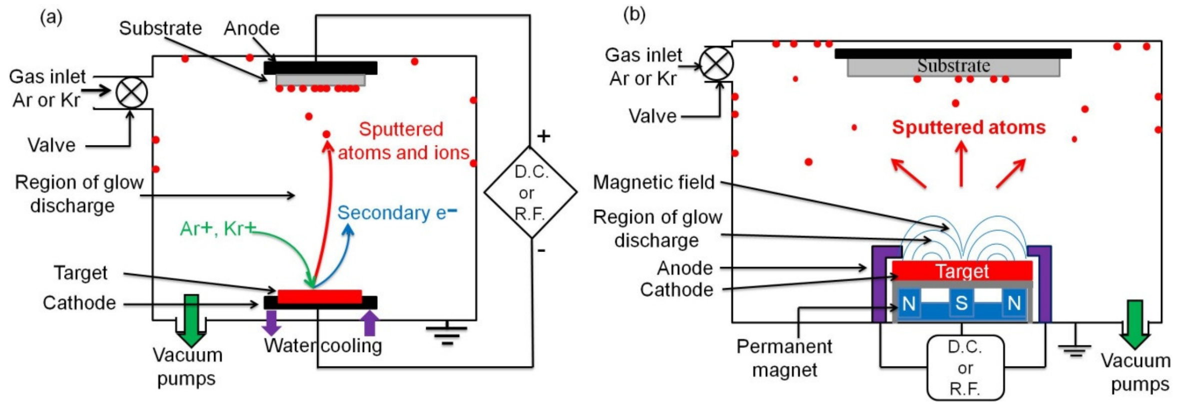

Figure 4.6 Schematic diagrams of (a) conventional, and (b) magnetron sputtering systems. Atoms are ejected from the target surface as a result of bombardment by ions such as argon or krypton ions. A series of permanent magnets is placed behind the target to capture the escaping electrons and increase the sputtered atoms.

arge (plasma) between the two electrodes [22-24]. Due to the negative voltage of the target, the positive ions are accelerated toward the target and as a result different phenomena can occur depending on the type of the material making up the target, the ion type, the ion energy, and other factors, including gas flow rate, pressure, plasma power, electrode dimensions, electrode spacing, ratio of electrode dimensions to electrode spacing [22-25]. These phenomenon are: the ejection of atoms from the target, scattering and neutralisation of ions, the production of secondary electrons and ions, and ion implantation in the target with or without simultaneous target atom ejection [22,25].

The most important phenomenon here is the ejection of atoms from the target. There are two different theories explaining this ejection [22,25]. The first theory is *thermal vaporisation* in which the ejection of atoms is due to the vaporisation of the target surface as a result of heating due to the bombardment of high energy ions [22,25]. The second concept is direct *momentum transfer* in which the sputtering occurs as a result of the transfer of kinetic energy from the incident ions to the target surface atoms and sputtering occurs as a result of the collision cascade in the surface of the target [22,25].

However, in the conventional sputtering system high gas pressure is required to create the plasma between the two electrodes because there is a problem that not all the free electrons contribute to produce the plasma reducing the rate of material deposited onto the substrate and increasing contamination [22,25]. Placing permanent magnets behind the target as schematically shown in Figure 4.6(b) to form a magnetron source was found to be effective in reducing the gas pressure needed for producing the plasma, increasing the rate of material deposited onto the substrate up to one order of magnitude with a very low contamination in the deposited films [22,26]. This is because the permanent magnet produces a magnetic field that extends parallel to the target surface and perpendicular to the plasma capturing the escaping electrons and densifying them in the immediate area of the target where they move in spiral motion and as a result increase the ion bombardment and hence the number of sputtered atoms [26]. As an example, Figure 4.7 shows photographic images of a Ni target before and after sputtering which clearly demonstrates the effect of using a permanent magnet behind the target.

The ratio of the number of atoms removed from the target material to the number of incident ions is referred to as the *sputtering yield* [22,25]. The sputtering yield is strongly dependent on the energy of the incident ions, target materials and angle of incidence. The sputter yield decreases with increasing incident angles [22,25]. The crystalline structure of the target surface is also significant depending on whether it is polycrystalline, single crystal or amorphous [25].

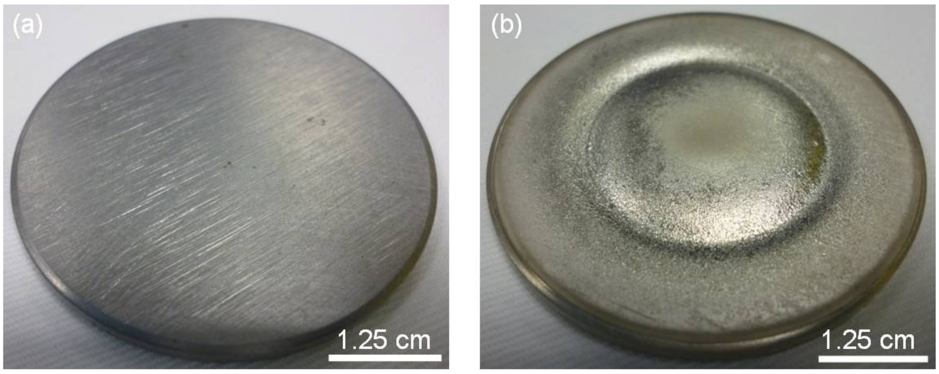

Figure 4.7 Photographs of a Ni target (a) before, and (b) after sputtering showing the race track effect from the permanent magnet (magnetron) to densify and confine the plasma on the target.

4-3.1.2 Experimental procedure for sputter-deposition

The magnetron sputtering system used in this research is shown in Figure 4.8(a). The lowest base pressure achieved within this system was around 2×10^{-6} Torr using a combination of rotary and *turbo molecular pumps*, this may have been limited by the very large O-ring seal on the top flange. The sputtering gas was argon with a purity of 99.9 % which entered the vacuum chamber through a variable leak valve. The gas flow rate in the chamber was controlled via the partial closing of a gate valve. When the gate valve was closed, a *low flow rate* was achieved, when the gate valve was half opened, *medium flow rate* was defined, and a *high flow rate* was obtained with a fully open gate valve. Different target materials can be used with this system. They were discs with a 50 mm diameter and 99.99% purity. The target was mounted by mechanical supports on a water cooled backing plate and surrounded by a metallic shield, which acts as the *anode.* The construction of the magnetron and target is shown in Figure 4.8(b). The distance between the anode and target surface (cathode) was kept constant at ~3 mm and the distance between the target surface and the substrate holder was also kept constant at ~90 mm throughout all the work presented here.

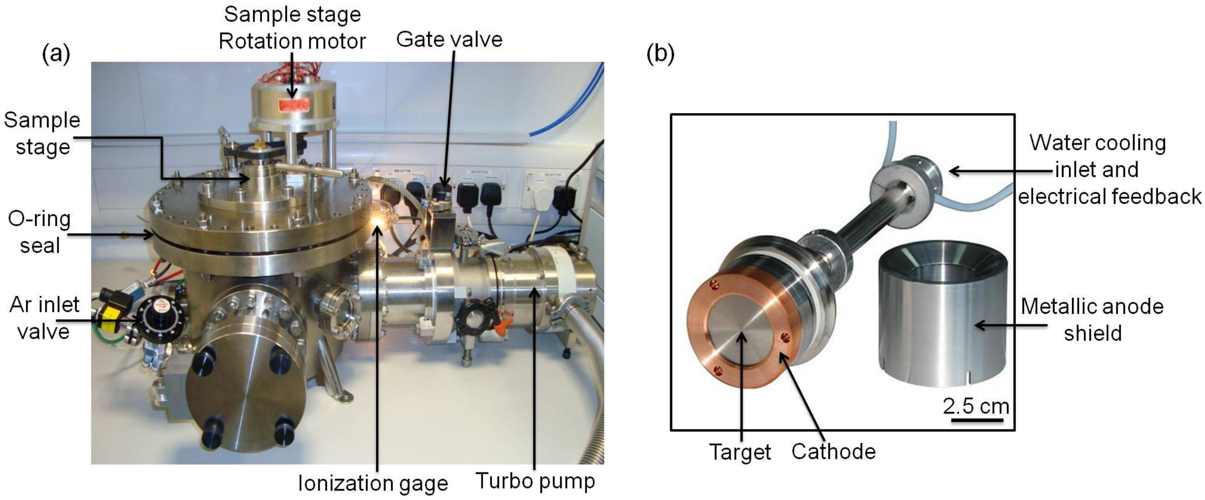

Figure 4.8 Photographs of (a) DC magnetron sputtering system used in this project to deposit ferromagnetic thin films and nanostructures, and (b) the target set of this system in which the cathode is a planar disc of the material to be deposited surrounded by a metallic anode shield.

The anode and cathode were connected to a DC power supply (with a maximum voltage 600 volt and a power around 3.6 kW), to provide the power needed to strike and maintain an argon plasma. The target voltage and plasma current were measured with digital multi-meters. The deposition rate and film thickness were monitored during film growth using a *quartz crystal oscillator*. The thickness monitor was calibrated using *grazing incidence X-ray reflectivity* measurements.

Special sample holders shown in Figure 4.9 were designed in the course of this research to deposit multiple thin films and nanostructures at different conditions within the same vacuum deposition run. This multiple substrate holder allows deposition on up to 15 samples in a single run without breaking the vacuum. The maximum stray magnetic field measured near the sample holder was around 20 Oe.

In order to obtain uniform thickness across all the samples, the substrate holder was rotated during the deposition process by an electrical motor at ~12 revolutions per minute. Prior to deposition, the chamber was flushed with argon gas for approximately 5 minutes, in order to remove the residual air molecules or water vapour inside the chamber if any were left after evacuation. To clean the target surface from oxides or any other contaminates, a pre-sputtering process was performed prior to deposition for a time of ~5 minutes, whilst the sample shutter was closed.

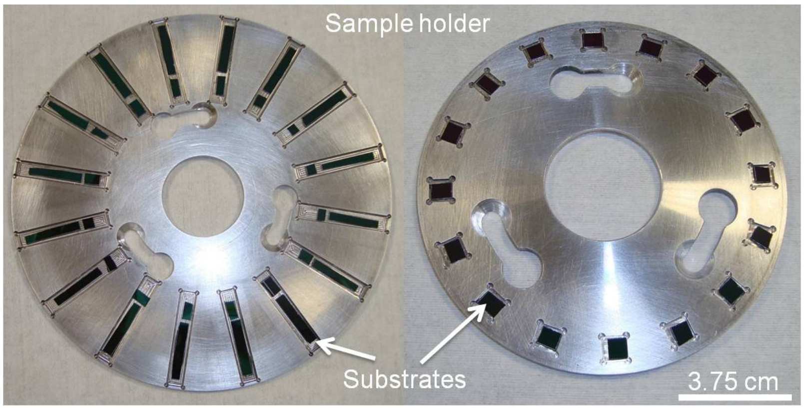

Figure 4.9 Photographs showing the special sample holder designed in the course of this research to deposit thin films under different conditions within the same vacuum run. This multiple substrate holder allowed sputtering of up to 15 samples in a single run without breaking the vacuum.

4.3.2 Thermal evaporation technique

Thermal evaporation is another physical vapour deposition technique and can be used to deposit many materials onto substrates [22]. It was mainly used here to deposit thin uniform layers of chromium and gold onto Si/SiO$_2$ substrates after patterning using electron beam lithography to create micro-scale markers, electrical contact pads and electrodes for connecting the electrodeposited isolated nanowires with the prefabricated electrical contact pads. A photograph of the system built in Durham is shown in Figure 4.10 together with a schematic illustration of this system.

The main part of this system is an evacuated chamber. This chamber was evacuated by *rotary and turbo molecular pumps* to create a base pressure around 10^{-7}-10^{-8} Torr. During deposition and film growth, the pressure was typically in the range of 10^{-6} Torr. At the top of this chamber there is a sample holder protected by a mechanical shutter which is opened when a stable deposition rate is achieved and is used to monitor the exposure time and film thickness. A piezoelectric crystal is used to control the deposition rate and the thickness of deposited material. There are three tungsten/alumina crucibles in the chamber and they are heated by passing a large electric current (typically 30-50 A) through the filaments within the crucibles.

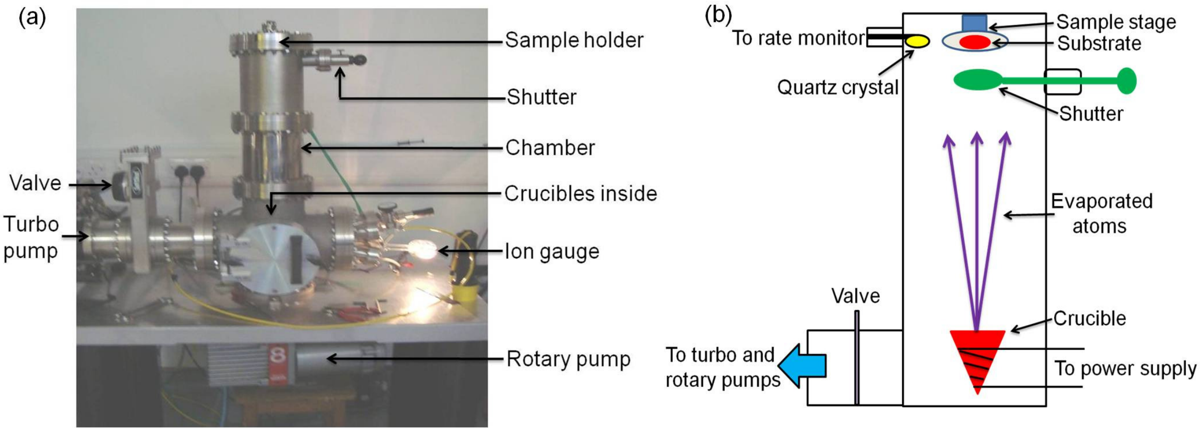

Figure 4.10 (a) Photograph, and (b) schematic diagram of the thermal evaporation system used in this project to deposit thin uniform layers of chromium and gold onto Si/SiO$_2$ substrates after patterning of micromarkers, electrical contact pads and electrical electrodes to connect the electrodeposited isolated nanowires with the prefabricated contact pads.

The target material melts and a vapour pressure is established, the atomic vapour reaches the substrate, located approximately 37 cm above the source, where it cools down and solidifies to form a thin film with a stable and uniform deposition over the entire surface. A high vacuum and the large distance between the sample holder and crucibles is significant, as the long mean free path of the molecules allows the deposition of films that are uncontaminated and of high uniformity [22].

4-4 Dual beam system: focused ion and electron beam methods

A *dual beam system* that combines a *focused ion beam* column and an *electron beam* column was extensively used throughout this project to perform different operations or functions. This system was used as a scanning electron microscope for imaging and as a fabrication tool. For instance, it was used to fabricate micromarkers and electrical contact pads on chips to allow location of the isolated nanowires for MOKE measurements, as well as to connect the isolated wires with the prefabricated contact pads for the electrical measurements (MR) presented in chapter eight. Therefore, a brief theoretical description and details of the experimental procedure followed to achieve the fabrication processes within this technique are given in the following subsections along with some examples.

4-4.1 Components and principles

The dual beam apparatus is a combination of two systems, a *scanning electron microscope (SEM)* and a *focused ion beam (FIB)* system. This type of apparatus first appeared in the late 1970s and early 1980s. A decade later the first commercial system was introduced [27]. A photograph together with the schematic diagram of the *FEI-Helios Nanolab dual beam FIB/SEM system* used in Durham are shown in Figure 4.11. This system consists of four parts; the *ion and electron columns* which lie on the top, an *evacuated chamber* underneath the columns, *gas delivery tools* and a *computer system* with *specialised software* which allow performing all the operations necessary for imaging and nanofabrication process.

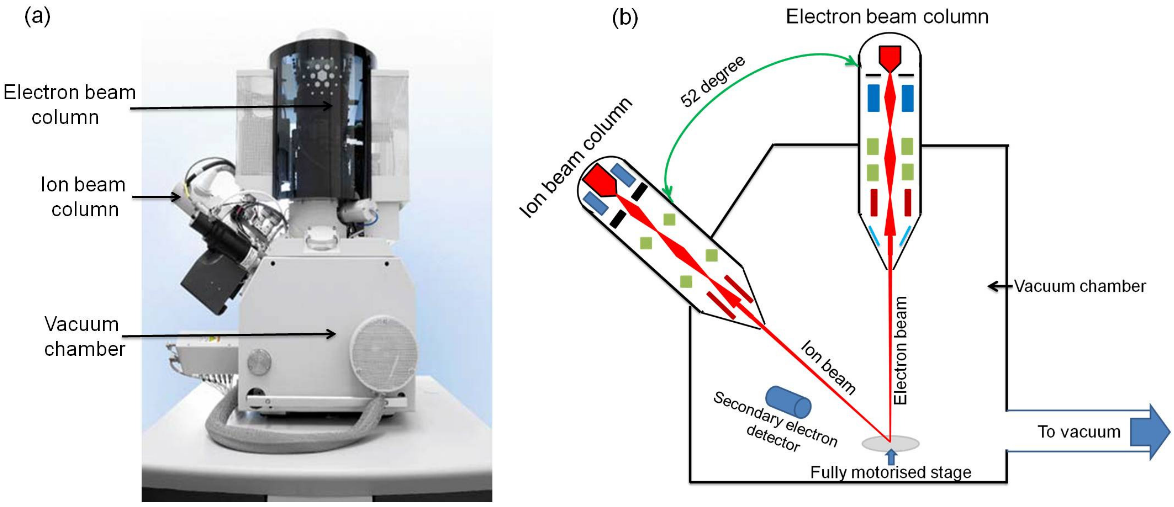

Figure 4.11(a) Photograph, and (b) schematic diagram of the dual beam system, with a focused ion and an electron beams, used in Durham. It was used extensively in this work as a SEM for imaging and for a number of different nanofabrication applications.

Figure 4.12 shows the detailed schematic diagrams of the system. The SEM produces electrons from an *electron gun* located at the top of the column. The electron gun is very important in determining the final imaging performance of the system which depends on three factors [28]. The first is the *virtual source size* which determines the spot size at the sample and gives the resolution of the system. The second factor is the *brightness,* which is related to the current density in the beam.

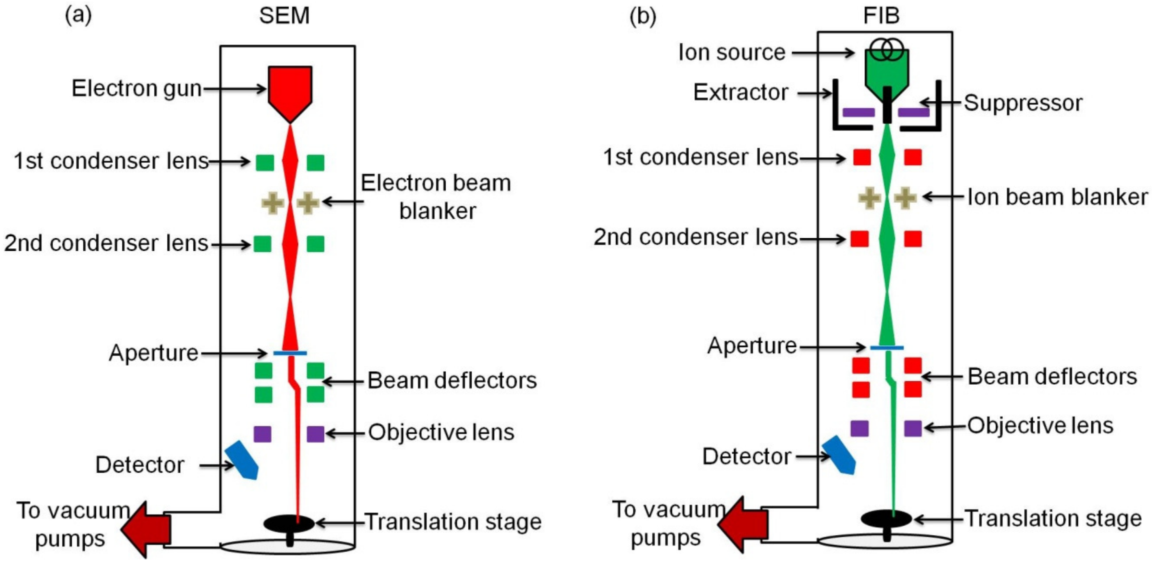

Figure 4.12 Schematic diagrams showing the main components of (a) electron beam, modified from [30,33,36], and (b) ion beam columns in the dual beam system.

Finally, the *energy spread* of the beam is responsible for widening the spot size. Different approaches and various types of materials have been utilized to fabricate electron sources, but a *Schottky emitter* or *thermal field emission* source is widely used and is used in the FEI system [29-32]. In this source, a conductive needle with a low work function barrier is heated-up to produce excited electrons on its surface. By applying an electric field, the free electrons are provided with the required energy to escape from the needle. This method can produce a good image with a very high stability for electron beam lithography [33-34]. These electrons are accelerated by the application of a high voltage, to follow a vertical path down through the column, where there are many electrostatic or magnetic lenses. These lenses focus the electron beam to a very fine point onto the specimen with a typical spot size around 5-10 nm depending on the system and focusing process [30,34]. These lenses suffer *astigmatism* and two types of aberration; *spherical* and *chromatic aberration* [29,32]. In spherical aberration, the outer zones of the lens bend the electron beam more strongly than the centre of the lens, leading to a spread of the focal point, whilst in chromatic aberration, electrons of slightly different energies (colours) will have different focal lengths, thus will be focused at different image planes [29,32]. Aberration and astigmatism in the SEM distorts the image of every point, leading to an overall loss of quality and resolution in the image and for lithography will affect the quality of the final feature on the nanometer scale. Therefore, a special type of lens called as*tigmator* is used to balance the imperfection in the astigmatism by forcing the beam to go back into its optimum shape.

Apertures are small holes through which the beam passes on its way down the column [32,35,36]. There are different kinds of apertures with various applications, such as the *stray aperture* which can be used to stop stray electrons. The *blanking apertures*, are used to turn the beam *ON* and *OFF* when the beam transfers from one pattern to another in EBL [32,36].

In order to scan a region on the specimen surface, the electron beam is deflected back and forth. This deflection is achieved using electrostatic or electromagnetic coils [30,36]. The most important elements in the SEM are the *detectors* which are located close to the end of the objective lens just above the sample. The *vacuum chamber* is usually evacuated to a pressure below appropriate level around 2×10^{-5} mbar in order to prevent scattering and attenuation of the electron beam or production of additional ions by impact ionisation. These ions have the potential to react with the sample and lower the quality of the image produced. Different types of pumping systems are available which are explained in some detail in Ref [22,31]. The chamber contains a fully motorised stage in all directions on which the sample is mounted. Details of the many other components necessary for the operation of the SEM system can be found elsewhere [28,30,32].

The components of the focused ion beam column are similar to the SEM, as shown schematically in Figure 4.12(b). There are a number of ion sources which can be used in the FIB, such as In, *Bi*, *Sn*, and *Au*, but the most widely used in commercial systems and in Durham are *gallium ions* due to the low melting temperature of Ga (~30^{o}C), the low volatility, and low vapour pressure [27]. The ion beam is produced at the top of the column by placing the gallium metal in contact with a tungsten needle which heats the gallium and make it flow to the tip of the needle. Applying a suitable electric field to the needle relative to the tip (greater than 1×10^{8} volt/cm) can lead to ionisation and field emission of the gallium ions [27].

The ion beam column consists of several electro-optical components. For instance, condenser and objective lenses are used to accelerate and focus the beam with energy between 1-30 keV onto the specimen with a diameter of ~5 nm and high degree of brightness [27]. Theses lenses are electrostatic lenses rather than electromagnetic lenses as in the electron column, because the focusing process is related to the particle charge and mass ratio, so it is impractical to use electromagnetic lenses with ion beam column [27]. There are also deflection plates to raster the beam over the specimen. The size (current) of the ion beam hitting the specimen determines the imaging resolution and the fabrication precision [27].

4-4.2 The physics of electron and ion beam interactions with a specimen

When an incident beam of focused electrons strike a specimen, different types of rays and electrons are obtained from the interactions [30-32] as illustrated in Figure 4.13(a). For instance, *reflection of high energy electrons* by elastic scattering, emission of *secondary electrons* by inelastic scattering, the emission of *electromagnetic radiation (cathodoluminecence)*, *characteristic X–ray*, *Auger electrons* and for very thin samples (~30 nm) *transmitted electrons* might occur.

The size of the interaction between the focused electron beam and the specimen is referred to as the *interaction volume*, which can be accurately determined using *Monte Carlo simulations* [30,31]. The interaction volume was found to depend on the energy of the incident beam, the atomic number and the density of the specimen [30,32]. S*econdary electrons* are emitted as a result of the ionisation process occurring within the specimen. Typical energies of these electrons are of the order of few electron volts (less than 50 eV) [28,30]. Secondary electrons are the key to SEM imaging. The *backscattered electrons* come from the main beam of electrons and are reflected from the specimen by elastic scattering.

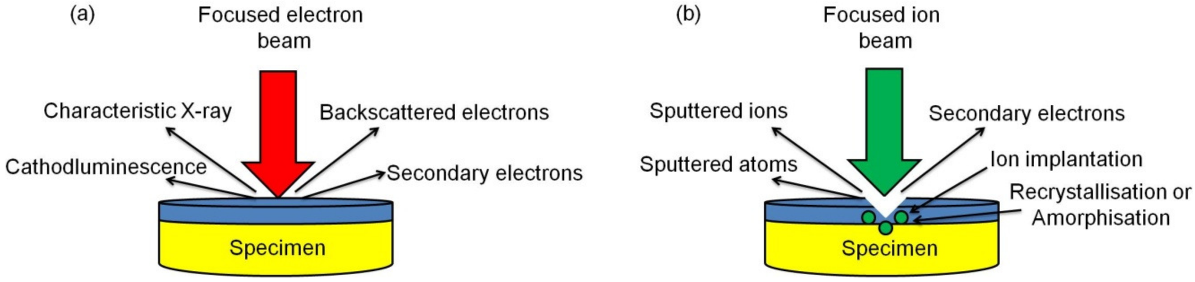

Figure 4.13 Schematic representation of the interaction of focused (a) electron [30], and (b) ion beams [27] with a specimen. Various phenomenon occur from this interaction depending on different parameters.

When highly energetic electrons knock out inner shell electrons from a material, *characteristic X-rays* may be emitted which can be used to identify the atomic species [28,31,32]. Additionally, atoms of luminescent specimens excited by the incident high-energy electrons and returned back to their ground state will emit light and this process is known as *cathodluminescence* [30].

On the other hand, when a focused ion beam strikes a specimen, different phenomenon can occur, as illustrated in the schematic diagram shown in Figure 4.13(b). *Atom removal* (*milling or sputtering*) from the specimen surface can occur when atoms gain enough kinetic energy to overcome their surface binding energy [27]. Sputtering can occur as a result of series of elastic collisions [27]. Another possibility is the formation of ions due to the ionisation of a portion of the sputtered atoms. These ions can be collected to form an image. Additionally *secondary electrons* can be produced [27]. *Ion implantation* and *re-crystallisation* or *amorphisation* can also occur as a result of this interaction, where the ions are not backscattered out from the specimen and settle at some depth below the specimen surface.

Thus, a dual beam system can be used to perform different applications at the same time. For instance, it can be used for imaging by scanning either the ion (with low currents) or electron beam across the surface of a specimen and collecting the emitted secondary electrons or ions using suitable detectors, as will be investigated in chapter five. The ion beam cannot be so finely focused onto the specimen and the imaging process always produces implantation and sputtering of the substrate surface [27,30]. Therefore, image resolution with an ion beam is generally lower than with the electron beam and the sample is modified. Image resolution with the ion beam is around 5 nm depending upon the ion energy and the detector efficiency [27,30]. Furthermore, it can be used to create nanopatterns using lithography and ion beam milling and also to deposit materials via ion or electron beam induced deposition, as described in the following subsections.

4-4.3 Electron beam lithography (EBL)

Lithography in general has wide applications in the electronic industry and it is extensively used in support of integrated circuit technology and for researching in a wide range of fields with very small dimensions [33,37]. The principles of the lithographic process including the most significant resists in use are covered within the following discussion.

The basic idea in any lithographic process is transferring patterns to the surface of a clean substrate. To do that, the substrate is covered by a uniform film referred to as a *resist*. This resist needs to be sensitive to the incident electron beam. The physical or chemical properties of the resist change upon exposure to the radiation [33,34,37]. The exposed areas become more soluble and can be dissolved in a specific solvent this occurs for a *positive resist*, whilst the exposed area will cross-link to the specimen and this resist will be characterised as a *negative resist*, as demonstrated in Figure 4.14. The process of dissolving the resist in a chemical solvent is called *development*, which is similar to the development of photographic films. After developing, a thin metallic layer can be deposited on the substrate using a physical vapour deposition such as sputtering or evaporation techniques [38]. This process is referred to as *metallisation*. In a positive resist, the areas that were exposed to the radiation and subsequently developed are clear and the deposited film will stick directly onto the substrate, while on the unexposed regions the metal will stick to the resist surface. In contrast, in a negative resist, the areas that were exposed to the radiation remain and the deposited film will adhere to the resist, while the unexposed areas are clear and the film will stick on the substrate, as shown in Figure 4.14. After the metallisation process, the remaining resist and the unwanted metal film are removed in a specific solvent leaving behind only the desired patterns on the substrate and this process is known as *lift-off*.

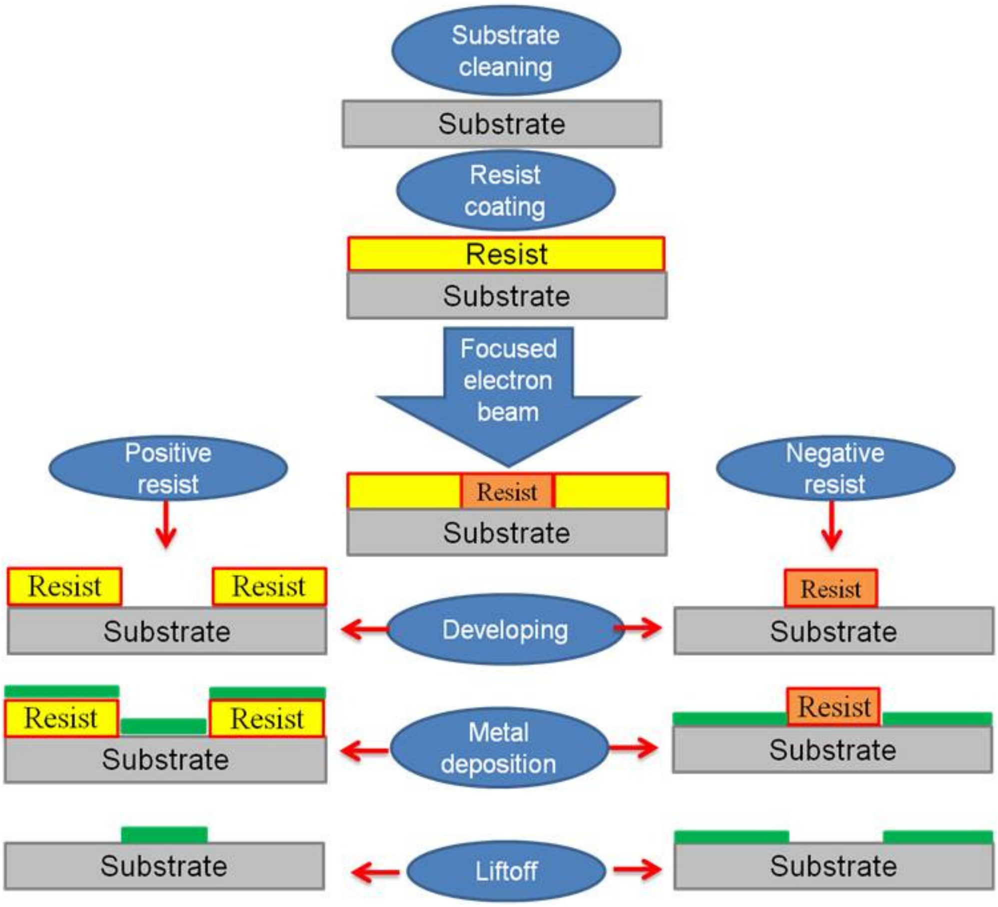

Figure 4.14 Illustration of the pattern definition in positive and negative resists. The electron beam causes physical-chemical changes in the exposed region and only the changed properties of the resist can be dissolved in a specific solvent [34,38].

There is a variety of different lithographic resists with different properties [38]. Each one requires different chemical solution for development and lift-off. One of the most important materials developed for electron beam lithography is *poly-methyl-methacrylate (PMMA)* [38]. PMMA is a very common positive tone electron beam resist and it remains one of the highest resolution resists available [33]. Figure 4.15 shows the chemical structure of this polymer which is composed of a long chain with repeating units of methyl-methyacrylate monomer [38]. The long carbon backbone of this resist is divided into small chains with lower molecular weights upon exposure to sufficient radiation [38]. It was found that the scission of the resist occurs with energies greater than 5 eV indicating that the most effective exposure is due to the secondary electrons produced as a result of the dissipated energy of the primary beam in the resist through electron cascade [38].

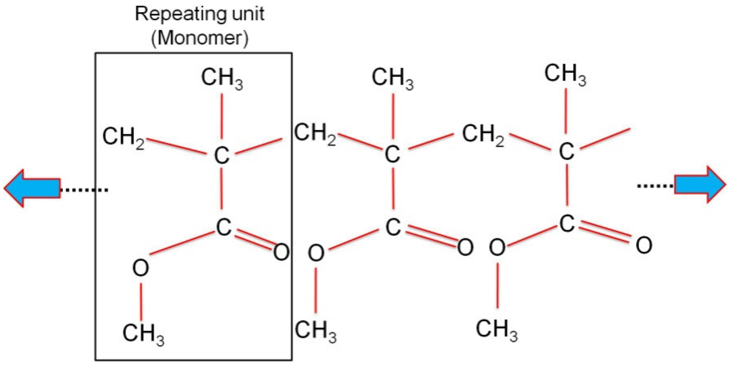

Figure 4.15 The chemical structure of PMMA resist. It is composed of repeating units of a monomer. The long chain backbone of this resist is divided into chains of lower molecular weight upon exposure to a focused electron beam which make it more soluble in the solvent. Reproduced from [38].

This effect might produce a broadening of the exposed region related to the exposed beam and is referred to as the *proximity effect* which can be accurately measured using *Mont Carlo simulations* [38]. For further information see reference [38]. However, EBL offers line widths down to a few nanometer ranges, but tens of nanometers is more typical (example 20-50 nm) [38]. This is much smaller than can be achieved by optical lithography techniques [33]. The drawback of EBL is that the writing of patterns is a serial processes and hence very time consuming for larger area structures.

4-4.4 Experimental procedure for patterning

In order to study the magnetic and electrical properties of template released isolated nanowires, EBL and lift-off techniques were carried out to create two kinds of chips, as shown in Figure 4.16.

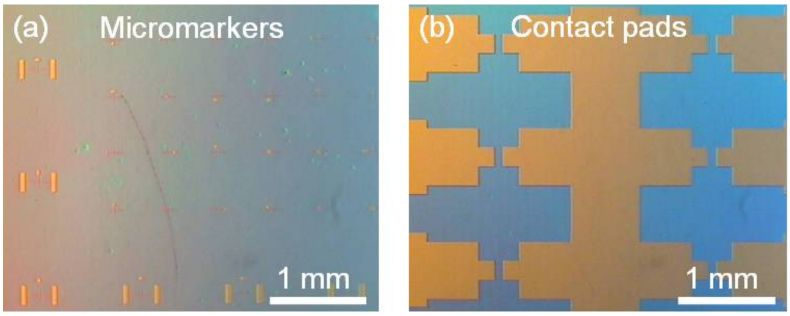

Figure 4.16 Optical microscope images showing gold (a) micro markers, and (b) electrical contact pads fabricated on the Si/SiO$_2$ substrates using electron beam lithography and lift-off techniques. These chips were used to investigate the magnetisation behaviour and electrical properties of isolated nanowires, respectively.

The first type of chip contains a set of gold micro-markers of several microns. These patterns were designed to be large enough to be observed in the optical microscope of the MOKE system. The second kind of chip had gold contact patterns which were made to be thick enough to withstand the different steps required in lithography for electrical connections. These patterns were designed in a finger-like pattern to increase the probability of nanowires being dispersed between them for the electrical connection. After the nanowire were dispersed on the chips, EBL and electron beam induced deposition were used as a second step to electrically connect the dispersed electrodeposited nanowires with the pre-patterned gold contact pads. Finally, ion beam milling was employed to remove a layer from the nanowires where the connection was to be made before patterning or any spread of gold after patterning and lift-off. The following sub-sections describe the experimental procedure that was followed to achieve the fabrication process of these patterns using the dual beam system and gives some examples and discusses the most important technical difficulties arising from connection of the nanowires to the prefabricated contact pads.

4-4.4.1 Patterning using EBL

A film of PMMA resist was applied to a clean surface of Si/SiO_2 with approximate area of 4 × 4 mm^2 by placing the substrate on a rotating sample holder of a spin coat unit. The sample was held in a place by a vacuum chuck and a drop of 2% PMMA-495 in anisole solution was placed on the surface. The substrate was spun at ~3000 rpm for ~30 seconds to produce a uniform film with thickness ~70 nm [38,39]. The substrates were then removed carefully so that the resist was not scratched or damaged and were placed on a hot plate at a temperature of ~117 ^{o}C for a time of ~90 seconds [38]. This baking process had the effect of removing any residual solvents (anisole) from the resist. This process was repeated for 2-4 times depending on the thickness required for the resist and hence the deposited materials.

The substrate was placed on the movable stage inside the SEM and the chamber was evacuated. Two types of SEM systems were used in this project: a FEI Raith Elphy Plus SEM instrument and a FEI-Helios Nanolab dual beam FIB/SEM system. The accelerating voltage was set to 30 kV, the working distance was ~4 mm and the beam spot size selected for the desired beam current. The designs for the patterning were created using the software available and saved for use in the fabrication process. To obtain high resolution patterns, the electron beam was focused onto features on the sample edge at the highest magnification level possible. Exposure parameters were calculated using the equation [38]:

$$\text{Area Dose } = \frac{\text{Beam Current} \times \text{Dwell time}}{\text{Pixel area}} \tag{4-1}$$

An area dose of ~400 μCcm^{-2} was used, based on calibration tests for the system carried out by previous users. The beam current was measured on the sample and the time is the exposure time set by the user. The write field is the area in which the exposure is carried out, and it can be divided into small points known as *pixels*. A pixel can be defined as the smallest allowed movement of the electron beam on the write field. A smaller pixel can be achieved by decreasing the write field. The above equation was used to estimate the time required for drawing one pixel from the pattern and is known as *dwell time*. Finally, control of the SEM was given to the lithography system to raster the electron beam over the surface of the substrate using the designs created earlier in the fabrication process.

To develop the chips, they were ultrasonically immersed in *methyl isobutyl ketone (MIBK)* and *IPA* in a ratio of 1: 3 for a time of ~30 seconds at a temperature of 20 ± 1 ^{o}C according to the manufacture recommendations [38,39]. The chips were then immediately washed for ~30 seconds with an IPA solution in the ultrasonic bath to remove the traces of the MIBK and then dried with nitrogen gas. To ensure that the exposure had worked well, the developed chips were examined using both optical and SEM microscopes. Thermal evaporation and magnetron sputtering techniques were used to deposit the required film as described in the previous sections. For lift-off, the substrates were placed in an acetone bath for a time of one hour. This enabled the resist to dissolve and hence be removed from the chips leaving behind the final pattern of the metal structures. The chips were then transferred to IPA for a time of ~15 minutes to remove any residual acetone before being dried in nitrogen gas.

4-4.4.2 Electrically connecting electrodeposited isolated nanowires

Two techniques were tried to connect template released ferromagnetic isolated naonowires with the prefabricated electrical contact pads. The first method employed EBL and lift-off techniques as discussed previously. The thickness of the gold electrodes was ~35 nm and the width was ~1 μm. It is noteworthy that selecting, locating and imaging of the isolated wires relative to the gold patterns was carried out using optical and scanning electron microscope before patterning the connection electrodes.

The second method was achieved via *ion or electron beam induced deposition* which also known as *local chemical vapour deposition (LCVD)*. This can be achieved by introducing a suitable precursor gas to the vacuum chamber which is allowed to interact with the focused ion or electron beam to break down the precursor and allow chemisorption onto the substrate, as schematically shown in Figure 4.17 [27,34]. It is found that the secondary electrons produced as a result of the interaction are responsible for the gas decomposition by breaking the chemical bonds of the precursor gas and the material is deposited on the substrate surface whilst the volatile products are removed by pumping.

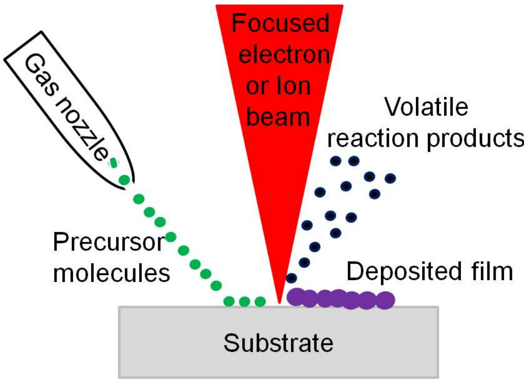

Figure 4.17 Schematic representation of the interaction between the focused ion or electron beams with the precursor gas resulting in chemisorption onto the substrate of the deposition materials.

Different precursor gases can be used including those containing *platinum*, *tantalum* and *gold*, but here only methylcyclopentadienyl-trimethyl platinum ($C_9H_{16}Pt$) was used for the deposition of platinum. For further information about different types of precursors in use see Refs [27,38,40-42]. This connection process was performed with help from *Erhan Arac* (Department of Physics, Durham University, U.K.). The thickness of the deposited Pt was ~150 nm and the width was ~1 μm. The deposition was performed using electron beam energy of 5 keV chosen as a result of optimisation experiments. This energy was found to be more efficient of producing platinum. The beam current was chosen according to the deposition time, where it was found that smaller currents yield better quality of deposited material but the time becomes longer. As an example, Figure 4.18 shows scanning electron micrographs of electrodeposited individual nanowires connected by Au and Pt electrodes to the prefabricated gold electrical contact pads using both EBL and electron beam induced Pt deposition techniques, respectively.

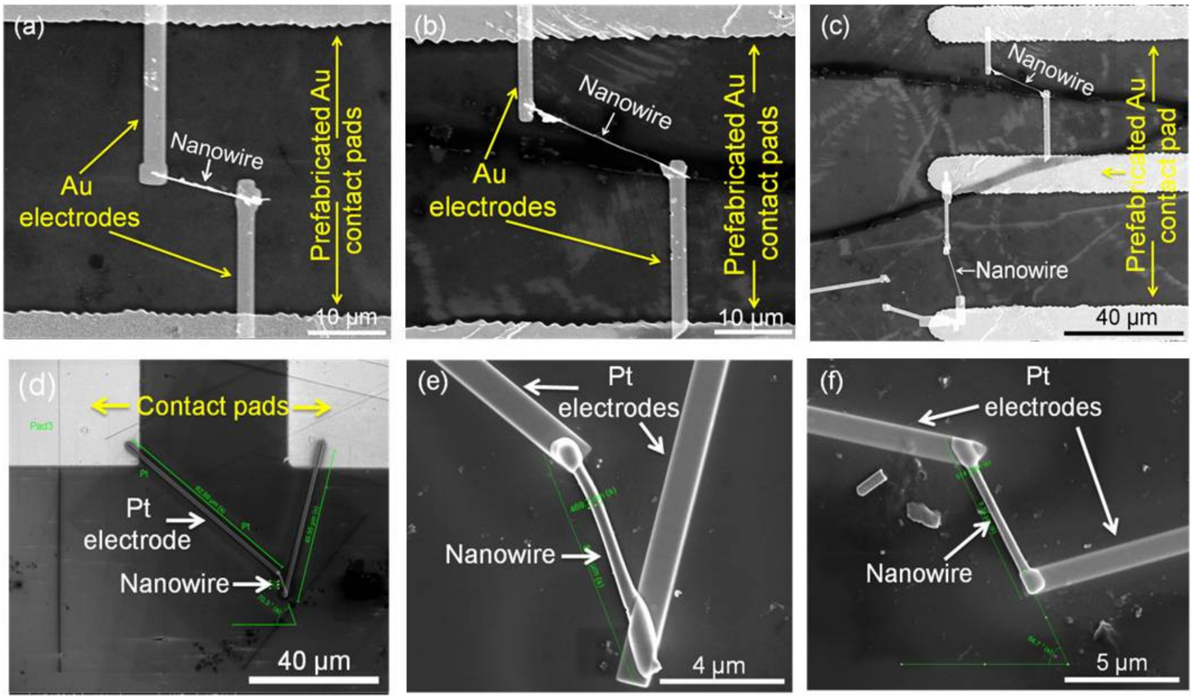

Figure 4.18 Examples of scanning electron micrographs showing electrodeposited individual nanowires connected to the prefabricated Au contact pads using (a-c) EBL and lift-off techniques, and (d-f) electron/ion beam induced deposition. Pt deposition images from [43].

4-4.4.3 Ion beam milling

Ion beam milling was used here to remove a layer of thickness around 5 nm from the wires where the gold electrode connections were to be made before patterning. This was performed in order to remove the oxides or hydroxides or any other residue on the wires. In this method, the ion and electron beams were focused onto a feature (e.g. damage) on the sample corner at perpendicular direction after finding the eucentric focus point. The stage was then fixed at that point with an approximate working distance of 3.8 mm from the electron column. The milling process was performed manually by first selecting the dimensions of the features to be milled, the current and the depth of the milled material was determined by the total beam exposure time. This was achieved by allowing the beam of gallium ions with a current as required to be rastered over these locations. The ion beam milling, in general was employed with great care to ensure that the ion beam never scanned directly over all the area of the wire.

4-4.4.4 Technical difficulties associated with electrical connection to isolated wires

As mentioned earlier, the spinning process is one of the requirements for resist application for EBL. Sonication is also necessary during the development and lift-off techniques after patterning. These requirements make the electrical connection of isolated nanowires with the prefabricated gold contact pads very challenging. Figure 4.19 show examples of scanning electron micrographs demonstrating the effect of resist spinning and sonication on the connection of such wires. For instance, the wires or the gold electrode connections were damaged or moved during development or lift-off processes as demonstrated in Figure 4.19(a-c). If sonication times were reduced or eliminated excess gold remained on the surface, as demonstrated in the examples shown in Figure 4.19(d,e). As it is impossible to look at the sample during the patterning process, the existence of template residue or any other impurities or other nanowires in the vicinity will makes connections difficult to achieve, as shown in Figure 4.19(f).

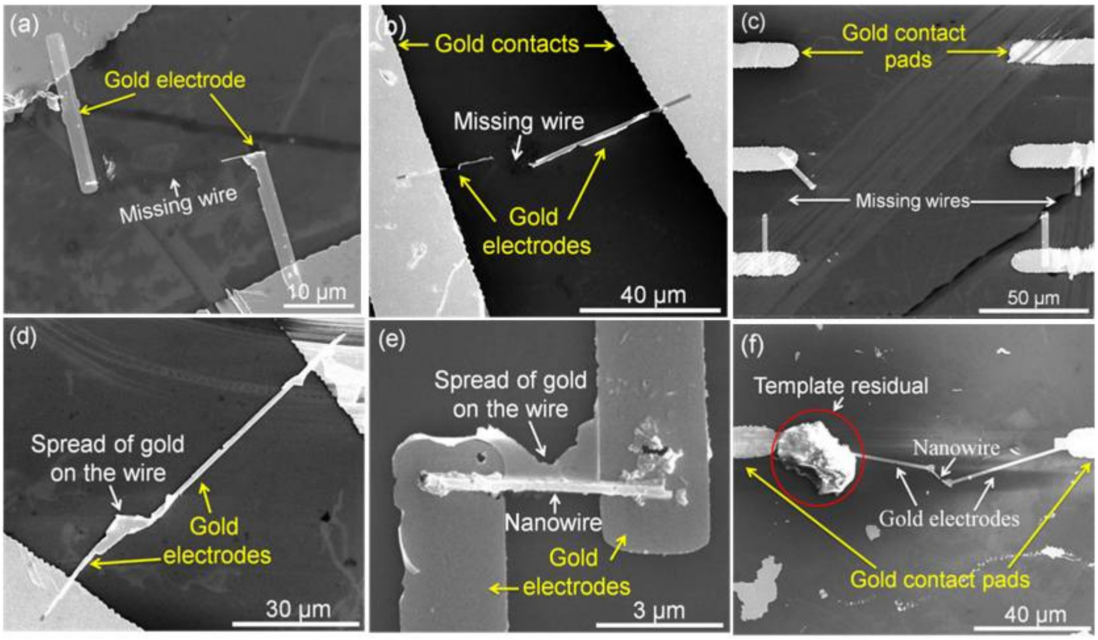

Figure 4.19 Examples of scanning electron micrographs demonstrating the difficulties arising from the electrical connection of electrodeposited isolated nanowires with prefabricated gold contact pads. The effect of (a-c) sonication, (d,e) without or with reduced sonication during the development and lift-off techniques and (f) the existence of residue preventing contact to proposed electrodes.

4-5 Wire bonding

In order to study the magnetoresistance behaviour of the isolated ferromagnetic nanowires that are electrically connected on a chip to lithographic contact pads, *wire bonding* was required to connect the contact pads with a chip carrier [44-46]. This was performed using the *wire bonding machine* shown in Figure 4.20(a). This is controlled by computer system. In this machine, a gold ball is formed by melting the end of fine gold wire with a diameter of around 15 µm and held by a capillary tool [47]. This ball is then brought into contact with the terminal of the chip carrier and by applying a sufficient amount of pressure, heat and ultrasonic forces onto the ball for a period of time, a metallurgical weld between the ball and the chip carrier can be achieved [48]. Then, moving the capillary tool to the desired electrical contact on the silicon chip to form a loop of wire a second bond is formed again by applying ultrasonic forces to the end of the wire [48]. The machine then breaks the wire for the next wire bonding. Figure 4.20(b) shows an example of the electrical contacts of a silicon chip bonded to the chip carrier by gold wire.

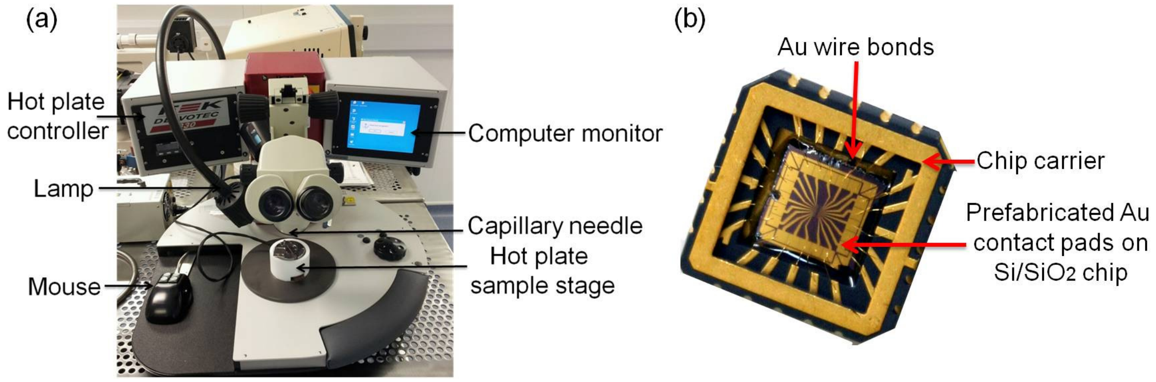

Figure 4.20 Photographs showing (a) the wire bonding machine used in this work to electrically connect the gold prefabricated contact pads on the silicon chip with the terminals of chip carrier, and (b) example of chip carrier bonded to the contact pads by gold wires [49].

4-6 Chapter references

1. Langbein, G. & Brannt, William T. "Electro-dposition of metals" New York, Henry Carey Baird & Co., Inc., 1924.
2. Jin, C. G., Liu, W. F., Jia, C., Xiang, X. Q., Cai, W. L., Yao, L. Z. & Li, X. G. "High filling, large-area Ni nanowire arrays and the magnetic properties" *J. Cry. Growth*, 258(3-4), 337, 2003.
3. Escrig, J., Lavín, R., Palma, J. L., Denardin, J. C., Altbir, D., Cortés, A & Gómez, H. "Geometry dependence of coercivity in Ni nanowire arrays" *Nanotech*., 19(7), 075713, 2008.
4. Gao, T. R., Yin, L. F., Tian, C. S., Lu, M., Sang, H. & Zhou, S. M. "Magnetic properties of Co–Pt alloy nanowire arrays in anodic alumina templates". *J. Mag. Mag. Mat.*, 300(2), 471, 2006.
5. Rheem, Y., Yoo, B., Beyermann, W. P. & Myung, N. V. "Electro- and magneto-transport properties of a single CoNi nanowire" *Nanotech*., 18(12), 125204, 2007.
6. Elhoussine, F., Vila, L., Piraux, L. & Faini, G. "Multiprobe perpendicular giant magnetoresistance measurements on isolated multilayered nanowires" *J. Mag. Mag. Mat.*, 290-291, 116, 2005.
7. Fert, A. & Piraux, L. "Magnetic nanowires" *J. Mag. Mag. Mat*., 200, 338–358, 1999.
8. Bard, J. Allen & Faulkner, R. Larry "Electrochemical methods: Fundamentals and Applications" 2nd edition, John Willy & Sons, Inc., New York, 2001.
9. Rieger, H. Philip "Electrochemistry" 2nd edition, Chapman & Hall, Inc., New York, 1994.
10. "http://www.cheml.com/acad/webtext/elchem/ecl.html" accessed on 20 March 2010.
11. West, J. M. “Electrodeposition and corrosion processes" D. Van Nostrand Com. Ltd., London, 1965.
12. King J. in private communication, 2010.
13. Wu, M. T., Leu, I. C., Yen, J. H. & Hon, M. H. " Preparation of Ni nanodot and nanowire arrays using porous alumina on silicon as a template without a conductive interlayer" *Electroch. Sol. Stat. Lett.*, 7 (5), C61, 2004.

14. Han, X.-F., Shamaila, S., Sharif, R., Chen, J.-Y., Liu, H.-R., & Liu, D.-P. "Structural and Magnetic Properties of Various Ferromagnetic Nanotubes" *Adv. Mat.*, 21(45), 4619, 2009.
15. Escrig, J., Daub, M., Landeros, P., Nielsch, K. & Altbir, D. "Angular dependence of coercivity in magnetic nanotubes" *Nanotech.*, 18(44), 445706, 2007.
16. Nasirpouri, F. "Template electrodeposition of magnetic nanowire arrays" *Trans world Research Network*, 661, 37, 2007.
17. Grzegorz, D. Sulka "Nanostructured materials in electrochemistry: Highly ordered anodic porous alumina formation by self-organized anodizing" Wiley-VCH, Verlag GmbH & Co., KGaA, Weinheim, 2008.
18. Yin, A. J., Li, J., Jian, W., Bennett, A. J. & Xu, J. M. "Fabrication of highly ordered metallic nanowire arrays by electrodeposition" *Appl. Phys. Lett.*, 79(7), 1039, 2001.
19. Li, X., Wang, Y., Song, G., Peng, Z., Yu, Y., She, X. & Li, J. "Synthesis and growth mechanism of Ni nanotubes and nanowires" *Nano. Res. Lett.*, 4(9), 1015, 2009.
20. Xiao, Z. L., Han, C. Y., Welp, U., Wang, H. H., Kwok, W. K., Willing, G. a., Hiller, J. M., Cook, R. E., Miller, D. J. & Crabtree, G. W. "Fabrication of alumina nanotubes and nanowires by etching porous alumina membranes" *Nano. Lett.*, 2(11), 1293, 2002.
21. "http://en.wikipedia.org/wiki/Sodium_hydroxide", accessed on 1st Oct 2013.
22. Stuart, R. V. "Vacuum technology, thin films and sputtering: An introduction" Academic Press, Inc., Ltd., London, 1983.
23. Penning, F. M. "Electrical discharges in gases" Philips Technical Library, Netherlands, Holland, 1957.
24. Chapman, Brian "Glow discharge processes sputtering and plasma etching" John Wiley & Sons, Inc., USA, 1980.
25. Kiyotaka, Wasa & Shigeru, Hayakawa "Hand book of sputter deposition technology principles: Technology and Applications" Noyes Publications, New Jersey, USA, 1992.
26. Kelly, P. & Arnell, R. "Magnetron sputtering: A review of recent developments and applications" *Vacuum*, 56(3), 159, 2000.
27. Volkert, C. A., Minor, A. M. & Editors, G. "Focused ion beam micromachining" MIRS Bulletin, 32, 389, 2007.
28. O'Connor, D. J., Sexton, B. A. & Smart, R. St. C. "Surface analysis methods in materials science" Springer-Verlag, Berlin Heidelberg, 1992.
29. Grundy, P. J. & Jones, G. A. "Electron microscopy in the study of materials" Edward Arnold Ltd., London, 1976.
30. Goodhew, J. Peter, Humphreys, John & Beanland, Richard "Electron microscopy and analysis" 3rd edition, Taylor & Francis, London, 2001.
31. Luth, Hans "Surfaces and interfaces of solids" 2nd edition, Springer-Verlag, Berlin Heidelberg, 1993.
32. Golstein, J. I., Newbury, D. E., Echlin, P., Joy, D. C., Romig, A. D. Jr., Lyman, C. E., Fiori, C. & Lifshin, E. "Scanning electron microscopy and X-ray microanalysis" 2nd edition, Plenum press, New York & London, P. 177,1992.
33. Ghandhi, K. Sorab, "VLSI fabrication principles silicon and gallium arsenide" John Wiley & Sons, New York, 1984.
34. Guozhong, Gao "Nanostructures and nanomaterials synthesis, properties and applications" Imperial College Press, London, 2004.

35. Mark, A. McCord & Michael, J. Rooks "SPIE Handbook of microlithography, micromachining and micro-fabrication" edited by P. Rai Choudhury (SPIE, Bellingham, WA), Vol. 1, link.aip.org/ link/APL/ 79/ 1721/ 1, 1997.
36. Ampere, A. Tseng "Nanofabrication fundamentals and applications" World scientific publishing Co. Pte. Ltd., USA, 2008.
37. Harry, J. Levinson "Principles of lithography" 3rd edition, SPIE Press, Bellingham, Washington, USA, 2010.
38. Atkinson, Del "Post graduate lectures in nanoscale structuring: Lithographic patterning and structure preparation" Durham University, Physics Department, 2010.
39. "http://microchem.com/pdf/PMMA_Data_Sheet.pdf.", accessed on 17th March 2013.
40. Nikulina, E., Idigoras, O., Vavassori, P., Chuvilin, A., & Berger, A. "Magneto-optical magnetometry of individual 30 nm cobalt nanowires grown by electron beam induced deposition" *Appl. Phys. Lett.*, 100(14), 142401, 2012.
41. Fernández-Pacheco, A., Teresa, De, Szkudlarek, A., Córdoba, R., Ibarra, M. R., Petit, D., O'Brien, L., Zeng, H. T., Lewis, E. R. Read, D. E., Cowburn, R. P. "Magnetization reversal in individual cobalt micro-and nanowires grown by focused-electron-beam-induced-deposition" *Nanotech.*, 20(47), 475704, 2009.
42. Fernández-Pacheco, A., Teresa, De., Córdoba, R. & Ibarra, M. R. "Magnetotransport properties of high-quality cobalt nanowires grown by focused-electron-beam-induced deposition" *J. Phys. D: Appl. Phys.*, 42,5, 2008.
43. Arac E. in private communication, 2011.
44. Li, X., Gao, F. & Gu, Z. "Nanowire joining methods" Surface Science, 3, 91, 2011.
45. Servais, G. E., Brandenburg, S. D., & Corp, D. E. "Wire Bonding – A Closer Look" ISTFA'91: The 17th International Symposium for Testing & Failure Analysis, Los Angeles, California, USA, 11-15 of Nov., 1991.
46. Armstrong, Helen "Technical note: Step by step for the operation of the wire bonding" Durham University, Physics Department, 2010.
47. "http://en.wikipedia.org/wiki/Wire_bonding", accessed on 17th March 2013.
48. "http://www.siliconfareast.com/wirebond.htm", accessed on 17th March 2013.
49. Burn D. in private communication, 2013.

Chapter five

Experimental methods: Investigative techniques for analysis of thin films and nanowires

5-1 Introduction

The physical principles of the techniques used for characterising the morphology, structure, magnetic and electrical properties of electrodeposited ferromagnetic thin-films and nanowires are described and discussed in this chapter. The methods employed to analyse the data are also described. A variety of investigative techniques were employed within this research including *scanning electron microscopy (SEM)*, *grazing incidence X-ray reflectivity (GIXR)*, *magneto-optical Kerr effect (MOKE) magnetometry*, *magnetoresistance (MR) measurements* and *micromagnetic modelling*. An understanding of these systems and their principles will aid in understanding the analysis presented in the results chapters.

5-2 Scanning electron microscope (SEM)

In this project, a *FEI-Helios Nanolab dual beam FIB/SEM system* and a *Phillips SEM equipped with* a *Raith Elphy Plus electron beam controller* were widely used for electron beam lithography, ion beam milling and local chemical induced Pt deposition as mentioned in the previous chapter. It has also been used to investigate the morphology, diameter, and length distributions of nanowires, as well as to determine the chemical composition of thin films and to select, identify and locate the position of isolated individual and clustered nanowires with respect to the prefabricated micro-markers. The main components of SEM, their functional principles and the physics of electron interactions with the specimen are described in the previous chapter. Therefore, the following subsections are focusing on the most important detectors used in this work for characterising the samples, namely *secondary electron and X-ray detectors.*

5-2.1 Secondary electron detectors

Figure 5.1 shows a photograph taken inside the chamber of *FEI-Helios Nanolab dual beam FIB/SEM* system showing the most important parts including secondary electron detector. As mentioned in chapter four, the interaction of the focused electron beam with a specimen yields different rays. The emitted secondary and backscattered electrons are usually detected by an *Everhart–Thornley detector* [1-3]. The schematic diagram of this type of detector is shown in Figure 5.2(a) [2]. It is a *scintillator-photomultiplier system* in which the secondary electrons are attracted by a positively biased grid and accelerated to the scintillator creating a flash of light (photons) which is amplified by the photomultiplier and converted back to electron current [2].

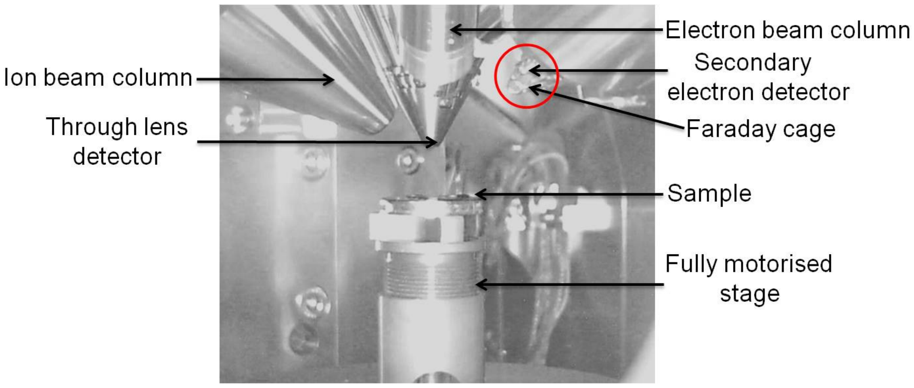

Figure 5.1 Photograph showing the secondary electron detector and the most important parts inside the SEM chamber of FEI-Helios Nanolab dual beam system.

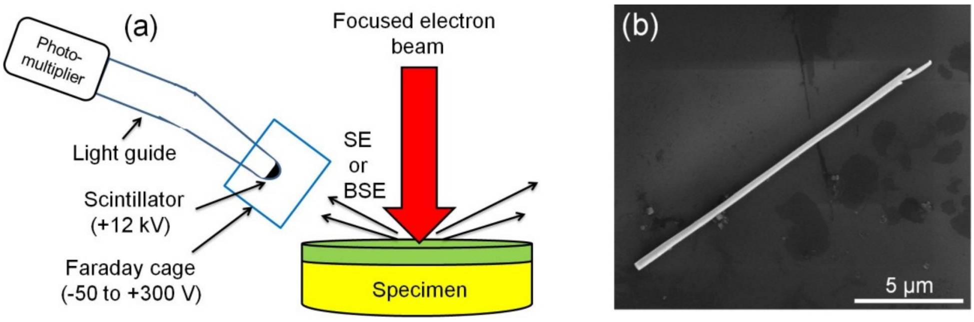

Figure 5.2 (a) Schematic diagram of Everhart–Thornley detector which is widely used in this work for imaging. Modified from [2]. (b) Example of scanning electron microscopy image of released and deposited individual nanowire on a substrate detected using this type of detector.

This current is amplified and converted to a digital image on the screen. To protect the detector from unwanted beams, it is surrounded by a *Faraday cage* [2]. This type of detector was widely used in this research for secondary electron imaging processes. An example image of an individual nanowire lying on a substrate recorded by the detector is also shown in Figure 5.2(b).

5-2.2 EDS and WDS detectors

As mentioned earlier in chapter four, when highly energetic electrons hit a sample, a core electron may be ejected from the sample leaving behind a hole which is filled with an electron from a higher energy level [3]. This results in emission of an *X-ray* with a characteristic energy equal to the energy difference of these shells. The emitted X-ray can be used to characterise the chemical composition of the investigated sample [2,3]. The characteristic X-rays can be detected using either *energy dispersive spectroscopy (EDS)* or *wavelength dispersive spectroscopy (WDS).* In both techniques the X-ray counts are recorded as a function of the energy. WDS measurements are more precise but time consuming since it depends on the rotating of the diffracting crystal. Thus, the chemical composition of a wide range of electrodeposited ferromagnetic thin films were measured by either *energy or wavelength dispersive X-ray analysis* with the aid of *L. Bowen* (Scanning Electron Microscopy Facility, Department of Physics, Durham University, U.K.) using scanning electron microscope *SEM Hitachi-SU 70* and *JEOL 2100F TEM* systems, respectively.

5-3 Grazing incidence X-ray reflectivity (GIXR)

Grazing incidence X-ray reflectivity (GIXR) is a non-destructive surface sensitive analytical technique first reported in 1954 by *Lyman G. Parratt* [4]. The grazing incidence means that the angle of incidence is either at or just above the critical angle of transmission into the specimen. This technique is commonly used to study thin films and multilayers [5].

It is able to offer quantitative information of *layer thickness*, *density*, and both *surface and interface roughness* [5,6]. The thickness ranges that can be measured within this technique are approximately between 1 to 1000 nm and surface roughness between 0.01 to 4 nm depending on the material and system in use [5,7]. It can be used to measure virtually any material with amorphous or crystalline structure depending only on the differences in the electron density of the layers [5,6].

This technique was mainly used here to estimate the thickness and roughness of the electrodeposited thin films and to calibrate the thickness monitor of the magnetron sputtering system that was developed in this work and presented in chapter six. The interpretation of the results was performed by numerical comparison with the simulations using *Bede REFS software* [8]. A brief theoretical and experimental description of this technique is provided in the following sub-sections elucidated with some examples.

5-3.1 Principles of GIXR

If *X-ray radiation* is allowed to interact with a specimen, absorption, reflection, or scattering (diffraction) may occur. The reflected radiation is determined by both the difference in the refractive index of the surfaces and by the width of interface region, which in turn depends upon the atomic number and electron density of the material [5]. The refractive index, n, is defined as the ratio of the phase velocity of an electromagnetic wave in a vacuum, c, to it is velocity in a material, υ [5]:

$$n = \frac{c}{\upsilon} \tag{5-1}$$

For visible light, the refractive index of a material is greater than one, whereas for X-rays can be written as [5]:

$$n = 1 - \delta - i\beta \tag{5-2}$$

Where, δ and β are *dispersion* and *absorption coefficients*, respectively. These parameters are positive and extremely small of the order of 10^{-6} and 10^{-8}, respectively, giving a refractive index that is very slightly less than one [5]. Therefore, when X-ray beam is incident on a material with a refractive index, $n_{specimen}$ from air or vacuum, the specimen appears optically less dense and the transmitted beam is refracted away from the surface normal, as demonstrated in Figure 5.3 [5,6].

If the angle of the reflected beam with respect to the sample surface, θ_r, has the same angle with the incident beam, θ_i, the reflected beam is referred to as a *specular reflection*, whilst if the angle of the reflected beam makes different angle with the incident beam then the reflection is said to be *diffuse scatter* or *off-specular*, as shown in Figure 5.3 [5,6]. The diffuse scatter is a result of the existence of sample curvature, roughness and composition grading which leads the reflected beams to interfere destructively leading to loss of intensity [5].

If the incident angle, θ_i, with the sample surface is decreased, the transmitted angle, θ_t, is also decreases. There is a *critical angle*, θ_c, at which the transmitted wave moves parallel to the specimen surface. *Total external reflection* occurs when the incidence angle is below the critical angle ($\theta_i < \theta_c$) [5]. The correlation of incident angle with the transmitted angle is described by *Snells law* via [5]:

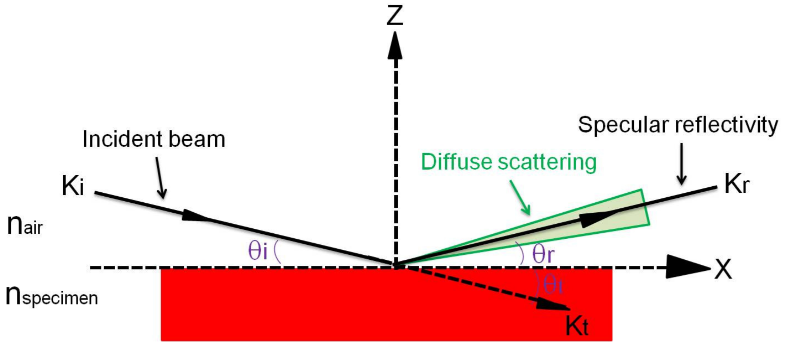

Figure 5.3 Schematic diagram of grazing incidence X-ray reflectivity from the interface between two materials of different electron density. Specular reflection (or diffuse scatter) occur when the incident and reflected beams makes the same (or different) angle with respect to the sample surface [5,6].

$$n_{air}\cos\theta_i = n_{specimen}\cos\theta_t \qquad \text{5-3}$$

Thus, when the X-ray is incident from the vacuum or air in which $n_{air} = 1$, then the critical angle, θ_c, at $\theta_t = 0$ is [5]:

$$\cos\theta_c = n_{specimen} \approx 1 - \frac{\theta_c^2}{2} + \cdots\cdots\cdots\cdots\cdots \qquad \text{5-4}$$

Assuming that, $\beta = 0$, which means that there is no absorption, therefore equation 5-4 can be written as [5]:

$$n_{specimen} = 1 - \delta = 1 - \frac{\theta_c^2}{2} \qquad \text{5-5}$$

$$\theta_c = \sqrt{2\delta} \qquad \text{5-6}$$

This equation indicates that the critical angle is dependent on the electron density in the near surface region [5].

For a film with refractive index, n_1, and a thickness, d, deposited on an infinitely thick substrate with refractive index, n_2, grazing incidence X-ray radiation is partially reflected at both the air-film interface and film-substrate interface, as shown in Figure 5.4 [5].

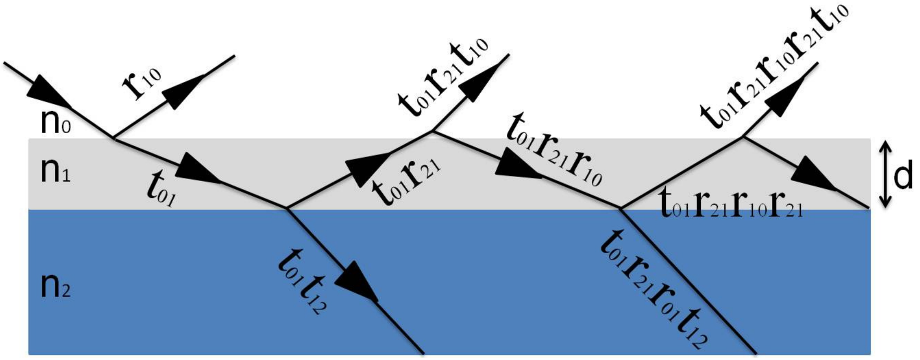

Figure 5.4 Reflection and transmission of X-ray radiation from a finite layer of thickness *d* and refractive index n_1 intermediate between an infinitely thick substrate and air with refractive index n_2 and n_0, respectively. The letters, *r*, denotes for reflection whilst, *t*, for transmission, and 0,1,2 refers to the air, film, and substrate, respectively [5].

Note that the letters, *r* and *t*, used in the figure denotes to the reflected and transmitted beams, whilst 0, 1, 2 refers to the layers air, film and the substrate, respectively. Interference can occur as a result of changing the angle of incidence. This is due to the changes in the path difference between the reflected waves from the different surfaces leading to fringes that are referred to as *Kiessig fringes* [5]. These fringes appear when the path difference equals an integral number, n, of wavelengths, λ, exactly as in the *Bragg condition* for diffraction, where *d* is the distance between the top and bottom of the deposited layer. Thus,

$$n\lambda = 2d\ sin\theta_T \qquad 5\text{-}7$$

Changing the angle of incidence, the period of the oscillated intensity is given by [5]:

$$\Delta\theta_i \approx \Delta\theta_T = \frac{\lambda}{2d} \qquad 5\text{-}8$$

Thus, the period of the oscillation is inversely proportional to the film thickness [5]. As an example, Figure 5.5 show reflectivity simulations for 10 nm and 30 nm thick Ni films on infinitely thick SiO_2 substrate with perfectly sharp interfaces.

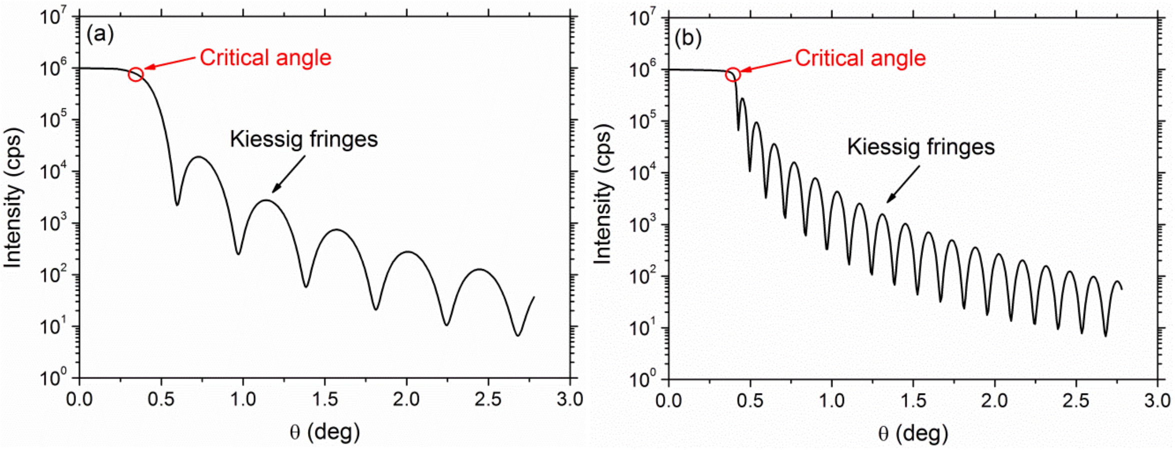

Figure 5.5 Examples of REFS simulation reflectivity measurements of Ni thin films with thicknesses of (a) 10 nm, and (b) 30 nm on infinitely thick SiO_2 substrate with perfectly sharp interfaces. The Kiessig interference fringes and the critical angle are clearly shown.

Kiessig fringes and the critical angles are clearly marked in the figure. The amplitude of the *Kiessig fringes* depends on the electron density difference between the layers, as well as roughness and grading of the interfaces [5,6]. The number of these fringes increases with increasing film thickness [5]. The decay in the reflected beam intensity as a function of angle is determined by the roughness of the interfaces. For rough interfaces the reflectivity decreases faster than the sharp interface [5].

5-3.2 Experimental setup for GIXR

In this research, the thickness and roughness of a wide range of electrodeposited Ni and NiFe films were measured using a *Bede diffractometer (Jordan Valley) D1 System.* This system was provided with a CuKα radiation source (anode) equipped a channel cut Si filter to monochromatise the X-ray beam. Figure 5.6 shows the measurement geometry. The acceleration voltage was ~40 kV, the maximum power used was approximately 1.6 kW and the X-ray wavelength was 0.1541 nm [6,7]. To decrease the angular divergence of the beam, narrow slits of 0.5 mm × 2 mm were used at the source giving a divergence of approximately 0.01^{o} [7]. To precisely define the angle of collection that is needed to separate the specular scattering from diffuse scattering events, narrow slits of 0.5 mm × 0.5 mm were located in front of the detector.

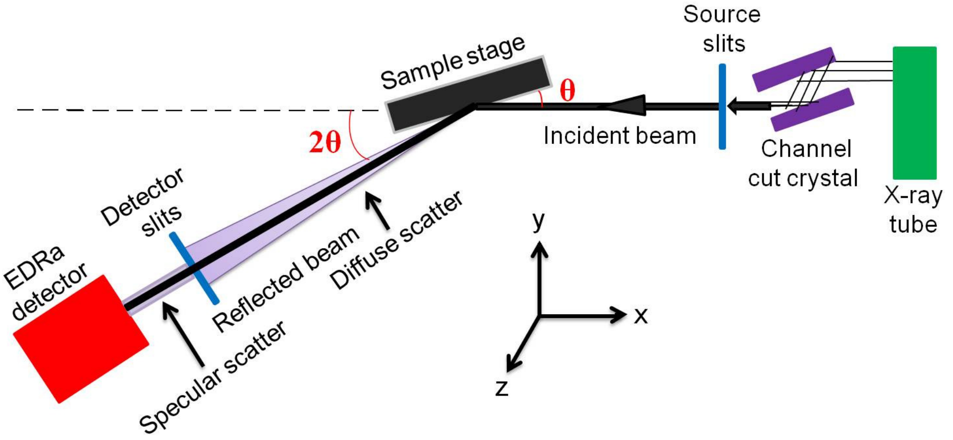

Figure 5.6 Geometry diagram of X-ray reflectivity setup used in this research to measure the thickness and roughness of electrodeposited ferromagnetic thin films.

However, these slits decrease the intensity of the beam which leads to an increase in the experimental time. The incident beam makes an angle θ with respect to the sample surface, whilst the reflected beam was measured at an angle 2θ using an *EDRa detector (a scintillation counter)* [7].

Samples were mounted on a plate that was installed on a higher resolution stage called a *goniometer*. The alignment process is important to obtain meaningful data. Therefore, the reflectivity measurements were performed after highly precise alignment, which was carried out first by adjusting the angle of the detector, 2θ, with respect to the incident beam to maximise the intensity when the sample is out of the beam. Then, by adjusting z and θ (these parameters are defined in the figure) to achieve an optimum position of the sample with respect to the incident beam. This was achieved by optimising z and θ until approximately the half intensity of the incident beam was incident on the detector. Further optimisation of x and y positions was made to maximise the intensity of the beam at the detector [7]. The specular and off-specular reflectivity curves were recorded using $\theta /2\theta$ scan by setting θ at 0^o-6^o and 0.1^o-6^o, respectively. Increments of 0.01^o were used with a count time of 15 seconds for each step, giving a total time of approximately 7 hours per sample measurement. The count time was selected as a compromise to give a good signal to noise ratio and to enable the analysis to take place over a reasonable period.

An example of specular and off-specular reflectivity curves obtained from measuring sputter deposited Ni films with a nominal thickness of ~10 nm are shown in Figure 5.8(a). To remove the background and forward scatter effects, the off-specular reflectivity data were subtracted from the specular reflectivity data to yield the *true specular curve*, as shown in Figure 5.7(b). The true specular curve can then be fitted and analysed using suitable software.

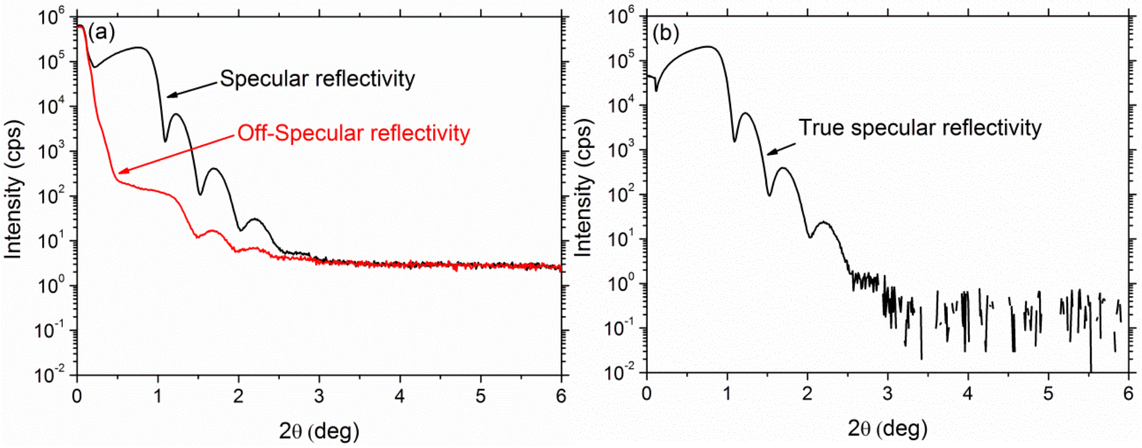

Figure 5.7 (a) An example of specular and off-specular reflectivity curves obtained from measuring a sputtered Ni film with a nominal thickness of 10 nm using the D1 reflectometer, and (b) true specular reflectivity curve obtained by subtracting the data of off-specular from specular to remove the effect of forward diffuse scatter.

5-3.3 Data analysis for GIXR

As stated above, the specular and off-specular reflectivity data were used to give the true specular reflectivity. The true specular reflectivity curve was fitted with simulations using *Bede REFS software package* [8] which is based upon the *Parratt recursive formulism* [4]. Using this software, solutions for the thickness, density and roughness of the specimen could be accurately determined. The details of the algorithm can be found elsewhere [4-9]. In each simulation, the layer thickness, roughness and density were allowed to vary as free parameters with nominal values of film thickness introduced as starting values to ensure the simulation ended in a reasonable time.

All of the simulations were performed on the nominal structure of the as-deposited films with the addition of an oxide layer or sub-layer with a thickness up to a few nanometres as needed to improve the quality of simulation fit to the data. This is quite reasonable since a partial oxidation of the surface might occur during the time elapsed between deposition and characterisation of samples. The simulations were completed when the free parameters and the *goodness of fit parameter* (a statistical measurement of the agreement between the simulation and the experimental data) remain constant for more than 15000 iterative generations. Examples of grazing incidence X-ray reflectivity measurements for a sputter-deposited NiFe film with a nominal thickness of 15 nm and the best-fit simulations with and without the inclusion of a top oxide layer are shown in Figure 5.8. Clearly, both cases produce the same number of *Kiessig fringes*, but the inclusion of the top oxide layer results in a better fit to the experimental data and in this case, a lower value for the goodness of fit parameter is obtained. A range of oxides are available with each composition investigated here, for instance Fe_2O_3 and NiO were used with NiFe films. However, the difference is unnoticeable using these different oxide layers in the simulations as demonstrated in Figure 5.8(b). This is because the X-ray reflectivity measurements are only sensitive to the electron density difference which is very small between these materials.

5-4 Magneto-optical Kerr effect (MOKE) magnetometry

Magneto-optical effects occur when polarised light interacts with magnetic materials. In 1886 *Faraday* noticed a slight rotation of the plane of polarisation in the light transmitted through a transparent magnetic material [10]. Later, *John Kerr* observed similar behaviour for light reflected from a magnetic material [11,12].

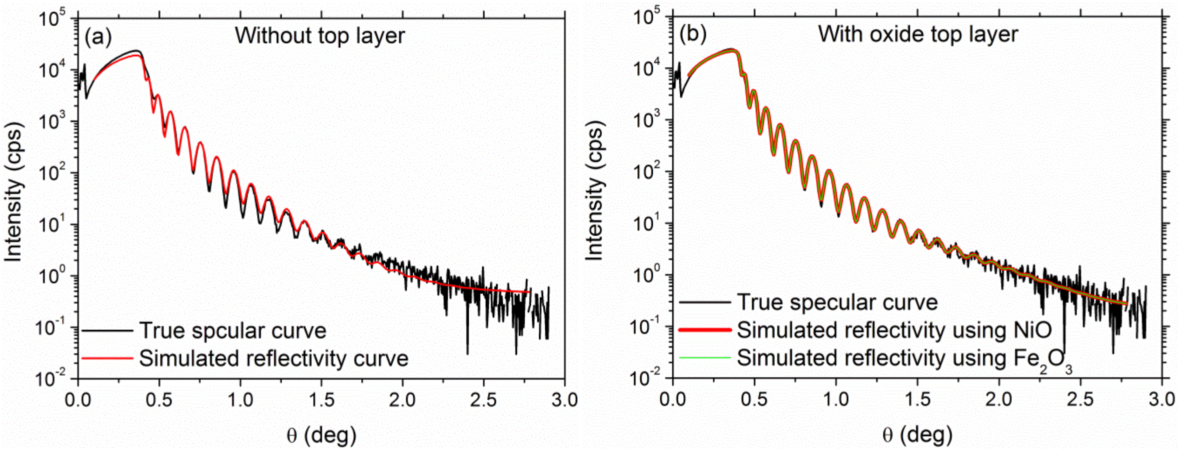

Figure 5.8 True specular X-ray reflectivity measurements (black curves) and the corresponding simulated reflectivity (red curves) obtained using Bede REFS simulation software for 15 nm thick NiFe films (a) without using top oxide layer, and (b) using both Fe_2O_3 (red curve) and NiO (green curve) top oxide layers.

These effects are known as *Faraday* and *Kerr effect*, respectively. The magnitude of the rotation for the *Faraday effect* is higher than that of *Kerr effect*. This rotation is strongly related to the magnitude and direction of the magnetisation within the material [13,14].

The *magneto-optical Kerr effect* is a non-destructive technique with a lateral resolution of around 0.3-0.5 µm for typical wavelengths depending on the diffraction limit of the light source [13]. This technique has been widely used to study the magnetic behaviour of a wide range of magnetic materials. As an example, it has been used to study the magnetic properties of thin films [15,16], individual and arrays of planar nanowires [17-24], arrays of cylindrical wires [26] and very recently isolated nanowires [25]. It can be used to determine the direction of net magnetisation of magnetic materials. The following sub-sections briefly describe the fundamental theory and the principles of the magneto-optical Kerr effect. The experimental MOKE setup used in this research to investigate the magnetisation behaviour of ferromagnetic thin films and isolated nanowires is then described. Finally, an explanation is given of how isolated nanowires were located and measured.

5-4.1 Geometries of magneto-optical Kerr effect

From a practical point of view, the magneto-optical Kerr effect can be classified into three different geometries, depending on the relative orientation of the planes of incident and reflected light with respect to the magnetisation vector within the magnetic sample and applied magnetic field orientation [13]. A schematic description of these geometries is shown in Figure 5.9 [13,27]. When the magnetisation vector of the sample lies normal to the reflection surface (sample surface) and parallel to the plane of incidence, the *polar Kerr effect* occurrs, as shown in Figure 5.9(a). When the magnetisation vector within the magnetic material is parallel to the reflecting surface and the plane of incidence, the *longitudinal Kerr effect* appears, as shown in Figure 5.9(b) [28].

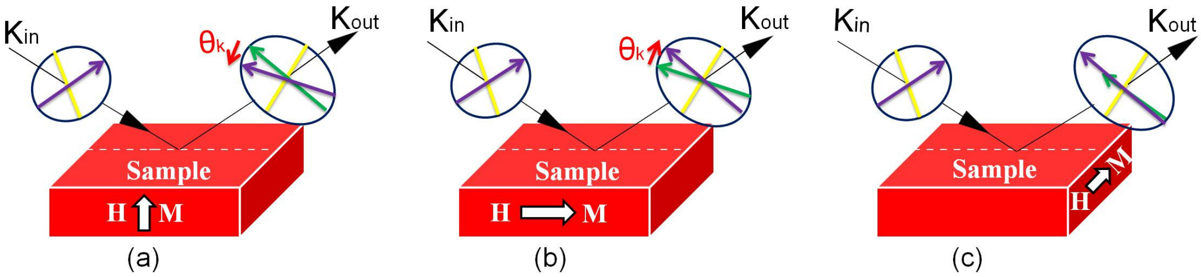

Figure 5.9 The three geometries of Kerr effects depending on the relative orientation of the magnetisation at sample surface with respect to the planes of incident and reflected surface. These geometries are referred to as (a) polar, (b) longitudinal, and (c) transverse Kerr effects. In both polar and longitudinal geometries there is a slight rotation and some ellipiticity of the reflected light, whilst in the transverse Kerr geometry there is only a change in the intensity of the reflected light. Modified from [13,27].

In this geometry, it is found that the rotation of the reflected light falls to zero at normal incidence and increased to maximum at an incident angle of 60^{o} [28]. If the magnetisation of the sample is normal to the plane of incidence and parallel to the reflected surface, then the geometry is said to be in the *transverse configuration*, as illustrated in Figure 5.9(c) [27]. In this configuration, there is no rotation of polarisation, there is only a change in the intensity of the reflected light [29]. It is noteworthy to mention that in both longitudinal and transverse MOKE measurements, the incident light comes in at oblique angle with respect to the magnetic material, whilst normal angles of incidence is best for polar MOKE configuration [28,29]. The longitudinal Kerr effect has been widely used to study the surface magnetic properties of thin films and nanostructures with in-plane magnetisation. Thus, longitudinal MOKE setup is used in this work to study the magnetisation behaviour of electrodeposited ferromagnetic thin films and isolated nanowires, because their magnetisation vector is expected to lie parallel to the sample surface.

5-4.2 Physical origin of longitudinal Kerr effect

Two orientations of linearly polarised light are available, *s* and *p polarised light*, in which the plane of polarisation is perpendicular and parallel to the plane of incidence, respectively [13], as schematically shown in Figure 5.10. When *s* or *p* polarised light is

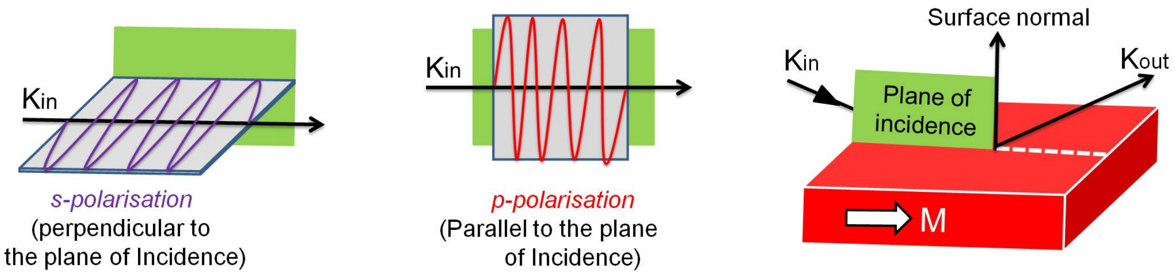

Figure 5.10 Schematic illustrations of the two forms of linearly polarised light *s* and *p* which mean that the plane of polarisation is perpendicular and parallel to the plane of incidence, respectively.

incident on a medium, the electric component of the light interacts with the conduction electrons of the medium and generates an oscillation of these electrons [13]. The oscillating electrons re-radiate a spherical wave front in the polarisation direction of the incident light. When the medium is non-magnetic, the re-radiated light has the same polarisation as the incident light, resulting in no rotation in the polarisation of the reflected light [13]. However, in the case of a magnetic medium, an orthogonally polarised component known as *Kerr component* emerges in the reflected beam which is superimposed with the initial polarisation direction of the incident light causing a small rotation in the polarisation of the reflected light. The magnitude of this orthogonal component is related to the longitudinal magnetisation state. The origin of the Kerr effect is directly related to the optical properties of the magnetic material, which are determined by its dielectric characteristics [13].

To understand the physics of this interaction consider that polarised light can be described as a linear combination of left and right circularly polarised light, as schematically illustrated in Figure 5.11. The interaction with a non-magnetic material occur such that the electrons in both directions are in-phase with each other, so light is linearly polarised [13], as shown in Figure 5.11(a). In contrast, the speed and absorption of polarised light in the magnetic material are different for the left and right directions. Therefore, the difference in the speed of the left and right polarised parts give rise to the *Kerr rotation*, as shown in Figure 5.11(b), whereas the difference in the absorption coeffici-

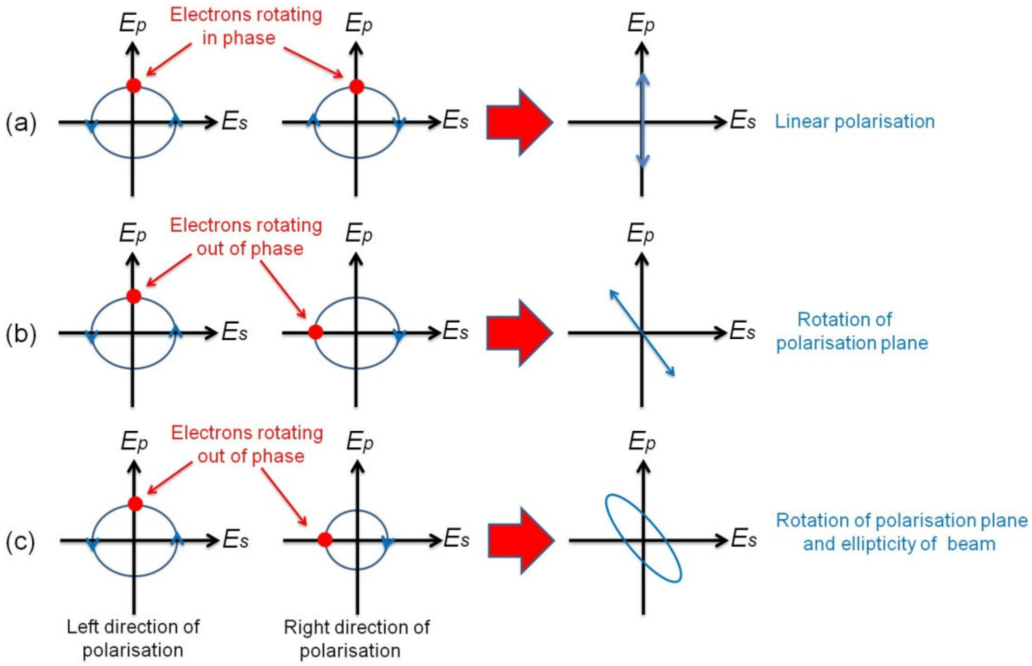

Figure 5.11 Schematic diagrams showing the effect of electrons oscillations in a sample to give rise to the rotation and elliptical components of the reflected light in longitudinal magneto-optical Kerr effect. Reproduced from [30].

ent between the two directions changes the linearly polarized light into elliptic polarized light and yields the *Kerr ellipticity*, as demonstrated in Figure 5.11(c).

Importantly, in the context of this work, the magnitude of the detected MOKE signal is limited by the depth that the light penetrates into the specimen, this is called the *penetration depth or optical skin depth*, λ_{MOKE} , due to the absorption of light in the medium [13] and it can be defined as the distance at which the intensity of the incident light, I_o, is attenuated to, I, of the initial value and it is given by [13]:

$$\frac{\mathrm{I}}{\mathrm{I_o}} = \exp\left(\frac{-\mathrm{t}}{\lambda_{\mathrm{MOKE}}}\right) \qquad 5\text{-}9$$

Where, t is the optical path length. The penetration depth is calculated to be approximately 10-20 nm for good conductive metals at visible frequencies [13]. Therefore, the skin depth is very important for thick nanowires investigated here as the MOKE can only probes the surface of these nanowires.

5-4.3 Experimental usage of longitudinal MOKE magnetometry

Since the magnetisation lies in the plane of the electrodeposited thin films and nanowires, the longitudinal Kerr effect was employed to investigate the magnetic properties of those samples. Therefore, the following subsections describe the experimental setup and the procedure used to locate the nanowires, as well as the method employed to perform the measurements.

5-4.3.1 Description of MOKE apparatus

A schematic diagram of the longitudinal MOKE setup used in this research is shown in Figure 5.12 [31]. This setup combines two optical systems, one for performing magnetic measurements and the other for imaging the samples to locate the nanostructures. A highly stable 30 mW diode laser with a wavelength of ~658 nm was attenuated to about 5 mW using a neutral density filter. In order to focus the laser light into a small spot size, the light passed through a beam expander. The light then passed through a *Glan-Taylor* polarising prism to polarise the laser light linearly.

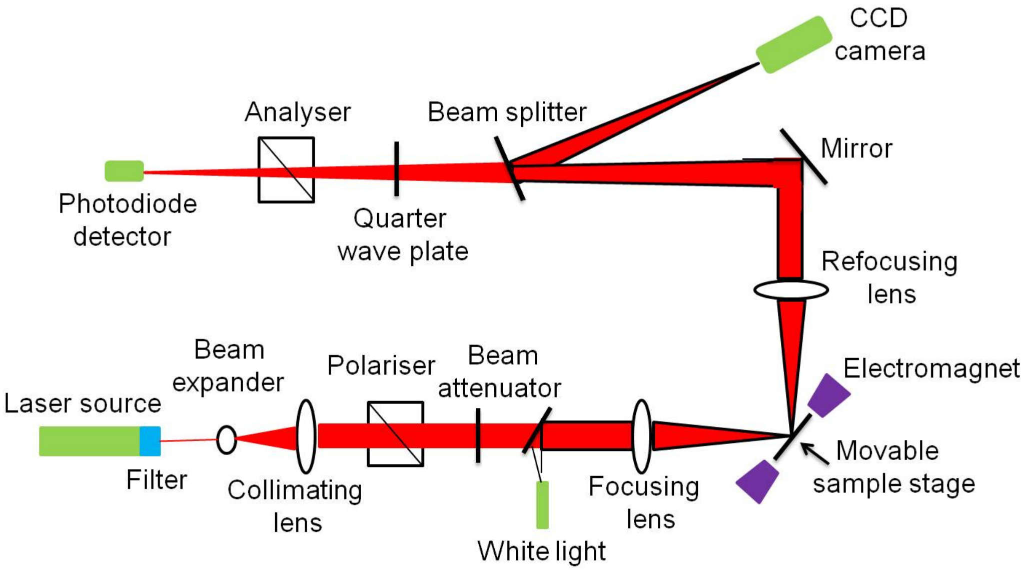

Figure 5.12 A schematic diagram of longitudinal MOKE setup used in this work to investigate the magnetic behaviour of electrodeposited thin films and template released isolated ferromagnetic nanowires. Reproduced from [31].

The polarised beam was then focused onto the specimen with a spot size of approximately 5 μm using a focusing lens. A quarter-wave retardation plate was used to remove the ellipticity of the reflected laser light and restores it to a linear polarized light beam. The reflected light then passed through an analyser prism (*Glan-Taylor polariser*). Finally, in order to eliminate the background light into the diode detector, a narrow band pass filter was placed in front of the detector (*silicon photodiode*). The detector was connected to a digital voltmeter (DVM) via a trans-impedance amplifier (*Melles Griot Large Dynamic Range Amplifier*) to amplify the weak detected signal. The output signal was connected to a digital storage oscilloscope (*Tektronix TDS 71041 GHz bandwidth oscilloscope*) and a computer system for processing the data and producing the hysteresis loops [31].

The electromagnet coils of this system were supplied by an alternating current with a frequency of approximately 21-27 Hz from a bipolar operational power supply (*KEPCO BOP 20-5M*). A maximum magnetic field of approximately ± 400 Oe was produced in the plane of the specimen using two pole iron pieces of electromagnet with approximately 5 cm separation gap [18,30,31].

The change in the Kerr signal was strongly dependent on the magnitude and orientation of the magnetisation within the sample. The measured Kerr signal was usually plotted as a function of the external magnetic field to obtain the hysteresis loops. As an example, Figure 5.13(a) shows a typical hysteresis loop obtained from measurements of template released individual Ni nanowire with a ~300 nm diameter using this setup.

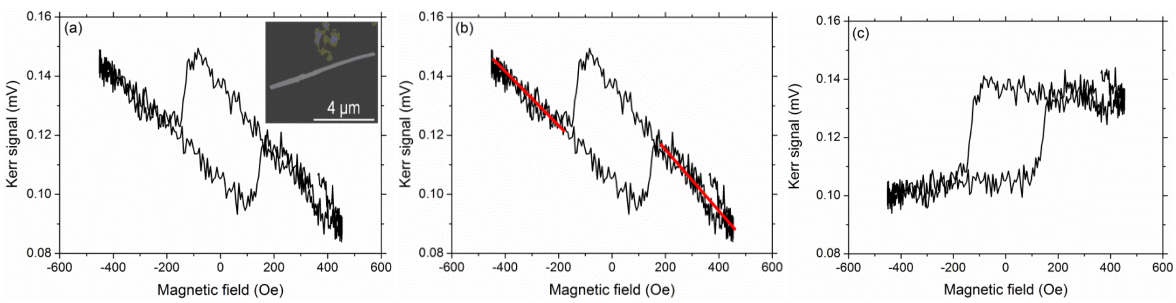

Figure 5.13 An example of typical hysteresis loop obtained from measuring template released individual Ni nanowire with a ~300 nm diameter using longitudinal MOKE setup (a,b) before, (c) after correction.

The figure inset is a scanning electron micrograph showing the measured wire. The loop is quite tilted due to the small sample size and the influence of a background optical effect from the substrate. Therefore, all the MOKE measurements of nanostructures were corrected by fitting a linear line of best fit to the high field data where the magnetisation is saturated, as shown in Figure 5.13(b). The gradient of the slope was then subtracted from the Kerr signal to yield the corrected hysteresis loop as shown in Figure 5.13(c). These loops are then normalised.

5-4.3.2 Locating isolated nanowires within the MOKE setup and their measurement

Due to the particularly small sizes, very small magnetisation and the rounded surfaces of the nanowires, the locating, positioning and measurement of these wires using the MOKE setup was a major technical challenge in this work. The isolated clusters and individual nanowires were first selected and identified with respect to the pre-patterned micromarkers using both scanning electron microscopy and optical microscopy. Then, the micromarkers were located using the optical microscopy imaging facility available on the MOKE magnetometer. Based on the SEM measurements the sample was moved to locate the laser spot as close as possible to the selected nanowire using the CCD microscope image as a guide. Then, using an *optical reflectivity scan* with laser spot illumination, the exact position of the nanowires on the chip was achieved. This was performed by rastering the sample through the laser spot at a desired area and spatial resolution. Figure 5.14(a) shows such a 20 μm × 20 μm reflectivity map with a pixel resolution of 1 μm used to locate an individual NiFe nanowire on a pre-patterned silicon chip. The white areas in the map correspond to the highest reflected signal, whilst the grey or black areas represent the lower reflected signal that comes from the chip. The sample was then moved to the desired position on the nanowire and the measurements were carried out.

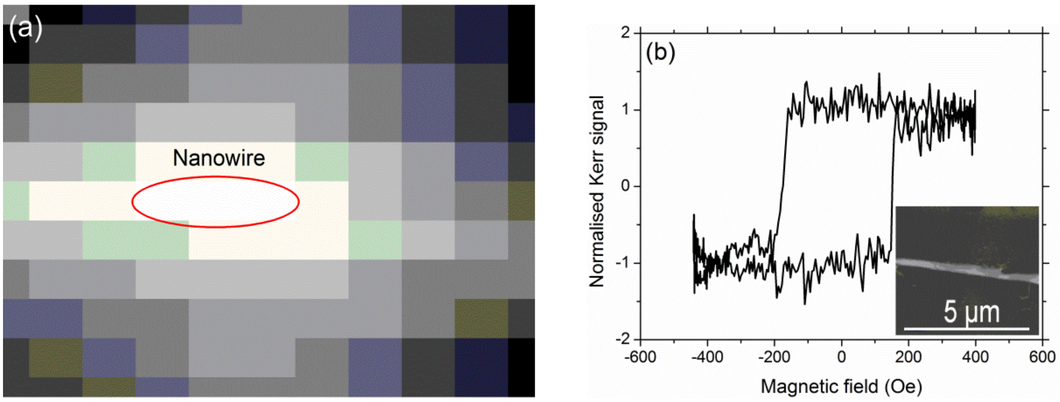

Figure 5.14 (a) Optical reflectivity scan on an area of 20 µm × 20 µm with a resolution of 1 µm on a pre-patterned silicon chip used to locate and measure an individual template released NiFe nanowire within the MOKE setup, (b) an example of a normalised hysteresis loop obtained from measuring the same nanowire located using this method. The figure inset shows an SEM image of the measured wire.

Moreover, it allows the measurements to be performed at different positions and angles on the same isolated nanowires as will be seen in chapter eight.

As the laser spot was focused onto desired position on the sample, the quarter-wave plate and the analyser were iteratively rotated until a high optical extinction of the *Kerr signal* was detected. The analyser then was rotated by a suitable angle from the extinction in order that the photodiode detected the extinction polarisation change as a variation in the intensity of the detected signal [18,31]. To improve the signal to noise on the data, the MOKE measurements were averaged over many hundreds of field cycles, taking approximately 3 minutes. An example of normalised hysteresis loop obtained from measuring an individual template released NiFe nanowire following this procedure is shown in Figure 5.14(b). The figure inset shows an SEM image of the measured wire.

In order to study the magnetisation reversal behaviour of thin films, isolated clusters and individual nanowires, the hysteresis loops were recorded at different angles from parallel, 0^{o}, to perpendicular, $\pm 90^{o}$, directions in steps of 5^{o}. These measurements were extremely time consuming as the nanowires had to be relocated using a reflectivity scan after each rotation or changing the position.

5-5 Anisotropic magneto-resistance (AMR)

The change in the electrical resistance of a ferromagnetic material upon applying magnetic field is referred to as *magnetoresistance (MR)* [28]. This change in the resistance has various physical origins depending upon the system, but here the discussion is limited to anisotropic magnetoresistance which was used in this work to investigate the electrical transport properties and magnetisation behaviour of electrodeposited isolated ferromagnetic nanowires.

William Thomson found that the resistance increases when electrical current, *I*, was flowing in a ferromagnetic material (iron) in the same direction as the external applied magnetic field, whilst it decreases when the current was flowing normal to the magnetic field [32]. This effect is referred to as *anisotropic magnetoresistance (AMR)* [28]. The relation between electrical resistance and the applied magnetic field however is nonlinear, as shown in Figure 5.15(a) which shows an example of anisotropic magnetoresistance profile of an isolated NiFe nanowire measured at room temperature when the magnetic field was applied parallel and perpendicular to the current flow. The schematics of the magnetisation orientation with respect to the current flow at both directions of applied magnetic field are presented in Figure 5.15(b).

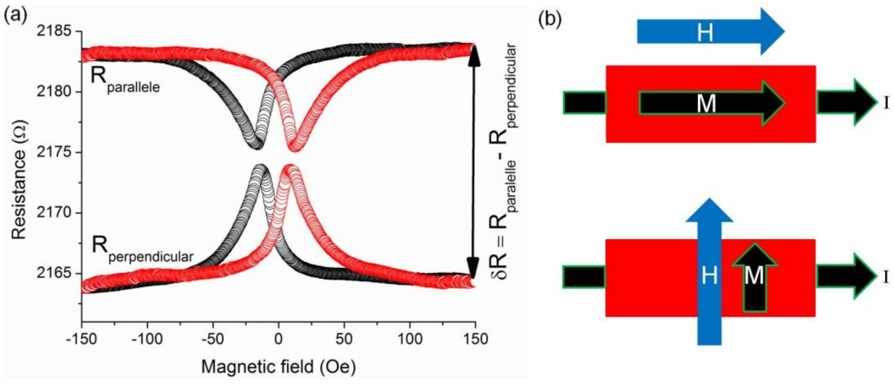

Figure 5.15 (a) An example of anisotropic magnetoresistance profile of isolated NiFe nanowire measured at room temperature when the magnetic field was applied parallel and perpendicular to the current flow. (b) The schematics of the magnetisation orientation with respect to the current flow at both directions of applied magnetic field.

5-5.1 Microscopic origin of anisotropic magnetoresistance

The microscopic origin of anisotropic magnetoresistance in ferromagnetic materials lies in the *spin-orbit coupling* which was first described by *Smit* in 1951 [33]. This coupling causes a difference in scattering of the conduction electrons when they are moving parallel or perpendicular to the magnetisation.

If an external magnetic field is applied to a ferromagnetic material, the electron spins rotate towards that direction depending on a combination of the strength and direction of the applied magnetic field and the intrinsic magnetic properties of the material [34]. The change in the direction of the magnetic moments slightly distorts the closed electronic orbitals of the ferromagnetic material, which in turn changes the amount of scattering of the conduction electrons [33-35]. If the magnetic moments are oriented perpendicular to the current, then the relevant electronic orbitals are in the same plane as the electric current, and there will be a little effect of scattering, yielding a *low resistance state*. In contrast, when the magnetic moments are parallel to the current the electronic orbits are oriented perpendicular to the current and the scattering increases giving rise to a *high resistance state*.

It is more convenient to use resistivity, ρ, rather than resistance which is given by [36]:

$$\rho = \frac{\mathrm{RA}}{\mathrm{L}} \qquad 5\text{-}10$$

Where, *R* is the resistance. *A* and *L* are the cross-sectional area and length of the specimen, respectively. The change in the resistivity, $\delta\rho$, upon applying a magnetic field is defined as the difference between the resistivity when the applied magnetic field is parallel, $\rho_{||}$, and perpendicular, $\rho_{\perp}$, to the current flow, as shown in Figure 5.16 and it is given by [34]:

$$\delta\rho = \rho_{||} - \rho_{\perp} \qquad 5\text{-}11$$

Since the resistivity at saturation for any angle, θ, is defined as [34,37]:

$$\rho_{(\theta)} = \rho_{\perp} + \delta\rho cos^2\theta \qquad 5\text{-}12$$

Therefore, the AMR can be used to investigate the magnetisation reversal in ferromagnetic nanostructures.

Since the resistivity in the absence of magnetic field depends on the domain configuration, which depends on the magnetic history of the material, it is more convenient to use the following relation to define an average resistivity [34]:

$$\rho_{ave} = \frac{1}{3}(\rho_{\parallel} + 2\rho_{\perp}) \qquad \text{5-13}$$

The change in the resistivity of a ferromagnetic material upon applying a magnetic field is usually expressed in terms of the fractional change, $\frac{\delta\rho}{\rho_{ave}}$, which is known as *anisotropic magnetoresistance ratio* and given by [34]:

$$\frac{\delta\rho}{\rho_{ave}} = \frac{(\rho_{\parallel} - \rho_{\perp})}{\frac{1}{3}(\rho_{\parallel} + 2\rho_{\perp})} \qquad \text{5-14}$$

The anisotropic magnetoresistance ratio at any angle, $(\frac{\delta\rho}{\rho})_{\theta}$, can be given by [38,39]:

$$(\frac{\delta\rho}{\rho})_{\theta} = \frac{\rho_{\theta}\,(H) - \rho_{\theta}\,(H_{Max})}{\rho_{\theta}\,(H_{Max})} \qquad \text{5-15}$$

Hence, the longitudinal, $(\frac{\delta\rho}{\rho})_{\parallel}$, and transverse, $(\frac{\delta\rho}{\rho})_{\perp}$, anisotropic magnetoresistance can be written as [38,39]:

$$(\frac{\delta\rho}{\rho})_{\parallel} = \frac{\rho_{\parallel}\,(H) - \rho_{\parallel}\,(H_{Max})}{\rho_{\parallel}\,(H_{Max})} \qquad \text{5-16}$$

$$(\frac{\delta\rho}{\rho})_{\perp} = \frac{\rho_{\perp}\,(H) - \rho_{\perp}\,(H_{Max})}{\rho_{\perp}\,(H_{Max})} \qquad \text{5-17}$$

where, $\rho_{\theta}(H)$ and $\rho_{\theta}\,(H_{Max})$ are the resistivity at 0 and maximum applied magnetic field, respectively. The AMR ratios for ferromagnetic materials and their alloys are typically very small (around few percent) [40]. As an example, Figure 5.16 shows the variation in the anisotropic magnetoresistance ratio as a function of Ni content in the alloys of Ni_xFe_{1-x} [40]. For instance, a maximum value of ~5% was noticed in the $Ni_{0.9}Fe_{0.1}$ nanowires [34,40].

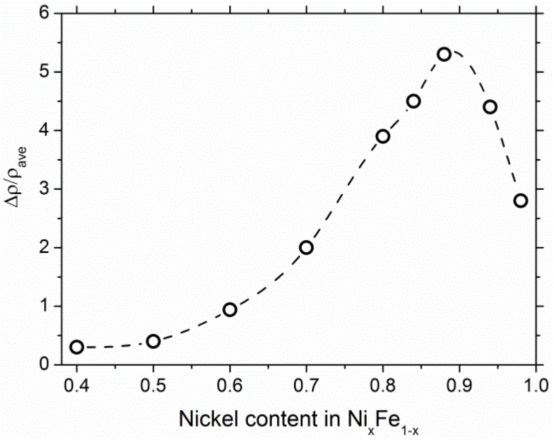

Figure 5.16 Anisotropic magnetoresistance ratio as a function of nickel content in the alloys of Ni_xFe_{1-x} measured at room temperature. Reproduced from [40].

5-5.2 Experimental methodology for magnetoresistance measurements

Magnetoresistance measurements of electrodeposited ferromagnetic isolated nanowires were carried out using a room temperature magnetoresistance setup which is illustrated as a block diagram in Figure 5.17 [41]. This setup was controlled by a computer system using *LabVIEW* software. Samples were placed on a rotation stage between the pole pieces of an electromagnet with a maximum field strength of 1 kOe and covered with an electrically and thermally shielded cover. Two main types of measurements were performed with this system [41]. It was used to measure the resistance at a particular angle as a function of magnetic field, or rotating the sample and measuring the resistance under a fixed magnetic field. Further detail of this setup and their measurements can be found in Ref [41].

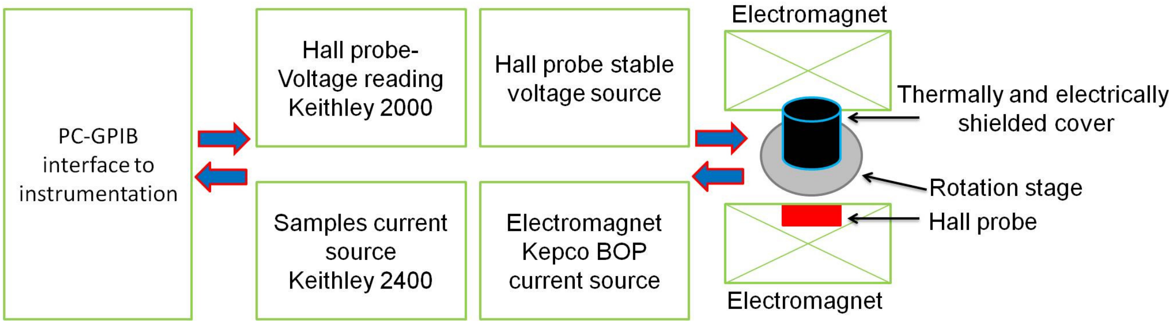

Figure 5.17 Block diagram of anisotropic magnetoresistance setup used in this research to investigate the electrical transport properties and magnetisation behaviour of template released isolated nanowires. Modified from [41].

This setup is provided with different sample holders and connecting methods to allow measurement of different geometries, shapes and sizes of samples. As an example, Figure 5.18 shows the two point probe system which is designed to measure the AMR of isolated nanostructures. In this geometry the voltage across the nanowire is the current passing through the nanowire multiplied by its resistance and the connection (lead) and contact resistance. All the measurements were carried out using a direct current of ~0.1 mA. This gave an equivalent current density of approximately 10^8 Am^{-2} [30,41]. Using higher currents could lead to increase the *Joule heating* which might damage the sample [42]. The sample holder could be rotated with an angle of 0-180^o with respect to the applied magnetic field direction allowing the magnetisation reversal to be studied. At each field step, 50 measurements of voltage were made and averaged to give the resistance [41].

Prior to MR measurements, an initial test was carried out for all samples and at different angles of the applied magnetic field with respect to the current flow in order to get an insight into the signal to noise ratio. All measurements employed a magnetic field that was gradually increased or decreased at a steady rate of ~0.5 Oe/s. This was repeated for two full sweeps in which the magnetic field was applied between +1 kOe and -1 kOe. Since each field sweep took about two hours, there was a very slight increase of saturation

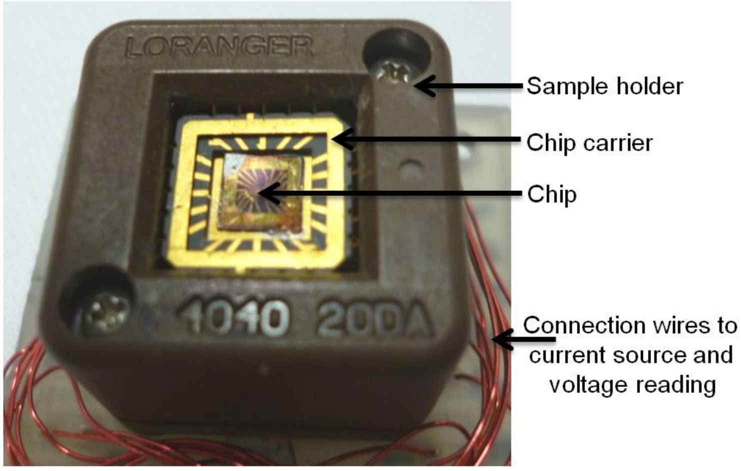

Figure 5.18 Photograph of the sample holder used in magnetoresistance setup to measure the electrical transport properties of isolated nanowires.

resistance with time due to the effect of heating. All AMR measurements were then corrected according to the following procedure. Figure 5.19(a) shows the raw resistance as a function of magnetic field for isolated NiFe nanowires measured when the current was applied nominally parallel to the magnetic field. The measurements was corrected by fitting a linear line of best fit to the resistance time curve, as shown in Figure 5.19(b). The periodic features appearing in the figure are related to the switching fields within the sample. Then, the gradient of the slope was subtracted from the measured resistance, as shown in Figure 5.19(c) to give a final corrected profile as shown in Figure 5.19(d).

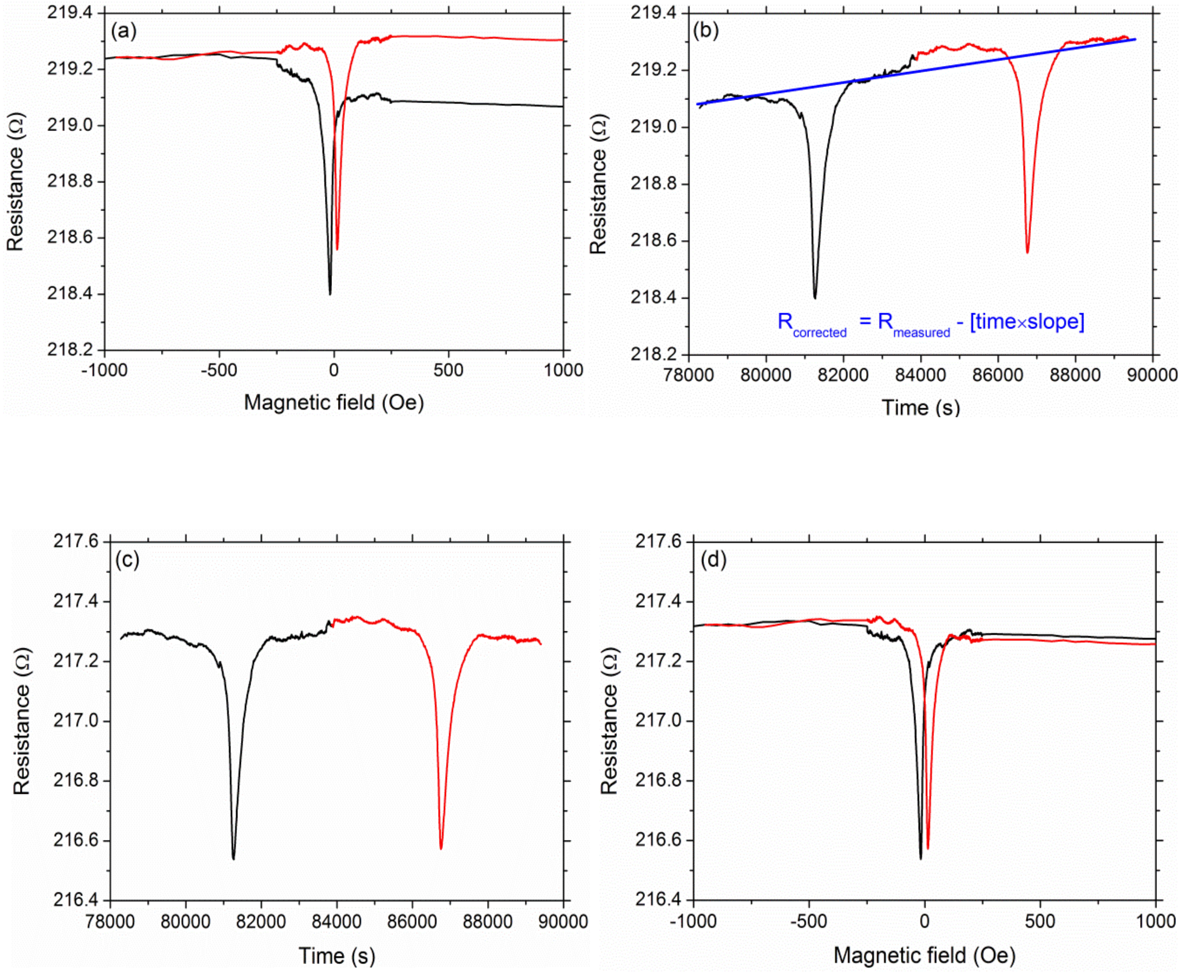

Figure 5.19 (a) An example of the resistance as a function of magnetic field for isolated NiFe nanowires measured by MR setup when the current was applied parallel to the magnetic field. The resistance as a function of time (b) before, and (c) after corrections. (d) The resistance as a function of magnetic field after corrections. The periodic jumps correspond to the switching field within the sample.

5-6 Micromagnetic modelling

In this study, micromagnetic simulations were used to investigate the magnetic behaviour of cylindrical and planar (rectangular) cross-sectioned individual $Ni_{81}Fe_{19}$ nanowires with different diameters and dimensions, respectively. These simulations were performed in order to gain a significant insight into the magnetic behaviour of such nanowires and to compare these results with the experimental MOKE and AMR results. The software used is based on numerically solving the *Landau–Lifshitz–Gilbert* equation as discussed in chapter two using the *object oriented micromagnetic framework (OOMMF) package*. A brief description of this code and how it is used to investigate the magnetic and magnetisation reversal behaviour are described in the following subsections.

5-6.1 OOMMF software

The *OOMMF code* is public domain software available freely from the *National Institute of Standards and Technology (NIST)* website and it was developed by *Donahue and Porter* in 1997 [43]. It is a collection of programs working together to solve magnetic problems. This software has the ability to simulate any shaped elements and display the changes in the magnetic configuration at each field step in the hysteresis loop [44].

Within this package, it is first necessary to define the magnetic problem to be solved which is managed by creating a *micromagnetic input file (MIF)*. This file contains all the information required to solve the problem, such as nanowire dimensions, geometry and cell size, as well as the energy contributing terms (mentioned in chapter two) and the magnetic parameters for which the simulation is employed. It is very important however to use the values for the parameters which are representative of the sample under simulation so that the program can provide relevant and insightful results.

5-6.2 OOMMF 3D problems solver

Cylindrical and planar $Ni_{81}Fe_{19}$ nanowires with diameters and dimensions ranging from 10 to 200 nm and a fixed length of 1 µm were simulated to investigate their magnetic and magnetisation reversal behaviour. Calculations were performed by dividing these nanowires into three dimensional arrays of cubic cells with dimensions of 5×5×5 nm^3, as shown in Figure 5.20. This cell size was selected to be less than the exchange length of NiFe nanowires to allow the exchange interaction to be correctly modelled as defined in chapter two [45,46] and to reasonably approximate the shape [47]. The magnetisation in these cells were assumed to be constant and located at the centre of each cell. All the simulations here were performed using the university mainframe computer. The values of saturation magnetisation, M_s, and exchange stiffness parameter used here were: 8.6×10^5 *A/m* and 13×10^{-12} *J/m*, respectively [48,49]. The magnetocrystalline anisotropy, K_1, was set to zero because permalloy (81:19) has zero magnetocrystalline anisotropy [50]. The *Gilbert damping parameter*, *α* (defined in chapter two) was selected to be equal to *0.5*, to speed up the computations and decrease the simulation time which took around a month for thick nanowires, where the typical simulations needs around 1.5 kB per cell [51,52]. Using smaller values of the damping parameter is however preferable but the simulation will take longer time and a huge amount of computer memory.

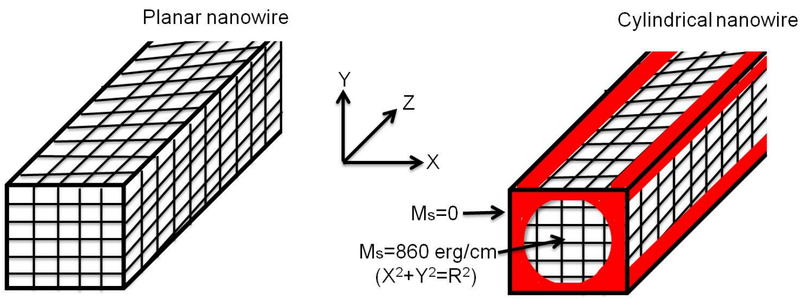

Figure 5.20 Micromagnetic simulations were performed on planar and cylindrical nanowires by dividing these wires into 3D arrays of cubic cells. The cylindrical nanowires were created by setting the saturation magnetisation at the circumference surface of the planar wires to be zero using the mathematical cylinder equation.

The gyromagnetic ratio was $\gamma=17.59\ MHz/Oe$. The shape anisotropy was incorporated in the calculation of the demagnetising field of the system via magnetostatic energy calculations.

The magnetic field was varied according to the nanowire dimensions with a typical range of +4 to −4 kOe in steps of 10 Oe. A field step of 5 Oe was sometimes used to observe finer details. The computational stopping condition is given by the torque $M\times H$. The exchange energy was computed via an eight neighbour dot product and the magnetostatic energy was calculated alone using a *fast Fourier transform (FFT)* based scalar potential due to the nonlocal magnetic structure [47].

To create cylindrical nanowires the saturation magnetisation on the circumference surface of the planar nanowires was setting to zero using the mathematical circle equation, as demonstrated in Figure 5.20. To investigate the magnetisation reversal in all these nanowires, the magnetic field was applied along and perpendicular to the nanowire long axis using different strengths of magnetic fields to create a vector sum for the angles used for the measurements. More details are given in chapter nine.

All micromagnetic simulations were carried out at *0K*, because OOMMF is limited to zero temperature calculations. If another temperature was instead used, thermal fluctuation would complicate the simulations and also increases the simulation time [48].

5-7 Chapter references

1. Everhart, T. E. & Thornley R. F. M. "Wide-band detector for micro-microampere low-energy electron currents" *J. Sci. Instr.*, 37 (7), 246, 1960.
2. Golstein, J. I., Newbury, D. E., Echlin, P., Joy, D. C., Romig A. D. Jr., Lyman C. E., Fiori C. & Lifshin E. "Scanning electron microscopy and X-ray microanalysis" 2nd edition, Plenum press, New Yourk & London, P 177,1992.
3. Goodhew, P. J., Humphrey, J. S & Beanland, R. "Electron microscopy and analysis" 3rd edition, Taylor & Francis, London, 2001.
4. Parratt, G. Lyman "surface studies of solids by total reflection of X-rays" *Phys. Rev.*, 95, 359, 1954.
5. Bowen, K. D. & Tanner, B. K. "X-ray metrology in semiconductor manufacturing" Taylor & Francis Group, LLC, USA, 2006.

6. Jordan Valley "D1 Installation, operation and maintains manual" Jordan Valley Semiconductors Ltd., 2008.
7. Jordan Valley "Bede X-ray applications manual" Jordan Valley Semiconductors Ltd., 2008.
8. Bede REFS (version 4.5): User Manual, Bede PLC, Durham available from Jordan Valley PLC, 2007.
9. Wormington, M., Panaccione, C., Matney, K. M. & Bowen, D. K., "Characterization of structures from X-ray scattering data using genetic algorithms" *Philosophical Transactions of the Royal Society of London* - Series A 357, 2827, 1999.
10. Faraday, M. "On the magnetisation of light and the illumination of magnetic lines of Force" *Philosophical Transactions of the Royal Society, London*, 136, 1, 1846.
11. Kerr, J. "On reflection of polarised light from the equatorial surface of a magnet" *Philosophical Magazine*, 5, 161, 1877.
12. Kerr, J. "On rotation of the plane of polarisation by reflection from the pole of a magnet" *Philosophical Magazine*, 3, 321, 1877.
13. Brundle R. C., Evans C. A., Jr. & Wilson S. "Encyclopaedia of materials characterisation" Butterworth-Heinemann, a division of Reed publishing Inc., USA, 1992.
14. Gasche, T., Brooks, M. S. S. & Johansson, B. "Calculated magneto-optical Kerr effect in Fe, Co, and Ni" *Phys. Rev.*, 53, 1, 1996.
15. Contreras, M. C., Calleja, J. F. & Rivas, M. "TBIS measurements performed by MOKE for the study of soft ferromagnetic thin films and sandwiches: In-plane and biaxial anisotropies, local anisotropy and dispersion" *J. Mag. Mag. Mat.*, 53, 4, 1997.
16. Bergenti, I., Riminucci, A., Arisi, E., Murgia, M., Cavallini, M., Solzi, M., Casoli, F. & Dediu V. "Magnetic properties of cobalt thin films deposited on soft organic layers" *J. Mag. Mag. Mat.*, 316(2), e987, 2007.
17. Atkinson, D., Allwood, D., Xiong, G., Cooke, M. D., Faulkner, C. C. & Cowburn, R. P. "Magnetic domain-wall dynamics in a submicrometre ferromagnetic structure" *Nat. Mat.*, 2(2), 85, 2003.
18. Allwood, D.A., Xiong, G., Cooke, M. D. & Cowburn, R. P, "Magneto-optical Kerr effect analysis of magnetic nanostructures" *J. Phys. D: Appl. Phys.*, 36, 2175, 2003.
19. Adeyeye, A. O., Bland, J. A. C., Daboo, C., Lee, J., Ebels, U. & Ahmed, H. "Size dependence of the magnetoresistance in submicron FeNi wires" *J. Appl. Phys.*, 79(8), 6120, 1996.
20. Atkinson, D., Eastwood, D. S. & Bogart, L. K. "Controlling domain wall pinning in planar nanowires by selecting domain wall type and its application in a memory concept" *Appl. Phys. Lett.*, 92(2), 022510, 2008.
21. Allwood, D. A., Xiong, G., Faulkner, C. C., Atkinson, D., Petit, D. & Cowburn, R. P. "Magnetic domain-wall logic" *Science*, 309(5741), 1688, 2005.
22. Bryan, M. T., Atkinson, D. & Allwood, D. A. "Multimode switching induced by a transverse field in planar magnetic nanowires" *Appl. Phys. Lett.,* 88(3), 032505, 2006.
23. Faulkner, Colm C., Cooke, Michael D., Allwood, Dan A., Petit, Dorothée, Atkinson, D. & Cowburn, Russell, P. "Artificial domain wall nanotraps in $Ni_{81}Fe_{19}$ wires" *J. Appl. Phys.*, 95, 6717, 2004.

24. Bryan, M. T., Atkinson, D. & Cowburn, R. P. "Experimental study of the influence of edge roughness on magnetisation switching in Permalloy nanostructures" *Appl. Phys. Lett.*, 85, 3510, 2004.
25. Lupu, N., Lostun, M. & Chiriac, H. "Surface magnetisation processes in soft magnetic nanowires" *J. Appl. Phys.*, 107(9), 09E315, 2010.
26. Sharma, S., Barman A., Sharma, M., Shelford L. R., Kruglyak, V. V. & Hicken, R. J. "structural and magnetic properties of electrodeposited cobalt nanowire arrays" *Solid state communications*, 149, 1650, 2009.
27. Hubert, Alex & Schafer, Rudolf "Magnetic domains the analysis of magnetic microstructures" Springer-Verlag Berlin Heidelberg, 1998.
28. Jiles, D. "Introduction to magnetism and magnetic materials" 2nd edition, Chapman and Hall/CRC, New York, 1998.
29. Carey, R. & Isaac, E. D. "Magnetic domains and techniques for their observation" The English Universities Press Ltd., London, 1966.
30. Bogart, Lara & Atkinson, Del "An Investigation of the Structure, Pinning and Magnetoresistance of Domain Walls in $Ni_{81}Fe_{19}$ Planar Nanowires" A thesis submitted to Durham University for PhD degree in Physics, 2010.
31. Eastwood, David "Technical Note DSE4, Durham longitudinal focused MOKE: operation guide" Durham University, Physics Department, 2009.
32. Thomson, W. "On the electro-dynamic qualities of metals: effects of magnetisation on the electric conductivity of nickel and iron" *Proceedings of the Royal Society*, 8, 546-550, 1857.
33. Smit, J. "Magnetoresistance of ferromagnetic metals and alloys at low temperatures" *Physica*, 16, 612, 1951.
34. McGuire T. R. & Potter R. I. "Anisotropic magnetoresistance" *IEEE Trans. Mag.*, Mag-11, 1018, 1975.
35. Cullity, B. D. & Graham, C. D. "Introduction to magnetic materials" 2nd edition, John Wiley & Sons, Inc., Hoboken, New Jersey, USA, 2009.
36. Kronmuller, Helmut & Parkin, Stuart "Handbook of magnetism and advanced magnetic materials: Fundamentals and Theory" Volume 1, John Wiley & Sons, Ltd., USA, 2007.
37. Fert, A. & Piraux, L. "Magnetic nanowires*" J. Mag. Mag. Mat.,* 200(1-3), 338,1999.
38. Rheem, Y., Yoo, B., Beyermann, W. P. & Myung, N. V. "Electro- and magneto-transport properties of a single CoNi nanowire" *Nanotech.*, 18(12), 125204, 2007.
39. Tanase, M., Silevitch, D. M., Chien, C. L. & Reich, D. H. "Magnetotransport properties of bent ferromagnetic nanowires" *J. Appl. Phys.*, 93(10), 7616, 2003.
40. Bozorth, R. M. "Ferromagnetism: Magnetism and electrical properties" John Wiley & Sons, Inc., Hoboken, New Jersey, P. 757, 1951.
41. Armstrong, Helen "Magnetoresistance measurement system instruction manual V3.0" Durham University, Physics Department, 2010.
42. Oliveira, A. B. De, Silva, G. L. Da, Rezende, S. M. & Azevedo, A. "Magnetization reversal in single ferromagnetic rectangular nanowires" *J. Phys.: Conf. Series*, *200*(7), 072023, 2010.

43. Donahue, M. J. & Porter D. G. "OOMMF User's Guide, Version1.0" NISTIR 6376, National Institute of Standards & Technology, Gaithersburg, MD, 1999.
44. Dao, N., Homer S. R. & Whittenburge, S. L. "Micromagnetics simulation of nanoshaped iron elements: Comparison with Experiment" *J. Appl. Phys.*, 86, 6, 1999.
45. Fidler, J., Speckmayer, P., Schrefl, T. & Suess, D. "Numerical micromagnetics of an assembly of (Fe, Co) Pt nanoparticles" *J. Appl. Phys.*, 97(10), 10E508, 2005.
46. Fidler, J. & Schrefl, T. "Micromagnetic modelling - the current state of the art" *J. Phys. D: Appl. Phys.*, 33(15), R135, 2000.
47. Hertel, R. "Micromagnetic simulations of magnetostatically coupled Nickel nanowires" *J. Appl. Phys.*, 90(11), 5752, 2001.
48. Lu, J. & Wang, X. R. "Magnetization reversal of single domain permalloy nanowires" *J. Mag. Mag. Mat.*, 321(18), 2916, 2009.
49. Moon, K., Lee, J., Jung, M., Shin, K. & Choe, S. "Incoherent domain configuration along wire width in permalloy nanowires" *IEEE Trans. Mag.*, *45*(6), 2485, 2009.
50. Chikazumi, Soshin "Physics of ferromagnetism" 2nd edition, Clarendon Press, Oxford, New York, p. 286, 1997.
51. Fernández-Pacheco, A., De Teresa, J. M., Szkudlarek, A, Córdoba, R., Ibarra, M. R., Petit, D., O'Brien, L., Zeng H. T., Lewis E. R., Read D. E. & Cowburn R. P. "Magnetization reversal in individual cobalt micro-and nanowires grown by focused-electron-beam-induced-deposition" *Nanotech.*, 20(47), 475704, 2009.
52. Nian-mei, Han, Guang-hua, Guo, Guang-fu, Z., Wen-bing, S. & Gao-fu, Men "Domain wall structure transition during magnetization reversal process in magnetic nanowires" *Trans. Nonferrous Metals Society of China*, 17(60571043), 1034, 2007.

Chapter six

Results: Composition, morphology and statistical distribution of ferromagnetic thin films and template released nanowires

6-1 Introduction

In order to gain a full understanding of the fabrication system used to prepare ferromagnetic nanowires, the chemical composition, thickness and roughness of a range of electrodeposited Ni and NiFe thin films have first been studied using *energy & wavelength dispersive X-ray analysis* and *grazing incidence X-ray reflectivity measurements*, respectively. To emphasise the most important reason behind studying the isolated nanowires presented in the following chapters rather than large arrays, the statistical distribution of interpore wall thickness (spacing) of the individual templates, the diameter and length distributions, as well as the morphology of template released ferromagntic nanowires were investigated using *high resolution scanning electron microscopy*. The crystal structure and crystallite size of these ferromagnetic nanowires can have a strong influence on their magnetic and electrical behaviour, therefore the crystalline structure of as-deposited (templated) and isolated Ni and NiFe nanowires were investigated using both *X-ray diffraction* and *high resolution transmission electron microscopy* incorporating with *electron diffraction*, respectively.

6-2 Composition, roughness and thickness of ferromagnetic thin films

The following subsections investigate the chemical composition, thickness and roughness of a range of electrodeposited ferromagnetic thin films. These measurements were mainly used to gain an insight into the base materials which were used to prepare cylindrical nanowires using the same technique under the same conditions.

6-2.1 Compositional analysis of electrodeposited thin films

The chemical composition of electrodeposited ferromagnetic Ni and NiFe thin films with different growth times was analysed at different locations on the samples with the support from *Mr. L. Bowen* (Electron Microscopy Facility, Physics Department, Durham University, U.K.) using both energy & wavelength dispersive X-ray (EDS and WDS) analysis in scanning electron microscopy *SEM Hitachi-SU 70* and *JEOL 2100F TEM* systems, respectively [1]. Figure 6.1 show examples of *EDS measurements* of electrodeposited Ni nanowire and NiFe thin film. The atomic identification of the peaks in the spectrum relate to Ni, Fe, Cu, O, Si and Au. In general, a small amount of oxygen was seen in most of the samples and may have formed by oxidation during the fabrication process or subsequent storage. The Cu, Si and Au content reflect the chemical composition of the substrates. Importantly, these measurements confirm that these films are free from contamination of boron and sulphur which has been observed elsewhere [2].

Detailed compositional analysis of the Ni and Fe ratios in the NiFe films with different electrodeposition times and a nominal composition of 80:20 was undertaken using *standardised quantitative WDS analysis.* The results are plotted in the distribution histograms shown in Figure 6.2(a). These histograms demonstrate that the weight ratios of Ni and Fe in the NiFe films are close to 60:40. Clearly, a large shift of around 20% in the elemental composition was noticed. The effect of electrodeposition growth time on the elemental composition of the same films was investigated and plotted in Figure 6.2(b).

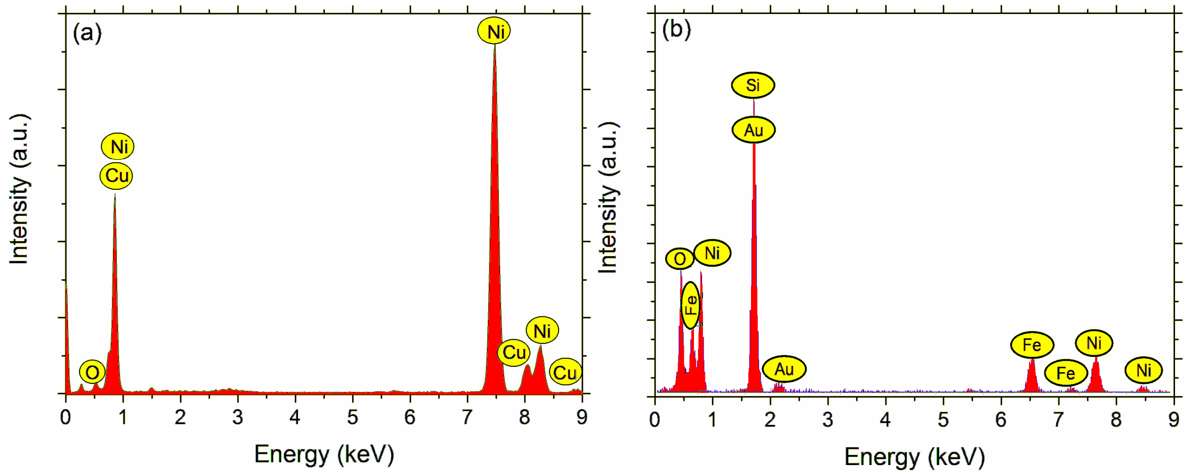

Figure 6.1 Examples of energy dispersive X-ray spectroscopy (EDS) measurements of electrodeposited (a) Ni nanowires, and (b) NiFe thin films [1].

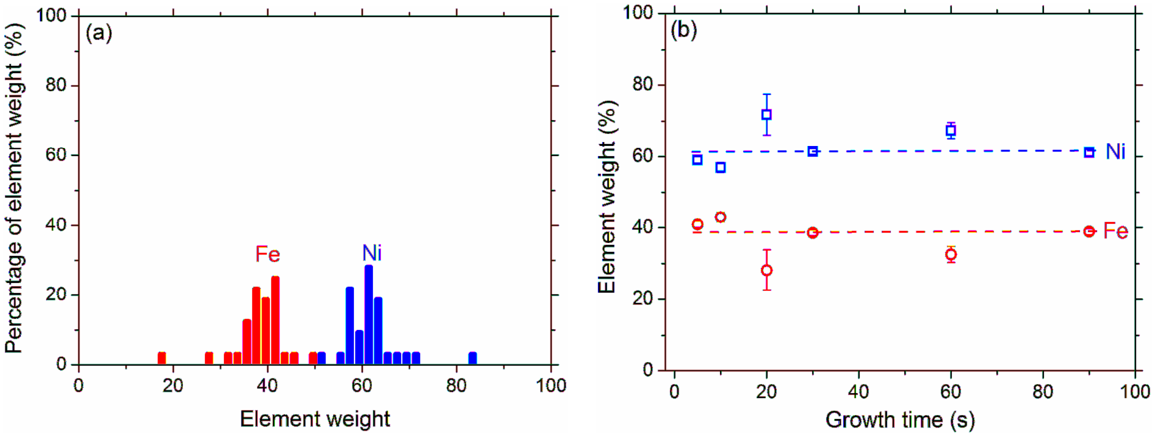

Figure 6.2 (a) Elemental weight distributions of electrodeposited Ni and Fe in NiFe films with a range of thicknesses and nominal composition of 80:20, and (b) the effect of growth time (film thickness) on the elemental composition of Ni and Fe in the NiFe films.

There is a slight variation in the elemental composition across the area of measured films of up to 8%, which is smaller than the data points and so does not appear in the figure. There is also a very limited variation in the elemental weight with growth time. These variations can be attributed to the variation in the concentration of Fe ions in the electrolyte, as demonstrated elsewhere [3,4]. This compositional change is likely to have some effect on the magnetic behaviour of these films and nanowires grown under these conditions, as will be seen in chapter eight.

6-2.2 Grazing incidence X-ray reflectivity (GIXR) measurements

In order to gain an insight into the thickness and roughness of the electrodeposited ferromagnetic thin films, GIXR measurements were made using a *Bede (Jordan Valley) X-ray D1 reflectometer* [5-7]. The interpretation of the experimental results was carried out using *Bede REFS simulation software* as discussed in chapter five. All the simulations were performed by starting with the nominal structure of the as-deposited films, with the addition of an oxide layer or sub-layer with a thickness up to a few nanometres in order to improve the quality of the simulation fit to the data. This is quite reasonable since the measurements were performed on these films some time after their preparation (see chapter five for more details). Figure 6.3 show the true specular X-ray reflectivity measurements of electrodeposited NiFe and Ni films prepared at different growth times and the corresponding best-fit simulations obtained by recursively fitting the layer thickness, percentage element weight, roughness and density. An example of the parameters obtained from the best-fit simulations of NiFe films are provided in Tables 6.1.

From the curves shown in Figure 6.3 and the parameters given in Table 6.1, it can be concluded that the electrodeposited NiFe films are composed of layers with different elemental weight and density. These films are very rough and highly nonuniform with an average mean square roughness of about 4-5 nm. The roughness is believed to be due to the presence of voids and defects which occur during the fabrication process as a result of the existence of impurities, gas bubbles or the density of the electrolyte solution which may not have been homogenous throughout the electrochemical cell. This topographical nonuniformity has a pronounced effect on the magnetic behaviour as will be seen later in chapter eight.

The relation between electrodeposition growth time and the corresponding NiFe film thickness is shown in Figure 6.4. In general, there is an increase in the film thickness with increasing the growth time and there is a large variation and hence uncertainty in the film thickness across the area of the sample. Again, this confirms the nonuniformity of these films, which clearly increases greatly for shorter growth times.

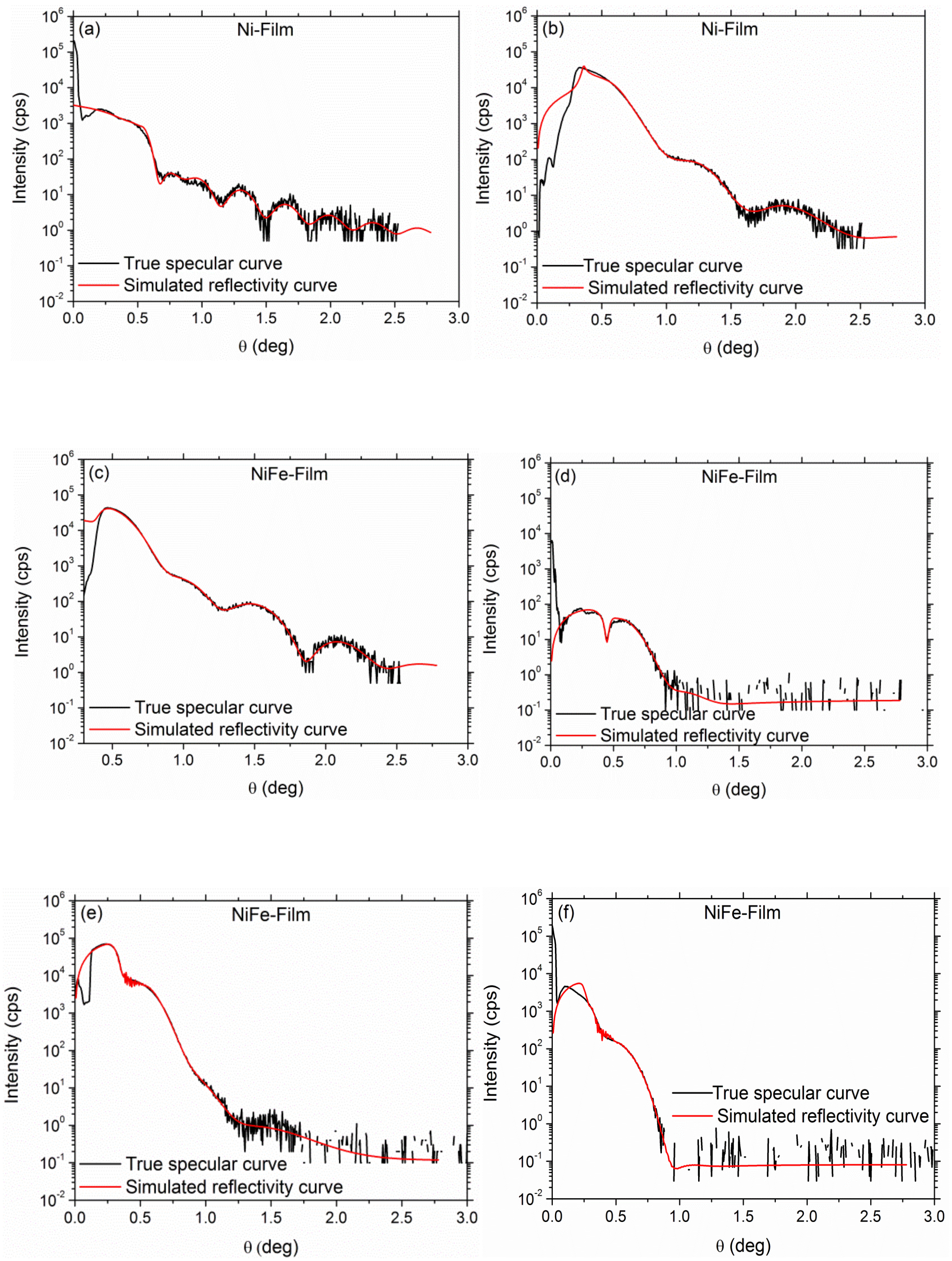

Figure 6.3 True specular X-ray reflectivity measurements of electrodeposited Ni and NiFe films (black curves) and the corresponding simulated reflectivity (red curves) obtained using Bede REFS simulation software for Ni films with different growth times (thicknesses) (a) 40 s, (b) 60 s, and (c-f) NiFe films with 10 s, 30 s, 60 s and 90 s, respectively.

Electro-deposition growth time (s)	**Total thickness (nm)**	**Layer**	**Layer thickness (nm)**	**Density (%)**	**Roughness (nm)**
10	25±199	Fe_2O_3	15± 187	20 ± 260	5 ± 129
		$Ni_{0.2}Fe_{0.8}$	9 ± 62	100 ± 128	5 ± 11
		$Ni_{0.6}Fe_{0.4}$	1 ± 27	31 ± 110	4 ± 23
		Au	5 ± 0.5	105 ± 44	0.6 ± 0.1
		Cr	2 ± 0.4	119 ± 98	1 ± 0.5
		SiO_2	∞	100	0.5 ± 0.4
30	25±40	Fe_2O_3	5 ± 37	120± 626	5 ± 20
		$Ni_{0.6}Fe_{0.4}$	20 ± 15	117 ± 37	4± 5
		Au	4 ± 10	130 ± 113	1 ± 2
		Cr	2 ± 7	140 ± 945	2 ± 7
		SiO_2	∞	100	1 ± 3
60	201±23	Fe_2O_3	3 ± 17	68 ± 483	2 ± 4
		$Ni_{0.41}Fe_{0.59}$	9 ± 11	60 ± 24	5 ± 5
		$Ni_{0.37}Fe_{0.63}$	189 ± 12	37 ± 7	3 ± 5
		Au	5 ± 3	87 ± 44	3 ± 2
		Cr	7 ± 1	81 ± 104	2 ± 1
		SiO_2	∞	100	1.5 ± 1
90	201±19	Fe_2O_3	2 ± 15	113 ± 412	4 ± 19
		$Ni_{0.7}Fe_{0.3}$	6 ± 8	90 ± 20	4 ± 3
		$Ni_{0.65}Fe_{0.35}$	193 ± 9	42 ± 4	5 ± 3
		Au	5 ± 0.9	99 ± 15	2 ± 0.4
		Cr	2 ± 0.4	98 ± 136	1 ± 0.4
		SiO_2	∞	99 ± 346	0.6 ± 0.2

Table 6.1 The best fit parameters obtained from REFS simulations software of electrodeposited NiFe thin films prepared under different growth times (different thicknesses).

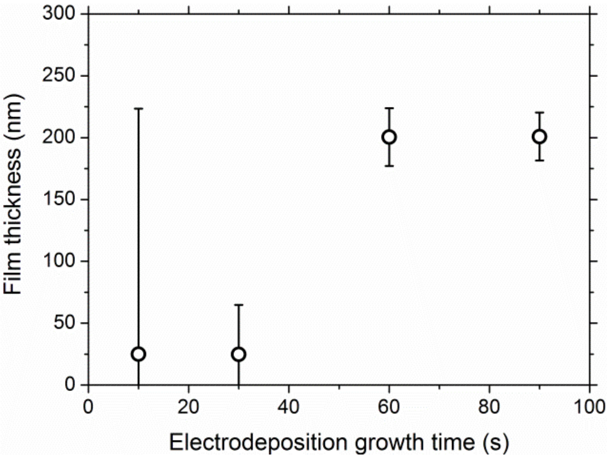

Figure 6.4 The relation between electrodeposition growth time and NiFe film thickness as measured using GIXR measurements and best fit REFS simulations.

6-3 Dimension distribution and morphology of electrodeposited nanowires

This section demonstrates the reasons behind studying the magnetic behaviour and electrical transport properties of isolated nanowires which are presented in chapter eight. Results obtained from measuring wall thickness of templates, the diameter and length distributions of electrodeposited ferromagnetic nanowires and the morphology of such nanowires after release and deposition on the substrates are discussed. These measurements were performed using *high resolution scanning electron microscopy analysis*.

6-3.1 Template interpore wall thickness distribution

Figure 6.5 show examples of scanning electron micrographs of alumina templates with nominal pore diameters of 300 nm and 200 nm and a polycarbonate template with nominal pore diameters of 50 nm. Some of the pores in the templates were not circular and the density of nanopores in the alumina templates was much higher than the pore density in polycarbonate templates. In both types of templates, different ordering of nanopores across the sample area was evident. The distribution of pores within the alumina membrane is more uniform than in the polycarbonate template. In order to measure and analyse the wall thickness among the pores, a detailed series of scanning electron microscopy imaging and measurements was performed.

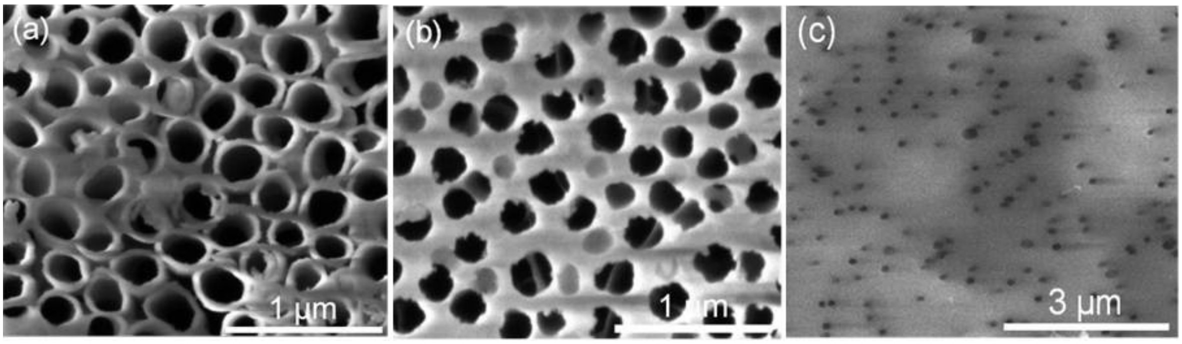

Figure 6.5 Scanning electron micrograph examples of top view of (a) alumina membrane with nominal pore diameter of 300 nm and spacing 50 nm, (b) alumina membrane with nominal pore diameter of 200 nm and spacing 150 nm, and (c) polycarbonate template with nominally 50 nm pore diameter.

For each sample more than five hundred interpore wall thicknesses were measured. As an example, Figure 6.6(a) shows the distribution of interpore wall thickness for alumina templates with nominal spacing of 150 nm. For comparison with other studies in literature, the interpore wall thickness of hexagonally ordered pores in alumina template with nominal wall thickness of 50 nm was measured and is plotted in Figure 6.6(b) [8]. The insets of Figure 6.6 show examples of scanning electron microscopy images of the area in which the measurements were performed.

Figure 6.6 shows the interpore wall thickness ranged from approximately 10 nm to 250 nm and 30 to 80 nm for templates with nominal wall thickness 150 nm and 50 nm, respectively. This variation in the spacing might be introduced during the fabrication process of the template itself [8,9]. Thus, the random variation in the interpore wall thickness even in well ordered templates will eventually cause the nanowires created in a such template to come closer to each other in some places. This might lead to a variation in the magnetostatic interactions among the wires and thus change the magnetic behaviour. Furthermore, the non-circularity of the pores and the variations of the interpore spacing will affect the magnetic properties and make the magnetic measurements of such arrays of wires not a true representation of uniform circular identical nanowires. Accordingly, this study

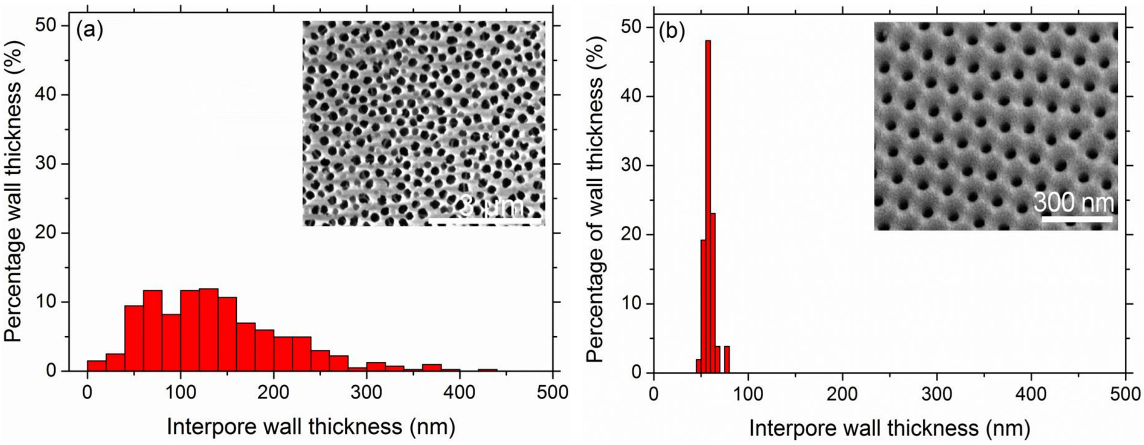

Figure 6.6 Statistical distribution of nearest neighbour interpore wall thickness in alumina templates with nominal interpore wall thickness of (a) 150 nm, and elsewhere (b) 50 nm [8]. The figure insets represent examples of the area in which the measurements were performed.

aims to investigate the intrinsic magnetic properties of isolated wires in order to overcome some of these variations observed with the nanowires embedded in their templates.

6-3.2 Diameter distributions of template nanopores and nanowires

Figure 6.7(a) shows the distribution of pore diameters measured at the surface of an alumina template (Whatman) with nominal pore diameters of 200 nm, whilst Figure 6.7(b) shows the distribution of diameters of template released NiFe nanowires grown in the same type of template. Both distributions are symmetrical about the peak and they are reasonably represented by a *Gaussian distribution*. The distribution of wire diameters is very similar to the template pore size distribution. Figure 6.7(c) and (d) shows the distribution of diameters for Ni nanowires grown in alumina template with pore diameters of ~50 nm and ~300 nm.

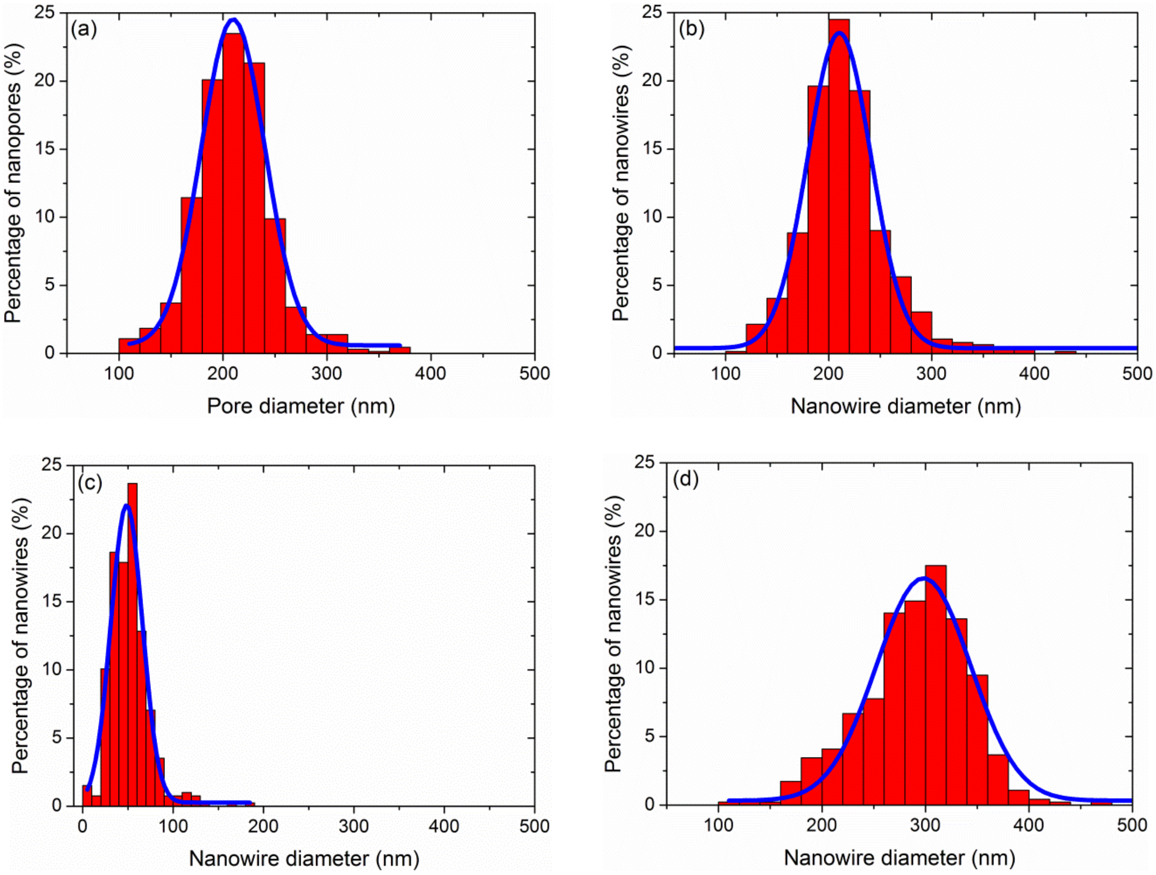

Figure 6.7 (a) Distribution of pore diameters in a nominally 200 nm pore alumina template, (b) distribution of diameters of released NiFe nanowires grown in nominally 200 nm pore template, and (c,d) distribution of diameters for Ni nanowires grown in a nominally 50 nm and 300 nm pore diameters. Gaussian curves have been fitted to the distributions.

In these cases the distribution are not *Gaussian* and not symmetrical about the peak but skewed to smaller or higher diameters. It is clear that the diameters of NiFe wires grown in templates with 200 nm nominal pores size range from ~125 to ~275 nm, whilst the diameter of Ni nanowires grown in templates with nominal pores diameter of 50 nm and 300 nm range from ~15 to ~75 nm and ~180 to ~400 nm, respectively. Again, this variation in the pore diameter may occur during the fabrication process of the template itself. Therefore, it is very difficult to fully describe the magnetisation behaviour of the nanowires by measuring templated arrays, which encompass such variations.

6-3.3 Morphology of template released ferromagnetic nanowires

The morphology of a range of template released ferromagnetic Ni and NiFe nanowires was investigated and interesting features were observed. Figure 6.8 shows examples of scanning electron micrographs of isolated Ni nanowires with a nominal diameter of 300 nm

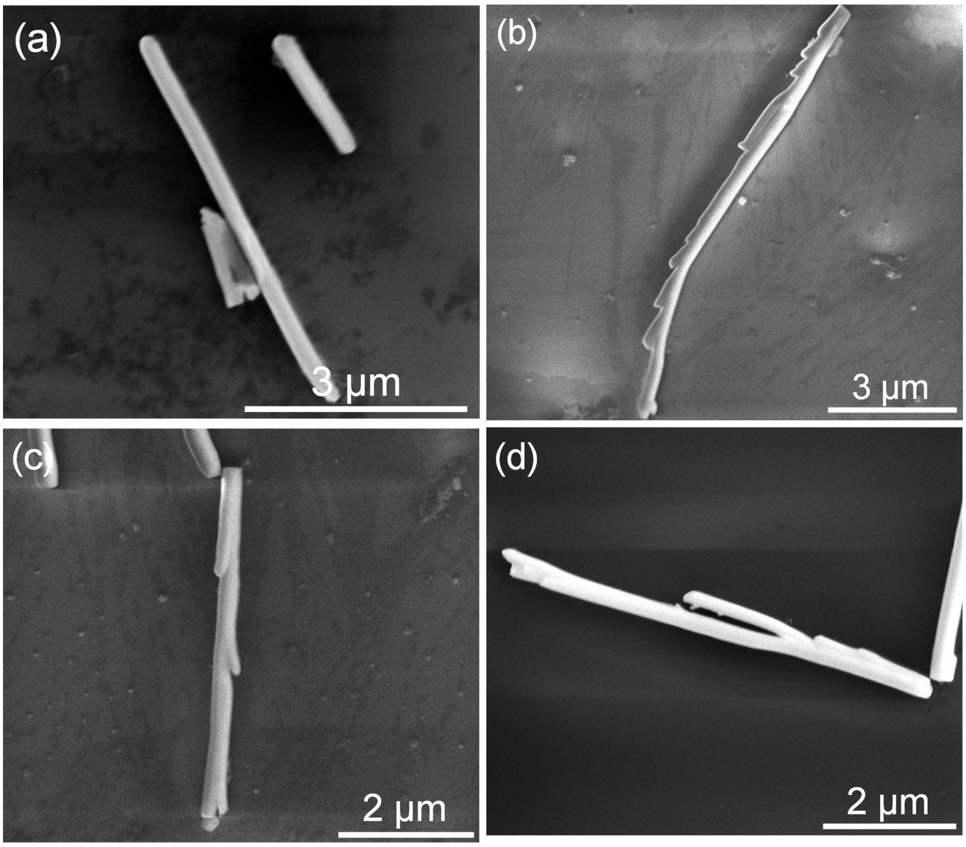

Figure 6.8 Scanning electron microscopy images showing examples of a range morphologies of Ni nanowires with nominal~300 nm diameter deposited from a dilute suspension after dissolving the alumina template.

deposited onto silicon substrates from a dilute suspension from the same type of alumina template mentioned in the previous section. Many of the wires are highly uniform as shown in Figure 6.8(a), however there are some wires which do not have constant diameters along the wire length (varying from ~240 to ~360 nm). This is in full agreement with other studies [10,11]. However, from the same template, some of the wires can be observed to be highly irregular with significant surface features. This include the appearance of protrusions, lobes, serrations and branches, examples of which are shown in Figure 6.8(b-d). This variation in the morphology most likely reflects the variations, defects or cracks that exist in the internal surfaces of the pores within the template itself [8,9], or in some cases may be associated with trapped air pockets or impurities within the pores during the nanowire growth as discussed in reference [8,10]. Significantly, the observed variation in the wire diameters and the existence of these structural variations and defects will lead to variable magnetic behaviour of the nanowires within two dimensional templates.

6-3.4 Formation of bundles of wires upon releasing process

Imaging of the released and deposited nanowires from a dilute suspension on the substrates revealed the presence of individual, small groups, clusters and chains of nanowires. In addition, bundles of nanowires were observed after sonication for a period of about 10 minutes. These bundles were found to consist of many wires of the same length that are aligned and tightly packed as shown in Figure 6.9(a). The uniformity of the alignment in these bundles suggests that they are beginning to form by electrostatic or magnetostatic forces between the wires during removal of the alumina template. Increasing the sonication time up to approximately 60 minutes did not significantly break-up these bundles, indicating the strong interactions between these wires. Longer sonication time did lead to some of the wires becoming bent or broken, rather than separating the wires, as shown in Figure 6.9(b-d).

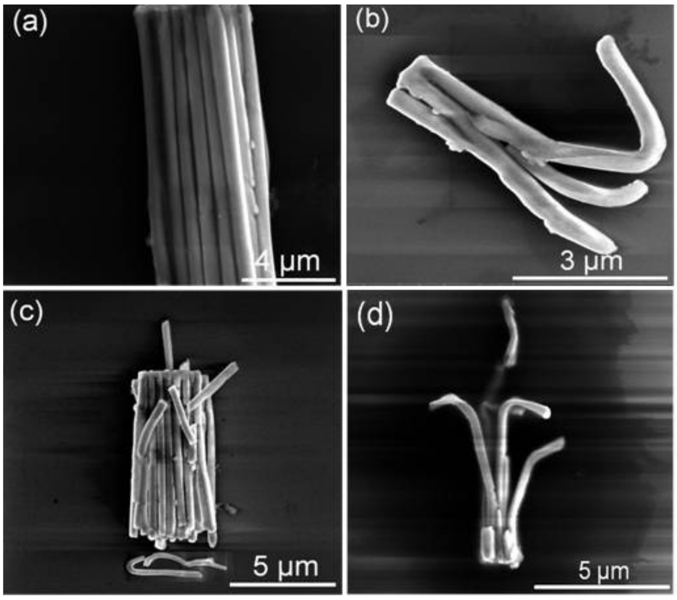

Figure 6.9 Examples of scanning electron micrographs showing (a) Ni nanowires stacked to form bundles as a result of the electrostatic or magnetostatic forces, (b), (c) and (d) bent and broken nanowires resulting from increasing the sonication time during the release from alumina template.

6-3.5 Length distribution of template released ferromagnetic nanowires

As mentioned in chapter four, the length of the as-grown nanowires was ~20 μm. This was controlled by selection of the current density and growth time. Results show that such growth creates nanowires with very similar lengths in the templates as demonstrated in Figure 6.10(a). However, it was found that the lengths of the released and deposited nanowires differed from the as-grown nanowires [8]. Figure 6.10(b) shows an example of the length distribution of NiFe nanowires deposited onto a silicon substrate after sonication of the suspension for about 10 minutes. The inset of Figure 6.10(b) is an example of an SEM image of measured wires. The nanowire lengths were found to range widely from about 500 nm up to about 20 μm, indicating that the sonication process used to separate the nanowires from their gold substrate causes the nanowires to break in different places and hence produce the wider distribution observed. This is supported by further tests involving an increased sonication of more than ~60 minutes for both NiFe and Ni nanowires, where the distribution broadens further and shifts to the shorter lengths as shown in Figure 6.11(a,b), respectively.

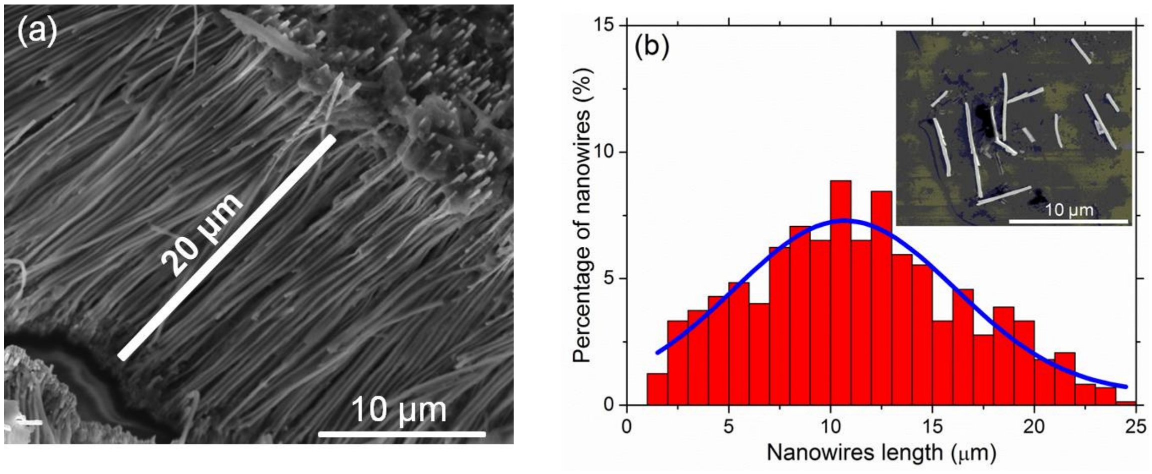

Figure 6.10 (a) NiFe nanowires attached to the gold substrate after removal of the alumina template, and (b) length distribution of the same nanowires after template release using ~10 minutes sonication time. The line is the best fit Gaussian distribution. The inset is an example of SEM imaging of the measured nanowires.

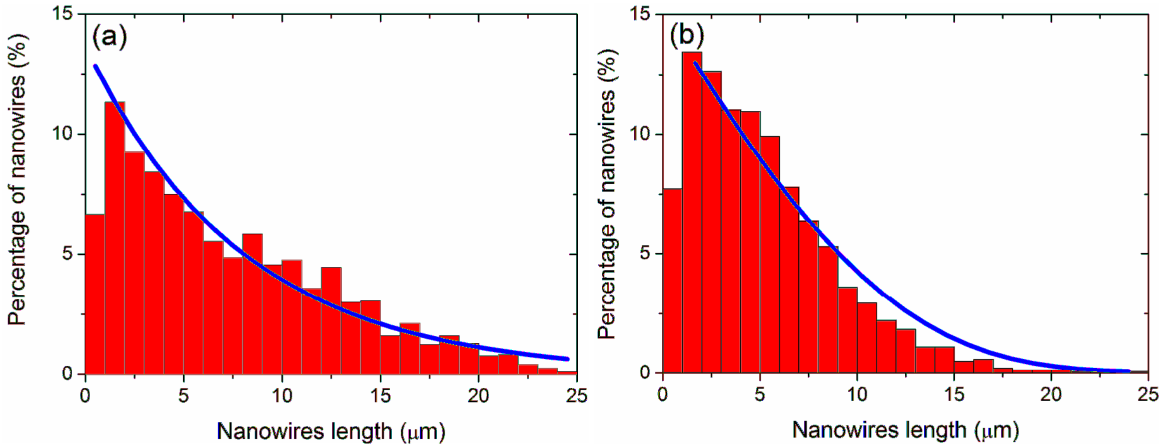

Figure 6.11 Distributions of (a) NiFe, and (b) Ni nanowire lengths as a result of increasing sonication time to 60 minutes. The lines represent the best fit exponential curves.

6-4 Crystalline structure of electrodeposited ferromagnetic nanowires

As it is well known that the crystalline structure of ferromagnetic materials and their crystallite sizes plays an important role on their magnetic behaviour, an understanding of these properties before starting with the magnetic and electrical measurements of such nanowires is extremely important. Therefore, the crystalline structure of the as-deposited and selected areas on individual Ni and NiFe nanowires are discussed in the following subsections using an *X-ray diffraction (XRD) patterns*, *high resolution transmission* *electron microscopy (HRTEM)* and incorporated *selected area electron diffraction (SAED)*, respectively.

6-4.1 Crystalline structure of templated ferromagnetic nanowires

The crystalline structure of as-grown electrodeposited Ni and NiFe nanowires were investigated using *X-ray diffraction analysis*. These measurements were performed by *B. Das* (SN Bose National Science Centre, Kolkata, India) using an *X-Pert-Pro* system [12]. The X-ray source of this machine was CuKα which has a wavelength of 0.15418 nm.

As expected [3,8,13], both compositions show FCC structures as demonstrated in Figure 6.12 which shows typical *XRD patterns* of Ni and NiFe nanowires embedded in their alumina templates and attached to the gold substrates. The measurements of Ni nanowires show peaks at $2\theta = 44.57^o$, 51.88^o, and 76.48^o which correspond to the FCC phase of Ni, and peaks at $2\theta = 38.21^o$, 44.48^o, 64.67^o, and 77.81^o which correspond to the FCC phase of the Au substrate, as compared with the standard reference patterns (Inorganic Crystal Structure Data base (ICSD)) [14]. On the other hand, the NiFe nanowires show peaks at $2\theta = 44.13^o$, 51.49^o, and 76.28^o which are related to the FCC phase of NiFe and a peak at $2\theta = 38.18^o$, corresponding to the FCC phase of the Au substrate. There are no peaks related to

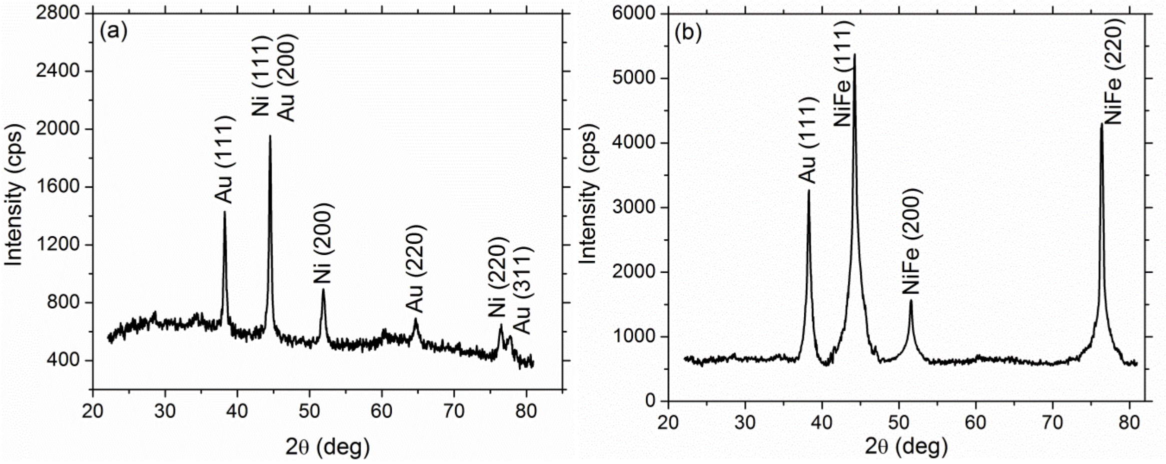

Figure 6.12 X-ray diffraction patterns of arrays of electrodeposited (a) Ni, and (b) NiFe nanowires embedded in alumina templates and attached to the gold substrates [12].

the alumina template in the patterns due to their amorphous structure which is in a full agreement with other research [15]. The peaks in the Ni nanowire pattern are narrower than the peaks in the NiFe nanowires indicating that the grains in the Ni nanowires are larger than the grains in the NiFe nanowires. To estimate the grain sizes, t, within these wires, the *Scherrer equation* was utilised [16,17]. The *Scherrer equation* is given by [17]:

$$t = \frac{0.9\lambda}{\Delta(2\theta)\, cos\, \theta_B} \qquad \text{6-1}$$

where, λ is the wavelength of the X-ray beam, θ_B, is the *Bragg angle*, $\Delta(2\theta)$ is the angular width at half the maximum intensity (in radian) and 0.9 is the correction factor. Thus, the grain size is found to be approximately 30 nm and 15 nm for Ni and NiFe nanowires, respectively. This is in excellent agreement with the results reported by other researchers [13]. The intensity of the diffracted peaks is related to the sample thickness or the presence of a *preferred crystallite orientation* (or *texture*). Texture is defined as the probability of certain crystallographic lattice planes to orient along the measured direction more than others. The measured intensity ratio of the peaks indicates that these nanowires have no preferred orientation along any direction.

6-4.2 Crystalline structure of individual ferromagnetic nanowires

HRTEM and *SAED* were used to investigate the crystalline structure and estimate the average grain sizes of individual electrodeposited ferromagnetic nanowires. This was performed with the guidance of *B. Mendis* (Electron Microscopy Facility, Physics Department, Durham University, U.K.) using a *JEOL 2100F TEM* system [18]. An IPA suspension of template released Ni and NiFe nanowires were deposited onto *holey carbon TEM grids*, as shown in Figure 6.13(a) where each cell in the grid has an approximate area of 60 µm × 60 µm as measured by SEM. The dried samples were then placed in the TEM. Images of one grid before and after NiFe nanowire deposition are shown in Figure 6.13(b,c).

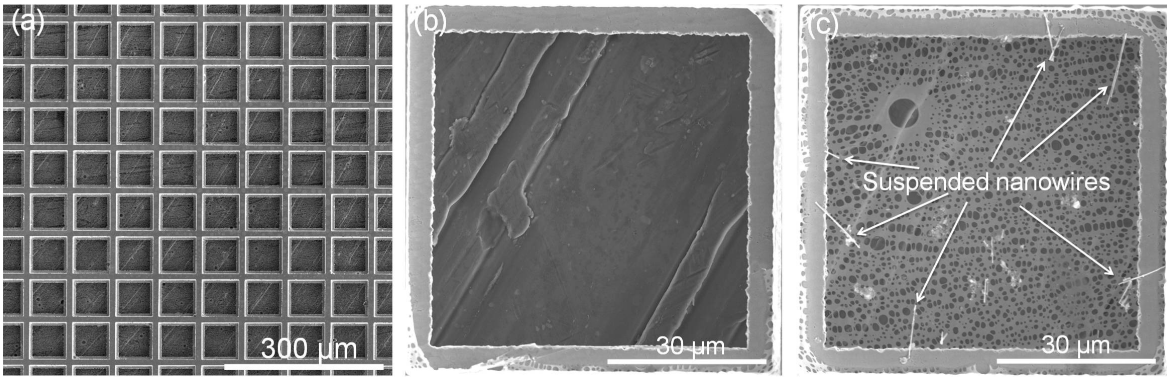

Figure 6.13 (a) Scanning electron micrographs of holey carbon grids used for characterising the crystal structure of individual electrodeposited Ni and NiFe nanowires, and (b,c) higher magnification images before and after NiFe nanowire deposition, respectively.

In the transmission electron microscope a beam of electrons are accelerated by ~200 kV from a cold field emission source and transmitted through a selected area of the nanowire to obtain high resolution images and electron diffraction patterns. For further information about HRTEM see for example Ref [19,20]. Figure 6.14 show examples of the electron diffraction patterns obtained from single Ni and NiFe nanowires with nominal diameter of 300 and 200 nm, respectively. Note that the scale bars in these images are in reciprocal space units.

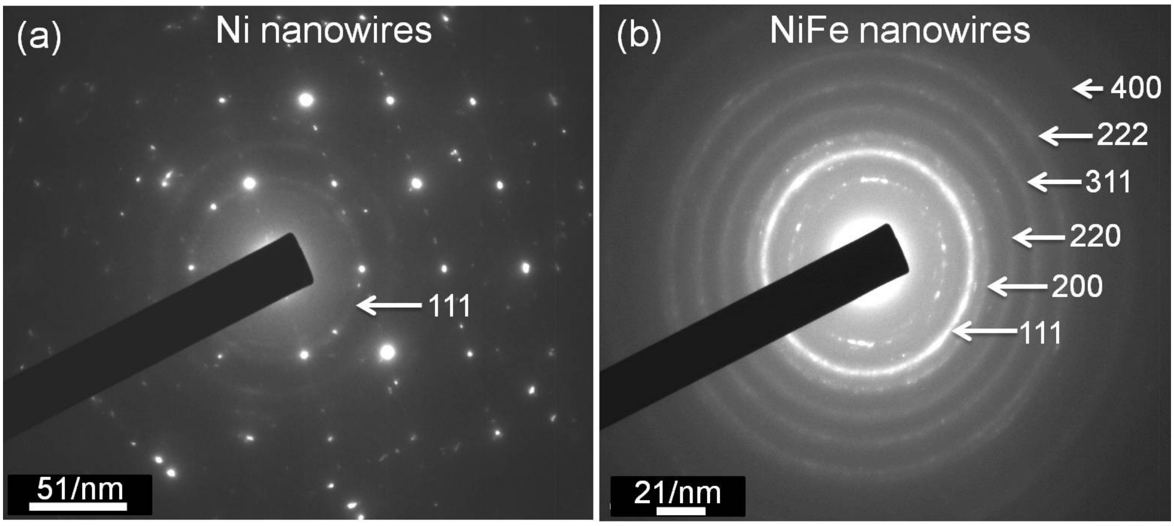

Figure 6.14 Selected area electron diffraction patterns on individual (a) ~300 nm diameter Ni, and (b) ~200 nm diameter NiFe nanowires [18]. The scale bar is in reciprocal space units. The diffraction planes are identified in the figures.

A weak continuous circular ring together with spot patterns appeared from Ni nanowires, whilst only continuous rings pattern appeared from NiFe nanowires. The appearance of these rings in the patterns indicates the diffraction of the electrons from favourably oriented crystallites, and hence the structure is polycrystalline. The regular spot patterns appearing in the Ni diffraction patterns suggest the existence of large grains which behave as a single crystalline structure. To identify the diffraction planes the following equation was used [19,20]:

$$d_{hkl} = \frac{\lambda l}{R} \qquad 6\text{-}2$$

Where, d_{hkl} is the plane spacing, *hkl* are the *Miller indices*, λ is the electron beam wavelength, *L* is the microscope camera length and *R* is the radius of the diffraction rings.

The assignment of the diffraction ring for Ni nanowires is (111), whilst for NiFe nanowires they are (111), (200), (220), (311), (222), and (400) planes, as shown in Figure 6.14.

To identify the grain sizes within Ni and NiFe wires, high resolution dark and bright field images were measured for different nanowires and at different locations on the same nanowire. As an example, Figure 6.15 shows dark field images of Ni and NiFe nanowires at two different locations. The bright features in these images correspond to strongly diffracting grains. Evident from Figure 6.15 are grains distributed in the Ni and NiFe nanowires with average sizes around 27 nm and 12 nm, respectively. These results are in a full agreement with the results obtained from X-ray diffraction analysis. Additionally, large crystallites distributed randomly in Ni nanowires were found with an approximate length extended up to about 200 nm.

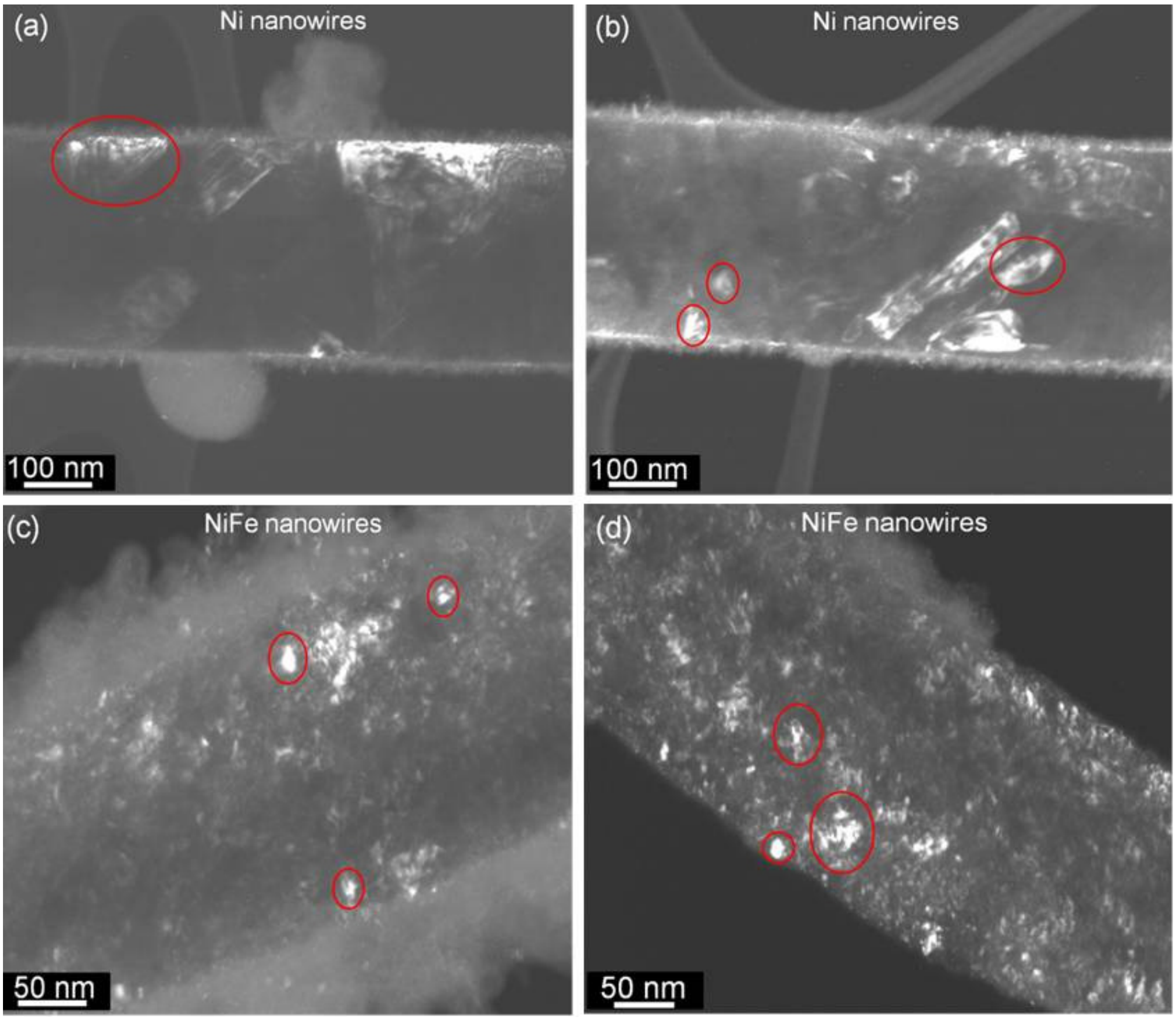

Figure 6.15 Dark field images obtained using high resolution transmission electron microscopy of (a,b) 300 nm diameter Ni nanowires, and (c,d) 200 nm diameter NiFe nanowires [18]. The bright features correspond to favourably orientated grains that are strongly diffracting.

6-5 Chapter conclusions

The chemical composition, thickness and roughness of a range of electrodeposited ferromagnetic thin films were investigated using both *energy & wavelength dispersive X-ray* analysis and *grazing incidence X-ray reflectivity* measurements, respectively. These studies were mainly carried out to confirm the formation of ferromagnetic films on the substrates and to ascertain their purity, as well as to measure their roughness and thickness. The results demonstrate that, these films were free from contamination and there was about 20% shift in the Ni and Fe contents in all the electrodeposited NiFe films with respect to the nominal composition. A slight variation in the elemental composition across the area of measured films was also noticed. A limited variation in the elemental weight with growth time was also observed. These variations were attributed to the variation in the concentration of Fe ions in the electrolyte.

The surface topography of electrodeposited thin films was studied using GIXR measurements and found to be nonuniform and very rough. The roughness was attributed to the presence of voids and defects which might occur during the fabrication process as a result of impurities, gas bubbles or the variation in the electrolyte density. The relation between electrodeposition growth time and film thickness was also investigated. There was a large variation and uncertainty in the film thickness across the area of the samples which again indicated the nonuniformity of these films.

The main reasons for the need to study the magnetic and electrical transport properties of isolated nanowires presented in chapter eight were demonstrated by analysis of the distribution of interpore wall thickness of the alumina templates and the dimensions and the morphology of template released ferromagnetic nanowires. A wide distribution was found in the wall thickness, with non-uniformity in their pore cross-section, wire diameter, and nanowires surface features being attributed to the template itself. These variations will lead to a variation in the magnetostatic interactions among the arrays of templated wires, thus making the understanding of intrinsic wire magnetic properties difficult to obtain. On the other hand, grouping, clusters and bundles of nanowires were noticed when the templates dissolved and the nanowires were released and deposited on the substrates. The formation of these bundles was attributed to the effect of electrostatic or magnetostatic forces among these wires. Increasing the sonication time up to approximately 60 minutes did not separate these bundles, but produced bent or broken nanowires with shorter lengths.

Finally, in order to understand the crystal structure and the grain size of the electrodeposited Ni and NiFe nanowires, the crystalline structures of nanowires embedded in their templates and analysis of selected areas on single nanowires were investigated using XRD and high resolution transmission electron microscopy measurements, respectively. The results demonstrate that these wires have a FCC structure and both Ni and NiFe nanowires have small grains with an average size of approximately 30 and 15 nm, respectively. Moreover, the HRTEM measurements on Ni nanowires reveal the existence of some large grains with lengths extended up to about 200 nm together with small grains.

6-6 Chapter references

1. Bowen L. in private communication, 2011.
2. Das, B., Mandal K., Sen, P. & Bandopadhyay, K. "Effect of aspect ratio on the magnetic properties of nickel nanowires" *J. Appl. Phys.*, 103, 013908, 2008.
3. Rheem,Y., Yoo B.-Y, Koo, B. K. & Beyermann, W. P. "Synthesis and magnetotransport studies of single nickel-rich NiFe nanowire" *J. Phys. D: Appl. Phys.,*40, 7267, 2007.
4. Rheem, Y., Yoo B.-Y, Beyermann W. P. & Myung, N. V. "Electro- and magneto-transport properties of a single CoNi nanowire" *Nanotech.*, 18, 1, 2007.
5. Jordan Valley "D1 Installation, operation and maintains manual" Jordan Valley Semiconductors Ltd., 2008.
6. Jordan Valley "Bede X-ray applications manual" Jordan Valley Semiconductors Ltd., 2008.
7. Bede REFS (version 4.5): User Manual, Bede PLC, Durham, available from Jordan Valley PLC, 2007.
8. Jin, C. G., Liu, W. F., Jia C., Xiang, X. Q., Cai, W. L., Yao, L. Z. & Li, X. G. "High filling large area Ni nanowires arrays and the magnetic properties" *J. Crystal Growth*, 258, 337, 2003.
9. Meier J., Doudin B. & Ansermet J. Ph. "Magnetic properties of nanosized wires" *J. Appl. Phys.*, 79, 6010, 1996.
10. Daub, M., Enculescu, I., Neumann, R. & Spohr, R. "Ni nanowires electrodeposited in single ion" *J. Optoelectronics & Advanced Materials*, 7(2), 865, 2005.
11. Rahman, I. Z., Razeeb, K. M., Kamruzzaman, Md., Serantoni, M. "Characterisation of electrodeposited Ni nanowires using NCA template" *J. Mats. Proc. Tech.*, 153-154, 811, 2004.
12. Das B. in private communication, 2012.
13. Rheem, Y., Yoo B.-Y., Beyermann, W. P. & Myung, N. V. "Magneto-transport studies of single ferromagnetic nanowire" *Physica Status Solidi (a),* 204(12), 4004, 2007.
14. "http://webelements.com/silicon/crystal_structure.html", accessed 17th March 2013.
15. Jian Qin, Josep Nogues, Maria Mikhaylova, Anna Roig, Juan S. Munoz, & Mamoun Muhammed "Differences in the magnetic properties of Co, Fe, and Ni 250-300 nm wide nanowires electrodeposited in amorphous anodised alumina templates" *Chem. Mater.*, 17, 1829, 2005.
16. Cullity, B. D. & Stock, S. R. "Elements of X-Ray Diffraction" 3rd edition, Prentice-Hall Inc., USA, 2001.
17. Bowen, K. D. &Tanner, B. K. "X-ray metrology in semiconductor manufacturing"

Taylor & Francis Group, LLC, USA, 2006.

18. Mendis B. in private communication, 2012.
19. Horiuchi, S. "Fundamentals of high-resolution transmission electron microscopy" Elsevier Science B. V. North Holand, 1994.
20. Ludwig, Reimer "Transmission electron microscopy: Physics of image formation and microanalysis" Springer-Verlag Berlin Heidelberg, 1984.

Chapter seven
Results: Magnetic field alignment of template released ferromagnetic nanowires

7-1 Introduction

For scientific study and for potential applications of template released nanowires, the manipulation and alignment of these structures is a significant and demanding issue in different fields. Therefore, the goal of the work presented in this chapter was to quantitatively investigate the details of magnetic field alignment for a range of ferromagnetic nanowires using an electromagnet. Specifically, this work investigates the deposition alignment of nanowires from suspension when deposited onto substrates as a function of the strength of the magnetic field, the effect of the composition and the effect of the aspect ratio of the nanowires upon the alignment process. This chapter also reports some further observations resulting from the magnetic alignment experiments and discusses the potential applications of the ferromagnetic nanowires aligned by magnetic fields.

7-2 Calibration of electromagnetic setup

The electromagnet system used to investigate the alignment process of template released NiFe, Ni and Co nanowires is shown in Figure 7.1. Due to the importance of the uniformity of the magnetic field across the sample area on the alignment process, the sample stage was divided into different positions, namely the centre and the edges of the sample holder, as demonstrated in the schematic diagram shown in Figure 7.1. Then, field was calibrated by measuring the magnetic field strength at these locations using a gaussmeter. The results of this study are shown in Figure 7.2(a). The maximum field obtained was approximately 1 kOe. A slight variation in the field strength across the sample stage was observed, especially at high magnetic field strength. To understand this variation, the distribution of magnetic field strength across the sample stage was obtained at different currents and at different positions, as shown Figure 7.2(b).

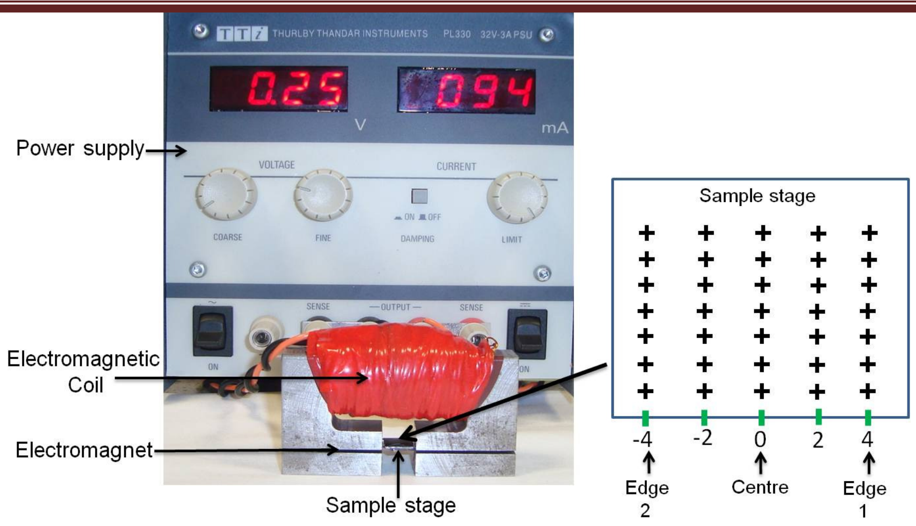

Figure 7.1 Electromagnet setup used to investigate the magnetic alignment of nanowires showing a schematic representation of the sample stage and the different locations where the magnetic measurements were performed.

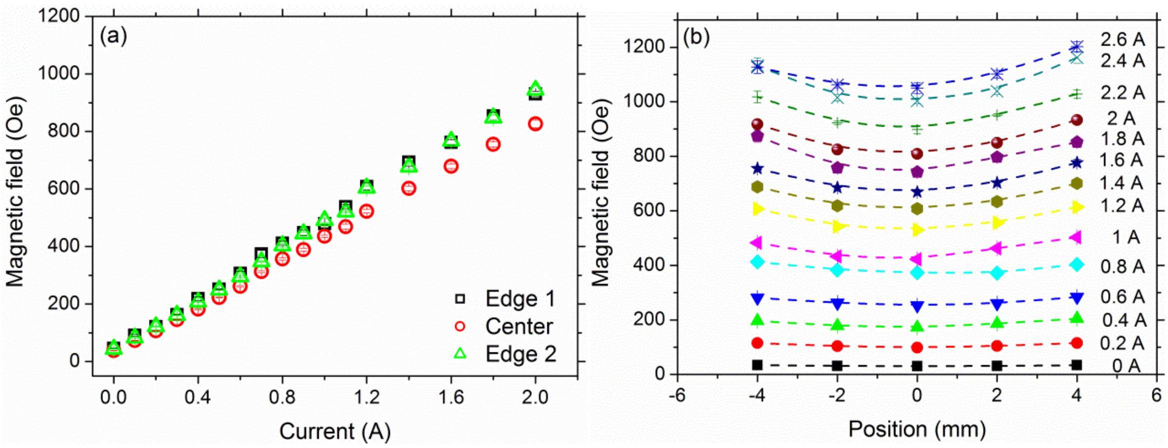

Figure 7.2 (a) The relationship between current and magnetic field strength at three locations on the sample holder, and (b) magnetic field strength as a function of position across the deposition area for different currents. The dashed lines provide a guide to the eye.

The results of this study show that there is an 8% variation in the uniformity of the magnetic field across the area of the nanowire deposition, which is small and it is considered negligible in this context.

7-3 Alignment analysis of nanowires

In order to assess and analyse the efficacy of the magnetic alignment process, a detailed series of scanning electron microscopy images were made on a number of samples prepared under different field strengths and with different nanowire compositions. Imaging and analysis was performed using a high-resolution field emission scanning electron microscopy column on a FEI-Helios Nanolab dual beam FIB/SEM system with an electron beam energy of 10 keV and current of 17 nA. Typically, for each sample, more than five hundred individual nanowires were studied to determine their angular orientation with respect to the alignment field axis.

7-4 Effect of magnetic field strength on the alignment of nanowires

The influence of the magnetic field upon the alignment of NiFe nanowires is demonstrated in the scanning electron micrographs shown in Figure 7.3. In the absence of an applied field, the wires are randomly oriented as in Figure 7.3(a). The random orientation of these wires can be attributed to various mechanical forces within the droplet of the suspension including *fluid drag force* and *Brownian motion*, as well as the *weight* of the nanowires and *buoyancy* forces [1]. For deposition in a moderate strength field, the nanowires show modest alignment as demonstrated in Figure 7.3(b), while a strongly aligned assemblage of nanowires occurs at the highest field investigated here (1 kOe), Figure 7.3(c). In order to quantitatively investigate the effect of magnetic field strength on the alignment process a detailed statistical analysis was undertaken to determine the orientation angles of NiFe, Ni, and Co nanowires deposited as a function of magnetic field for field strengths up to ~1 kOe.

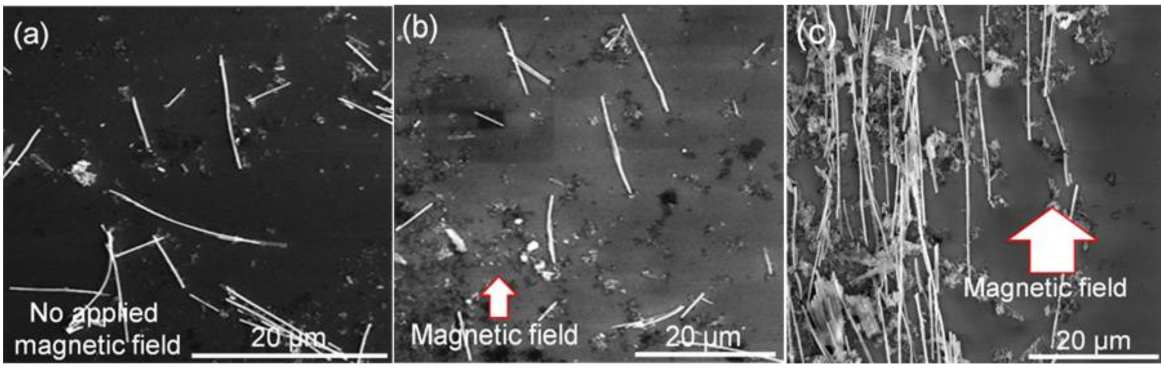

Figure 7.3 Examples of scanning electron micrographs of deposited NiFe nanowires under (a) no applied magnetic field, (b) moderate and (c) high magnetic field applied during deposition process.

Figure 7.4 shows the angular distribution histograms for assemblages of NiFe nanowires deposited at a range of magnetic field strengths. These wires have a nominal diameter of ~200 nm and a broad distribution of lengths centred around ~10 μm as investigated in chapter six. In the absence of an applied magnetic field no preferential alignment of the assemblage is observed (see Figure 7.4(a)). With increasing magnetic field up to ~200 Oe,

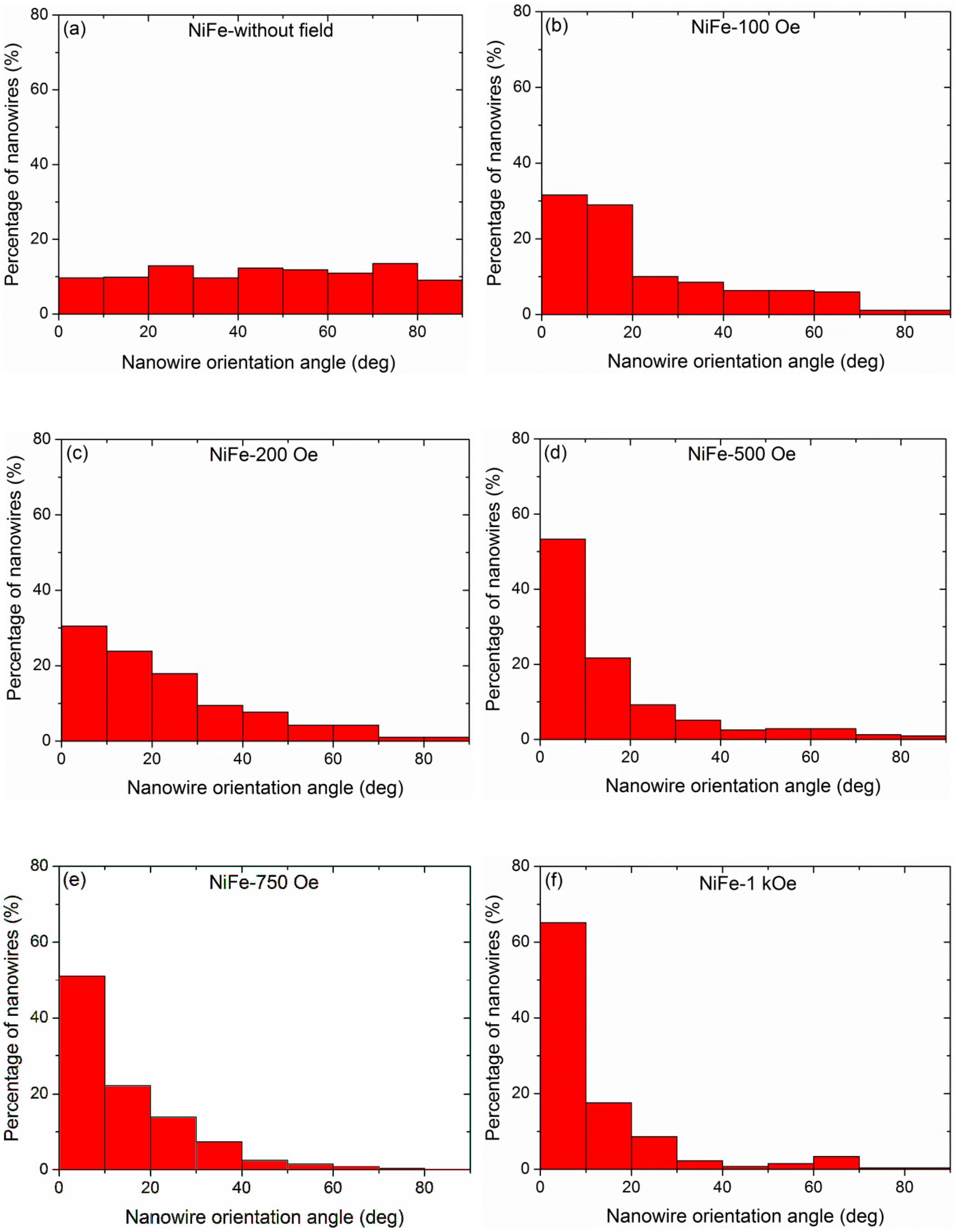

Figure 7.4 Angular distribution histograms for assemblages of ~200 nm diameter NiFe nanowires deposited at different field strengths (0-1 kOe) as indicated in the figure titles.

the distribution of nanowire orientation develops with respect to the field axis (Figure 7.4(b-c)), indicating the effect of the field. At higher fields, ~500, ~750 and ~1000 Oe, the peak in the alignment distribution develops further, as shown in Figure 7.4(d-f).

The angular distribution of nanowire orientation for field-aligned assemblages is not *Gaussian*, but it is characterised by a large number of nanowires oriented very close to the applied field axis surrounded by a distribution of nanowires over a wider range of angles. The wider distribution in the histograms may be attributed to the variation in the morphology and dimensions of these wires as investigated in the previous chapter or/and the variety of mechanical forces that can affect the alignment of the nanowires. The alignment process is also affected by the *resistive drag* of the suspension solvent, which is likely to influence the timescale of the alignment process that can be of the order of milliseconds. A further effect that may warrant consideration in the process is *thermal agitation* of the suspended nanowires; this will act to misalign the nanowires. In the situation where the suspension solution is evaporated to leave the nanowires deposited on a substrate, the interaction of the nanowires with the evaporating solvent and the substrate may further complicated the alignment process and this would be difficult to analyse. The field alignment behaviour for NiFe nanowires is summarised in Figure 7.5, which shows the proportion of nanowires aligned at angles between 0º-10º and 0º-20º of the applied field axis as a function of magnetic field.

It is clear that the percentage of NiFe nanowires aligned by the field increases rapidly up to ~200 Oe, then increases more slowly up to the maximum field, when ~64 % of the nanowires are aligned within 0º-10º and a total of ~82 % of the nanowires are aligned within 0º- 20º of the applied field axis. The high field dependence of the alignment suggests an approach to a maximum alignment with field, indicating that some further improvement in the proportion of aligned nanowires may be possible with magnetic fields greater than 1 kOe.

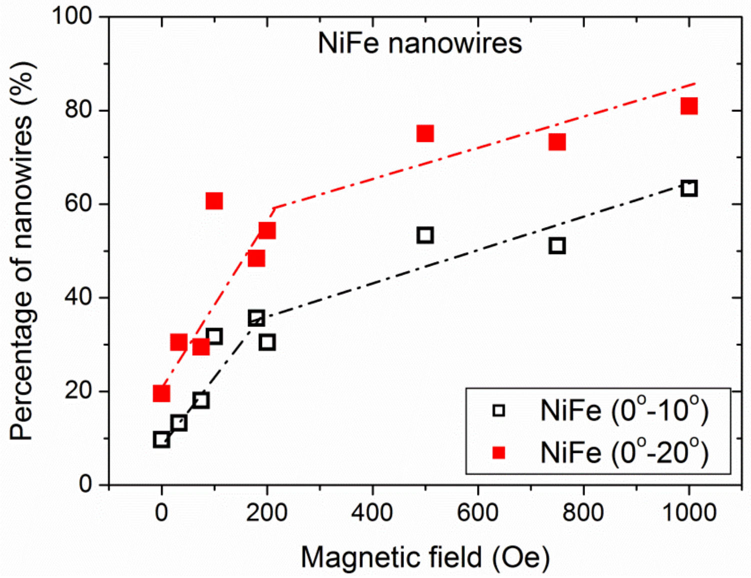

Figure 7.5 Proportion of NiFe nanowires aligned at angles within 10º and 20º of the field axis as a function of the magnetic field strength applied during the deposition process. The dashed lines provide a guide to the eye.

Figure 7.6 shows a comparison of the angular distribution histograms for assemblages of Co and Ni nanowires deposited on the substrates at different field strengths. These two compositions have nominal diameters of ~300 nm and a range of lengths centred around ~10 µm as discussed in chapter six. For all field strengths investigated here, the percentage of aligned Ni wires is higher than for Co wires. Furthermore, the Ni wires show the emergence of clear alignment at a relatively low field of ~100 Oe compared to the Co nanowires where similar alignment was not observed until the field was greater than ~180 Oe. The field dependence of the alignment behaviour for both Co and Ni nanowires are summarised in Figure 7.7(a-b), respectively, which shows the proportion of nanowires aligned at angles within 10º and 20º of the applied field axis. In general, the percentage of Ni nanowires aligned with the field increases rapidly with applied magnetic field up to ~200 Oe, then the percentage of aligned wires increases more slowly as the magnetic field increases up to the maximum field, where ~59 % of the wires are aligned within 10º and a total of ~71 % are aligned within 20º of the field axis. The high field dependence of the alignment (see Figure 7.7(b)) indicates an approximately linear increase in the proportion of nanowires aligned as a function of magnetic field. Again, this suggests further improvements in the proportion of aligned Ni nanowires are possible with magnetic fields greater than 1 kOe. In contrast, the assemblages of Co nanowires shows significant alignment at low fields, but the proportion of aligned nanowires at higher field strengths

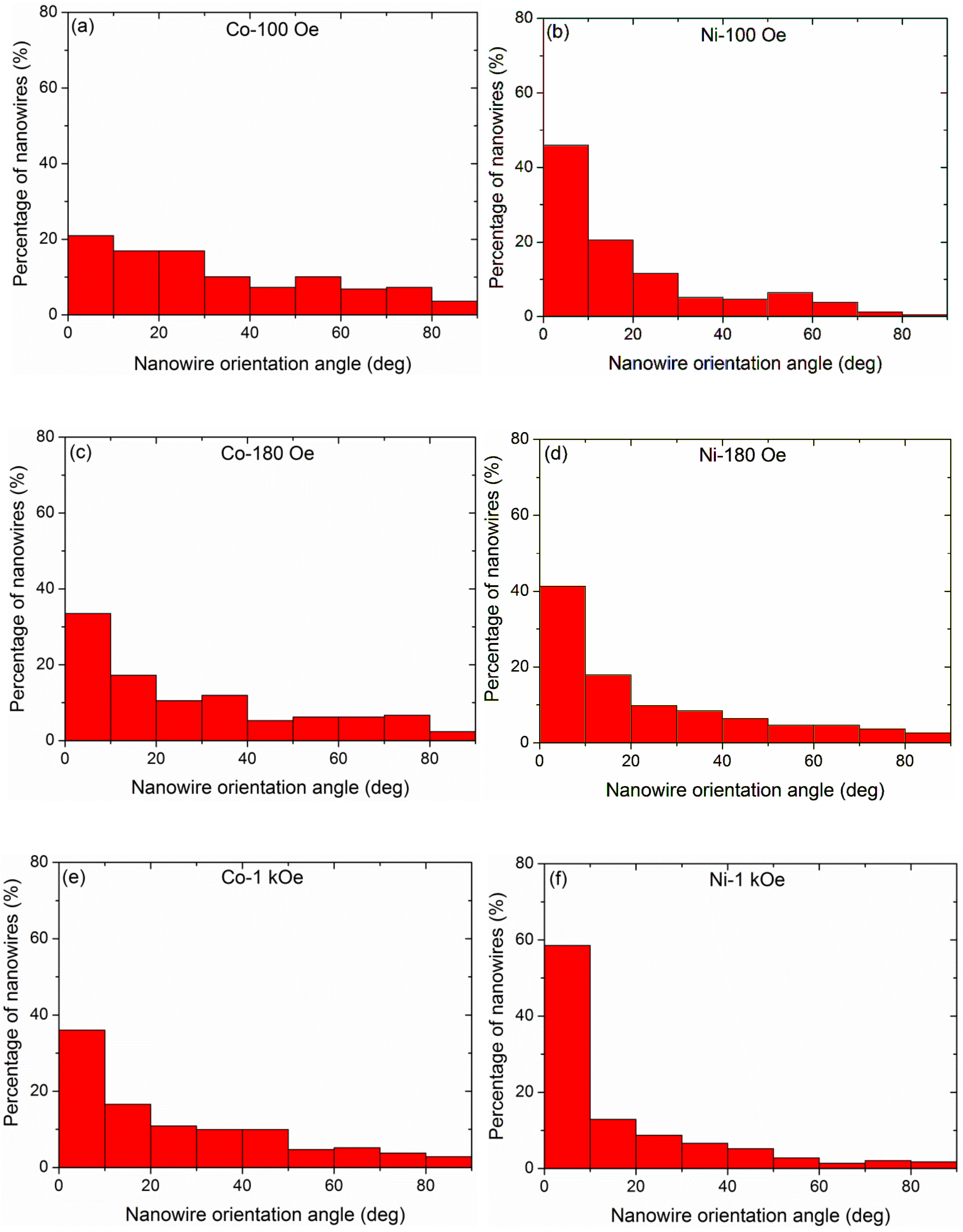

Figure 7.6 Comparison of angular distribution histograms for assemblages of ~300 nm Co and Ni nanowires deposited at the field strengths indicated.

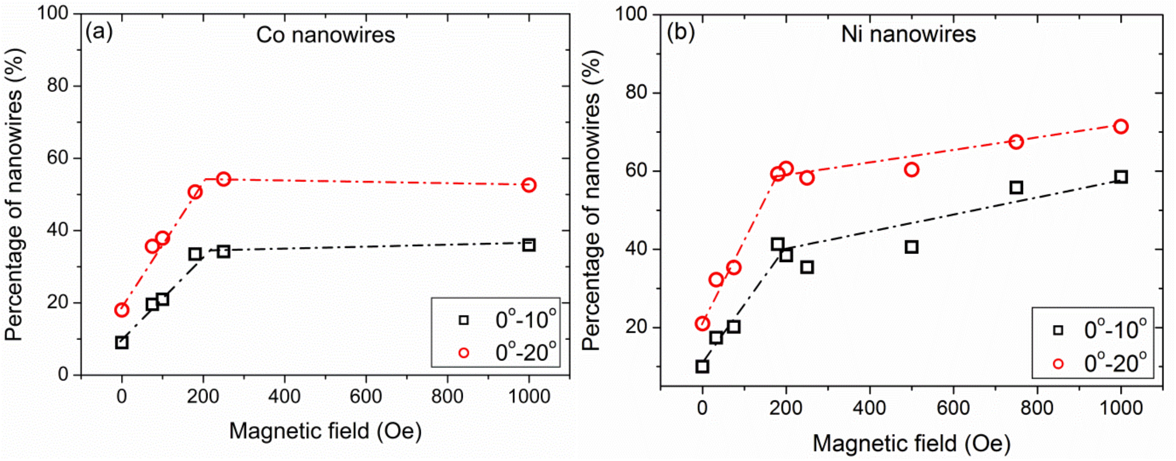

Figure 7.7 Proportion of (a) Co, and (b) Ni nanowires oriented at angles between 0º-10º and 0º-20º of the field axis as a function of the magnetic field strength applied during deposition process. The dashed lines are used as a guide to the eye.

seems to saturate when the fractional alignment is ~36 % aligned within 10º and a total of ~53 % of wires are aligned within 20º of the applied field axis.

7-5 Effect of nanowire composition on the alignment

The previous results show that the nanowires are strongly influenced by the magnetic field. As introduced earlier in chapter three, the magnetic torque due to the applied magnetic field is proportional to the effective magnetic moment, which depends upon the saturation magnetisation, the domain state and the dimensions of the nanowires. Thus, this dependence presents the opportunity to investigate the effects of the nanowire composition upon the alignment process.

Figure 7.8(a) shows the proportion of nanowires aligned within 0º-20º of the applied field axis for Ni, NiFe and Co nanowires. Since the nominal saturation magnetisation values of these wire compositions are: 485, 860 and 1440 emu/cm^3, respectively (assuming that Co is not oxidised) [2], it is not unreasonable to expect increasing efficacy of field alignment from Ni through NiFe to Co. This trend is observed for the Ni and NiFe, but in contrast, the Co shows the poorest field alignment, as shown in Figure 7.8(b).

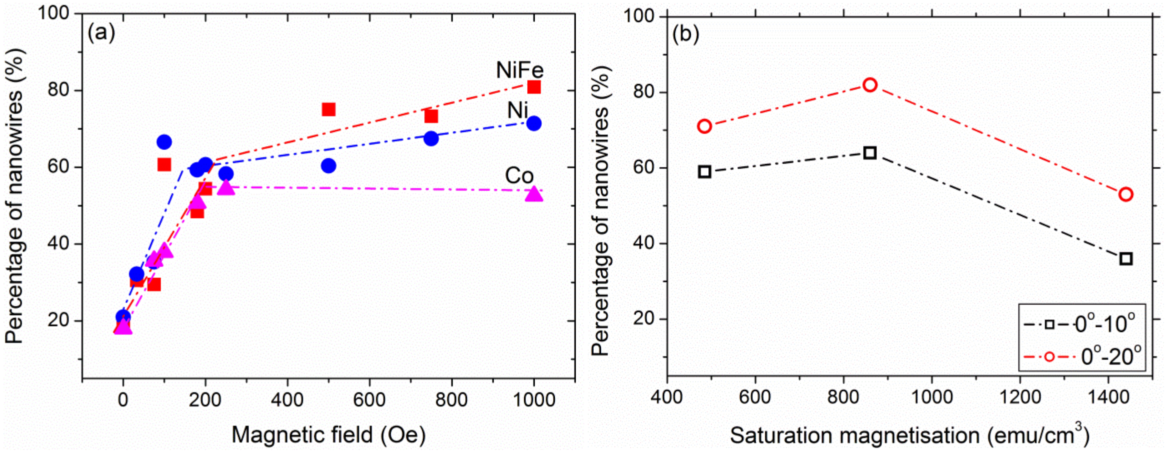

Figure 7.8 Proportion of Ni, NiFe and Co nanowires oriented with (a) 20º of the alignment field as a function of the magnetic field strength applied during the deposition process, and (b) 10º and 20º of alignment field as a function of the saturation magnetisation. The dashed lines are used as a guide to the eye.

The effect of saturation magnetisation upon the field alignment for NiFe nanowires may be complicated by the fact that these wires have a smaller diameter than the Ni and Co nanowires, although the relatively long length of the wires should minimise any differences in the demagnetizing factors. Nonetheless, comparing Ni and Co nanowires, which have nominally identical geometries, the results show that the percentage of aligned Ni wires is higher than Co nanowires in all field strengths investigated (e.g. see Figure 7.6) and also that the proportion of Co nanowires aligned does not increase greatly above ~200 Oe (see Figure 7.7(a)).

To explain the compositional variation of the magnetic field alignment, both the magnetostatic shape anisotropy and the magnetocrystalline anisotropy have been considered here. In the case of NiFe nanowires, the intrinsic magnetocrystalline anisotropy is vanishingly small and the magnetization orientation will be controlled by the magnetostatic shape anisotropy along the wire long axis. The situation is likely to be similar for nickel as the intrinsic magnetocrystalline anisotropy is relatively low, so the magnetisation will also be aligned along the wire long axis. For nanowires with these compositions, the alignment torque is therefore largely dependent upon the magnetic moment, which is larger for the NiFe than for the Ni nanowires. In contrast to both NiFe and Ni nanowires, where the crystal structure is FCC, the crystal structure of Co nanowires is more complex and depends upon the deposition conditions and the wire diameter, and can be FCC or HCP [3-7] or some combination of the two phases. In both cases the magnetocrystalline anisotropy is relatively large and may dominate the shape anisotropy. Indeed, HCP Co nanowires have been shown to have a component of magnetisation perpendicular to the wire axis [5,8,9]. Therefore, it is suggested that the magnetic field alignment of the Co is lower than for the NiFe and the Ni nanowires, because the dipole moment of the Co nanowires is not strongly developed along the wire axis, hence the torque arising from the magnetic field is reduced. There is also the possibility of the differential formation of oxide or hydroxide layers on the surface of these nanowires during and after removal the alumina template that may adversely affect the magnetisation of the Co nanowires. Thus, the magnetic field alignment is dependent upon the nanowire composition, but the dependence can be complex.

7-6 Effect of nanowire length on the alignment

The fluid drag for a mid-point rotating nanowire has been approximated using a prolate spheroid approximation by Lee et. al. [10], which showed a very strong dependence upon the length of the structure and the viscosity of the suspension fluid. This dependence presents the opportunity to study the effects of the nanowire aspect ratio upon the alignment process. Therefore, a systematic study was performed to examine the effect of length on the alignment process in a magnetic field for the Ni and NiFe nanowires. Figure 7.9 shows comparative histograms of the angular distribution for magnetic field deposited assemblages of NiFe nanowires with the wires divided into two length groups; one with wires less than 5 μm and the other with greater than 5 μm.

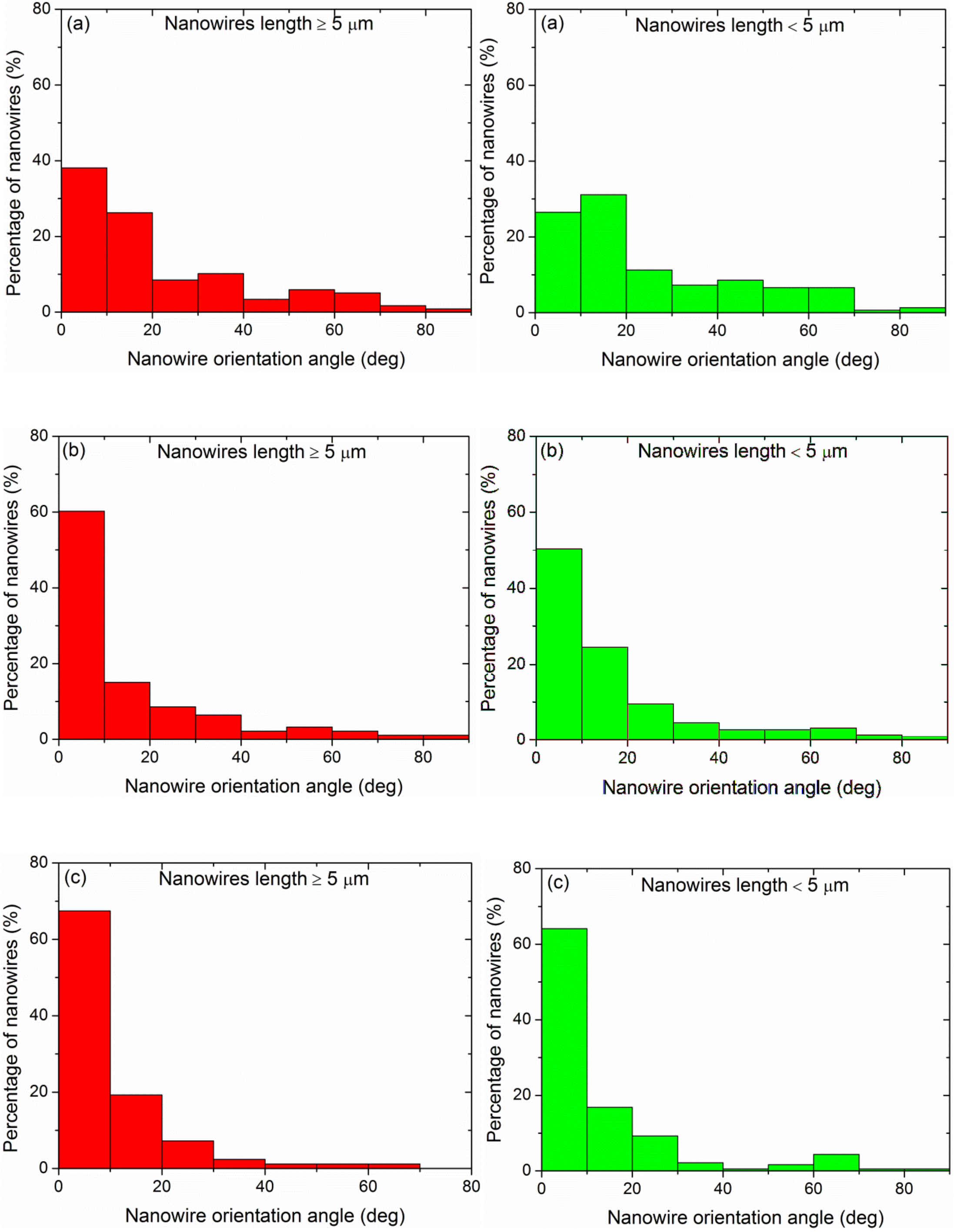

Figure 7.9 Examples of comparative histograms of percentage alignment for nanowires with lengths more or less than 5 μm for ~200 nm NiFe nanowires deposited at different field strengths (a) ~100 Oe, (b) ~500 Oe, and (c) ~1 k Oe.

There is a noticeable effect of nanowire length on the alignment process for all field strengths investigated here. The proportion of aligned wires for both lengths between 0º-10º for NiFe nanowires and within 0º-20º for Ni nanowires under application of different magnetic field strengths are summarised in Figure 7.10(a-b), respectively.

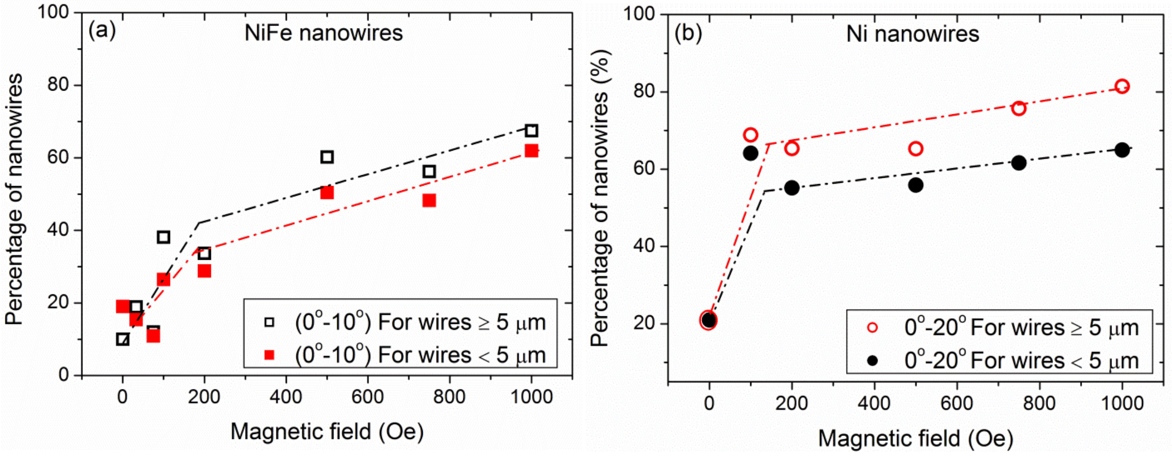

Figure 7.10 Proportion of aligned (a) NiFe nanowires oriented with 0º-10º, and (b) Ni nanowires oriented with 0º-20º for two different lengths (more and less than 5 μm). The dashed lines are used as a guide to the eye.

The trend in these figures suggests a consistently higher percentage of aligned wires are obtained for longer nanowires at fields above ~200 Oe, where the percentage of long NiFe wires (≥5 μm) was found to be ~7% within 0º-10º higher than shorter (<5 μm) wires, whereas this was ~12% higher between 0º-20º for long Ni wires than shorter wires (<5 μm). Thus, in all applications that require high percentage of aligned wires, it is very important to use wires with a higher aspect ratio.

7-7 Interesting observations resulting from the alignment experiments

During the course of these field alignment studies, a range of interesting features were observed. Firstly, it was found that the nanowires could be oriented in any preferable direction by simply rotating the substrate with respect to the magnetic field during the deposition process without any noticeable effect on the orientation of previously aligned and deposited nanowires. This behaviour was demonstrated in the scanning electron micrographs shown in Figure 7.11 which show examples of Ni nanowires lying perpendicular to each other produced by two sequential deposition steps using high magnetic field strength orientated normal to each other. This result agrees well with the other results in literature [11-13] and demonstrates that the *van der Waals* or/and the *electrostatic forces* between the wires and the substrates are dominant after deposition.

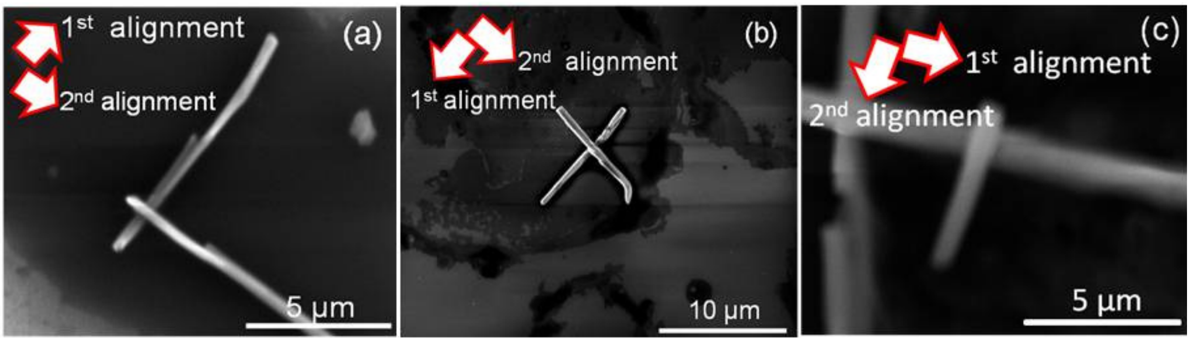

Figure 7.11 Examples of scanning electron micrographs of Ni nanowires deposited on substrates from a dilute suspension in two sequential steps using high magnetic fields normal to each other during the deposition process.

This behaviour may be useful from a practical point of view in the fabrication of complex devices that need sequential steps of nanowire alignment, for example to create memory or logic architectures.

Another interesting observation is the formation of continuous chains of head-to-tail nanowires during deposition in applied magnetic fields, as demonstrated in Figure 7.12, which show examples of scanning electron micrographs of parallel chains of Ni nanowires.

the electrical and magnetic properties of isolated nanowires. Reducing the concentration of the nanowires in the IPA suspension was found to reduce this effect. The lengths of these chains were observed to extend over hundreds of micrometres, in agreement with previous results [12,14]. Depending upon the concentration, the location and distance between these wires, in addition to the magnetisation, the viscous drag and the magnetic field strength, the inter-wire dipolar interactions can play an important role in the formation of chains during the deposition process.

The final interesting feature is the formation of cumulative clusters of nanowires as demonstrated in the examples of scanning electron micrographs shown in Figure 7.13. The formation of these clusters could be attributed to the high concentration of nanowires during the deposition process and the low viscosity of the IPA [12].

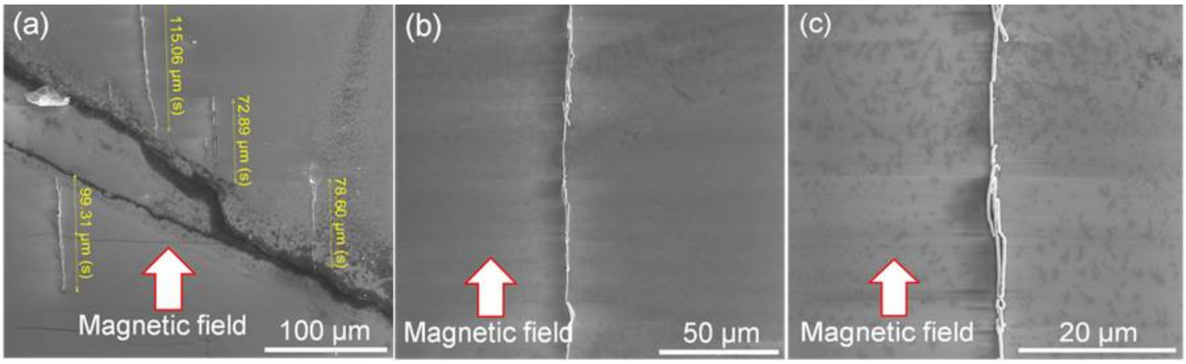

Figure 7.12 Examples of scanning electron micrographs showing (a) Chains of Ni nanowires formed as a result of magnetic dipole-dipole interactions between the nanowires during the deposition on substrates under high magnetic field strength, and (b,c) Magnified regions of the single chain of nanowires.

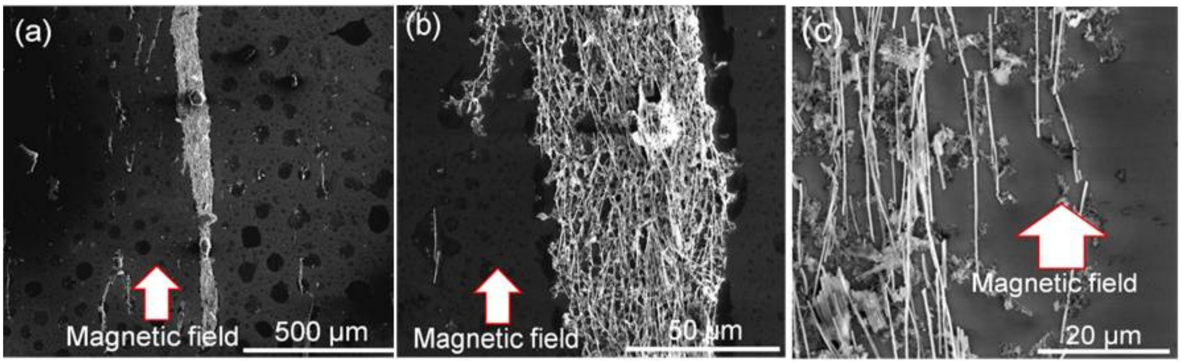

Figure 7.13 Examples of scanning electron micrographs showing cumulative clusters of Ni nanowires which occur due to the high concentration of these wires and magnetic dipole-dipole interactions during the dispersion process on the substrate under high applied magnetic field, and (b,c) higher magnification in the cluster.

These clusters of nanowires are usually undesirable in fabrication of nano-devices or for further studies on the electrical and magnetic properties of isolated nanowires. Reducing the concentration of the nanowires in the IPA suspension was found to reduce this effect.

7-8 Discussion of applications of magnetically aligned nanowires

As outlined earlier in chapter three, a variety of methodologies have been proposed and investigated for the alignment of quasi-one dimensional nanostructures for technological applications. Here, the efficacy of magnetic field alignment has been quantitatively assessed using magnetic nanowires, however, the results may be relevant to a wider range of functional materials where these nanostructures are capped, coated or incorporate magnetic material, as demonstrated elsewhere [12,13,15,16].

The applicability of such global magnetic alignment in technological applications depends upon the requirements of the particular application. The results show that at most ~80% of nanowires were aligned within 20^o of the field axis. There are a variety of applications in which this level of alignment imparts a level of useful anisotropy to the material properties. These include anisotropic polymer composites where electrical, electromagnetic, optical or acoustic damping behaviour depends upon the anisotropy introduced by the aligned nanostructures [17]. In solution, magnetic alignment of nanostructures can enhance thermal conductivity [12] and with fluorescent functionality magnetic alignment has potential benefits for optical tracking in biotechnology applications [14,18]. Magnetic alignment can also be effectively applied to control and manipulate mammalian cells [19].

For applications where site-specific location and orientation of nanostructures is required, such as electronic circuits and sensors, global magnetic alignment in conjunction with other methods for locating the nanowires onto specified positions on a device structure can assist in the orientation of nanowires. Such positioning techniques include; chemical bonding via biochemical functionalization [15,20], localized electric field assisted alignment [21-23], and localized magnetic field gradients [24]. For applications of nanowires in sensors, such as for biotechnology applications [21], where nanostructures need to make contact between electrodes but the precise orientation of the nanowires is not significant, then magnetic alignment would be beneficial. For applications in other sensors, such as for magnetic field detection [25] and for building electronic components and logic circuits [26,27] that require high levels of precision in orientation and location, magnetic alignment of nanostructures alone does not provide a technical solution.

7-9 Chapter conclusions

The effect of magnetic field strength, composition and the aspect ratio of template released NiFe, Ni and Co nanowires on the efficacy of magnetic field alignment of the nanowires was systematically investigated. In the absence of an applied magnetic field during deposition, the nanowires were found to be randomly oriented on the substrates due to various mechanical forces. However, under the application of different strength magnetic fields, the quality of the alignment was found to be strongly dependent upon the strength of the applied field. For all compositions investigated here, the percentage of nanowires orientated with the field axis was found to increase rapidly with increasing magnetic field up to ~200 Oe, followed by a slower increase up to ~1 kOe for both NiFe and Ni wires and constant for the Co nanowires.

The highest percentage of aligned wires was obtained for the NiFe nanowires, whereas the lowest percentage of aligned wires was obtained for the Co nanowires, with the percentage alignment of Ni nanowires falling between the two. The compositional dependence of the magnetic alignment observed was complex and may be attributed to the saturation magnetisation and the competition between magnetocrystalline anisotropy and shape anisotropy.

The effect of the length to diameter of the nanowires on the alignment process was also statistically investigated. It was found that the alignment was ~7% higher for the longer NiFe wires (≥5 μm) aligned within 0º-10º of the field axis than for the shorter wires (<5 μm) and was ~12% higher for longer Ni nanowires aligned between 0º-20º than for the shorter wires (<5 μm).

7-10 Chapter References

1. Hangarter, C. M., Rheem, Y., Yoo, B., Yang, E.-H. & Myung, N. V. "Magnetotransport studies of a single nickel nanowire" *Nanotech.*, 18(20), 205305, 2007.
2. Jiles, D. "Introduction to magnetism and magnetic materials" 2nd edition, Chapman and Hall/CRC, New York, 1998.
3. Narayanan, T. N., Shaijumon, M. M., Ci, L. & Ajayan, P. M. "On the growth mechanism of nickel and cobalt nanowires and comparison of their magnetic properties" *Nano. Res.*, 1, 465, 2008.
4. Sellmyer, D. J., Zheng, M. & Skomski, R. "Magnetism of Fe, Co and Ni nanowires in self-assembled arrays" *J. Phys.: Cond. Mat.*, 13, 433, 2001.
5. Rivas, J., Mukenga, A. K., Zaragoza, G. & Blanco, M. C. "Preparation and magnetic

behaviour of arrays of electrodeposited Co nanowires" *J. Mag. Mag. Mat.*, 249, 220, 2002.

6. Khan, H. & Petrikowski, K. "Magnetic and structural properties of the electrochemically deposited arrays of Co and CoFe nanowires" *J. Mag. Mag. Mat.*, 249(3), 458, 2002.
7. Vila, L., Piraux, L., George, J. M. & Faini, G. "Multiprobe magnetoresistance measurements on isolated magnetic nanowires" *Appl. Phys. Lett.*, 80(20), 3805, 2002.
8. Ye, Z., Liu, H., Luo, Z., Lee, H.-G., Wu, W., Naugle, D. G. & Lyuksyutov, I. "Changes in the crystalline structure of electroplated Co nanowires induced by small template pore size" *J. Appl. Phys.*,105(7), 07E126, 2009.
9. Das, B., Mandal, K., Sen, P., Bakshi, A. & Das, *P.* "Directional change of magnetic easy axis of arrays of cobalt nanowires: Role of non-dipolar magnetostatic interaction" *Phys. B: Con. Matt.*, 407, 3767, 2012.
10. Lee, S.-W., Ham, M.-H., Kar, J. P., Lee, W. & Myoung, J.-M. "Selective alignment of a ZnO nanowire in a magnetic field for the fabrication of an air-gap field-effect transistor" *Micro. Eng.*, 87(1), 10, 2010.
11. Bangar, M. A., Hangarter, C. M., Yoo, B., Rheem, Y., Chen, W. & Mulchandani, A. "Magnetically assembled multisegmented nanowires and their applications" *Electroanalysis*, 21(1), 61, 2009.
12. Horton, M., Hong, H., Li, C., Shi, B., Peterson, G. P. & Jin, S. "Magnetic alignment of Ni-coated single wall carbon nanotubes in heat transfer nanofluid" *J. Appl. Phys.*, 107(10), 104320, 2010.
13. Hangarter, C. M. & Myung, N. V. "Magnetic Alignment of Nanowires" *Chem. Mat.*, 17(6), 1320, 2005.
14. Tanase, M., Bauer, L. A., Hultgren, A., Silevitch, D. M., Sun, L., Reich, D. H., Searson, P. C., & Meyer, G. J. "Magnetic Alignment of Fluorescent Nanowires" *Nano Lett.*, 1(3), 155, 2001.
15. Bellino, M. G., Calvo, E. J. & Gordillo, G. J. "Nanowire manipulation on surfaces through electrostatic self-assembly and magnetic interaction" *Phys. Stat. Sol. (RRL)-Rapid Research Letters*, 3(1), 1, 2009.
16. Lee, S.-W., Jeong, M.-C., Myoung, J.-M., Chae, G.-S. & Chung, I.-J. "Magnetic alignment of ZnO nanowires for optoelectronic device applications" *Appl. Phys. Lett.*, 90(13), 133115, 2007.
17. Sun, L., Keshoju, K. & Xing, H. "Magnetic field mediated nanowire alignment in liquids for nanocomposite synthesis" *Nanotech.,* 19(40), 405603, 2008.
18. Chien, C. L., Sun, L., Tanase, M., Bauer, L. A., Hultgren, A. & Silevitch, D. M. "Electrodeposited magnetic nanowires: arrays, field-induced assembly and surface functionalization" *J. Mag. Mag. Mat.*, 249, 146, 2002.
19. Tanase, M. Felton, E. J., Gray, D. S., Hultgren, A., Chen, C. S. & Reich, D. H. "Assembly of multicellular constructs and microarrays of cells using magnetic nanowire" *Lab on a Chip*, 5, 598, 2005.
20. Wang, C. P. Michael & Gates, D. Byron "Directed assembly of nanowires" *Materials Today*, 12, 5, 2009.
21. Wanekaya, A. K., Chen, W., Myung, N. V. & Mulchandani, A. "Nanowire-Based Electrochemical Biosensors" *Electroanalysis*, 18(6), 533, 2006.
22. Smith, P. A., Nordquist, C. D., Jackson, T. N. & Mayer, T. S. "Electric-field assisted

assembly and alignment of metallic nanowires" *Appl. Phys. Lett.*, 77, 9, 2000.

23. Maijenburg, A. W., Maas, M. G., Rodijk, E. J. B., Ahmed, W., Kooij, E. S., Carlen, E. T., Blank, D. H. A. & Elshof, J. E.T. "Dielectrophoretic alignment of metal and metal oxide nanowires and nanotubes: A universal set of parameters for bridging prepatterned microelectrodes" *J. Col. Inter. Sci.*, 355, 2, 486, 2011.
24. Rheem, Y., Hangarter, C. M., Yang, E.-hyeok E. H., Member, S., Park, D.-yong, Myung, N. V. & Yoo, B., "Site-SpecificMagnetic Assembly of Nanowires for Sensor Arrays Fabrication" *IEEE Tran. Nanotech.*, 7(3), 251, 2008.
25. Rheem, Y., Yoo, B.-y, Beyermann, W. P. & Myung, N. V. "Magnetotransport studies of a single nickel nanowire" *Nanotech.*, 18, 1, 2007.
26. Huang, Y., Duan, X., Cui, Y., Lauhon, L. J., Kim, K. H. & Lieber, C. M. "Logic gates and computation from assembled nanowire building blocks" *Science*, 294, 1313, 2001.
27. Bachtold, A., Hadley, P., Nakanishi, T. & Dekker, C. "Logic circuits with carbon nanotube transistors" *Science*, 294, 1317, 2001.

Chapter eight

Results: Magnetic and electrical transport behaviour of template released isolated nanowires

8-1 Introduction

To remind the reader: the magnetisation behaviour of two-dimensional arrays of ferromagnetic nanowires cannot provide precise information about the intrinsic magnetic properties of individual nanowires. The interpretation of the data is limited due to the variation of diameters, morphologies, orientations, circularity and the separation among these wires as discussed in chapter six. Furthermore, the dipolar or magnetostatic interactions between neighbouring nanowires seen in the literature complicate the situation and may lead to inaccurate explanations of the magnetic behaviour of individual nanowires. Therefore, the magnetic, magnetisation reversal and electrical transport behaviour of template released isolated ferromagnetic nanowires form the main purpose of this research and this chapter presents the most important results and their interpretation.

Studying these properties experimentally on an individual nanowire is however very complicated and represents a real challenge because the magnetisation of such small wires is of the order of 10^{-11} emu (10^{-14}Am^2) [1-3], which cannot be measured with conventional magnetometry. Using high sensitivity *magneto-optical Kerr effect (MOKE)* is potentially interesting as it provide a very sensitive probe that is proportional to the change in the surface magnetisation to a depth of the order of skin-depth of the material [4,5]. But, the difficulties arising from locating the position of such nanowires within the MOKE illumination, the very small size of these structures with respect to the laser spot size, and the curved surfaces of these wires, which leads to the scattering of the reflected light in various directions may have contributed to the precious lack of measurements on isolated nanowires using this technique. There are only two other papers on the subject published during this work discussing the magnetisation behaviour of $Ni_{80}Fe_{20}$ and multilayer [5] and Co [6] nanowires using MOKE magnetometry.

The surface magnetisation and the electrical transport properties of a range of template released isolated ferromagnetic nanowires were investigated here using a combination of longitudinal MOKE magnetometry and magnetoresistance measurements to probe the surface and bulk behaviour, respectively. With *magnetoresistance (MR)* measurements, it is possible to probe the electrical transport and magnetisation behaviour of isolated nanowires using the *anisotropic magnetoresistance (AMR)* effect. In order to understand deeply the magnetic properties of such wires, electrodeposited thin films were also investigated.

8-2 Magnetic properties of electrodeposited thin films

Before starting the magnetic measurements of isolated nanowires, it was necessary first to start with more simple structures like ferromagnetic thin films in order to get a better understanding of their magnetic properties that form the basis of isolated nanowires. The following discussion is presented to investigate the magnetic behaviour of both Ni and NiFe thin films grown on Au/Cr/SiO_2/Si substrates with cross-sectional area of around 2.4×22 mm^2. These films were prepared by electrodeposition under the same conditions but using different growth times (different thicknesses) as for nanowires. The measurements were performed with the MOKE laser spot positioned at different arbitrary locations on the samples as a function of magnetic field applied at different angles from 0^o (parallel) up to $\pm 90^o$ (perpendicular) with respect to the sample long axis. These measurements provide an insight into the distribution of the switching fields across the whole sample area. Typical examples of normalised hysteresis loops obtained from measuements of Ni and NiFe thin films with various deposition times by applying the magnetic field along two orthognal plane axes are shown in Figure 8.1.

In general, hystersis loops with a high squareness ratio were obtained with a very small local variations. The similarity in loop shape between the two orthoganal axes observed in most cases indicates the isotropic magnetic behaviour in the plane of these films.

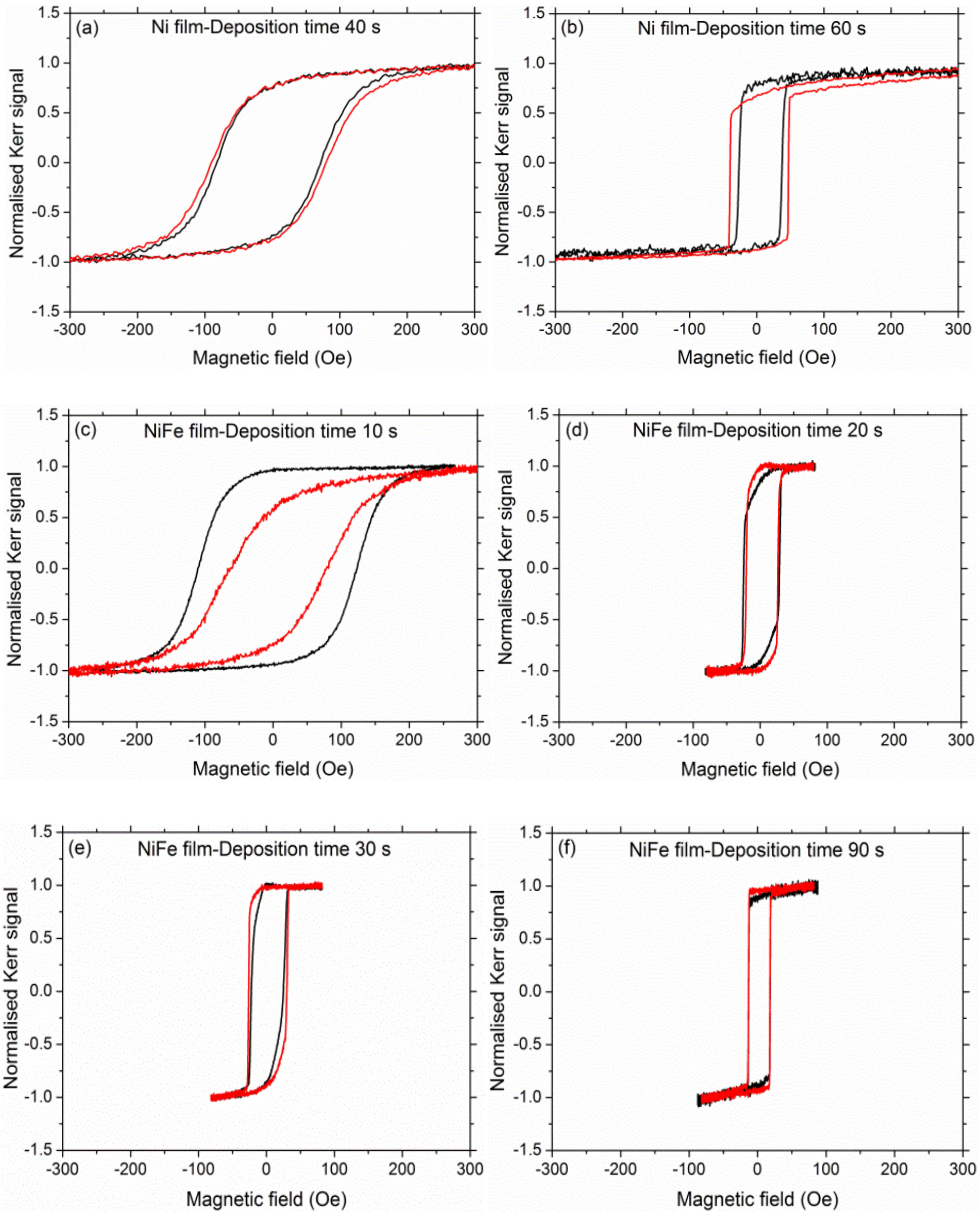

Figure 8.1 Typical examples of pairs of normalised hystersis loops obtained from MOKE measurements of (a,b) Ni, and (c-f) NiFe electrodeposited films measured along two orthognal in-plane axes. These films were prepared with different deposition times (thicknesses) as indicated in the figures.

The reversal behaviour is sharper for the thicker films and more rounded for the thinest films. To understand the magnetic behaviour of such films, coercivity distribution histrograms were obtained from repeating measurements with the MOKE laser spot positioned at many different locations across these samples are plotted in Figure 8.2. A reduction in the coercivity for both materials was observed with increasing deposition time.

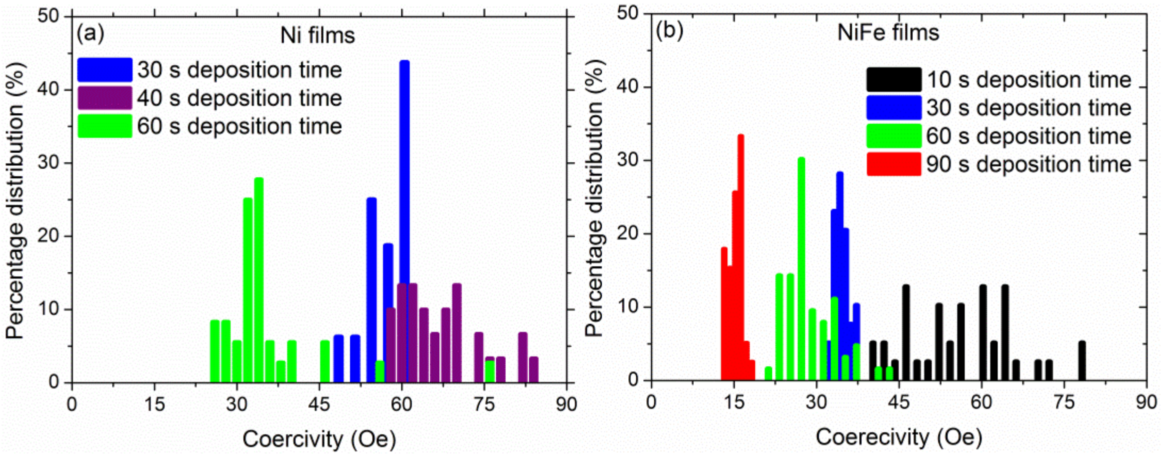

Figure 8.2 Histrograms showing the distribution of coercivity obtained from MOKE measurements of electrodeposited (a) Ni, and (b) NiFe thin films at different locations across each film prepared with different growth times.

For example, the coercivity of NiFe films peaked around 55 Oe and 15 Oe for deposition times of ~10 s and ~90 s, respectively. It should also be noted that there is a wide distribution of coercive fields across the sample area, which increases significantly for shorter deposition times. For instance, the coercivity of the NiFe films was found to range between 40-80 Oe and 12-19 Oe for the shortest (10 s) and longest (90 s) deposition times. These coercivity distributions may be attributed to variations in the film properties in particular roughness which measured and discussed in chapter six. The roughness is believed to be due to the presence of voids and defects which occur during the fabrication process as a result of the existence of impurities, gas bubbles or the density of the electrolyte solution which may not have been homogenous throughout the electrochemical cell. These defects have a more significant effect at shorter deposition times and prevent the formation of uniform thin films on the substrates. The existence of such structural variations can act as pinning centres during the domain wall reversal and hence can change the coercivity and the shape of the hysteris loops. Increasing the growth time increases the film thickness and hence the volume to surface ratio, which in turn reduce these defects and ultimatly reduce the coercivity.

The average coercivity for both the Ni and NiFe films as a function of growth time are plotted in Figure 8.3(a). Clearly, the NiFe films show softer magnetic behaviour (lower coercivity) than Ni films at small deposition times. For both compositions, the coercivity falls with increasing the film deposition time. This may be attributed again to a reduction in the surface strutural defects and the formation of multi-domain structures upon increasing the film thickness which in turn reduce the pinning sites and coercivity.

Figure 8.3(b) shows the average coercivitiy obtained from measurements of NiFe films (with different growth times) as a function of sample angle with respect to the magnetic field applied. For each sample, the coercivity was approximately constant for most angles investigated indicating the similarity in the magnetisation reversal behaviour in such films. However, the data for the shortest deposition time shows an increase in the coercivity with a wider distribution at different angles. This probably reflects again the variations in the surface roughness of the films as described earlier. Nonetheless, these measurments give an indication of the magnetic nature of the materials that forms nanowires investigated in the rest of this chapter namely; soft behaviour at longer deposition times that is largely isotropic.

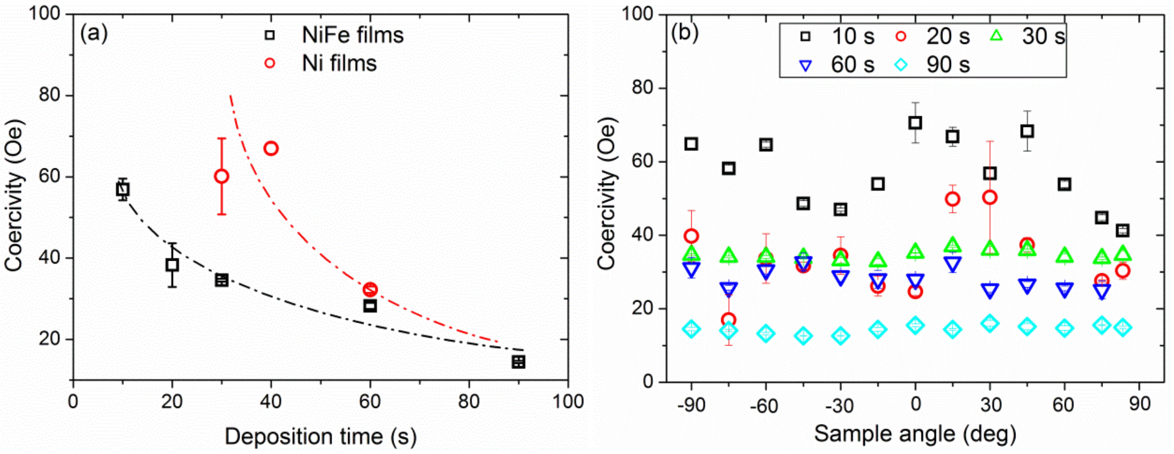

Figure 8.3(a) Coercivity as a function of deposition time for both Ni and NiFe films, the dashed lines are used as a guide to the eye, and (b) coercivity measured at different locations on the NiFe samples (with various growth times) as a function of sample angle with respect to the applied field.

8-3 Magnetic behaviour of template released ferromagnetic nanowires

Magnetic measurements of template released isolated ferromagnetic nanowires deposited from dilute suspension onto oxidised silicon substrates is the key aim of this research. The following subsections investigate the results obtained from measurements of isolated individual, small bundles and small clusters of Ni and NiFe nanowires using longitudinal MOKE magnetometry. These measurements were performed by applying the magnetic field nominally parallel to the nanowire long axis. These wires have dimensions of approximately 7 µm and 9 µm lengths and diameter of ~300 nm and ~200 nm, respectively, as measured by high resolution scanning electron microscopy.

8-3.1 Magnetic properties of individual nanowires

Figure 8.4 show examples of normalised hysteresis loops obtained from measurements of individual Ni and NiFe nanowires. The scanning electron micrographs inset in Figure 8.4 show the areas interrogated by the MOKE laser spot. In general, the signal to noise ratio (SNR) of the MOKE appears quite low, indicating the sensitivity needed to make these measurements on individual nanowires. The hysteresis loops have a high squareness ratio, indicating a characteristic magnetic easy axis along the long axis of the wires.

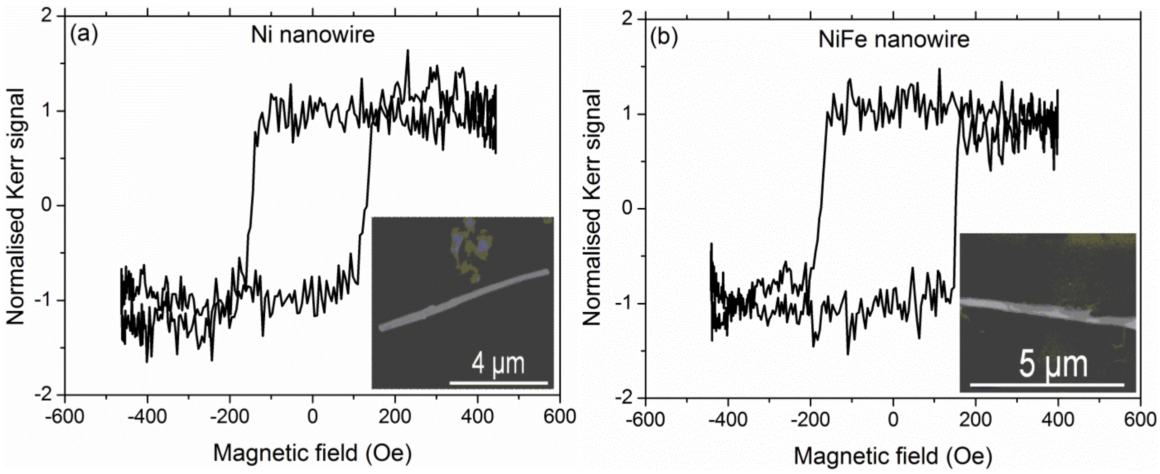

Figure 8.4 Normalised hysteresis loops of isolated individual (a) Ni, and (b) NiFe nanowires obtained using the MOKE setup by applying the magnetic field nominally parallel to the nanowire long axis. The insets are the scanning electron micrographs of the measured wires.

In order to understand deeply the magnetic properties of these wires, a series of MOKE measurements were performed with the focused laser spot positioned and repositioned at different locations on the wires, and multiple measurements were made at each location. The results show that there is a very small distribution of less than ~2 Oe in the switching fields obtained for repeated measurements at the same location, whereas the distribution of the switching fields obtained from approximately 50 hysteresis loops at various locations on each wire was found to be approximately 10 Oe, as shown in Figure 8.5. The average switching fields for the Ni and NiFe nanowires are centred at approximately 140 Oe and 165 Oe, respectively. This is significantly higher than the switching fields obtained from the continuous thin films prepared using the same technique as discussed in the previous section indicating, as expected, that the nanowire switching is dominated by shape-induced magnetic behaviour.

Comparing the switching fields of these different wires, the NiFe nanowire was perhaps expected to be magnetically softer than the Ni nanowire, but the switching field of NiFe nanowire was found to be higher than the Ni nanowire. This contradiction may be attributed to different dimensions of the nanowires as the diameter of the NiFe nanowire is smaller

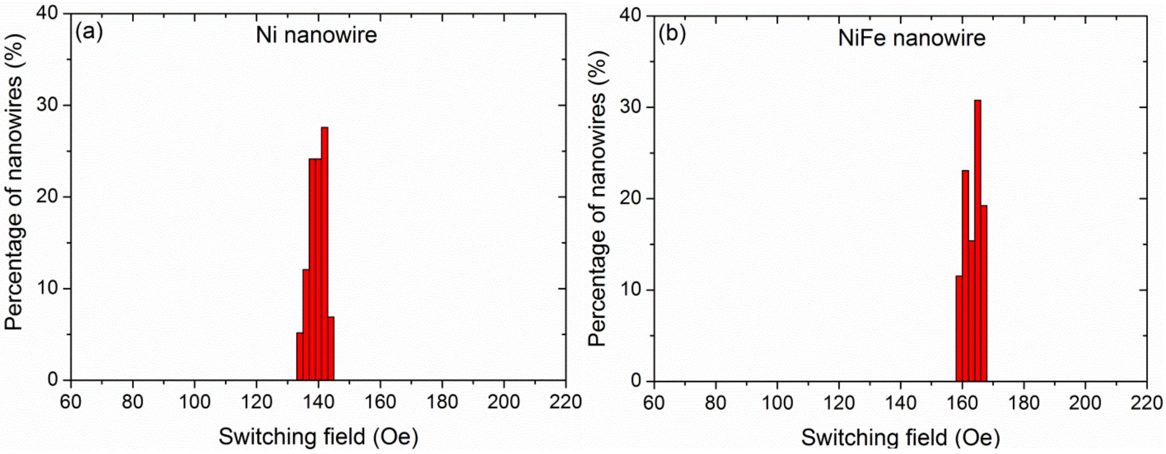

Figure 8.5 Histograms of switching fields distribution of isolated individual (a) Ni, and (b) NiFe nanowires extracted from MOKE loops by applying the magnetic field nominally parallel to the nanowire long axis and measuring at different locations on the wires.

and the length longer than the Ni wire. Therefore, calculations were performed to estimate the self-demagnetising field along the long axis of these wires using equation 2-12 presented in chapter two for the ellipsoid shaped object [7] and it was found to be 14 Oe and 38 Oe for NiFe and Ni nanowires, respectively which is consistent with the difference between Ni and NiFe wire coercivity. As a result, the NiFe wire has a relative enhanced switching field because the self-demagnetising field along the long axis is lower.

In both cases shown in Figure 8.5, the full width of the switching field distributions is around 10 Oe. This range is larger than the local measurement repeatability mentioned earlier and represents variation in the switching field due to different measurement locations of the laser spot on the nanowires. It indicates that the switching fields vary somewhat along the length of the nanowires. This position dependent variation may be related to either difference in the morphology along the nanowires (discussed in chapter six) as the onset of switching is very sensitive to the surface regularities or dimension variations in the nanowire or any differences in nanowire orientation with respect to the magnetic field, although in this case the nanowire long axis was nominally parallel to the field applied. Stochastic effects due to thermal fluctuations that can lead to peak broadening are unlikely to be relevant here as each MOKE loop represents the averaging of several hundred switching cycles and therefore stochastic effects will be included in the averaged loop.

8-3.2 Magnetic properties of isolated bundles of nanowires

In addition to the importance of investigating the magnetic behaviour of individual nanowires presented in the previous section, the magnetic behaviour of bundles of wires that are close enough to interact with each other is also of significant interest. Therefore, the magnetic properties of bundles of 3 and 7 closely packed NiFe nanowires were investigated. Figure 8.6 show typical examples of normalised hysteresis loops obtained from measurements of such nanowires. The scanning electron micrographs showing the areas interrogated by the laser spot are inset in Figure 8.6. A series of MOKE measurements were performed at many different locations on the wires and the histograms for the switching fields of each group are shown in Figure 8.7. The results show a distinct single peaked distribution for each bundle of wires. The average switching field falls with increasing the number of nanowires in the assemblage. The switching field was centred at ~134 Oe and ~82 Oe for 3 and 7 NiFe nanowires, respectively.

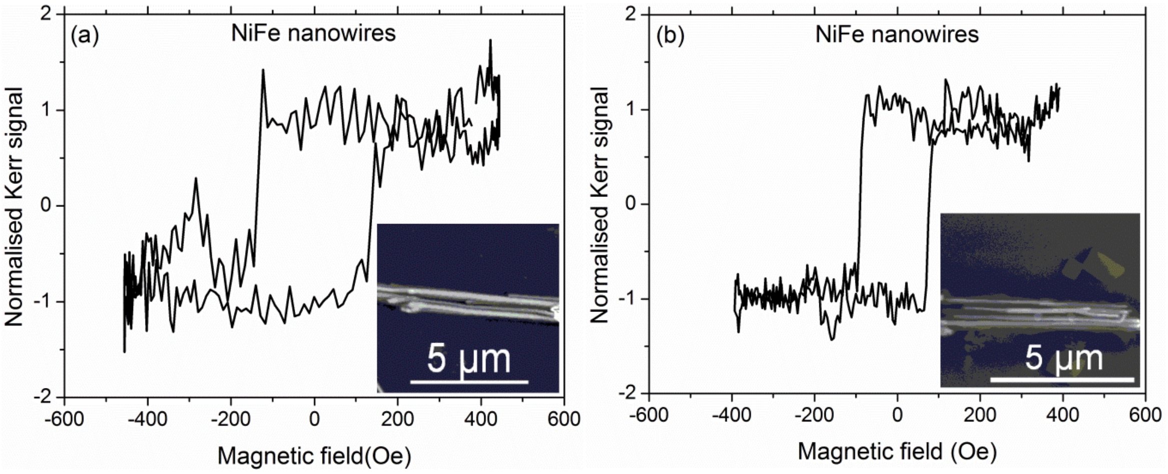

Figure 8.6 Normalised hysteresis loops of tight bundles of NiFe nanowires (a) 3 nanowires, and (b) 7 nanowires obtained using MOKE magnetometry with the field applied nominally parallel to the nanowire long axis. The insets are the scanning electron micrographs of the measured wires.

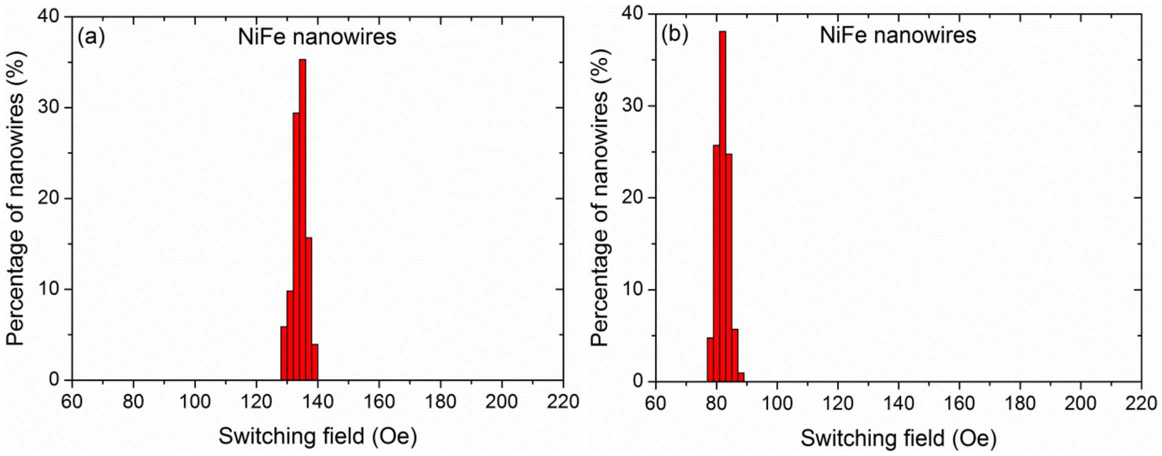

Figure 8.7 Switching fields distribution histograms of a bundle of NiFe as a (a) 3 nanowires, and (b) 7 nanowires extracted from MOKE loops by applying the magnetic field nominally parallel to the nanowire long axis and measuring at different arbitrary locations on the wires.

In fact when plotted as a function of the number of nanowires, the switching field decreases from 1 to 7 nanowires as shown in Figure 8.8(a). For comparison, the result presented here was plotted in Figure 8.8(b) along with the results from the literature for an array of hexagonal closely packed Ni nanowires with 40 nm diameter and 100 nm spacing obtained from micromagnetic simulations [8].

The key point from the data in Figure 8.8 concerns the reduction of the switching fields with increasing the number of nanowires in the bundles measured. This reduction can be understood in terms of magneto-static interactions between the neighbouring nanowires. Interaction effects have been widely investigated experimentally and theoretically in two dimensional arrays of various ferromagnetic compositions of cylindrical nanowires [8-19], arrays of planar wires [20] and amorphous nanowires [21,22]. However, the magneto-static interactions in these systems can be very complicated and found to depend on a variety of factors including the magnetic state of the individual wires in the array, the magnetic history, the wire diameter [9,10], spacing among the interacting wires [9,10,18], as well as filling factor [17] or number (density) [9,12] and length [12,17] of these wires. These studies demonstrate that the magneto-static interactions may aid switching or stabilise the

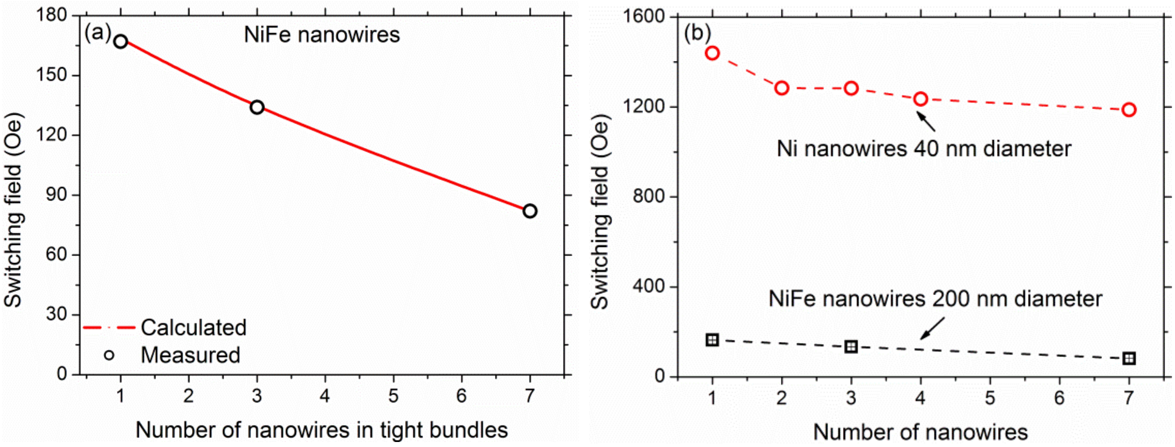

Figure 8.8 (a) Average switching field as a function of the number of NiFe nanowires in the tight bundles, the line represents theoretical calculations, and (b) comparison with a result from literature, the dashed lines provide a guide to the eye.

magnetisation, leading to a slight reduction in the remanent magnetisation and reduced or increased switching field. To understand in detail the behaviour presented here, the switching field was calculated using equation 2-12 presented in chapter two after calculating the demagnetising factor along the nanowire's long axis for the ellipsoid shaped object [7]. Assuming the saturation magnetisation is 90% of $Ni_{81}Fe_{19}$ and an intrinsic nucleation field 185 Oe. Very good agreement was obtained as shown by the continuous line in Figure 8.8(a). Therefore, the bundle of closely packed NiFe wires suggest that it behaves like a single system and the magneto-static interactions among these wires aids the external field, leading to a higher local field in neighbouring wires, and consequently decreasing the effective external applied magnetic field needed to switch the nanowires. The local field increases with the number of closely packed wires and subsequently the measured switching field falls. On the other hand, the remanent magnetisation is unchanged with increasing the number of wires as observed elsewhere [8]. Thus, it may be concluded that decrease in the separation between the nanowires, can lead the system to behave as a one large effective magnetic structure with a lower switching field.

8-3.3 Magnetic properties of isolated clusters of nanowires

In contrast to the measurements of closely packed bundles of NiFe nanowires, the effect of more variation in spacing and orientation between nanowires was also investigated in assemblages or clusters of Ni nanowires. Examples of normalised hysteresis loops are shown in Figure 8.9, which were obtained from MOKE measurements of one cluster of chains of nanowires and another cluster of poorly aligned Ni nanowires. The insets of Figure 8.9 again show scanning electron micrographs of the measured nanowires.

As before, the magnetisation curves are again noisy but have a high squareness ratio close to ~1, indicating a characteristic magnetic easy axis along the wire long axis, although more *"structure"* can be observed in the reversal behaviour of these clusters. The switching is not sharp as for the single wires and tightly packed bundles but has steps in it.

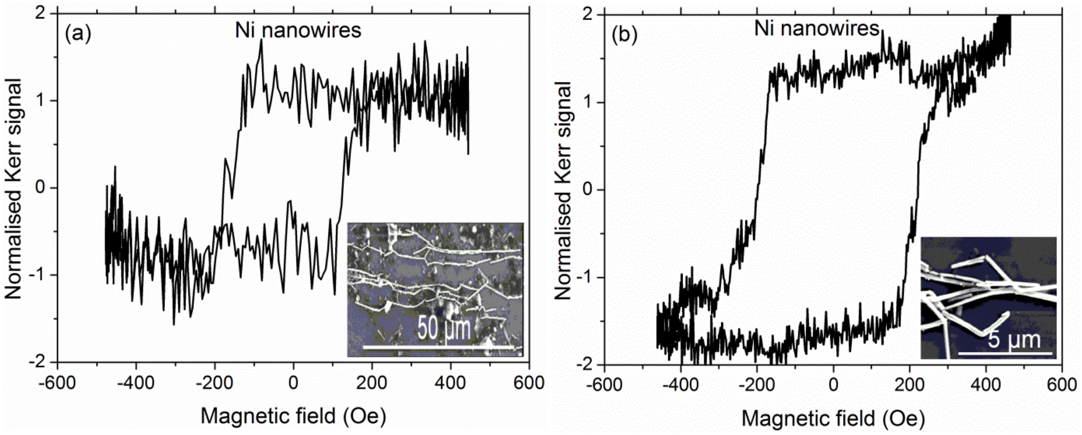

Figure 8.9 Normalised hysteresis loops of Ni as (a) a broad cluster of chains, and (b) a poorly aligned cluster of 7 nanowires obtained using a longitudinal MOKE with the magnetic field applied nominally parallel to the nanowire long axis. The insets are the scanning electron micrographs of the measured wires.

The histograms of the switching fields obtained from multiple measurements at different locations on these clusters are shown in Figure 8.10.

It is clear that, the switching field distributions are more complex than for the closely packed NiFe wires discussed in the previous section and in contrast to the closely packed bundles, the switching fields are larger than those measured from a single Ni nanowire. The switching field distribution for the broad cluster of chains was found to range widely from approximately 135 Oe to 185 Oe and the distribution for the cluster of 7 wires was bimodal with peaks centred around 185 Oe and 200 Oe.

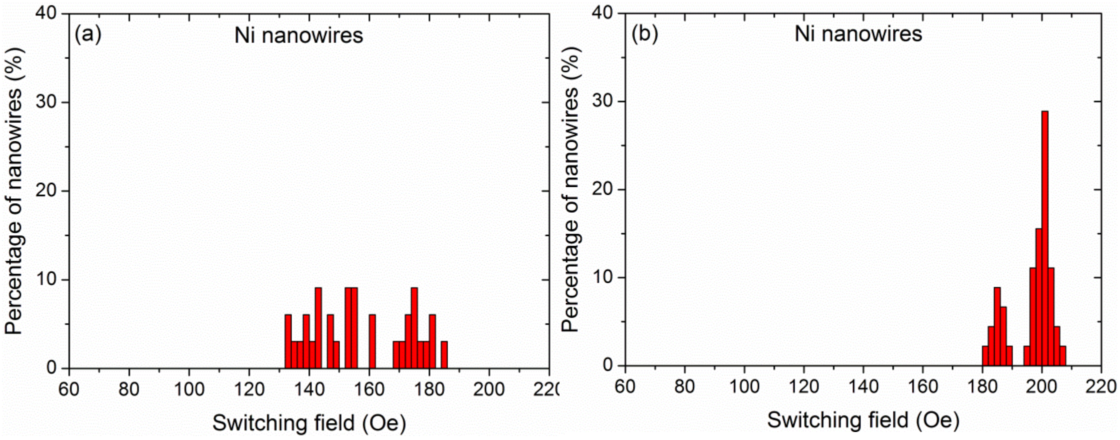

Figure 8.10 Switching field distribution histograms of Ni nanowires in (a) a broad cluster of chains, and (b) a poorly aligned cluster of 7 nanowires extracted from MOKE loops with the magnetic field parallel to the nanowire long axis and measuring at many different locations within the clusters.

The switching field distributions reflect the greater variation in orientation between the nanowires, the formation of chains and the more variable spacing between nanowires. The influence of this large variation on the magneto-static interaction may either aid switching or stabilise the magnetisation leading to reduced or increased switching fields, respectively depending on the different parameters mentioned previously. For example, chaining may effectively increase the magnetic length, stabilising the magnetisation and increasing the switching field. The exact switching field observed depends upon the local interactions and hence is highly sensitive to the MOKE measurement location. Furthermore, variation in the angular orientation between the nanowires increases the switching field. As will be discussed in the following section, the switching field increases with the angle away from the wire long axis. Therefore, for nanowires orientated with their long axes at higher angles to the magnetic field axis, the switching field will be higher, as observed in the nanowires clusters in Figure 8.9. Thus, it may be concluded that slightly increasing the separation distance, chaining or tilting of nanowires can enhance the switching field.

An important finding of all these measurements is the observation of a high remanence ratio. This is quite different from the results obtained from measurements of high density arrays of templated nanowires (see for example Refs [23-30]) which has been measured using other techniques, such as VSM and SQUID that often display sheared hysteresis loops due to the strong magneto-static interaction amongst these wires and may reflect bulk compared with surface measurements.

8-4 Magnetisation reversal of template released isolated nanowires

To understand the magnetisation reversal behaviour and the underlying physical mechanism in these nanowires, systematic measurements were performed to study the angular dependence of the switching fields using MOKE magnetometry. As mentioned earlier these measurements represent the most challenging part of this work. Typical examples of normalised hysteresis loops obtained from MOKE measurements of individual Ni and NiFe nanowires obtained by applying the magnetic field at different angles (where possible) with respect to the nanowires long axis are shown in Figures 8.11. Other examples from measurements of bundles of 3 and 7 closely packed NiFe nanowires are presented in Figure 8.12. The associated scanning electron micrographs showing the measured wires are presented in the insets of the first figures. The Ni nanowires were 7 μm long and 300 nm in diameter, whilst the NiFe nanowires were 9 μm long and 200 nm in diameter.

In many cases, the hysteresis loops were distorted with additional magneto-optical effects at higher magnetic fields and high angles. These loops were plotted without any corrections. From all of the measurements the loops generally show well-defined switching behaviour with high squareness ratio. Square hysteresis loops are expected to occur when the magnetic field is nominally applied parallel to the nanowires long axis owing to their high aspect ratio and the dominant shape anisotropy. However, theoretically the shape of the hysteresis loops should vary with increasing nanowire angle, therefore the square loops at higher angles indicates either that the easy axis of magnetisation rotates with the angle of applied field or the difficulty in recognising the change in the shape of these loops due to the distortion occurred with other magneto-optical effects. A further possibility is that the MOKE setup was actually detecting two signals arising from the transverse component in addition to the expected longitudinal component of magnetisation within these wires. The transverse component perhaps gives rise to the square hysteresis loops at higher angles. Importantly, these loops demonstrate that there is a strong correlation between the switching field and the angle of applied field.

To investigate the magnetisation reversal behaviour of the individual Ni and NiFe nanowires, the switching fields extracted from the loops were plotted as a function of the nanowires angle with respect to the applied field, as shown in Figure 8.13(a,b). Distributions of the switching field values were obtained from repeating measurements at

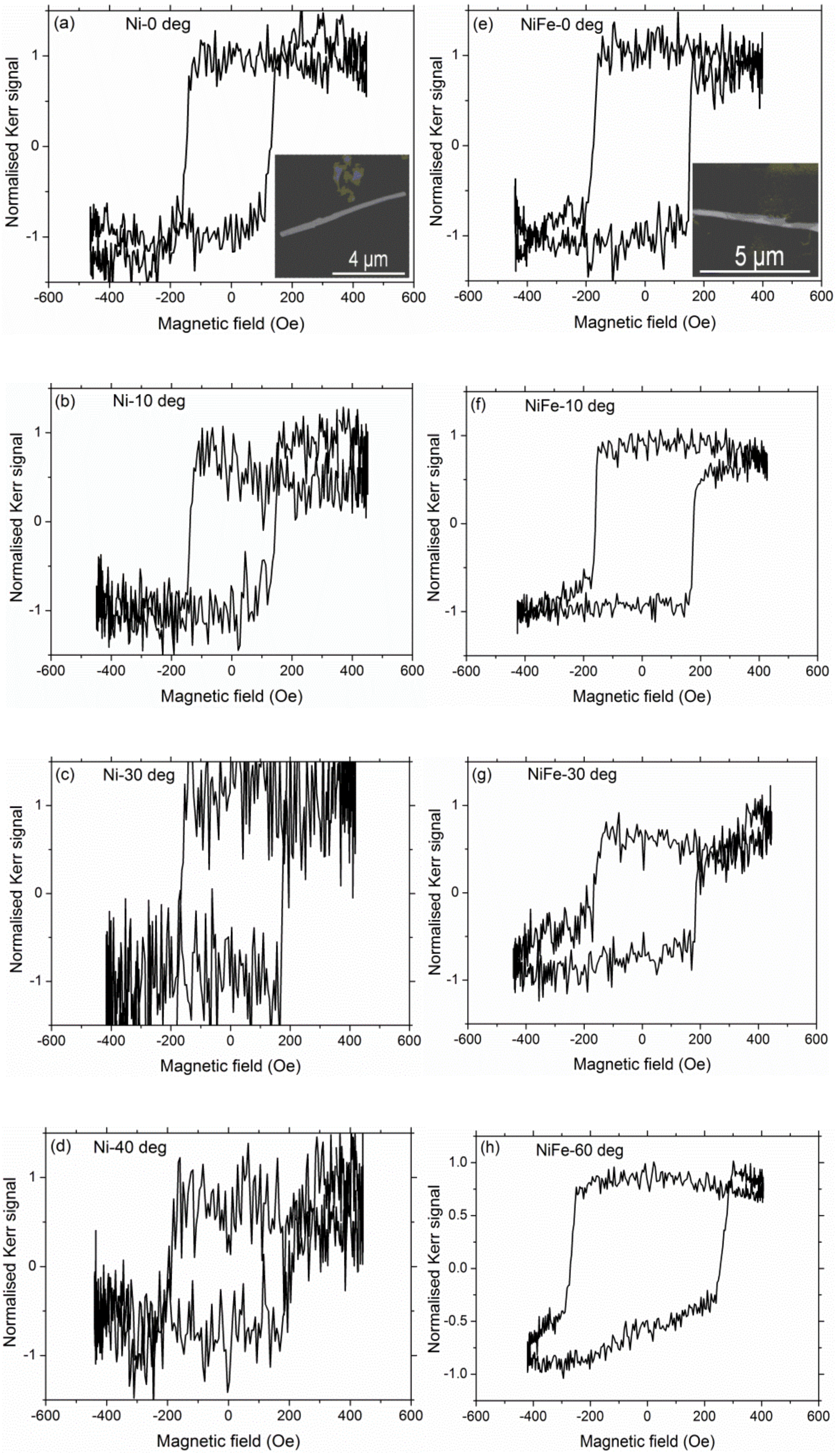

Figure 8.11 Examples of normalised hysteresis loops of a template-released individual (a-d) Ni nanowire, and (e-h) a NiFe nanowire measured using MOKE magnetometry with the magnetic field applied at different angles with respect to the nanowires long axis as indicated in the figures. The insets show scanning electron micrographs of the measured wires.

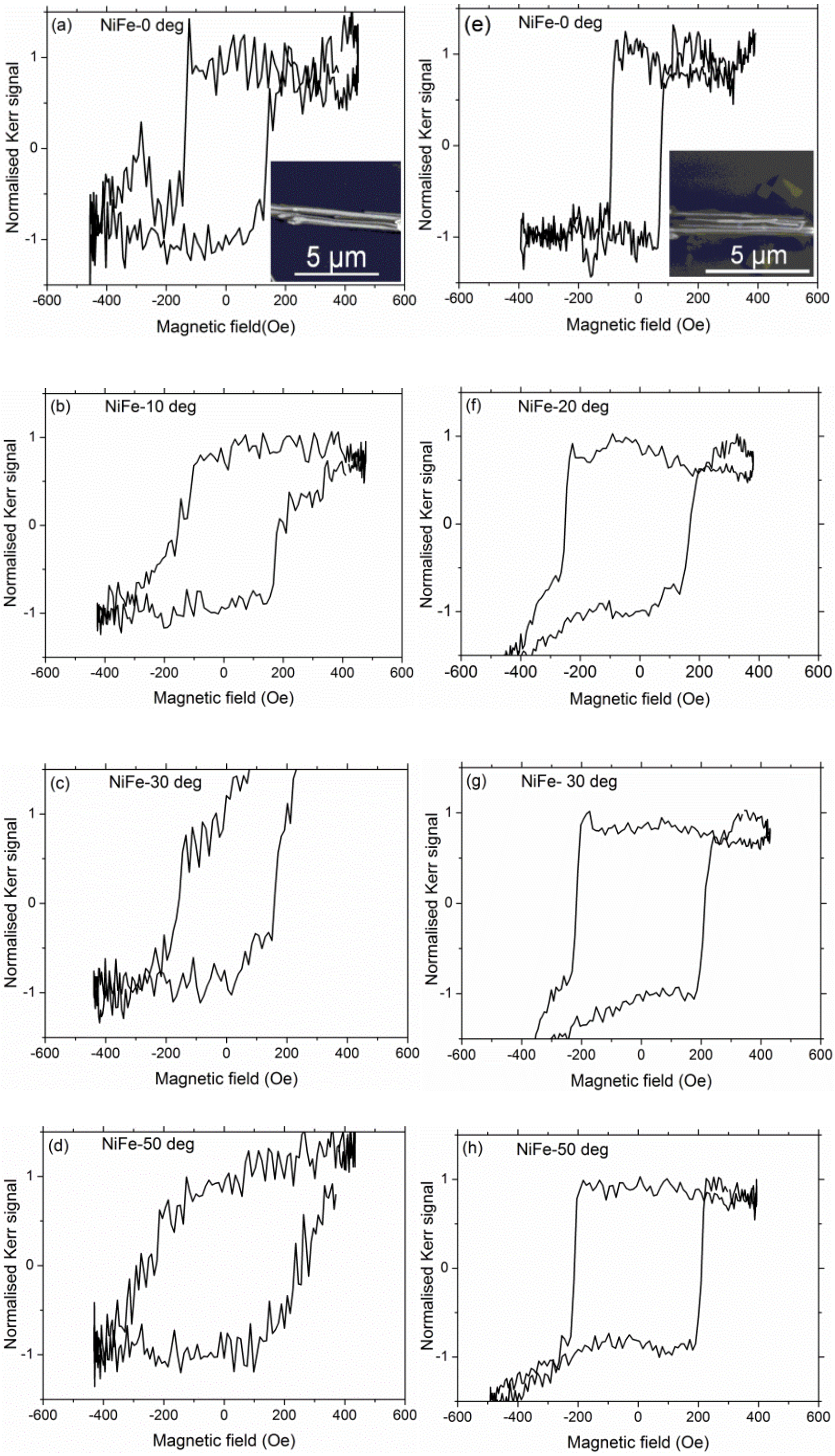

Figure 8.12 Examples of normalised hysteresis loops of template released bundles of closely packed NiFe nanowires for (a-d) 3 nanowires, and (e-h) 7 nanowires measured using MOKE magnetometry with the magnetic field applied at different angles with respect to the nanowires long axis as shown in the figures. The insets show scanning electron micrographs of the measured wires.

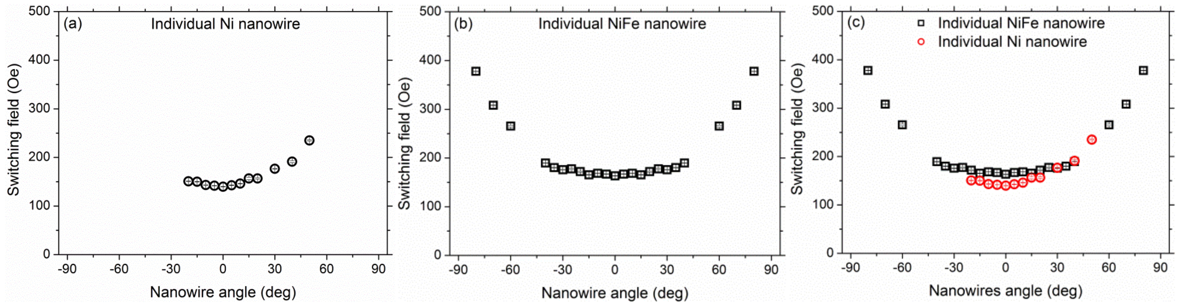

Figure 8.13 Average switching fields extracted from MOKE loops as a function of the nanowire long axis angle with respect to the applied field for an individual (a) Ni, (b) NiFe, and (c) both Ni & NiFe nanowires. The error bars are smaller than the data points.

more than 20 different locations on the wires at each angle and are included in the plots as an error bars. These error bars are smaller than the data points. The switching fields were increased slowly with increasing angle up to about 35^{o}, and then increased rapidly at higher angles.

Comparison of the data between the two different compositions is presented in Figure 8.13(c), different switching fields were noticed below ±20^{o}. At higher angles, the angular dependence of the switching fields were almost identical. The difference in the switching fields at low angles may be expected since the diameter of NiFe nanowire is smaller and the length longer than the Ni nanowire and may be attributed to the effect of demagnetising field as discussed earlier in the previous section. The similar switching field behaviour at higher angles (> 20^{o}) indicates that the effects of the specific nanowire diameter or composition on the behaviour are less significant.

To investigate the magnetisation reversal in the bundles of tightly packed NiFe nanowires, the switching fields were extracted from hysteresis loops and also plotted against nanowire angle, as shown in Figure 8.14. In general, the behaviour shows similar trends to the individual wires discussed above, where the switching fields increase slowly at low angles (< ±35^{o}) and increase rapidly at higher angles (> ±35^{o}). For all of the angles investigated a reduction in the switching field was noticed with increasing the number of

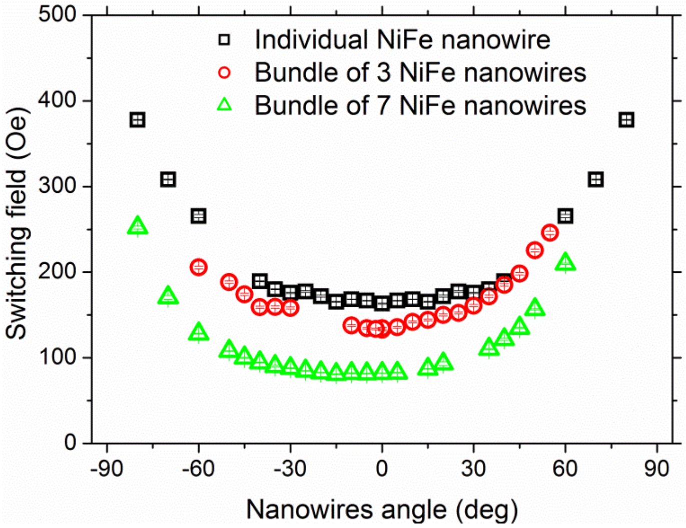

Figure 8.14 Average switching fields extracted from MOKE loops as a function of the angle of nanowires long axis with respect to the applied field for an individual and bundles of 3 and 7 NiFe nanowires. The error bars are smaller than the data points.

clumped NiFe wires. This reduction may be understood in terms of magneto-static interactions among the nanowires mentioned earlier.

In order to understand and explain this angular dependence, it should first be noted that since the diameters of these nanowires are much larger than the exchange length (defined in chapter two), therefore one can expect a deviations of the micromagnetic structure away from the uniform rotation behaviour that is described by the *Stoner-Wohlfarth* reversal model. Since buckling behaviour is expected to occur when the nanowire diameter is comparable to the exchange length (reduced radius around unity), buckling may also be excluded from the applicability here. The shape and aspect ratio of the nanowires investigated here is far from being a chain of spheres which would reverse as in the fanning model. Therefore, the angular dependence of the switching fields is likely to be the consequence of an *incoherent rotational* process following the *curling model* of reversal with a maximum reversal field obtained along the hard axis at perpendicular direction. Accordingly, all the experimental results were compared with the theoretical calculations of curling model after normalising the switching fields to the minimum values using the equation for the curling model presented in chapter two (equation 2-35). Good agreement was obtained at low angles, whilst there was some deviation at higher angles, as demonstrated in Figure 8.15. The agreements between the experimental and theoretical calculations suggest that the curling mode of reversal is a reasonable analytical representation of the magnetisation reversal processes in these isolated nanowires at low angles and the deviation may be due to more complex magnetisation structure. These results are also in agreement with the results reported in literature using other characterising techniques [31-33]. As examples, individual Ni [32] and $Ni_{85}Fe_{15}$ [33] nanowires with 200 nm diameters were investigated using MR measurements at 10K and room temperature, respectively.

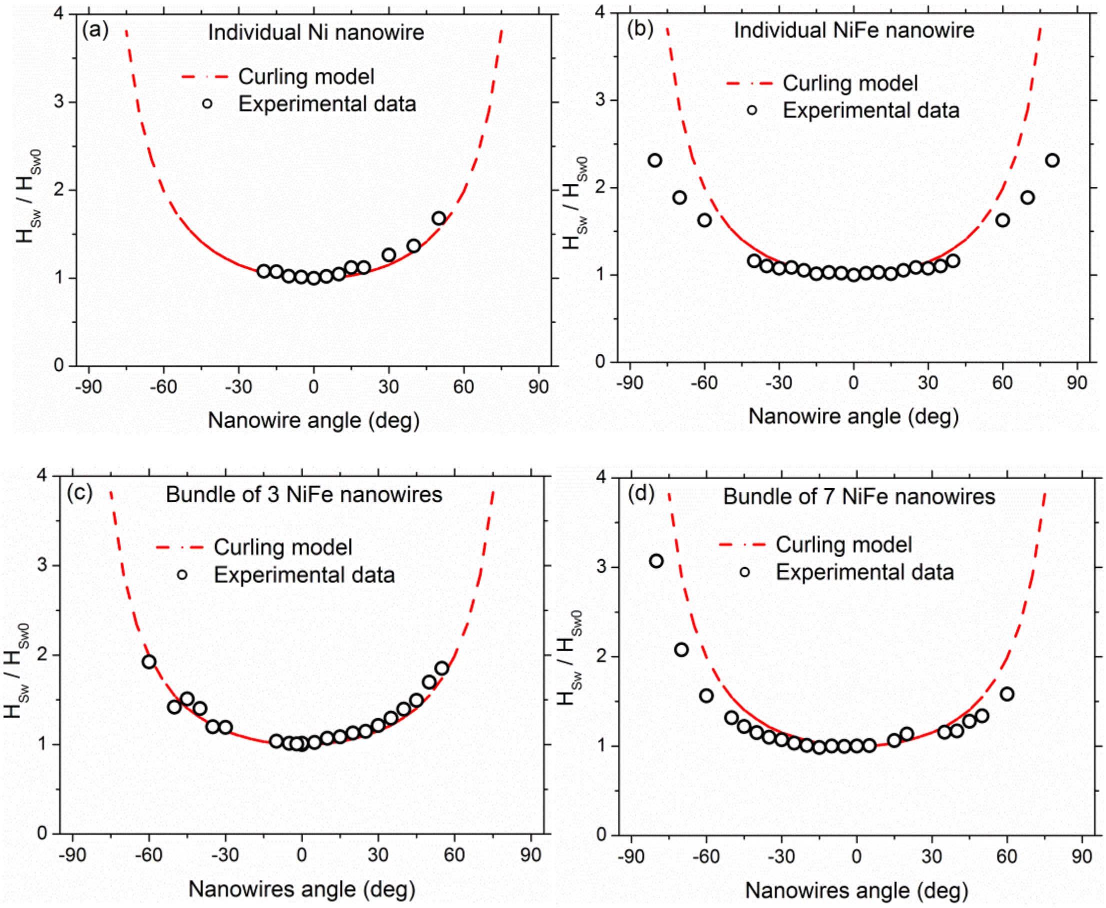

Figure 8.15 Normalised switching fields as a function of nanowires long axis angle with respect to the field applied for (a,b) individual Ni & NiFe nanowires, and (c,d) bundles of 3 & 7 NiFe nanowires, respectively. The dashed lines represent the theoretical curling model.

Their data were found to fit very well with the curling model of reversal and according to their calculations, the size of curling reversal was found to be much smaller than the nanowires diameter. Although, the experimental data was adequately fitted to the curling model, the magnetisation reversal within these wires may occur in a different way as will be seen in chapter nine.

8-5 Electrical transport behaviour of template released isolated nanowires

Magnetoresistance is a powerful technique adopted by many groups to obtain information on the magnetic state and magnetisation reversal behaviour of a range of ferromagnetic planar nanowires [34-39], cylindrical nanowires embedded in their templates [40-43] and isolated nanowires [2,32,33,44-48] using the *anisotropic magnetoresistance* effect. This is because the AMR is sensitive to the relative orientation of the magnetic moments within the nanowires with respect to the applied current, where the resistance is a maximum (minimum) when they are parallel (perpendicular) to each other. This dependence is related to the anisotropic behaviour of the electrons via a mechanism known as the *spin-orbit coupling* as described in chapter five. Here, the magnetisation behaviour of template released isolated nanowires was investigated using magnetoresistance measurements.

Figure 8.16 show scanning electron micrographs of two bundles of 3 NiFe nanowires electrically connected to the gold contact pads. These wires have lengths of ~13.2 μm and ~19.2 μm and diameters of ~200 nm, respectively. The measurements of these small assemblages of wires were conducted by applying the magnetic field at different angles with respect to their long axis (current flow) using a two probe configuration for the magnetoresistance setup after electrically connecting these wires to the external circuitry. For convenience here, these two sets of wires will termed: assemblage (A) and assemblage (B) throughout the following discussion.

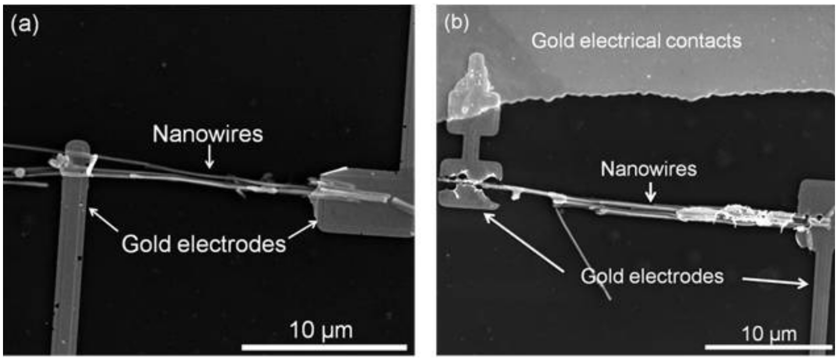

Figure 8.16 Scanning electron micrographs showing two bundles of 3 NiFe nanowires electrically connected to the contact pads. These assemblages (A & B) of wires were measured by applying the magnetic field at different angles with respect to the current flow (nanowires long axis) using two probes configuration of magnetoresistance.

The measured electrical resistance of these assemblages of wires was found to be ~395 Ω and ~218 Ω, respectively. This resistance can be understood in terms of three contributions. The first term is the *nanowire resistance*, R_n, which depends on the nanowires dimension, number of nanowires in the assemblage, scattering rates of the conduction electrons with phonons, imperfections and grain boundaries within the wires. The nanowires resistance is expected to be relatively higher than their counterparts thin films due to their small dimensions and increased surface to volume ratio [47]. The second term is the *electrodes (gold) resistance*, R_g, which appears as a result of the electrical connection of these nanowires with the contact pads and the external circuitry. Finally, the *contact resistance*, R_c, arising from the two connections of gold electrodes with the two nanowire terminals [48] and the two connections of wire bonding. So, the total resistance, R_T, can be expressed as:

$$R_{Total} = R_n + 2R_g + 2R_c \text{(Both gold electrodes \& wire bonding)} \qquad 8\text{-}1$$

The *nanowires resistance* was calculated roughly depending on their dimensions and their intrinsic resistivity (~25 μΩ.cm) [49]. It was found to be ~105 Ω and ~153 Ω for an individual nanowire in assemblages (A and B) at room temperature, respectively.

The *electrode and contact pad resistance* was approximately estimated as the bulk resistivity of gold and their dimensions were known. The resistivity of gold is ~2.2 μΩ.cm [50], the length and the cross sectional area of the gold electrodes was approximately ranged 3-30 $\times 10^{-6}$ m and 4.6×10^{-14} m^2, respectively. The thickness of the gold contact pads was around 35×10^{-8} m with different widths and lengths depending on the position of the nanowires on the chip. Thus, the *total gold resistance* was estimated to be ~85 Ω.

The *contact resistance*, R_c, occurs as a result of the existence of oxide or hydroxide layers or any other impurities or insulating residue remaining on the surfaces of these wires after releasing and deposition or due to the wires curved surfaces as discussed elsewhere [33,47,48,51]. These layers in general reduce the metallic cross-section of the wires resulting in extremely high contact resistance and potentially an open circuit and prevent the electrical measurements from being taken as will be discussed later in this chapter. Thus, the estimated *total contact resistance* was ~276 Ω and 85 Ω for assemblages (A&B), respectively. Table 8.1 summaries the measured and calculated electrical resistance for both assemblages of nanowires together with the calculated total gold resistance and estimated remaining contact resistance.

Figure 8.17 show typical results obtained from measurements of these assemblages of NiFe nanowires by applying the magnetic field at *parallel (longitudinal)* and *perpendicular (transverse)* directions to the current flow (nanowire long axis). These measurements were conducted by sweeping the magnetic field in one direction (black curve) for assemblage (A) and in both directions for assemblage (B) of nanowires (red and black curves). The arrows

Assemblage	**Diameter (nm)**	**Length (μm)**	**Measured total R_n (Ω)**	**Calculated individual R_n (Ω)**	**Calculated total R_g (Ω)**	**Estimated total R_c (Ω)**
A	200	13.2	396	105	85	276
B	200	19.2	218	152.5	82	85

Table 8.1 The experimental and calculated electrical resistance for both assemblages (A & B) of 3 NiFe nanowires together with the calculated total gold resistance and estimated total contact resistance.

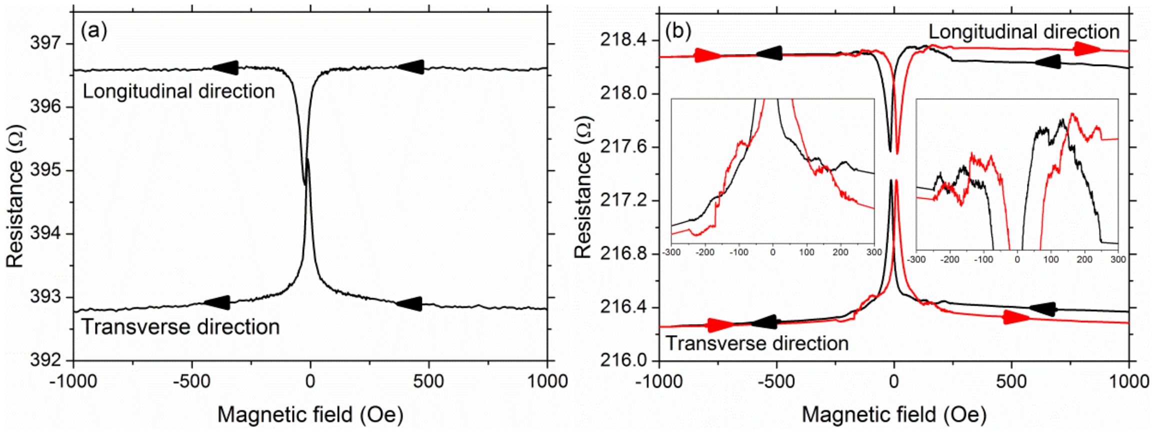

Figure 8.17(a,b) Magnetoresistance curves obtained from measurements assemblages A & B, respectively by applying the magnetic field either parallel or perpendicular to the current flow. The red curves represent the reversed measurements and the arrows indicate the direction of field change. The figure insets are magnifying the small features.

shown in the figure indicate the direction of the field change. Due to the difficulty of precisely aligning these wires with the applied field and the existence of a small angle offset in the MR setup, the nanowires angle were corrected in these profiles.

From these profiles, it is interesting to note the good quality of signal to noise ratio. For both longitudinal and transverse field measurements, three different regions were identified. At high magnetic field strengths, between 250-1000 Oe, the resistance displays saturation behaviour indicating that the magnetic moments within the nanowires are oriented parallel (with high resistance) or perpendicular (with low resistance) to the field applied. At moderate magnetic field strengths, between 100-250 Oe, the measurements of assemblage (B) show a series of nonmonotonic "*continuous small features*" in the resistance. These features have been magnified and plotted as insets in Figure 8.17(b). This behaviour was not seen in assemblage (A) of nanowires. When the magnetic field was less than ±50 Oe the resistance falls rapidly followed by positive jumps in the longitudinal measurements and jumped up followed by drop in transverse measurements. These small and large changes in the resistance are symmetric about zero field when reversing the field direction, as shown in Figure 8.17(b) using different colour of curves (red in this case).

Comparing the resistance at high magnetic fields (resistance at magnetic saturation) with the theoretical calculations for the angular dependence of AMR, using equation 5-12 presented in chapter five, for both assemblages of wires and for all the angles investigated here, good agreement was obtained, as shown in Figure 8.18. Clearly, there is a reduction in the saturated resistance as the nanowire angle increases with respect to the magnetic field applied. This can be understood in terms of the magnetisation orientations within these nanowires. When the magnetic moments lie parallel (perpendicular) to the nanowires long axis, the magnetisation will be collinear (perpendicular) to the current flow yielding the high (low) electrical resistance. This is the high and low resistance relative orientation of the current and magnetisation in *anisotropic magnetoresistance*.

The *anisotropic magnetoresistance ratio*, $\frac{\Delta R}{R}$, defined in chapter five was calculated for both assemblages of NiFe nanowires using equations 5-11, 5-13 and 5-14 and was found to be around 0.93% ± 0.04.

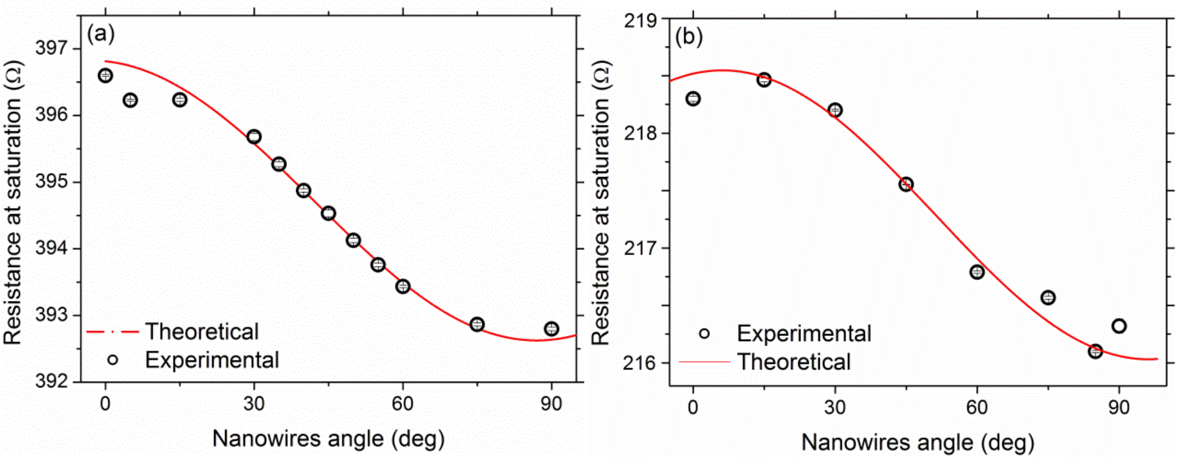

Figure 8.18 The resistance at magnetic saturation for both assemblages (A & B) of 3 NiFe nanowires as a function of their angle with respect to the field applied. The lines are theoretical curves based on anisotropy resistance, see text for details.

It has been reported elsewhere that the anisotropic ratio of bulk NiFe materials dependent on the Ni content, where it was found to vary from ~0.3% to 5% when the Ni content changes from 40% to 90% [51]. Since, the Ni content of the nanowires presented here is approximately 60% (see chapter six), therefore this value is in a good agreement with the value (~0.98%) reported in literature for the $Ni_{60}Fe_{40}$ [51].

For both assemblages of wires, the effective remanence to saturation magnetisation, $\frac{M_R}{M_S}$, derived from the resistance at zero field and saturation field were plotted against the nanowire angle in Figure 8.19. Saturation like behaviour was clearly seen at low angles for both assemblages of wires. At higher angles (75° to 90°) saturation behaviour was also seen for assemblage (A) of wires. A transition region was obtained between 30° to 75°. This indicates that about 92% of the magnetic moments are aligned parallel to the nanowire's long axis upon removing the magnetic field at low angles (< 30°) indicating that shape anisotropy dominated on the behaviour. At higher angles (> 75°), approximately 65% for assemblage (A) and 30% for assemblage (B) of the magnetic moments do not return back to be oriented along the long axis of the nanowires but remains aligned far from the nanowire's long axis upon removing the field. This indicates that there is a strong force that

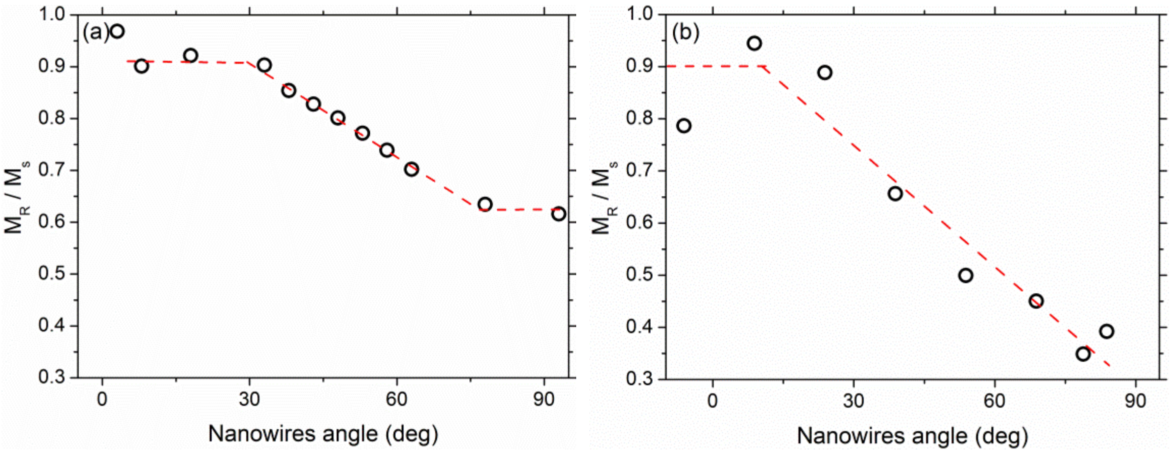

Figure 8.19 The remanent to saturation magnetisation as a function of nanowires angle for both assemblages (A & B) of NiFe nanowires. The dashed lines provide a guide to the eye.

can compete with the shape anisotropy that can impose a magnetic alignment away from the nanowires long axis. Since, such nanowires have zero magnetocrystalline and magnetostriction anisotropies [23,52,53] and as the crystal structure of these wires (investigated in chapter six) showed small grain sizes with no preferred orientation, this field induced effect could arise from magnetostatic interaction between theses wires or due to the nanowire's surface structural regularities. Furthermore, it may perhaps reflect the difference between surface and bulk magnetisation behaviour.

The magnetoresistance profiles obtained from measurements at different angles with respect to the nanowires long axis (for both assemblages of wires) are plotted in Figure 8.20 and 8.21. The arrows shown in these profiles indicate the direction of the field change. Similarly, three different regions were identified. At high magnetic field strengths, between 250-1000 Oe, the resistance showed saturation behaviour. At lower magnetic field strengths, between 100-250 Oe, the measurements of assemblage (B) showed a series of nonmonotonic "*continuous small features*" in the resistance which were magnified and are plotted in the insets of Figure 8.21. These features may correspond to the magnetisation reversal at the surface of these nanowires or due to the abrupt changes in the magnetic configuration and switching of one of the clumped nanowires as a result of the magnetostatic interactions between the clumped wires. Understanding these small features however is important and will be investigated in the following section. Reducing the magnetic field to < ±50 Oe, the resistance at low angles (< 40^o) drops followed by positive jumps, whereas for higher angles (> 40^o) the resistance jumped up then dropped. These changes in the resistance are also symmetric around zero field when reversing the field direction, as shown in the insets of Figure 8.21 using different colour of curves.

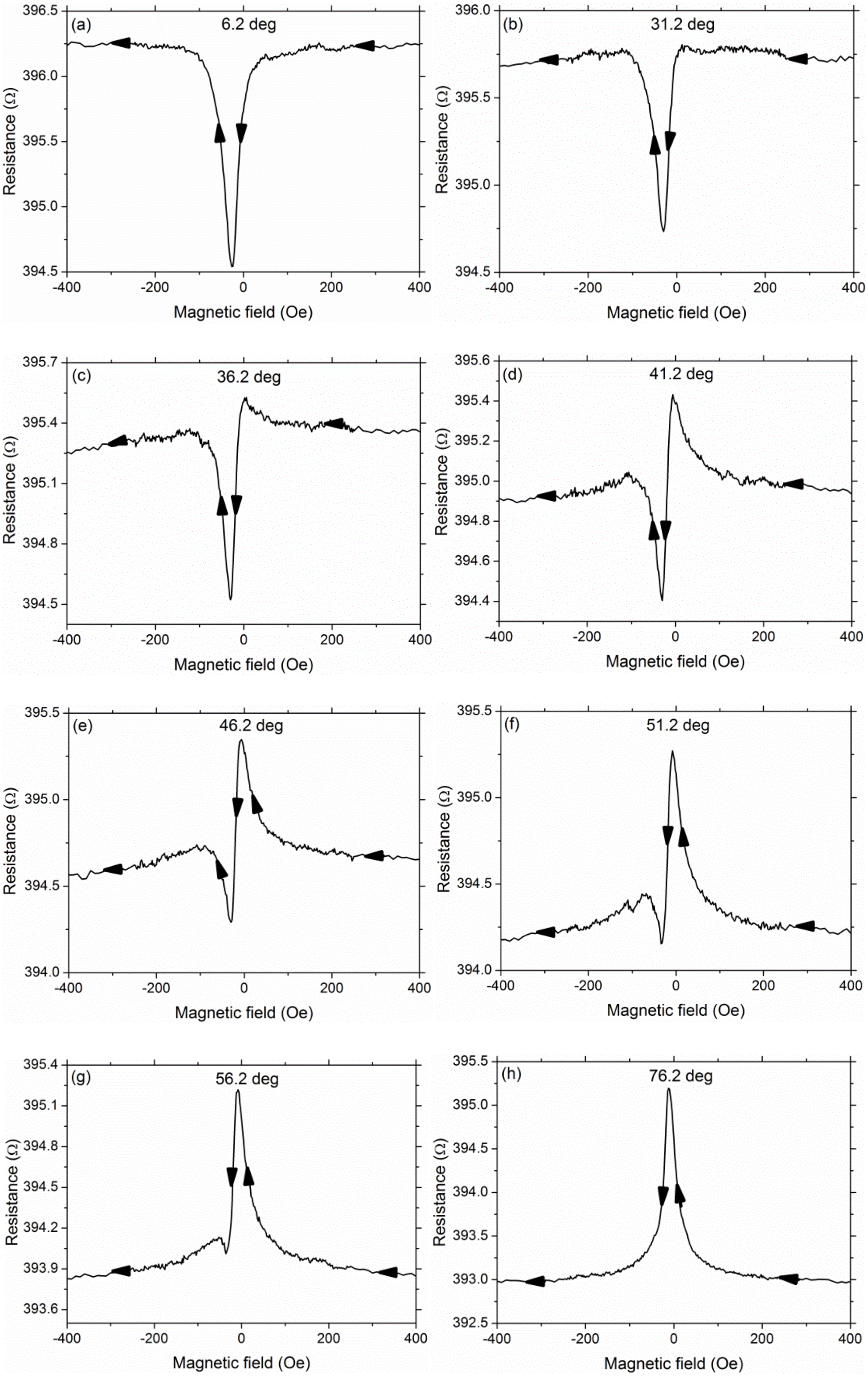

Figure 8.20 Magnetoresistance profiles of assemblage (A) of 3 NiFe nanowires measured by applying the magnetic field at different angles with respect to the nanowires long axis: (a) 6.2°, (b) 31.2°, (c) 36.2°, (d) 41.2°, (e) 46.2°, (f) 51.2°, (g) 56.2° and (h) 76.2°. The arrows indicate the sense of field change. The measurements were performed in one field direction only.

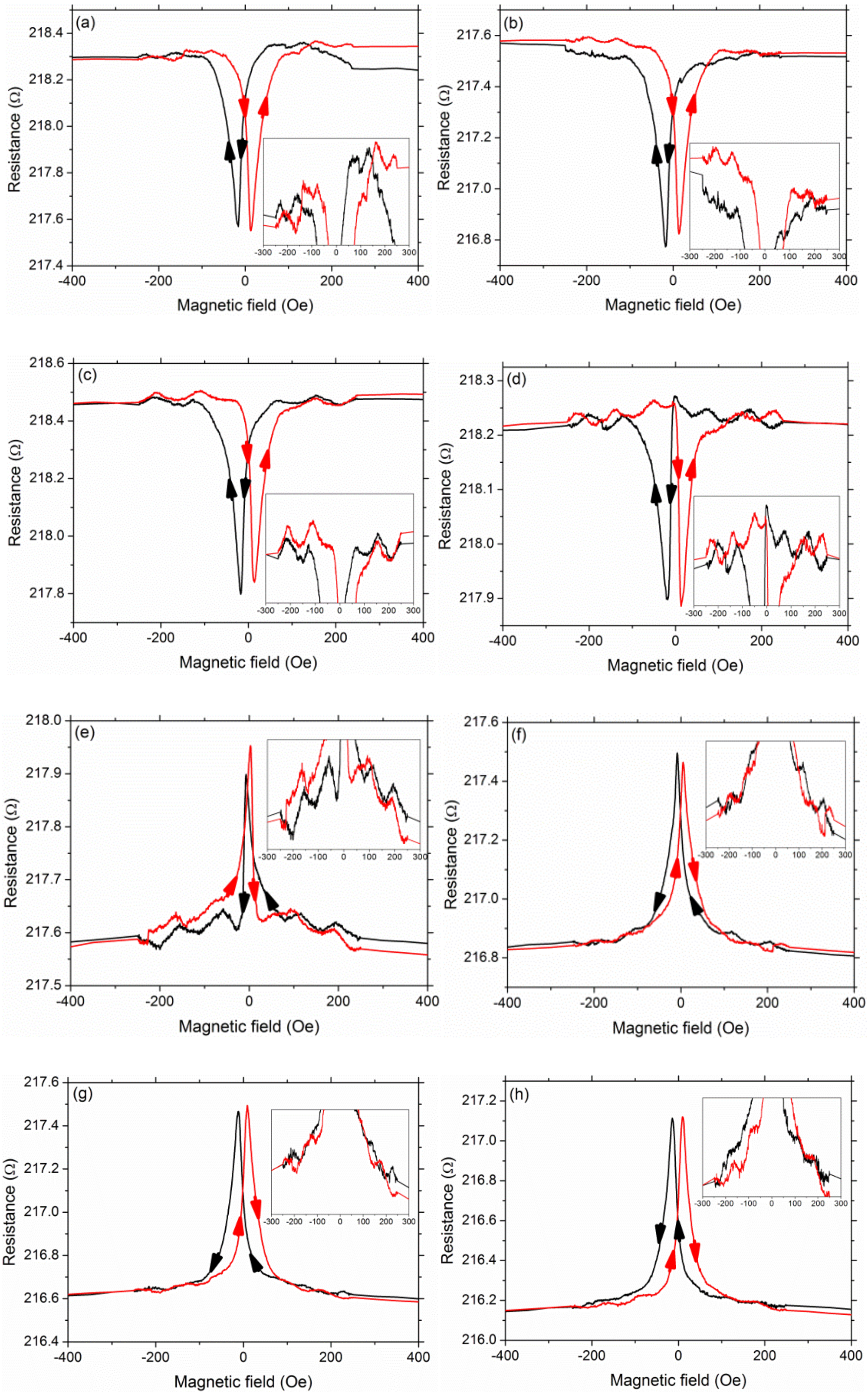

Figure 8.21 Magnetoresistance curves obtained from measurements of assemblage (B) of 3 NiFe nanowires by applying the magnetic field at different angles with respect to the nanowires long axis: (a) -6°, (b) -1°, (c) 9°, (d) 24°, (e) 39°, (f) 54°, (g) 69° and (h) 79°. The red curves represent the reversed measurements and the arrows indicate the direction of field change. The figure insets are magnifying in the small features.

To understand the magnetic properties and the underlying mechanism responsible on the magnetisation reversal in such assemblages of NiFe nanowires, the switching field extracted from the magnetic fields at which the strong peaks (troughs) occur were plotted as a function of the nanowire angle, as shown in Figure 8.22. In general, the switching field of assemblage (A) was slightly higher than the switching field of assemblage (B). For instance, the switching field for longitudinal measurements was ~24 Oe for assemblage (A) and 16 Oe for assemblage (B). This difference may be attributed to the difference in the length of these wires or due to the complicated magnetostatic interactions between these assemblages of wires. The behaviour in assemblage (A) demonstrates that the field increased slightly up to 60^{o} then dropped and increased very slowly up to 90^{o}. In contrast, the switching field in assemblage (B) is almost constant for low angles and decreases step wise close to 40^{o} before increasing again slowly at higher angles.

To understand this behaviour the experimental data were normalised and compared with the theoretical calculations of the curling model of reversal as shown in Figure 8.22(c). The experimental data agree with the theoretical curve at small angles up to 25^{o} and 60^{o} for assemblage (A) and (B), respectively, but the behaviour is very different at higher angles. It has been reported elsewhere that the magnetisation reversal in arrays of Ni and Fe wires

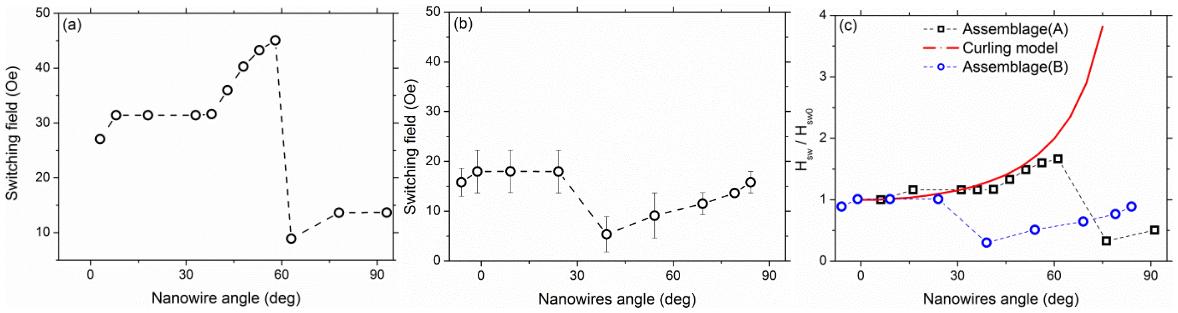

Figure 8.22(a,b) The switching field obtained from the fields at which the strong jumps occur in the MR profiles as a function of nanowires long axis angle for both assemblages (A & B) of 3 NiFe nanowires, and (c) normalised switching field for both assemblages of wires and the theoretical curling curve (red continuous line). The dashed lines provide a guide to the eye.

with 250-300 nm diameters and 3-8 μm lengths change from the curling to the S-W model at angles more than 60° and 75°, respectively [29]. They attributed this change to the competition between the shape anisotropy and magnetostatic interactions among the interacting wires. Rheem et. al. also used MR measurements to study the magnetisation reversal in isolated $Co_{20}Ni_{80}$ nanowires with 200 nm diameter and they found that the magnetisation reversal changes from curling to S-W at angle greater than 75° [47]. Therefore, the change in the magnetisation reversal here could be attributed to the complicated magnetostatic interactions among these wires. However, the difference in the angle of changing reversal between these two assemblages may be attributed to the difference in the effect of magnetostatic interactions among the interacting wires.

Nonetheless, the switching fields obtained from the main (large) features in the profiles of both assemblages of wires are much lower than the switching field obtained previously from MOKE measurements of the same assemblage of nanowires. Moreover, the angular dependence of the switching fields were also showed different behaviour than the angular dependence obtained from MOKE measurements. The significance of the differences will be discussed in the following section, since this is the first study to combine MR and MOKE measurements on the same nanowires.

8-6 Comparison of magnetisation behaviour between MOKE and MR measurements

In order to get a fuller understanding of the magnetisation behaviour of these small assemblages of nanowires, the switching fields obtained from MOKE and MR measurements were compared with the switching fields obtained from similar compositions and dimensions reported in the literature that adopted the same investigative techniques. Then, the results of MOKE and MR measurements were compared with each other. All of the switching fields reported in the following discussion were obtained when the magnetic field nominally applied parallel to the nanowire long axis.

The average switching field obtained from repeating MOKE measurements of bundles of three NiFe nanowires was found to be ~134 Oe (see Figure 8.7(a)). Very recently, Lupu et. al. used only the MOKE technique to probe the magnetic properties of a range of isolated $Ni_{80}Fe_{20}$ nanowires with diameters ranged from 35 to 300 nm [5]. The estimated switching field of 300 nm diameter from their data was found to be around 100 Oe. Comparing this value with the value presented here, a good agreement is clearly obtained since the diameter of nanowires investigated here was smaller than Lupu's wires.

The fields at which the small features occur in the MR profiles were found to be around 100-240 Oe (see for example Figure 8.21). Comparing these values with the switching field obtained from MOKE measurements, a comparable agreement is clearly observed. This agreement suggests that these features may correspond to the magnetisation reversal at the surface of these nanowires.

However, for both assemblages of wires investigated with MR measurements, the switching fields obtained from the fields at which the large features occur in the profiles were found to be around 24 Oe and 16 Oe, respectively (see Figure 8.17). Comparing these values with the switching field obtained from MOKE measurements, a large difference is clearly seen. Rheem et. al. studied the magnetic behaviour of individual $Ni_{85}Fe_{15}$ [33,46] and individual $Ni_{80}Co_{20}$ [47] nanowires with 200 nm diameters and more than 5 µm lengths using only MR measurements. The estimated switching fields from their data were found to be around 15 and 28 Oe, respectively. Comparing these values with the MR values reported here, again good agreement is obtained.

Now, comparing the behaviour of angular dependence of the switching fields obtained from MOKE (Figure 8.15(c)) and MR measurements (Figure 8.22(c)), a large difference is clear. This difference suggests that the magnetisation reversal within these wires may occur in different ways to the classical models mentioned earlier.

It is well known that MOKE setup is a sensitive technique to probe only the surface magnetisation to a depth of the order of the skin-depth of the nanowires [4,5,54]. In contrast, MR measurements are sensitive to probe the whole bulk of the nanowires but only when there are changes in the angular orientation of the magnetic moments. It has been reported elsewhere that the surface magnetisation of plane shaped iron single crystal thin film [54] and amorphous microwires behaves differently from the bulk magnetisation. Therefore, the two different behaviours obtained here from MR and MOKE measurements strongly suggest that the surface magnetisation behaves differently from the bulk magnetisation of such thick nanowires. Micromagnetic simulations on the similar composition and diameter of nanowires confirm that the magnetisation at the surface behaves differently from their bulk. Moreover, the micromagnetic spin structures of such wires indicate that the reversal is not a simple curling-like behaviour, as will be seen in chapter nine.

8-7 Technical difficulties associated with the electrical measurements of isolated wires

During the course of this research, various technical difficulties were faced in forming electrical connections and measuring the electrical transport properties of the template released isolated ferromagnetic nanowires. One of the most important difficulties was associated with the electrical connection of these wires to the contact pads, as described in chapter four.

In spite of all these difficulties, a range of nanowire samples were successfully connected to the contact pads by platinum and gold electrodes using both local chemical vapour deposition and electron beam lithography, respectively (e.g. see Figure 4.18). However, the magnetoresistance measurements of such nanowires showed that the connections were non-ohmic and highly resistive, 1 MΩ, or an open circuit. This was attributed to various reasons. The most important one being the formation of carbon and hydroxide contaminants during the Pt deposition, as investigated elsewhere using other compositions of wires [51]. The formation of oxides, hydroxides or any other residual layers during the release and placing of nanowires on the substrate is another significant reason cited in literature [32,33,48]. Thus, the contacts were improved by removing the undesired oxides or residual coatings layers at the areas along nanowires where the contacts were to be made using direct electron beam milling to remove a layer of thickness about 5 nm before electrode patterning. But, the magnetoresistance measurements resulted in an extremely high and noisy voltage readings. This noise was found to be larger than the signal of the voltage drop across the nanowire, making the desired measurement unviable, although the current–voltage measurements demonstrate that the contacts were ohmic. Finally, the deposited gold electrodes might be not thick enough (around 35 nm) to adequately connect these circular cross-section nanowires with the electrodes, although the SEM analyses showed that these wires are properly connected. This needs more investigations with increasing the thickness of the deposited gold electrodes.

8-8 Chapter conclusions

Magnetic and electrical transport behaviour of template released isolated ferromagnetic nanowires were systematically investigated using highly sensitive MOKE magnetometry and MR measurements, respectively. In order to understand the magnetic properties of the materials that form templated nanowires, a range of electrodeposited thin films were investigated. These measurements were performed by applying the magnetic field at different angles with respect to the samples long axis.

The results of studying the magnetic properties at different locations of the electrodeposited thin films revealed their isotropic nature with a distribution of coercivity across the samples area that was more noticeable with decreasing the deposition time (film thickness). This was attributed to the surface roughness that occurs as a result of the formation of voids or defects during the fabrication process. These structural variations behaves as a pinning centers for domain walls during the application of magnetic field which leads to enhanced coercivity. For both materials investigated here a reduction in the coercivity was noticed with increasing deposition time. This was attributed to a reduction of surface roughness and the formation of multi-domain structure. The coercivity of NiFe films was found to be lower than the counterpart Ni films at small deposition times indicating the softer behaviour of NiFe films.

In contrast to the results reported in literature for two dimensional arrays of nanowires, the shape of the hysteresis loops obtained from MOKE measurements of isolated individual, bundles of closely packed and clusters of spaced nanowires were found to have high remanence ratio with a well defined switching behaviour indicating that the magnetic easy axis directed along the nanowire long axis. The switching fields obtained from these wires were much higher than their counterpart thin films indicating the dominate shape anisotropy on the nanowires behaviour. A distribution of switching fields was observed by repeating the measurements at different locations on these nanowires. The width of the switching field distributions for individual nanowires was attributed to differences in the surface structure and dimensional variations. For bundles of closely packed wires and clusters of more widely spaced wires, the switching fields depend upon the magnetostatic interactions among the nanowires. The variation in the behaviour between different bundles of wires depends upon the separation among the interacting wires. In tightly bunched wires, the switching field was reduced for larger number of wires, while for more widely spaced and poorly aligned nanowires the switching field was more variable and depends on the details of the nanowire assemblage.

At all angles investigated here, square hysteresis loops were obtained from the angular MOKE measurements of such isolated wires. This behaviour was attributed to the rotation of the easy axis of magnetisation with the direction of applied field or the difficulty in recognising the change in the shape of these loops due to the distortion occurred with other magneto-optical effects, or due to the detection of the transverse component of magnetisation within these nanowire samples. The angular dependence of switching fields for all the wires investigated here showed some agreement with the theoretical calculation of curling model.

In spite of all the technical difficulties associated with the electrical connection and measurements of isolated nanowires, the electrical transport properties of two bundles of 3 NiFe nanowires were measured using two probe magnetoresistance setup after electrically connecting these wires to prefabricated gold contact pads and the external measurement circuitry. The electrical resistance was found in a reasonable agreement with the theoretical estimations. The experimental MR data was in agreement with the theoretical predictions of the anisotropic magnetoresistance. The anisotropic magnetoresistance ratio for both small assemblages of nanowires was in agreement with the value of bulk $Ni_{60}Fe_{40}$ reported in literature. Inhomogeneous magnetic structures were obtained at remanence, where ~92% of the magnetic moments were aligned parallel to the nanowire's long axis when the field was reduced to zero in longitudinal measurements indicating that the shape anisotropy was dominating the behaviour. In contrast, about 65% for assemblage (A) and 30% for assemblage (B) of the magnetic moments were aligned away from the nanowire's long axis upon removing the magnetic field in the transverse measurements. This behaviour was attributed to the stray field originating from the surrounding wires or due to the nanowire's surface regularties or the difference between surface and bulk magnetisation behaviour

The MR measurments of two assemblages of 3 NiFe wires showed small and large features in the resistance profiles. The angular dependence of the switching field obtained from the large features were compared with the theoretical calculations from the curling model. An agreement was obtained at small angles and disagreement at higher angles indicated that the magnetisation reversal in these wires changed from curling to S-W models. This behaviour was in agreement with other results reported in the literature using other compositions of wires and other investigative techniques.

The extracted fields from the small and large features in the MR profiles were compared with each other and with the switching field obtained from MOKE measurments on the same assemblages of nanowires. A slight difference was obtained between the two assemblages of wires and was attributed to the differnce in the length of these wires or the complicated magnetostatic intractions in these assemblages. The field values obtained from the small features were found to be in reasonable agreement with the MOKE switching fields, whilst the fields extracted from the main features were found to disagree with the MOKE measurements. Since this was the first study to combine the MR and MOKE measurements on the same wires, these values were compared (discussed) with the literature that adopted the same investigative techniques and similar composition and dimension of nanowires. Agreements obtained from these comparisons indicate that the magnetisation at the surface behaves differently from the bulk in such isolated nanowires.

8-9 Chapter references

1. Wegrowe, J.-E., Kelly, D., Franck, A., Gilbert, S. & Ansermet, J.-P. "Magnetoresistance of Ferromagnetic Nanowires" *Phys. Rev. Lett.*, 82(18), 3681, 1999.
2. Vila, L., Piraux, L., George, J. M. & Faini, G. "Multiprobe magnetoresistance measurements on isolated magnetic nanowires" *Appl. Phys. Lett.*, 80(20), 3805, 2002.
3. Silva, R., Machado, T., Cernicchiaro, G., Guimarães, A. & Sampaio, L. "Magnetoresistance and magnetization reversal of single Co nanowires" *Phys. Rev. B*, 79(13), 134434, 2009.
4. Brundle R. C., Evans C. A., Jr. & Wilson S. "Encyclopaedia of materials characterisation" Butterworth-Heinemann, a division of Reed publishing Inc., USA,1992.
5. Lupu, N., Lostun, M. & Chiriac, H. "Surface magnetization processes in soft magnetic nanowires" *J. Appl. Phys.*, 107(9), 09E315, 2010.
6. Sharma, S., Barman, A., Sharma, M., Shelford, L. R., Kruglyak, V. V. & Hicken, R. J. "Structural and magnetic properties of electrodeposited Cobalt nanowire arrays" *Solid State Communications*, 149(39-40), 1650, 2009.
7. Etienne du Tremolet de Lacheissrie, Damien Gignoux, & Michel Schlenker "Magnetism Fundamentals" Page 37, Springer, USA, 2005.
8. Riccardo H. "Micromagnetic simulations of magnetostatically coupled Nickel

nanowires" *J. Appl. Phys.*, 90(11), 5752, 2001.

9. Sun, D.-L., Gao, J.-H., Zhang, X.-Q., Zhan, Q.-F., He, W., Sun, Y. & Cheng, Z.-H "Contribution of magnetostatic interaction to magnetization reversal of Fe_3Pt nanowires arrays: A micromagnetic simulation" *J. Mag. Mag. Mat.*, 321(18), 2737, 2009.
10. Fodor, P. S., Tsoi, G. M. & Wenger, L. E. "Investigation of magnetic interactions in large arrays of magnetic nanowires" *J. Appl. Phys.*, 103, 07B713, 2008.
11. Raposo, V., Garcia, J. M., Gonza, J. M. & Va, M. "Long-range magnetostatic interactions in arrays of nanowires" *J. Mag. Mag. Mat.*, 222, 227, 2000.
12. Aravamudhan, S., Singleton, J., Goddard, P. A. & Bhansali, S. "Magnetic properties of Ni–Fe nanowire arrays: Effect of template material and deposition conditions" *J. Physics D*, 42, 2009.
13. Suarez, O. J., Pérez, L. M., Laroze, D. & Altbir, D. "Magnetostatic interactions in cylindrical nanostructures with non-uniform magnetization" *J. Mag. Mag. Mat.*, 324(9), 1698, 2012.
14. Ghaddar, G., Gloaguen, F. & Gieraltowski, J. "Magnetic properties of ferromagnetic nanowire arrays: Theory and experiment" *J. Phys.: Conf. Series*, 200(7), 072032, 2010.
15. Lavín, R., Gallardo, C., Palma, J. L., Escrig, J. & Denardin, J. C. "Angular dependence of the coercivity and remanence of ordered arrays of Co nanowires" *J. Mag. Mag. Mat.*, 324(15), 2360, 2012.
16. Vazquez, M., Pirota, K., Torrejo, J., Navas, D. & Herna, M. "Magnetic behaviour of densely packed hexagonal arrays of Ni nanowires: Influence of geometric characteristics" *J. Mag. Mag. Mat.*, 294, 174, 2005.
17. Gubbiotti, G., Tacchi, S., Carlotti, G., Vavassori, P., Singh, N., Goolaup, S., Adeyeye, A., Stashkevich A. & Kostylev M. "Magnetostatic interaction in arrays of nanometric permalloy wires: A magneto-optic Kerr effect and a Brillouin light scattering study" *Phys. Rev. B*, 72(22), 1, 2005.
18. Ke-hua, Z., Zhi-gao, H. & Zhi-gao, C. "Numerical calculation of magnetization behaviour for Co nanowire array" *Trans. Nanoferrous Metals Soc.*, 18, 700, 2008.
19. Escrig, J., Lavín, R., Palma, J. L., Denardin, J. C., Altbir, D., Cortés, A & Gómez, H. "Geometry dependence of coercivity in Ni nanowire arrays" *Nanotech.*, 19(7), 075713, 2008.
20. Adeyeye, A. O., Bland, J. A. C., Daboo, C. & Hasko, D. G. "Magnetostatic interactions and magnetization reversal in ferromagnetic wires" *Phys. Rev. B*, 56(6), 3265,1997.
21. Velazquez, J. Garcıa, C. Vazquez, M. & Hernando, A. "Dynamic magnetostatic interaction between amorphous ferromagnetic wires" *Phys. Rev. B*, 54(14), 9903,1996.
22. Piccin, R., Laroze, D., Knobel, M. & Vargas, P. & Vazquez M. "Magnetostatic Interactions between two magnetic wires" *Euro. Phys. Lett.*, 78, 2007.
23. Sun, L., Hao, Y., Chien, C.-L. & Searson, P. C. "Tuning the properties of magnetic nanowires" *IBM J. Res. Devel.*, 49(1), 79, 2005.
24. Lin, S. W., Chang, S. C., Liu, R. S., Hu, S. F. & Jan, N. T. "Fabrication and magnetic properties of Ni nanowires" *J. Mag. Mag. Mat.*, 282, 28, 2004.
25. Jin, C. G., Liu, W. F., Jia C., Xiang, X. Q., Cai, W. L., Yao, L. Z. & Li, X. G. "High filling large area Ni nanowires arrays and the magnetic properties" *J. Cry. Gro.*, 258, 337, 2003.

26. Kafil, M. Razzeb, Fernando, M. F. Rhen & Saibal Roy "Magnetic properties of nickel nanowires: Effect of deposition temperature" *J. App. Phys.*, 105, 083922, 2009.
27. Imran, M. M. A. "Structural and magnetic properties of electrodeposited Ni nanowires" J. *Alloys and Compounds*, 455(1-2), 17, 2008.
28. Yeh, W. J. & Yang Kun "Fabrication of uniform magnetic nanowire array" *J. Phys.: Conference Series*, 61, 1299, 2007.
29. Qin, J., Nogue, J., Mikhaylova, M., Roig, A. & Mun, J. S. "Differences in the magnetic properties of Co, Fe and Ni 250-300 nm wide nanowires electrodeposited in amorphous anodized alumina templates" *Chem. Mater.*, 17,1829, 2005.
30. Beck, G., Petrikowski, K. & Khan, H. R. "Magnetism in magnetic nanowire arrays" *Microstructure Analysis in Materials Science*, *Freiberg*, 15, 2005.
31. Wernsdorfer, W., Doudin, B., Mailly, D., Hasselbach, K., Benoit, A, Meier, J., Ansermet, J.-Ph. & Barbara B. "Nucleation of magnetization reversal in individual nanosized nickel wires" *Phys. Rev. Lett.*, 77(9), 1873, 1996.
32. Rheem, Y., Yoo, B. B.-Y., Beyermann, W. P. & Myung, N. V. "Magnetotransport studies of a single nickel nanowire" *Nanotech.*, 18, 015202, 2007.
33. Rheem Y., Yoo B.-Y., Koo B. K., Beyermann W. P. & Myung N. V. "Synthesis and magnetotransport studies of single nickel-rich NiFe nanowire" *J. Phys. D: Appl. Phys.*, 40(23), 7267, 2007.
34. Dumpich, G., Krome, T. P. & Hausmanns, B. "Magnetoresistance of single Co nanowires" *J. Mag. Mag. Mat.*, 248(2), 241, 2002.
35. Oliveira, A. B. De, Silva, G. L. Da, Rezende, S. M. & Azevedo, A. "Magnetization reversal in single ferromagnetic rectangular nanowires" *J. Phys.: Conf. Series*, 200(7), 072023, 2010.
36. Oliveira, A. B., Rezende, S. M. & Azevedo, A. "Magnetization reversal in permalloy ferromagnetic nanowires investigated with magnetoresistance measurements" *Phys. Rev. B*, 78(2), 024423, 2008.
37. Adeyeye, A. O. & White R. L. "Magnetoresistance behaviour of single castellated $Ni_{80}Fe_{20}$ nanowires" *J. Appl. Phys.*, 95(4), 2025, 2004.
38. Adeyeye, A. O., Bland, J. A. C., Daboo, C., Lee, J., Ebels, U. & Ahmed, H. "Size dependence of the magnetoresistance in submicron FeNi wires" *J. Appl. Phys.*, 79(8), 6120, 1996.
39. Hausmanns B., Krome, T. P., Dumpich, G., Wassermann, E. F., Hinzke, D., Nowak, U. & Usadel, K. D. "Magnetization reversal process in thin Co nanowires" *J. Mag. Mag. Mat.*, 240, 297, 2002.
40. Fert, A. & Piraux, L. "Magnetic nanowires" *J. Mag. Mag. Mat."* 200, 338–358, 1999.
41. Pignard, S., Goglio, G., Radulescu, A., Piraux, L., Dubois, S., Declémy, A. & Duvail, J. L. "Study of the magnetization reversal in individual nickel nanowires" *J. Appl. Phys.*, 87(2), 824, 2000.
42. Ferré, R., Ounadjela, K., George, J., Piraux, L. & Dubois, S. "Magnetization processes in nickel and cobalt electrodeposited nanowires" *Phys. Rev. B*, 56(21), 14066–14075 1997.
43. Daub, M., Enculescu, I., Neumann, R. & Spohr, R. "Ni nanowires electrodeposited in single ion track templates" *J. Opt. Adv. Mat.*, 7(2), 865, 2005.

44. Vila L., George J. M., Faini G., Popa A., Ebels U., Ounadjela K. & Piraux L. "Transport and magnetic properties of isolated cobalt nanowires" *IEEE Trans. Mag.*, 38(5), 2577, 2002.
45. Liu, T., Wu, Y. H., Long, H. H., Liu, Z. J., Zheng, Y. K. & Adeyeye, A. O. "Transport properties and micromagnetic modelling of magnetic nanowires with multiple constrictions" *Thin Solid Films*, 505(1-2), 35, 2006.
46. Rheem Y., Yoo, B.-Y., Beyermann W. P. & Myung N. V. "Magneto-transport studies of single ferromagnetic nanowire" *Phys. Stat. Sol. (a)*, 204(12), 4004, 2007.
47. Rheem Y., Yoo B.-Y., Beyermann W. P. & Myung N. V. "Electro-and magneto-transport properties of a single CoNi nanowire" *Nanotech.*, 18(12), 125204, 2007.
48. Yoo, B., Rheem, Y., Beyermann, W. P. & Myung, N. V. "Magnetically assembled 30nm diameter nickel nanowire with ferromagnetic electrodes" *Nanotech.*, 17(10), 2512, 2006.
49. Jiles, D. "Introduction to Magnetism and Magnetic Materials" 2nd edition, Chapman and Hall/CRC, New York, Page 393, 1998.
50. Liu, Y., Shindo, D. & Sellmyer D. J. "Hand book of advanced magnetic materials" Tsinghua University Press, Springer, USA, 2005.
51. Cronin, S. B., Lin, Y.-M., Rabin, O., Black, M. R., Ying, J. Y., Dresselhaus, M. S., Gai, P. L., Minet, Jean-Paul & Issi, Jean-Paul "Making electrical contacts to nanowires with a thick oxide coating" *Nanotech.*, 13(5), 653, 2002.
52. Bozorth, R. M. "Ferromagnetism" John Wiley & Sons Inc., Hoboken, New Jersey,1951.
53. Chikazumi, Soshin "Physics of ferromagnetism" 2nd edition, Clarendon Press, Oxford, 1997.
54. Maruyama, K., Namikawa, K., Konno, M. & Maruyama, H. "Magnetization process of iron surface observed by transverse Kerr magnetometry" *J. Appl. Phys.*, 81(8), 5675, 1997.

Chapter nine

Results: Magnetic and magnetisation reversal behaviour of individual cylindrical and planar nanowires investigated by micromagnetic simulations

9-1 Introduction

Micromagnetic modelling is a rigorous approach widely used to investigate the magnetic properties of a wide range of ferromagnetic structures including nanodots, nanotubes and nanowires [1-12]. It has the ability to simulate hysteresis loops and to visualise the magnetisation configurations at any point during a field cycle. Micromagnetic simulations were systematically used here in order to understand the magnetic and magnetisation reversal behaviour of a range of individual cylindrical and planar (rectangular) $Ni_{81}Fe_{19}$ nanowires with the same length and different diameters and thicknesses/widths, respectively. The effects of nanowire geometry, diameter and thickness on the magnetic behaviour including the switching fields, squareness ratio and magnetic states before and during switching have been studied. The magnetisation reversal behaviour of these wires was investigated by applying two magnetic fields: parallel and perpendicular to the nanowire long axis. The micromagnetic results for the cylindrical and rectangular structures are discussed and compared with each other and with the experimental results obtained from MOKE and MR measurements presented earlier. The micromagnetic results for the angular dependence of magnetisation reversal are also discussed and compared with the experimental results and theoretical calculations of curling model of reversal.

9-2 Magnetic properties of individual cylindrical and planar $Ni_{81}Fe_{19}$ nanowires

Micromagnetic simulations using the OOMMF code [13] were systematically performed to investigate the magnetic behaviour of a range of cylindrical and planar $Ni_{81}Fe_{19}$ nanowires with different diameters and thicknesses/widths, respectively. The details of the methodology are presented in chapter five. The diameters and thicknesses of the wires studied were in the range between 10-200 nm with a fix length of 1 μm. This length was chosen with consideration to the available computer memory and the computation time.

The simulated structures are relatively short but the aspect ratio of these wires exceeds 5 and therefore no detrimental effects are expected in terms of self demagnetising effect. Even with a 1 µm length, the computation time and memory available were insufficient to make a reasonable study of nanowires with diameters above 200 nm in the time available. The simulations were carried out by applying a large magnetic field along the long axis of the nanowires oriented at a slight tilt with respect to the wire axis of around 1^{o}. The tilting of the applied field was used in micromagnetic simulations of nanowires and nanotubes to break the symmetry of the magnetic structure and hence to avoid numerical artefacts in the simulations and hence yield stable meaningful results [1,2]. The magnitude of the maximum magnetic field and the field steps were chosen according to test simulations performed to roughly evaluate the hysteresis shape. In full simulations, the magnetic field was decreased from saturation in steps of 5 to 10 Oe through zero to the opposite sign. In the following subsections, the effect of nanowire geometry on the magnetic behaviour is studied.

9-2.1 Magnetic state of individual cylindrical $Ni_{81}Fe_{19}$ nanowires

Figure 9.1 show examples of normalised hysteresis loops obtained from simulations of cylindrical $Ni_{81}Fe_{19}$ nanowires with different diameters and the same length when the magnetic field was applied nominally parallel to the nanowire long axis. As expected, the hysteresis loops for nanowires with diameter less than 100 nm are square shaped with a well defined switching behaviour, indicating the dominant shape anisotropy on the magnetisation behaviour owing to their high aspect ratio. For nanowires with diameters greater than 175 nm, the loop shape is quite complicated showing different switching behaviours. For these loops, the switching field and remanent magnetisation are strongly dependent on the wire diameter.

To investigate the effect of nanowire diameter on the magnetic properties, the switching fields and the remanent magnetisation were plotted against the nanowires diameter, as

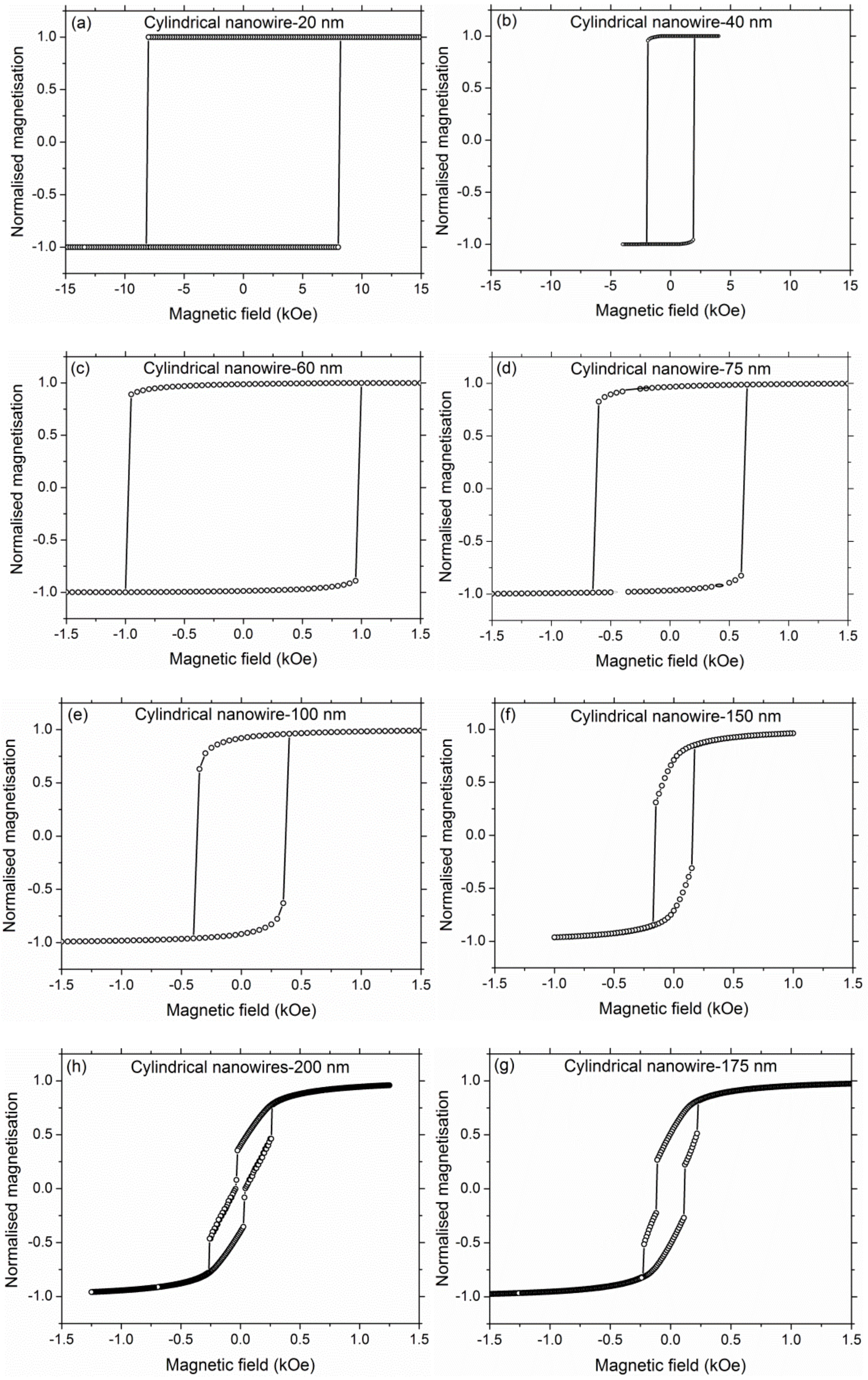

Figure 9.1 Normalised hysteresis loops obtained from simulations of cylindrical $Ni_{81}Fe_{19}$ nanowires with different diameters and the same length using the OOMMF code when the field was nominally applied parallel to the nanowires long axis. The wire diameters are marked in the titles. Note the difference in the field scale bar of the loops.

shown in Figure 9.2. Clearly, for nanowires with small diameters the switching fields decrease very rapidly with increasing nanowire diameter up to 40 nm, as shown in Figure 9.2(a). For nanowires with larger diameters (>50 nm), the switching field decreases more slowly, as demonstrated in the inset of Figure 9.2(a). For nanowires with diameter up to 100 nm, the squareness ratio is close to unity, as shown in Figure 9.2(b). For diameters greater than 100 nm, the squareness ratio decreases rapidly above 125 nm.

The reduction in the switching fields with increasing nanowire diameter may be attributed to the formation of multi-domain structures or moment rotations within the magnetic structure due to the reduction in the shape anisotropy with increasing nanowire diameter. The effect of nanowire diameter on the magnetic properties has been extensively investigated experimentally and theoretically elsewhere [14-25]. However, here the simulations are of individual nanowires with no magnetostatic interactions with other nearest nanowires as observed in literature in two dimensional arrays of wires. These wires have no defects or impurities, therefore the reduction in the squareness ratio with increasing nanowire diameters can be attributed to the effect of the demagnetising field which increases with increasing nanowires diameter.

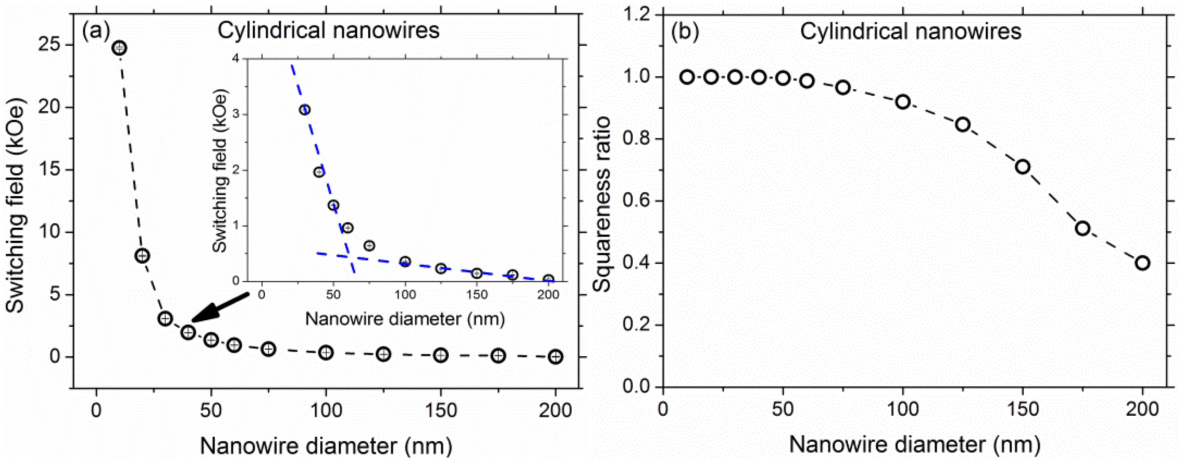

Figure 9.2 (a) Switching field, and (b) squareness ratio obtained from the loops of cylindrical $Ni_{81}Fe_{19}$ nanowires as a function of their diameter. The inset shows detail in the data. The dashed lines provide a guide to the eye.

The remanence ratio provides one useful measure of the magnetisation within the nanowires. However, the switching behaviour is more complex in wires with diameters greater than 100 nm. Therefore, the magnetisation volume involved in sharp switching has also been determined in order to interrogate the magnetisation process. The ratio of the change in the magnetisation during the switching behaviour, ΔM, to the total saturation magnetisation, M_{Total}, was used to define the magnetic state during the switching behaviour, $\frac{\Delta M}{M_{Total}}$. These terms are shown in the loop example presented in Figure 9.3(a).

The $\frac{\Delta M}{M_{Total}}$ state was obtained as a function of the nanowire diameter and is shown in Figure 9.3(b). It is clear that the magnetisation fraction involved in sharp switching is nearly constant up to 60 nm then decreases with increasing nanowires diameter up to 150 nm. For diameters greater than 150 nm, the fraction was nearly constant at their lowest values (60%). This indicates that the single domain switching volume decreases with increasing nanowire diameter. This behaviour can again be consistently attributed to the formation of more complex domain structure in larger diameter (>150 nm) nanowires.

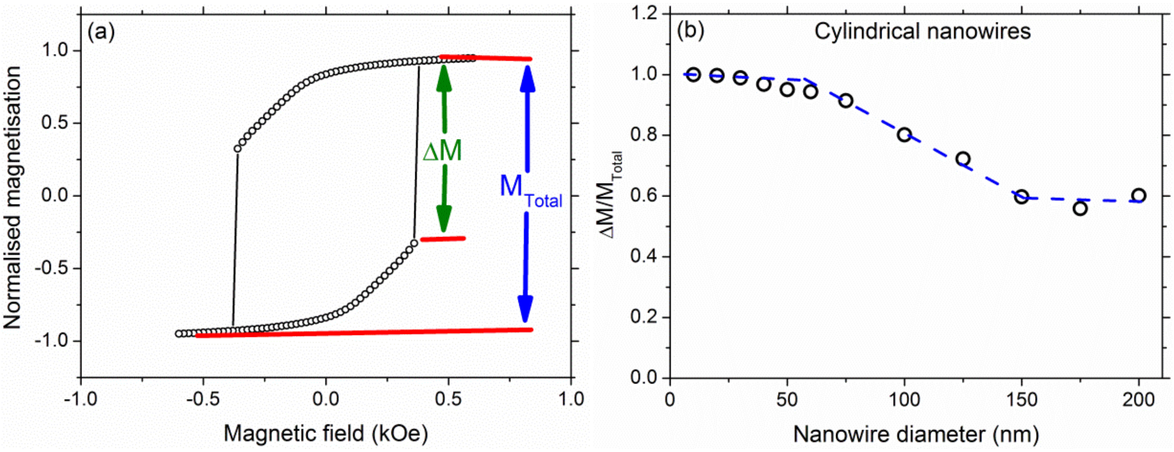

Figure 9.3(a) Definition of the magnetic state during the switching behaviour in a loop example, and (b) magnetic state during the switching behaviour as a function of the nanowire diameter, the dashed line provide a guide to the eye.

9-2.2 Magnetic properties of individual planar $Ni_{81}Fe_{19}$ nanowires

Normalised hysteresis loops were obtained from simulations of planar $Ni_{81}Fe_{19}$ nanowires with different thicknesses/widths and the same length are presented in Figure 9.4. As with the cylindrical cross-section nanowires the hysteresis loops of these square-section nanowires are square shaped with a very high remanent magnetisation for nanowire dimensions up to 100 nm. For nanowire dimensions greater than 175 nm, the loops are complicated showing some different features with different switching fields. The switching field and remanent magnetisation of these loops are strongly dependent on the nanowire dimensions.

Figure 9.5 summarise the effect of nanowire thickness/width on the switching field and remanent magnetisation behaviour. The planar nanowires show very similar trends to those seen for the cylindrical cross-section nanowires. Two different regimes were identified. For nanowires with small thickness/width (<40 nm), the switching field decreases very rapidly with increasing nanowire dimension, as shown in Figure 9.5(a). For larger dimensions (>50 nm), the switching field decreases much more slowly, as shown in the inset of Figure 9.5(a). This behaviour is in a good agreement with simulated individual rectangular Ni nanowires reported in the literature [9]. This behaviour again might be related to the tendency of these wires to form single domain structures or due to the increase of the shape anisotropy when decreasing the nanowire cross-sectional dimensions. Figure 9.5(b) shows the squareness ratio as a function of nanowire thickness/width. For nanowires with dimensions up to 100 nm, the squareness ratio is close to 1.0, and then it decreases up to the maximum dimensions of 200 nm. This can be attributed again to the effect of demagnetising field which leads to the formation of multi-domain structures.

To better understand the magnetisation behaviour as a function of magnetic field, the change in the orientation of the magnetic moments within the nanowire prior to the main

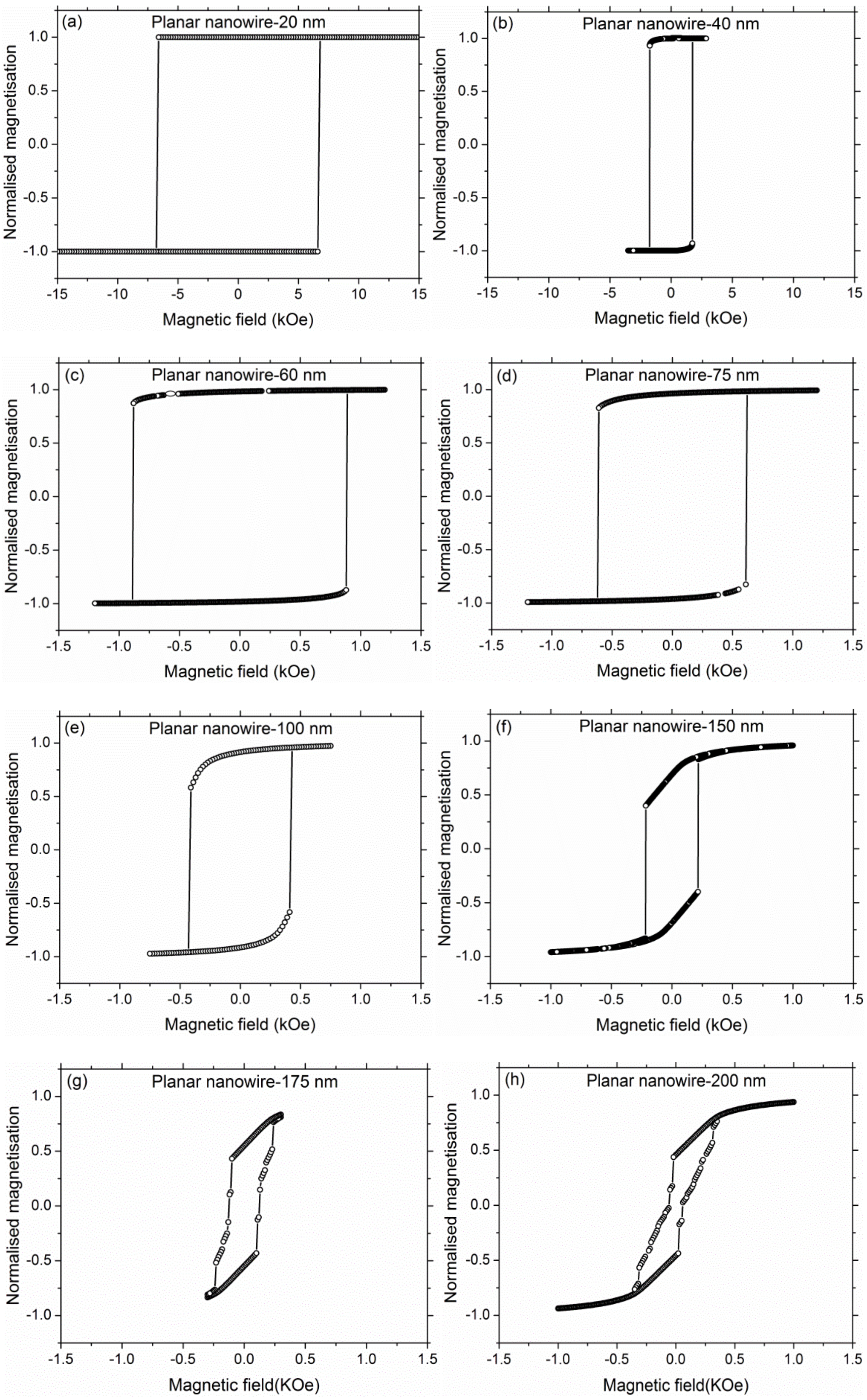

Figure 9.4 Normalised hysteresis loops obtained from simulations of planar $Ni_{81}Fe_{19}$ nanowires with different thicknesses/widths using the OOMMF software when the field was applied nominally parallel to the nanowire long axis. The thicknesses/widths are marked in the loop titles. Note the difference in the field scale bar of the loops.

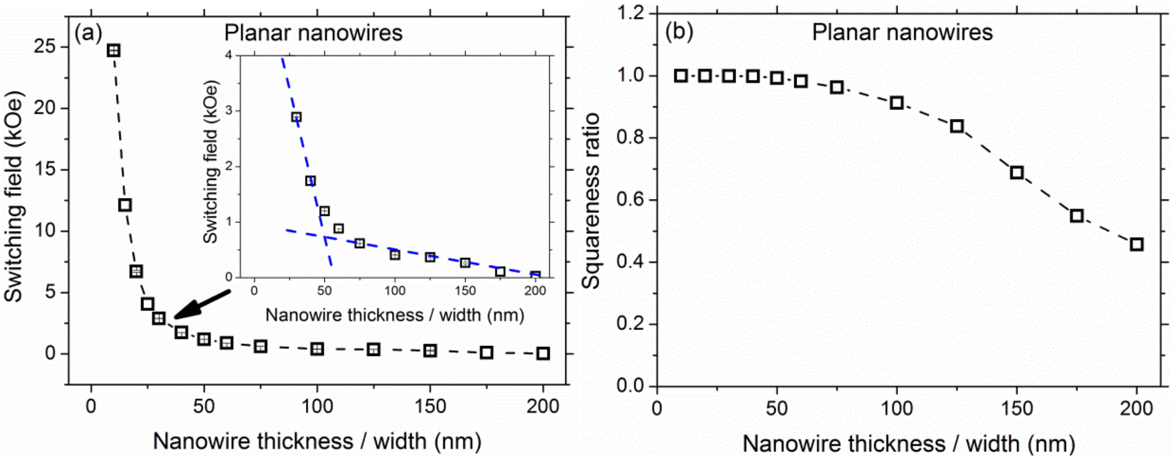

Figure 9.5 (a) Switching field, and (b) squareness ratio as a function of nanowire thickness/width. The inset shows detail in the data. The dashed lines provide a guide to the eye.

switching event (reversal) had been obtained from the simulations performed in this field region. This was carried out by sweeping the magnetic field up and down in the field region where the magnetic moments start to rotate and take up to just before the switching behaviour. Examples of the behaviour are shown in Figure 9.6 for four different dimensions of wires. These simulations demonstrate that the changes in the magnetisation within the wires are largely reversible with some complications occurring for thicker (>150 nm) nanowires.

As for the cylindrical cross-section nanowires, the ratio of the change in the magnetisation during the switching behaviour to the total saturation magnetisation, $\frac{\Delta M}{M_{Total}}$, was also investigated. Figure 9.7 shows the fractional magnetisation involved in the switching behaviour as a function of nanowire thickness/width. Again, the magnetisation fraction was constant up to 60 nm and then drops between 60 nm and 125 nm. For nanowires with diameter greater than 125 nm, the magnetisation fraction appears constant at about 65%. This behaviour indicates the formation of domain structures as the system moves from a simple single domain state to a multi-domain structure.

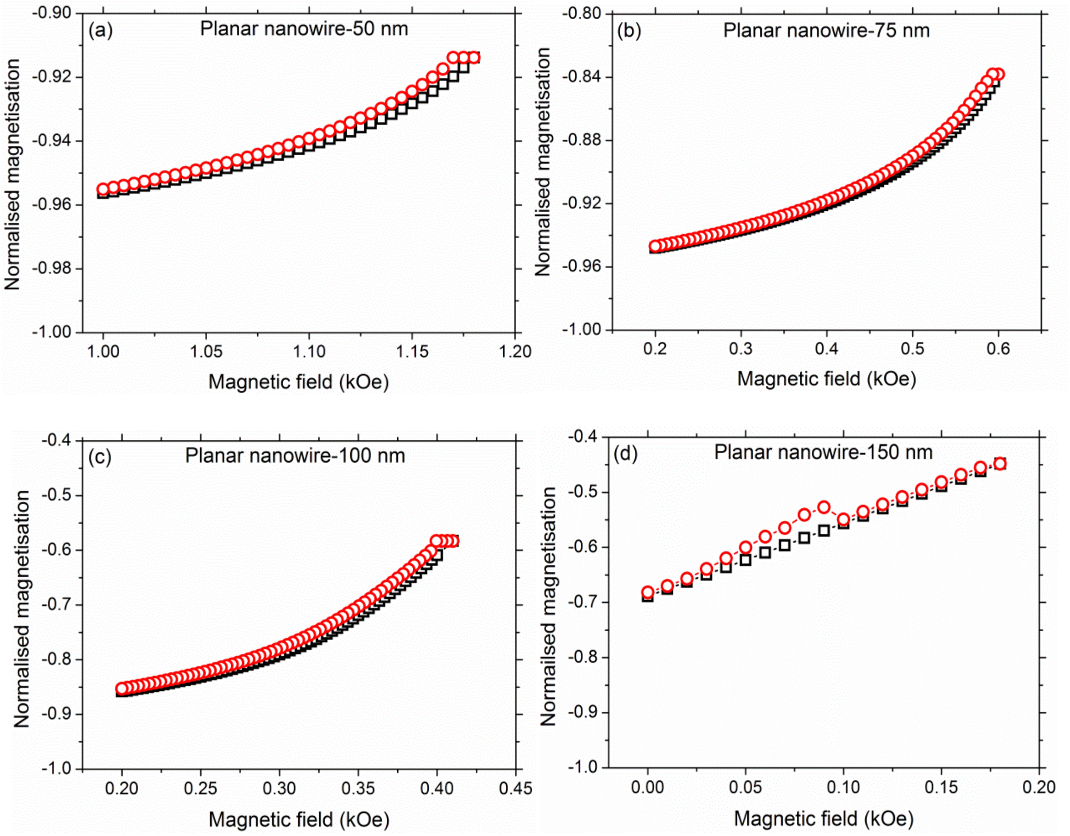

Figure 9.6 The magnetisation behaviour obtained as a function of applied field below the switching behaviour of different nanowire thicknesses as indicated in the loops title. Note the difference in the vertical scales.

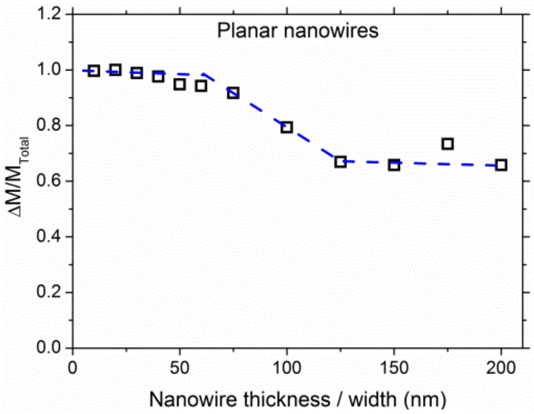

Figure 9.7 The magnetic state during the switching behaviour as a function of the nanowire thickness/width. The dashed line provides a guide to the eye.

9-2.3 Comparison of magnetisation behaviour between cylindrical and planar wires

In order to compare the effect of nanowires geometry on the magnetic behaviour, the switching fields of the cylindrical and square cross-section nanowires were plotted as a function of nanowires diameter/thickness in Figure 9.8. The switching fields behaviour for

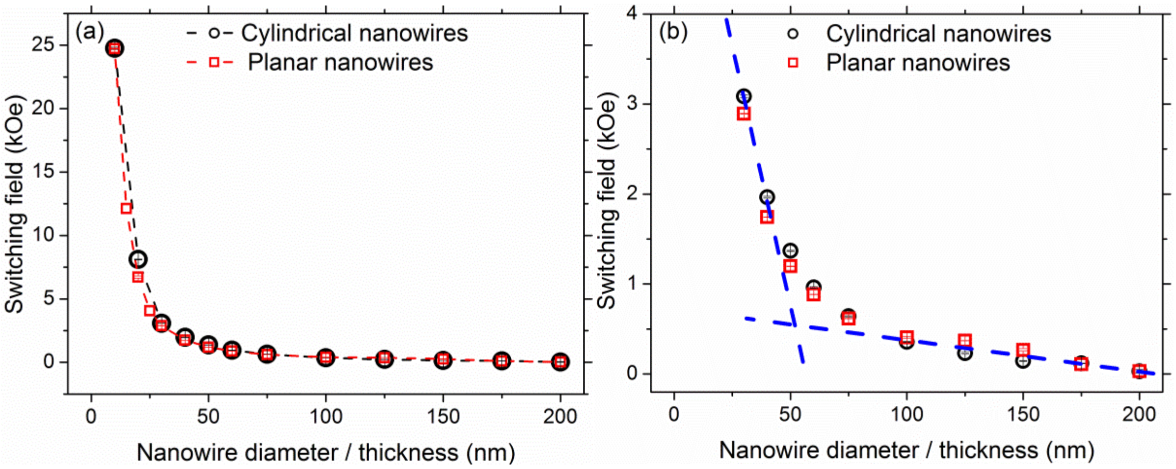

Figure 9.8(a) Switching field as a function of nanowire diameter/thickness, and (b) zoom in the measurements. The dashed lines provide a guide to the eye.

both geometries of wires were almost identical. The switching field of the cylindrical nanowires were very slightly higher than the switching field of planar nanowires (see Figure 9.8(b)) at the smallest cross-sections. Since, the magnetic parameters used for the simulations and the size of the wires are the same, therefore it is reasonable to expect that the slight difference in the switching fields are related to the discretisation effect. This effect may appear as a result of the step wise curving surfaces used to create the cylindrical wires meshes, which was more noticeable with decreasing the nanowires diameter. This staircase-like structuring may add complexity to the domain structure and hence slightly increasing the magnetic field required to switch the magnetisation from one state to another. Moreover, the existence of sharp corners in the planar nanowires may prevent the occurrence of the vortex state easily at the edges of the wires.

The effect of nanowire geometry on the remanent magnetisation was also investigated. The squareness ratio of both geometries as a function of nanowires diameter/thickness was plotted in Figure 9.9(a). The general behaviour for both geometries was again the same. There was no noticeable difference between the two geometries of nanowires with diameters up to 150 nm.

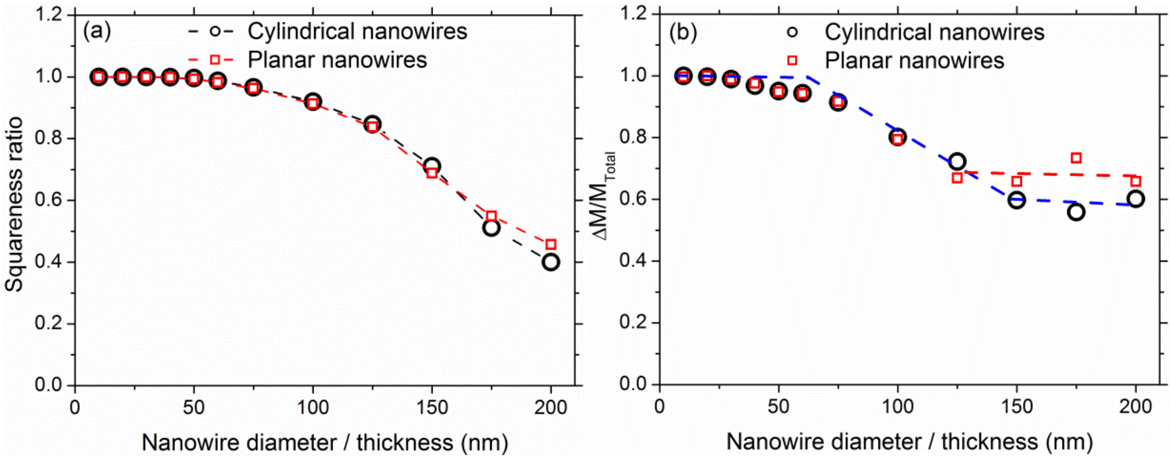

Figure 9.9(a) Squareness ratio, and (b) the magnetic state during the switching behaviour as a function of nanowire diameter/thickness for both geometries of nanowires. The dashed lines provide a guide to the eye.

However, the planar nanowires with diameters greater than 150 nm show slightly higher squareness ratio than their cylindrical counterparts. This behaviour reveals the slight difference in the domain structures within these wires. Figure 9.9(b) shows the change in the magnetic state during the switching behaviour for both cylindrical and planar nanowires as a function of their diameter/thickness. For both geometries, the behaviour is almost identical up to 125-150 nm. Above 150 nm, the cylindrical nanowires show slightly lower values than for planar wires. This again may be consistently attributed to the difference in domain structures formed with increasing wire diameter.

9-2.4 Comparison of simulated magnetisation behaviour with experimental results

In order to get a full understanding of the magnetisation behaviour of thick nanowires, the switching fields obtained from simulation of a cylindrical $Ni_{81}Fe_{19}$ nanowire of 200 nm diameter were compared with the switching field of their counterpart nanowires obtained experimentally from MR and MOKE measurements. It should be noted that the composition of the nanowires investigated experimentally was approximately $Ni_{60}Fe_{40}$.

As mentioned earlier in this chapter, two different switching behaviours were noticed in the loops obtained from the simulation of cylindrical and planar cross-section nanowires of greater than 175 nm diameter/thickness (see for example Figure 9.1(h) and 9.2(h)). The extracted switching fields from the loop obtained for a cylindrical nanowire with diameter of 200 nm are approximately 31 Oe and 263 Oe (see Figure 9.1(h)). These two switching events indicate that there are at least two magnetisation features in the reversal of such relatively thick nanowire.

The switching fields obtained from the large and small features in the MR measurements of the NiFe wires of similar dimensions were 16-24 Oe and 100-240 Oe (see for example Figures 8.22 and 8.17), respectively. The average switching fields obtained from MOKE measurements of individual and bundles of 3 NiFe nanowires was around 165 Oe and 134Oe (see Figures 8.5(b) and 8.7(a)), respectively. Comparing all these switching fields with the switching fields obtained from the simulations, reasonably good agreement is observed, although the simulation values are higher than the experimental results. It has been reported elsewhere that the switching fields of arrays of Ni, Fe and Co nanowires decreases with increasing the temperature from liquid helium to room temperature [14-16,25]. Thus, the difference between the experimental and simulation switching field values may reasonably attributed to the temperature difference between the room temperature measurements and zero temperature simulations. The nanowire compositional variations may have also an influence on the switching field difference. This is due to the difference in the saturation magnetisation and hence the demagnetising field. Moreover, the simulated nanowires are free from impurities, defects and structural variations that were noted in the real nanowires (discussed in chapter six). These imperfections can distort the spin configuration structure and give different values of switching fields as discussed in Ref [26].

Both micromagnetic simulations and the MR setup are techniques sensitive to the orientation of the whole magnetic moments within the bulk of the wires, whilst the MOKE is sensitive to the surface magnetisation, the micromagnetic simulations may therefore also suggest that the magnetisation at the surface of thick nanowires behaves differently from their bulk.

To confirm this result, the magnetic moment distributions obtained during the magnetisation reversal of this nanowire is presented in Figures 9.10 and 9.11. These micromagnetic spin structure snapshots represent a cross-section through the centre of nanowire along its axis and normal cross-sections of the left, middle, and right hand ends of the nanowire, respectively at different field strengths, as marked in the loop shown in Figure 9.10(a). The spin configuration in snapshot (i) is obtained at saturation magnetisation, whilst snapshot (ii) at remanence and (iii), (iv), (v) & (vi) are obtained during the reversal behaviour (switching events). As expected, the magnetic moments were aligned parallel to the applied field at saturation magnetisation with the existence of vortex states at both ends of the wire. At remanent magnetisation (ii), the nanowire shows multi-domain structure and the magnetic moments are in a vortex state along the length of the wire. During the first switching behaviour (iii) to (v), very complicated domain structures are obtained. During the second switching behaviour (vi), the magnetic moments change their orientation to the opposite direction forming again vortex state at both ends of wires. These snapshots however reflect the complexity in the spin structure in such nanowire, which further support the difference in the magnetic moment behaviour between the surface and the bulk of the nanowires. Thus, it may be concluded that the magnetisation behaviour at the surface of thick nanowires reverse differently from their core. This explains the previously disparate observations for MR and MOKE for other researchers and the combined MR and MOKE study presented here. The micromagnetic spin structures also indicate that the reversal is not a simple curling-like behaviour, although the angular switching field dependence is compared with curling later in the following section.

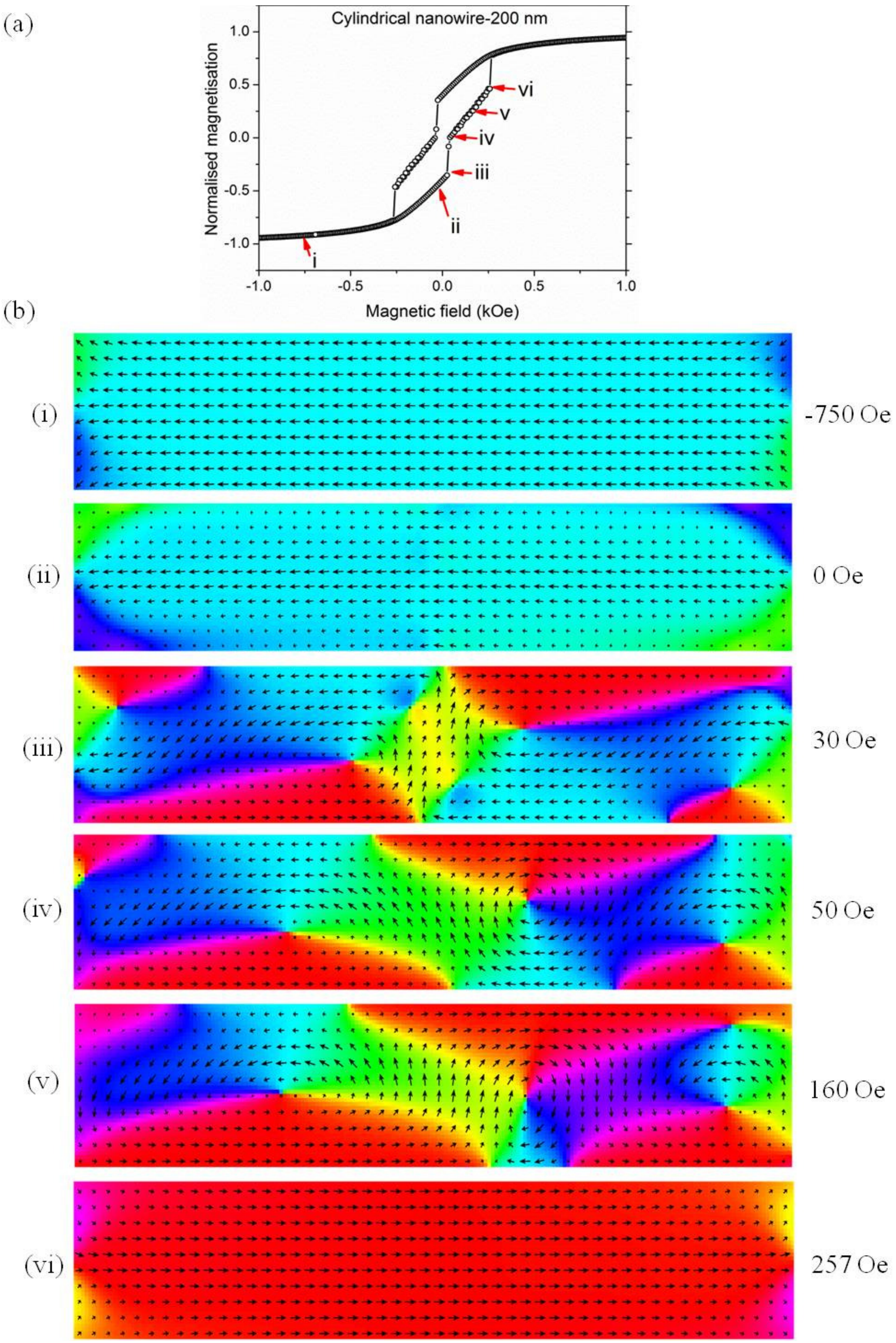

Figure 9.10(a) Normalised hysteresis loop obtained from simulations of cylindrical $Ni_{81}Fe_{19}$ nanowire with 200 nm diameter showing the positions at which the spin configurations were obtained, and (b) snapshots of magnetic moment distributions along the centre of the nanowires long axis at different field strengths. The colour variation represents the x-z angle of the spin.

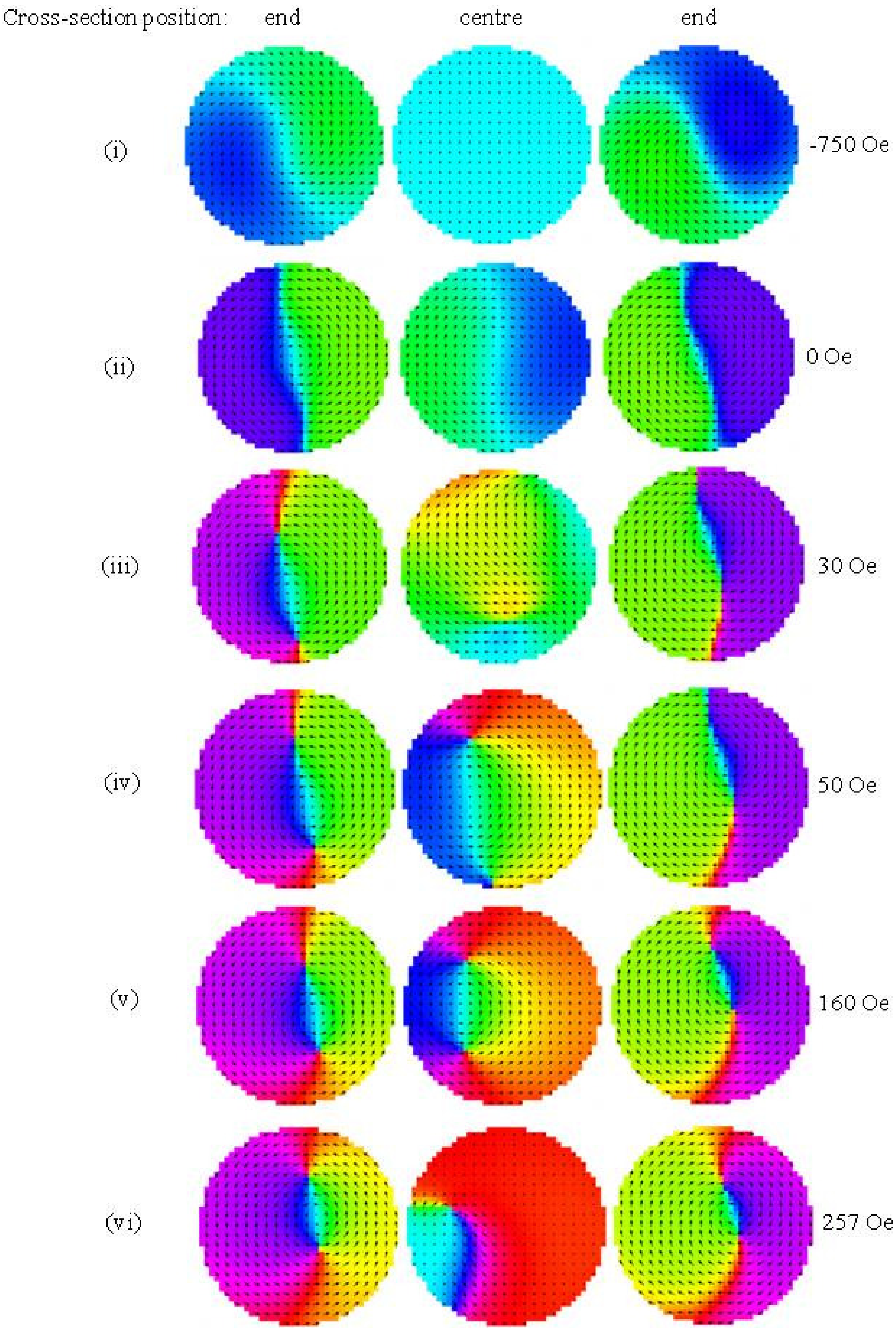

Figure 9.11 Snapshots of magnetic moment distributions obtained at normal cross-section of the left end, middle, and right end of the cylindrical $Ni_{81}Fe_{19}$ nanowire with 200 nm diameter at different field strengths. The colour variation represents the x-y angle of the spin.

9-3 Angular dependence of magnetisation reversal

In order to understand the details of the magnetisation reversal behaviour and the underlying mechanism in these wires, a series of micromagnetic simulations were performed to investigate the angular dependence of switching fields and remanent magnetisation for both cylindrical and planar $Ni_{81}Fe_{19}$ nanowires with a range of diameters and thicknesses, respectively. Then, the angular dependence of switching fields for the thicker nanowire was compared with the curling mode of reversal and with their counterpart nanowire measured experimentally by MOKE magnetometry.

9-3.1 Angular dependence of magnetisation reversal in cylindrical and planar wires

Since, there is no simple method within the OOMMF software to rotate the nanowire with respect to the axis of the applied magnetic field, the simulations of angular dependence were performed by combining magnetic fields along two orthogonal directions with respect to the nanowires long axis. One was applied along the long axis of the nanowire with a strength of, H_x, and the other was applied normal to the nanowire long axis with a strength of, H_y, as schematically shown in Figure 9.12.

Using trigonometric relations, the vector sum of the magnetic field along the selected angle, θ, with respect to the nanowire long axis was determined using the following relation:

$$H_\theta = \sqrt{H_x^2 + H_y^2} \tag{9-1}$$

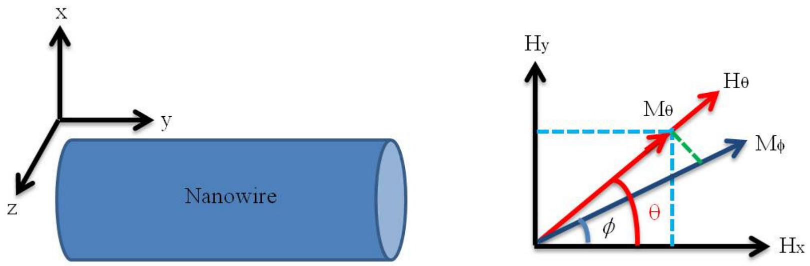

Figure 9.12 Schematic diagrams showing the two fields applied along and normal to the nanowire long axis and the projections of the two components of the magnetisation. The calculated field at a specific angle was then defined within the OOMMF code to study the angular dependence of magnetisation reversal in individual $Ni_{81}Fe_{19}$ nanowires.

In response to this magnetic field the magnetisation changes within the nanowire to a net state, M_ϕ. For hysteresis loops the component of M_ϕ, called M_θ, along H_θ, was calculated. The angle ϕ, can be obtained from:

$$tan\phi = \frac{M_y}{M_x} \quad 9\text{-}2$$

The magnetisation along the angle, $\emptyset$, was obtained using the following relation:

$$M_\phi = \sqrt{M_x^2 + M_y^2} \quad 9\text{-}3$$

whilst, the magnetisation along the angle, θ, is given by:

$$M_\theta = M_\phi \cos(\theta - \phi) \quad 9\text{-}4$$

Accordingly, the magnetic field, H_θ, was defined in the *micromagnetic input files, MIF,* within the OOMMF code to simulate the hysteresis loops at different angles. Then, the hysteresis loops and the angular dependence of the switching fields and remanent magnetisation were calculated using the relations 9-1 to 9-4.

Figures 9.13 to 9.15 show three typical examples of normalised hysteresis loops obtained from the simulations of three different dimensions (30, 75 and 150 nm) of planar $Ni_{81}Fe_{19}$ nanowires for different angles (0°, 15°, 30°, 45°, 60°, 75°, and 90°).

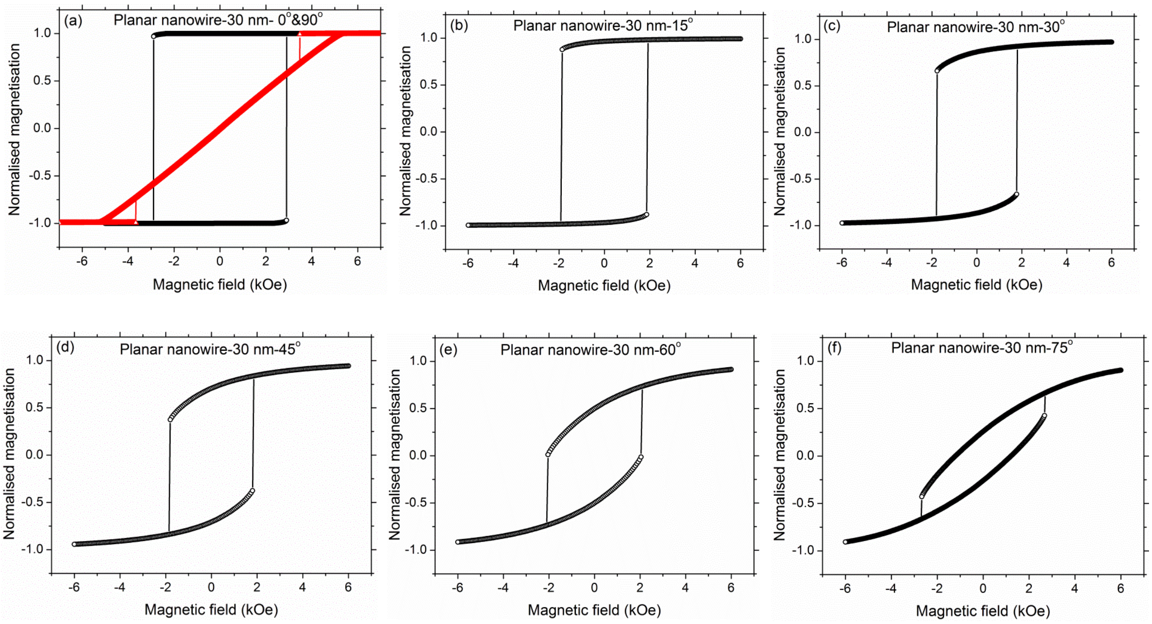

Figure 9.13 Normalised hysteresis loops obtained from simulations of planar $Ni_{81}Fe_{19}$ nanowires with dimensions of 30 nm at different angles as indicated in the loops title.

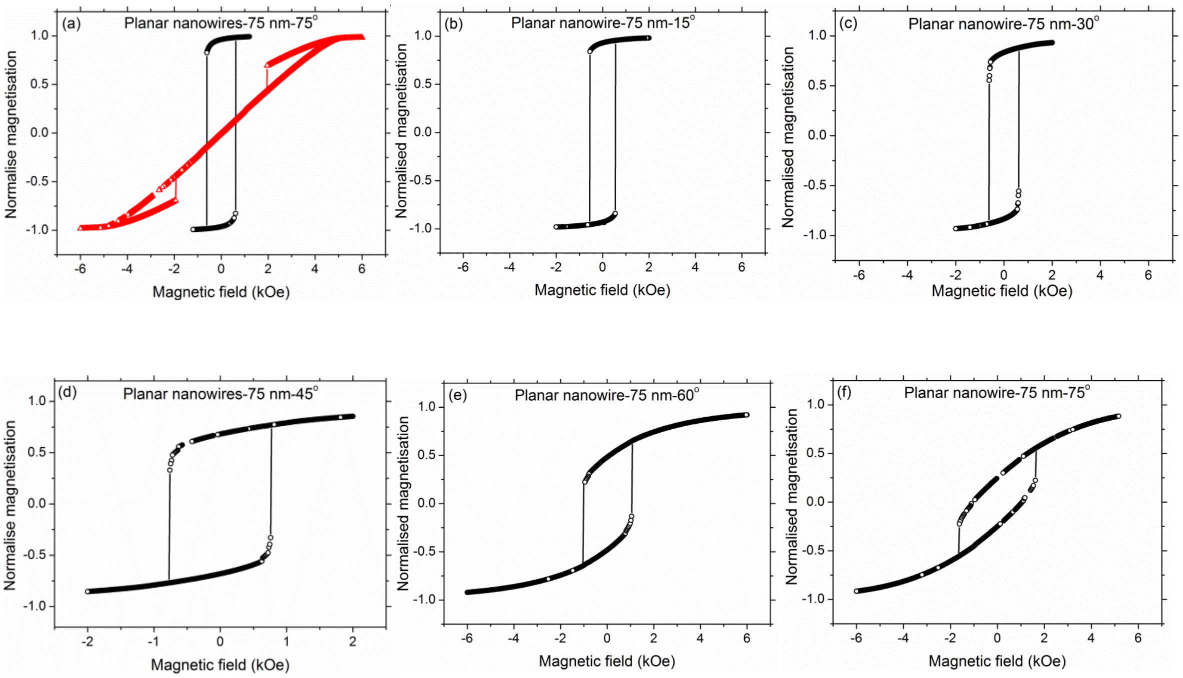

Figure 9.14 Examples of normalised hysteresis loops obtained from simulations of planar $Ni_{81}Fe_{19}$ nanowires with dimensions of 75 nm at different angles as indicated in the loops title.

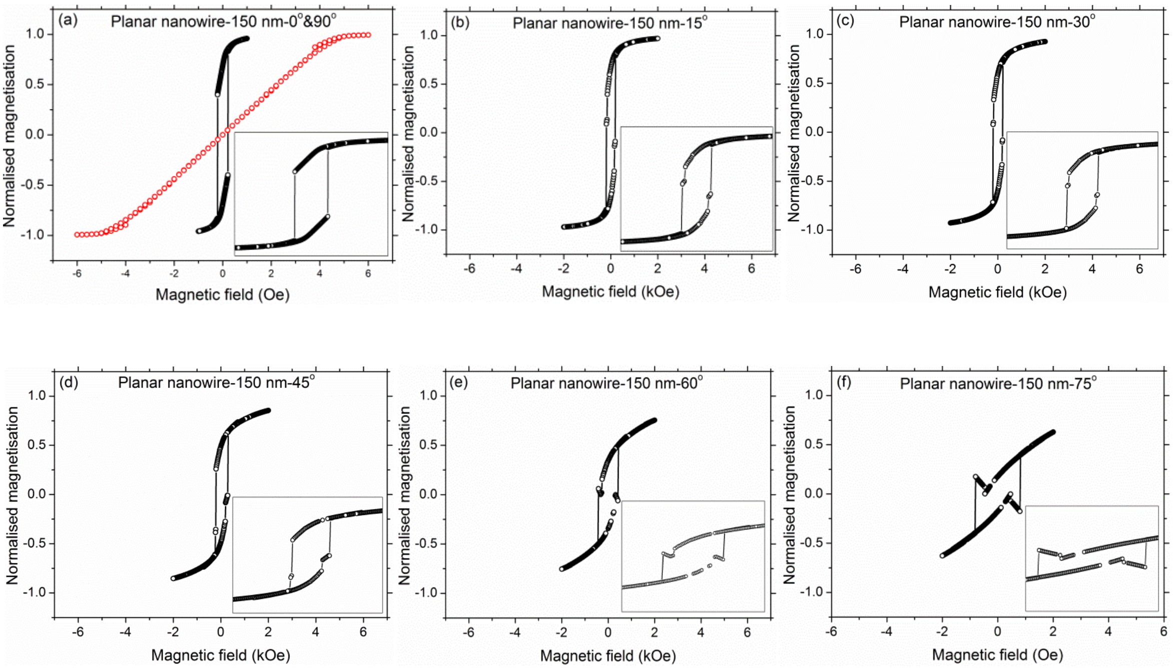

Figure 9.15 Examples of normalised hysteresis loops obtained from simulations of planar $Ni_{81}Fe_{19}$ nanowires with dimensions of 150 nm at different angles as indicated in the loops title. The insets are zoom in the loops.

For both geometries of cylindrical and square cross-section nanowires, the hysteresis loops have a well-defined switching behaviour up to 125 nm diameter/thickness and for all angles investigated here. For nanowires with diameters/thicknesses greater than 150 nm, the loops shape are complicated showing different switching features with increasing the nanowires angle as shown in Figure 9.15 and their insets. With increasing angle, the loops become less rectangular for all diameters/thicknesses. From all these results, a strong dependence of the remanent magnetisation and the switching field was observed.

The angular dependence of the remanent magnetisation of four different diameters/thicknesses (30, 50, 100, and 150 nm) are plotted in Figure 9.16. There is no appreciable difference in the remanent magnetisation between the two geometries for all the angles investigated. There is a slight reduction in the remanent magnetisation with increasing the nanowire diameter above 100 nm. This reduction was noticed for all angles of measurement. As an example, the remanence ratio is ~1 for nanowires up to 100 nm and decreases to ~0.7 for nanowires with 150 nm diameter when the field was applied parallel

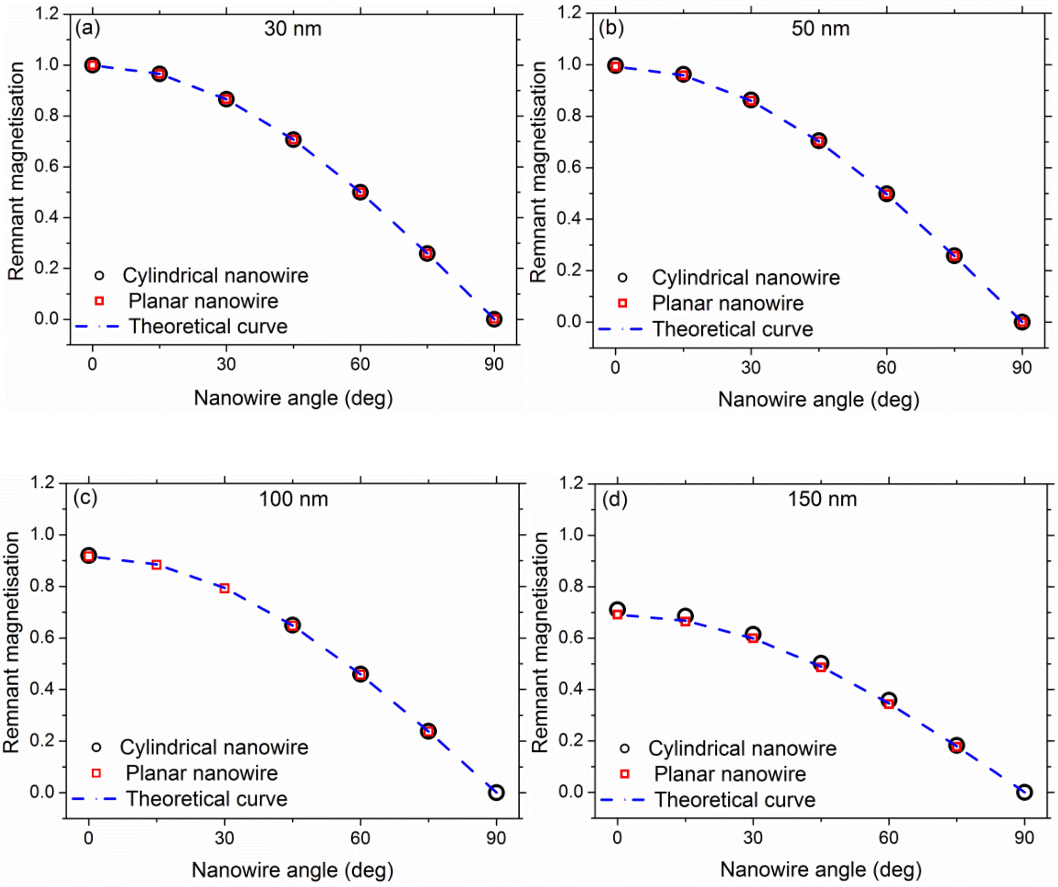

Figure 9.16 Remanent magnetisation as a function of nanowires angle for both cylindrical and planar nanowires with four different examples of diameters/thicknesses as indicated in the figure titles. The dashed lines are theoretical fitting curves from equation 9-5.

to the nanowire long axis. The remanent magnetisation was highest when the field was applied parallel to the nanowire long axis. It then decreases continuously with increasing angle and vanishes for field applied at an angle of 90°.

The slight reduction in the remanent magnetisation with increasing nanowire diameter/thickness can again be attributed to the formation of multi-domain structures, as described in the previous sections. The reduction in the remanent magnetisation with increasing the nanowire angles can be explained as follows:

When the nanowire is parallel to the applied magnetic field, H_θ, and upon removing the field, the remanence ratio, as expected, show the highest value in all nanowires investigated. This is because the magnetic moments are largely oriented along the easy axis of magnetisation owing to the high shape anisotropy. Increasing the field angle with respect to the easy axis of magnetisation and upon removing the applied field, the magnetic moments relax and reoriente again along the nanowire long axis due to the dominance of shape anisotropy on the behaviour, thus reducing the remanent magnetisation at that direction with increasing the nanowire angles.

Returning to the schematic diagram presented in Figure 9.12, the remanent magnetisation, M_R, at any angle, θ, can be approximated by the projection of the magnetisation along the direction of the measurements using the following relation [27-29]:

$$M_R(\theta) = M_R(\|)|cos\theta| \qquad 9\text{-}5$$

where, $M_R(\|)$, is the remanent magnetisation at an angle $\theta=0$ (i.e. when the magnetic field, H_θ, is parallel to the nanowire long axis). Using the above approximation, an excellent agreement was obtained for all diameters/thicknesses and angles investigated here as shown by the fitting curves in Figure 9.16. This indicates that the easy axis of magnetisation is maintained along the long axis of the nanowires due to the dominant shape anisotropy on the behaviour.

The switching fields obtained from the angular dependent simulations for both geometries of nanowires were plotted as a function of angle of the nanowire's long axis in Figure 9.17 for four different diameters/thicknesses (30, 50, 100, and 150 nm). Similar behaviour is clearly seen for both geometries of nanowires. For all angles investigated, the thin cylindrical nanowires (30 and 50 nm) show slightly higher switching fields than their planar counterparts. This may again related to the discretisation effect of the cylindrical nanowires as discussed in the previous sections or due to the existence of sharp corners in the planar wires which may prevent the occurrence of the vortex state at the edges of the wires.

From these figures, two regimes were identified. For very thin nanowires less than 30 nm, a sharp decrease in the switching field was noticed with increasing the nanowire angle

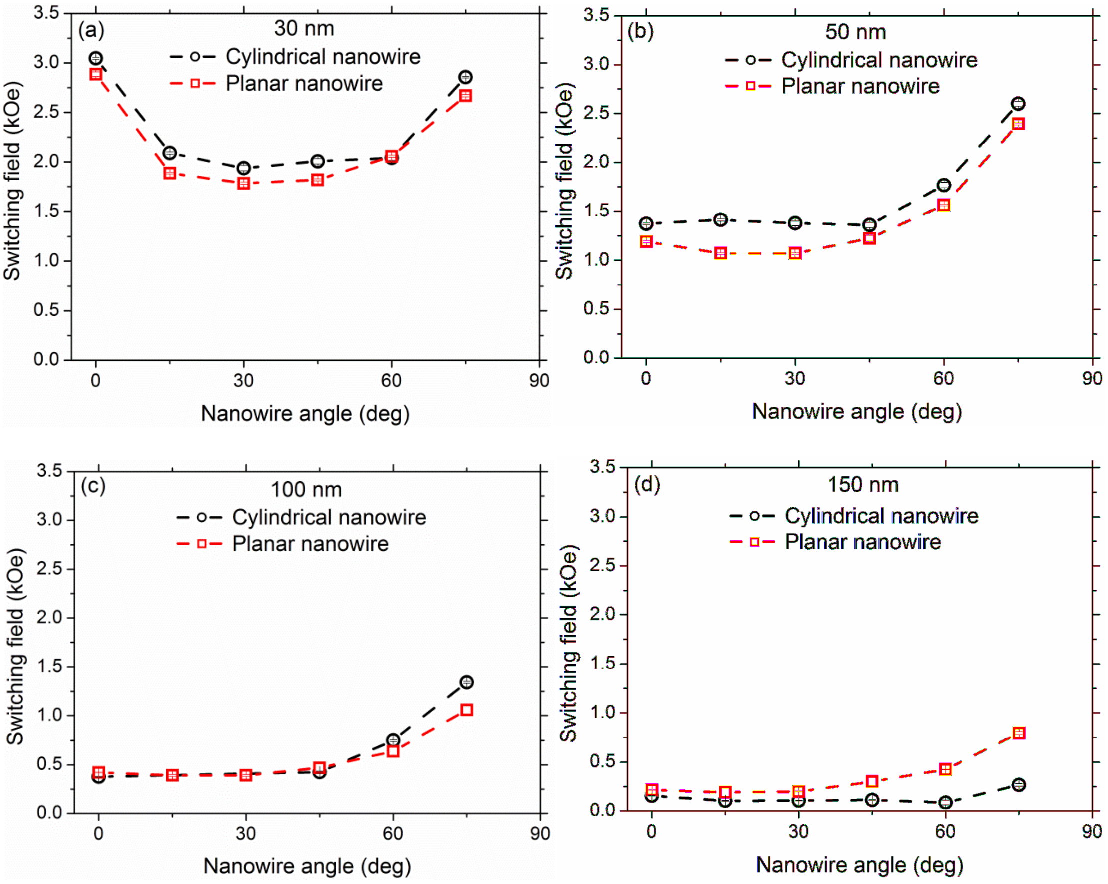

Figure 9.17 Switching field as a function of nanowire angle extracted from the loops of both geometries of $Ni_{81}Fe_{19}$ nanowires with four different examples of diameters / thicknesses as indicated in the figure titles. The dashed lines provide a guide to the eye.

up to ~20°. The switching field is nearly constant between 20° up to 60°. Then it increases rapidly at higher angles (>60°). In contrast, for nanowires with diameter/thickness greater than 50 nm, the switching fields increase very slowly up to about 40°. Then it increase more rapidly to the highest value up to 75°. This behaviour suggests a transition in the magnetisation behaviour between nanowires 30 nm and 50 nm in diameter/thickness. This observation is in a full agreement with the other results in the literature using different compositions of nanowires and investigative techniques [10,30,31]. For instance, Wernsdorfer et. al. used micro-SQUID to measure the magnetisation reversal behaviour of individual Ni nanowires with diameters ranged from 40 to 100 nm and they found a transition diameter 34±4 nm [30].

9-3.2 Angular dependence: comparison with the curling model and MOKE results

Comparing the angular dependence of the switching field obtained from the simulations of the largest thickness investigated here (150 nm) with the theoretical calculations of curling model of reversal, after normalising the switching fields to the minimum values, good agreement was obtained at all angles investigated as shown in Figure 9.18(a). This agreement suggests that the curling model is a reasonable analytical representation of the magnetisation reversal processes in such a nanowire. However, the micromagnetic structure presented earlier in Figure 9.10 is more complex and is not a simple curling-like behaviour.

Now comparing the angular dependence of the switching field obtained from simulation of the $Ni_{81}Fe_{19}$ wire with the experimental MOKE measurement of a 200 nm diameter $Ni_{60}Fe_{40}$ nanowire presented in chapter eight: The general trend in switching field agrees at small angles (< 35°) as shown in Figure 9.18(b). At higher angles (> 35°), a deviation in the switching field values is observed indicating that the magnetisation reversal behaviour in the experimental wire may change at higher angles although the wire diameter is likely to have an effect. However, for all angles investigated the simulated wire show higher switching fields than their counterpart experimental wire.

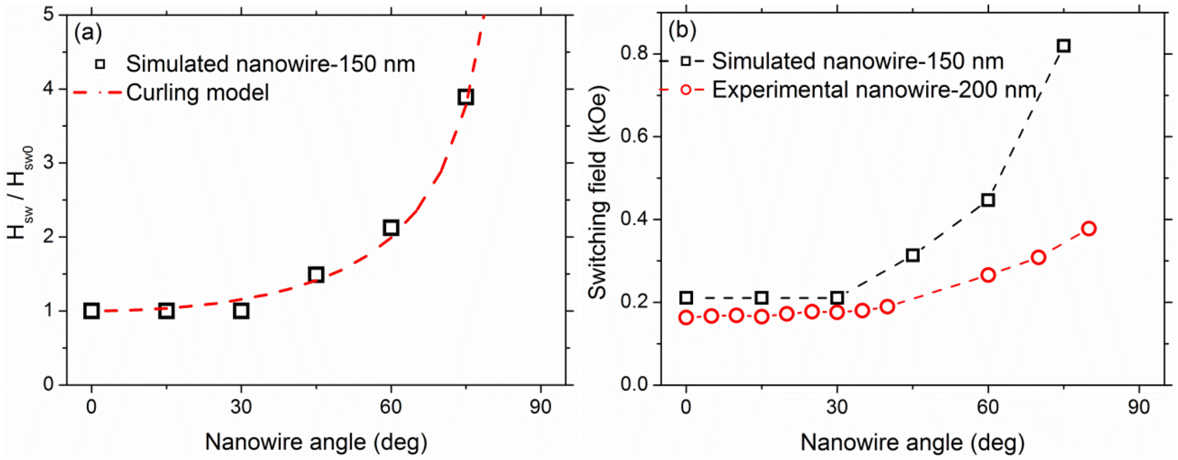

Figure 9.18 Normalised switching field as a function of nanowire angle with 150 nm thickness, the dashed line is a curling model fit. (b) switching field as a function of nanowire angle for both simulated (150 nm) and MOKE experimental nanowires (200 nm), the dashed lines provide a guide to the eye.

As an example, the switching field obtained from the simulated wire was 210 Oe when the field was applied parallel to the nanowire long axis, whilst 165 Oe for nanowire measured with MOKE magnetometry. This difference is expected since the simulation was performed at 0K and the simulated wire has smaller diameter than the experimental wire [14-16,22,25]. Furthermore, the Ni to Fe content of the experimental wires was 60:40 (see chapter six), whereas the simulation was used parameters of 81:19. As reported elsewhere increasing the Ni content increases the switching field [32].

9-4 Chapter conclusions

Micromagnetic simulations were employed using the OOMMF software to investigate the magnetic and magnetisation reversal behaviour of both cylindrical and planar cross-section $Ni_{81}Fe_{19}$ nanowires with a range of diameters and thicknesses up to 200 nm with the same length of 1 μm. The results of these studies were compared with the experimental results and the theoretical calculations of the curling model of reversal.

The effect of nanowire geometry and dimensions on the magnetic properties including switching fields, remanent magnetisation and magnetic state before and during the switching behaviour were discussed and compared with each other. In both geometries of nanowires, the switching fields increased with decreasing nanowires diameter and thickness. This was attributed to the formation of a more well defined single domain structure due to the enhanced shape anisotropy as the diameter/thickness of nanowires get smaller. The cylindrical nanowires showed slightly higher switching fields than their counterparts planar nanowires. This was more noticeable in thinner wires and was attributed to the discretisation effect of cylindrical nanowires or the existence of sharp corners in the planar wires which may prevent the occurrence of the vortex state at the edges of the wires.

Nanowires with diameters and thicknesses up to 100 nm showed higher squareness ratio than thicker nanowires. This was attributed to the effect of the demagnetising field which decreased with decreasing the nanowires diameter. There was no noticeable difference in the remanent magnetisation between the two geometries of nanowires up to 150 nm. The planar nanowires with diameters greater than 150 nm showed slightly higher squareness ratio than the cylindrical nanowires. This was attributed to the formation of complicated domain structures as the nanowires became thicker.

The values of switching fields extracted from the simulation loop of nanowire with 200 nm diameter were compared and discussed with the results obtained from the experimental MOKE and MR measurements. Simulations suggest that the surface magnetisation of thick nanowires behaves differently from their bulk in agreement with the experimental results found here. Snapshots of the micromagnetic moment distributions from simulations of the reversal behaviour in such thick nanowires showed a complex evolving domain structure.

For both geometries of nanowires, the angular dependence of the remanent magnetisation and the switching fields of a range of diameters and thicknesses were investigated. The remanent magnetisation was higher when the field was applied parallel to the nanowire long axis due to the dominant shape anisotropy. The remanent magnetisation decreased with increasing nanowire angle and showed a good agreement with the theoretical calculations indicating the dominance of shape anisotropy.

The angular dependence of the switching field showed that nanowires with less than 30 nm diameter reverse differently from the nanowires with diameters greater than 50 nm. This behaviour was in a full agreement with the results reported in literature using other compositions of wires and investigative techniques. The simulated wire showed a higher switching field than the counterpart experimental wire. This variation was attributed to the difference in the nanowire diameter and composition in addition to the difference of temperature between the simulation and measurements. The angular dependence showed a good agreement with the classical curling model of reversal at all angles indicating that the curling model of reversal was a reasonable analytical representation of the magnetisation reversal process in such a nanowire. On the other hand, a deviation in the switching fields between the simulated and measured wires at higher angles was obtained, indicating that the reversal in real nanowires may be different at higher angles.

9-5 Chapter references

1. Hertel R. "Micromagnetic simulations of magnetostatically coupled nickel nanowires" *J. Appl. Phys.*, 90(11), 5752, 2001.
2. Lebecki, K. M. "Modelling of magnetization reversal for long ferromagnetic nanotubes" *Materials Science-Poland*, 26(4), 2008.
3. Hertel, R. & Kirschner, J. "Magnetization reversal dynamics in nickel nanowires" *Physica B: Condensed Matter*, 343(1-4), 206, 2004.
4. Hertel R. "Computational micromagnetism of magnetization processes in nickel nanowires" *J. Mag. Mag. Mat.*, 249(1-2), 251, 2002.
5. Li, Y. L., Tang, S. L., Xie, R., Wang, Y., Yang, M., Gao, J. L., Xia, W. B., Gao, J. L. Xia, W. B. & Du, Y.W. "Fabrication and magnetic properties of free-standing Ni nanotube arrays with controllable wall thickness" *Appl. Phys. Lett.*, 100(5), 052402, 2012.
6. Allende, S., Escrig, J., Altbir, D., Salcedo, E. & Bahiana, M. "Angular dependence of the transverse and vortex modes in magnetic nanotubes" *Eur. Phys. J. B*, 66(1), 37, 2008.
7. Chen, A. P., Gonzalez, J. & Guslienko, K. Y. "Domain walls confined in magnetic nanotubes with uniaxial anisotropy" *J. Mag. Mag. Mat.*, 324(22), 3912, 2012.
8. Gao, J.-H., Sun, D.-L., Zhan, Q.-F., He, W. & Cheng, Z.-H. "Magnetization reversal process and magnetic relaxation of self-assembled Fe_3Pt nanowire arrays with

different diameters: Experiment and micromagnetic simulations" *Phys. Rev. B*, 75(6), 064421, 2007.

9. Han, N., Guo, G., Zhang, L., Zhang, G. & Song, W. "Magnetization reversal for Ni nanowires studied by micromagnetic simulations" *J. Mater. Sci. Technol.*, 25(2), 151, 2009.
10. Han N., Guo Guang-hua, Guang-fu, Z., Wen-bing, S. & Gao-fu, Men "Domain wall structure transition during magnetization reversal process in magnetic nanowires" *Trans. Nonferrous Met. Soc. China*, 17(60571043), 1034, 2007.
11. Liao, Z.-M., Lu, Y., Zhang, H.-Z. & Yu, D.-P. "Hysteresis magnetoresistance and micromagnetic modelling of Ni microbelts" *J. Mag. Mag. Mat.*, 322(15), 2231, 2010.
12. Bisero, D., Cremon, P., Madami, M., Tacchi, S., Gubbiotti, G., Carlotti, G. & Adeyeye, A. O. "Magnetization reversal of rectangular particles: Closure states and effect of dipolar coupling" *IEEE Trans. Mag.*, 48(4), 1593, 2012.
13. Donahue, M. J. & Porter D. G. "OOMMF User᾿s Guide, Version1.0" NISTIR 6376, National Institute of Standards & Technology, Gaithersburg, MD, 1999.
14. Sellmyer, D. J., Zheng. M. & Skomski, R. "Magnetism of Fe, Co and Ni nanowires in self-assembled arrays" *J. Phys.: Condens. Matter*, 13, 433, 2001.
15. Zeng, H., Skomski, R., Menon, L., Liu, Y., Bandyopadhyay, S. & Sellmyer, D. "Structure and magnetic properties of ferromagnetic nanowires in self-assembled arrays" *Phys. Rev. B*, 65(13), 134426, 2002.
16. Das, B., Mandal, K., Sen, P. & Bandopadhyay, S. K. "Effect of aspect ratio on the magnetic properties of nickel nanowires" *J. Appl. Phys.*, 103, 013908, 2008.
17. Gao, T. R., Yin, L. F., Tian, C. S., Lu, M., Sang, H. & Zhou, S. M. "Magnetic properties of Co–Pt alloy nanowire arrays in anodic alumina templates" *J. Mag. Mag. Mat.*, 300(2), 471, 2006.
18. Zheng, M., Menon, L., Zeng, H., Liu, Y., Bandyopadhyay, S., Kirby, R. D. & Sellmyer, D. J. "Magnetic properties of Ni nanowires in self-assembled arrays" *Phys. Rev. B*, 62(18), 282, 2000.
19. Chien, C. L., Sun, L., Tanase, M., Bauer, L. A., Hultgren, A., Silevitch, D. M., Meyer, G. J., Searsonb, P. C. & Reich, D. H. "Electrodeposited magnetic nanowires: Arrays, field-induced assembly, and surface functionalization" *J. Mag. Mag. Mat.*, 249(1-2), 146, 2002.
20. Lin, S. W., Chang, S. C., Liu, R. S., Hu, S. F. & Jan, N. T. "Fabrication and magnetic properties of Ni nanowires" *J. Mag. Mag. Mat.*, 282, 28, 2004.
21. Vazquez M., Pirota, K., Torrejo, J., Navas, D. & Herna, M. "Magnetic behaviour of densely packed hexagonal arrays of Ni nanowires: Influence of geometric characteristics" *J. Mag. Mag. Mat.*, 294, 174, 2005.
22. Escrig, J., Lavín, R., Palma, J. L., Denardin, J. C., Altbir, D., Cortés, A. & Gómez, H. "Geometry dependence of coercivity in Ni nanowire arrays" *Nanotech.*, 19(7), 075713, 2008.
23. Nielsch, K., Wehrspohn, R. B., Barthel, J., Kirschner, J., Go, U., Fischer, S. F. & Kronmu, H. "Hexagonally ordered 100 nm period nickel nanowire arrays" *Appl. Phys. Lett.*, 79(9), 1360, 2001.
24. Whitney, T. M., Jiang, J. S., Searson, P. C. & Chien L. C. "Fabrication and magnetic properties of arrays of metallic nanowires" *Science*, 261, 1316, 1993.

25. Kehua Zhong, Zhicheng Zhang, Baohua Shen, Meimei Lin, Qian Feng & Zhigo Huang "The size and temperature effects of coercivity for the magnetic nanowire: Monte carlo simulation" *Solid State Phenomena*, 121-123, 1081, 2007.
26. Bryan, M. T., Atkinson, D. & Cowburn, R. P. "Edge roughness and coercivity in magnetic nanostructures" *J. Phys.: Conf. Series*, 17, 40, 2005.
27. Sun, L., Hao, Y., Chien, C.-L. & Searson, P. C. "Tuning the properties of magnetic nanowires" *IBM Journal of Research and Development*, 49(1), 79, 2005.
28. Lavín R., Denardin, J. C., Escrig, J., Altbir, D. Cortes A. & Gomez H."Angular dependence of magnetic properties in Ni nanowire arrays" *J. Appl. Phys*., 106, 103903, 2009.
29. Lavín, R., Gallardo, C., Palma, J. L., Escrig, J. & Denardin, J. C. "Angular dependence of the coercivity and remanence of ordered arrays of Co nanowires" *J. Mag. Mag. Mat.*, 324(15), 2360, 2012.
30. Wernsdorfer, W., Doudin, B., Mailly, D., Hasselbach, K., Benoit, A, Meier, J., Ansermet, J.-Ph. & Barbara B. "Nucleation of magnetization reversal in individual nanosized nickel wires" *Phys. Rev. Lett.*, 77(9), 1873, 1996.
31. Pal, S., Saha, S., Polley, D., & Barman, A. "Magnetization reversal dynamics in Co nanowires with competing magnetic anisotropies" *Solid State Com.*, 151(24), 1994, 2011.
32. Takeshi Ohgai "Fabrication of functional metallic nanowires using electrodeposition technique: Electrodeposited nanowires and their applications" Edited by Nicoleta Lupu *Intech.*, Olanjnic, India, 2010.

Chapter ten

Conclusions and suggestions for further work

10.1 Conclusions

Magnetic measurements of template released isolated individual and small bundles of closely packed cylindrical ferromagnetic nanowires allowed new insight and understanding of the magnetic and magnetisation reversal behaviour in such nanowires through the combination of both MOKE and MR measurements complemented by detailed micromagnetic simulations.

Chapter six mainly presented an investigation of the elemental composition, morphology and statistical distribution of electrodeposited thin films and template released ferromagnetic nanowires. EDS &WDS analysis was utilised to confirm the formation of the electrodeposited thin films on the substrates and to ascertain their composition. The results demonstrate that these films were free from contamination of boron and sulphur. There was approximately 20% shift in the Fe content in all electrodeposited NiFe films with respect to the nominal composition. This was attributed to a high concentration of Fe during the electrochemical growth. The topography of the electrodeposited thin films was also studied using grazing incidence X-ray reflectivity measurements. These films were found to be nonuniform and very rough which was attributed to the formation of voids and defects during the deposition process. The relationship between electrodeposition growth time and film thickness was also investigated.

The statistical distributions of the interpore wall thickness (spacing) and nanopore diameters of the alumina templates were investigated. A wide distribution in the wall thickness and non-uniformity in the nanopore cross-sections were found even in well ordered templates (used in other reports) and attributed to a variation in the fabrication of the template itself. The morphology, distributions of the diameters and lengths of template released Ni and NiFe nanowires deposited from a dilute suspension onto the substrates were also studied. The morphology of wires was found to range from smooth cylindrical structures to non-uniformity in diameters, surface roughness and surface features that were attributed to defects or impurities in the internal surfaces of the pores or trapped air pockets that occurred within the pores during nanowire growth. The distribution of wire diameters was very similar to the template pore size distribution. The variation of nanowire diameter was Gaussian in some cases and skewed in some other cases. These variations can lead to variations in the magnetostatic interactions among the templated wires, making the intrinsic magnetic properties of individual nanowires difficult to obtain from array measurements. The distribution of wire lengths for template released nanowires was observed to depend upon the sonication time, with longer sonication leading to a higher percentage of shorter nanowires. Bundles of nanowires were also found after releasing and deposition onto substrates and their formation was attributed to the effect of electrostatic or magnetostatic forces among these wires. Increasing the sonication time up to approximately one hour was ineffective for separating these bundles. Bent or broken nanowires with shorter lengths were noticed with increasing sonication time.

To better understand and interpret the magnetic and electrical transport properties of isolated nanowires presented in the later chapters, the crystalline structure and the grain sizes within templated and isolated nanowires was also investigated in chapter six. These studies were carried out using both XRD analysis and HRTEM measurements incorporating SAED, respectively. The results demonstrated that these wires have an FCC structure with small grains distributed randomly and with an average size of about 30 nm for the Ni and 15 nm for the NiFe nanowires. Moreover, larger grains with lengths extending up to ~200 nm were also observed in the Ni nanowires.

In chapter seven, a quantitative investigation showed details of magnetic field assisted alignment of template released NiFe, Ni and Co nanowires using high resolution scanning electron microscopy. This process was ultimately performed in order to align these wires with respect to prefabricated micromarkers and electrical contact pads to allow the MOKE and MR measurements to be carried out, respectively. The effect of field strength, elemental composition and aspect ratio on the efficacy of the magnetic field alignment of the nanowires was statistically analysed. During the dispersion of nanowires onto the substrates from a dilute suspension and in the absence of magnetic field, randomly oriented nanowires were obtained, attributed to various mechanical forces. Under the application of magnetic fields, the alignment was strongly dependent upon the strength of the applied field. For all compositions, the percentage of nanowires orientated with the field axis was found to increase rapidly with increasing magnetic field up to ~200 Oe, followed by a slower increase up to ~1 kOe for both the NiFe and Ni wires and there was no further significant change for the Co nanowires. The highest percentage of aligned wires was obtained for the NiFe nanowires, whereas the lowest percentage of aligned wires was obtained for the Co nanowires, with the percentage alignment of Ni nanowires falling between the two. The compositional dependence of the alignment was attributed to both saturation magnetisation and the competition between magnetocrystalline anisotropy and shape anisotropy. The effect of the nanowire length on the alignment behaviour was also statistically investigated. The percentage of longer wires aligned was found to be higher than the shorter wires. This behaviour was attributed to the increased shape anisotropy obtained with increasing nanowire length. This chapter also reported some further observations resulting from the magnetic alignment experiments in addition to the possible applications of the ferromagnetic nanowires aligned by magnetic fields.

The magnetic and electrical transport behaviour of isolated template released ferromagnetic nanowires was systematically investigated in chapter eight using both longitudinal MOKE magnetometry and MR measurements, respectively. In order to deeply understand the magnetic properties of such nanowires, a range of electrodeposited thin films were also investigated. To gain an insight into the distribution of the switching fields across the whole samples (films and wires), the measurements were carried out using a focused laser spot at different locations on these samples. To investigate the angular dependence of the switching fields in these samples, the measurments were performed at different angles (parallel to perpendicular) with respect to the magnetic field applied.

Square hysteresis loops with high remanence ratios were obtained from measurments of Ni and NiFe thin films with small local variations when the magnetic field was applied along two orthognal in-plane axes, indicating an isotropic magnetic nature for these films. A distribution of the coercive field across the sample area was observed that was larger for the shorter deposition times. This was attributed to the existence of impurties or surface roughness introduced during the electrodeposition growth. For both materials investigated here, a reduction in the coercivity with increasing deposition time was noticed and attributed to a reduction of surface roughness upon increasing the film thickness and to the formation of multi-domain structures. The coercivity of the NiFe films at small deposition times was found to be lower than for the Ni films, indicating the softer behaviour of NiFe films.

The shape of the MOKE hysteresis loops obtained from measurements of a range of template released isolated individual, bundles and clusters of ferromagnetic nanowires when the field was applied parallel to their long axis were found to be largely square, with well-defined switching behaviour and a high squareness ratio indicating a magnetic easy axis along the nanowire long axis. This result is quite different from the results reported in literature using two-dimensional arrays of nanowires measured with VSM and SQUID. This was attributed to the strong magneto-static interaction amongst these wires or may reflect the difference between bulk and surface magnetisation behaviour. A distribution of the switching fields was observed by repeating the measurements at different locations on the same nanowires. For bundles of closely packed wires and clusters of spaced wires, the switching fields depend upon the magnetostatic interactions among the interacting nanowires. The width of the measured switching field distribution for the individual nanowire was attributed to the differences in the surface structure and dimension variations along the nanowire length, whereas the variation in the switching behaviour between the bundles of wires depends upon the separation between the wires. In the tightly bunched and aligned wires, the switching field was reduced for increased numbers of wires, whilst for the more widely spaced and poorly aligned nanowires the switching field was more variable and depends on the details of the nanowire assemblage. The general behaviour of a reduction in the switching field in the tightly packed NiFe wires with increasing the number of nanowires was found in agreement with other results reported in literature using micromagnetic simulation on other composition and dimension of nanowires. The switching field obtained from individual NiFe nanowires was higher than their counterpart Ni nanowire. This was attributed to the difference in length and diameter of these wires. These results were in agreement with the theoretical calculations performed to calculate the demagnetising field along the long axis of the wires.

Square hysteresis loops were also obtained from the angular MOKE measurements of these isolated nanowires as a function of field angle. This behaviour was attributed to some rotation of the easy axis of magnetisation with the direction of the applied field or the difficulty in recognising the change in the shape of these loops due to the distortion occurred with the small signal to noise and possibly other magneto-optical effects, or perhaps due to the detection of a transverse component of magnetisation in the MOKE setup. The angular dependence of the normalised switching fields for all of the wires investigated here showed an agreement with the theoretical calculation for the curling model at small angles and a deviation from this analytical model at larger angles. This indicated that the curling model was a reasonable analytical representation of the magnetisation reversal processes at low angles, whereas more complicated magnetisation structure occurs at higher angles.

The electrical transport properties of two assemblages of bundles of 3 NiFe nanowires were successfully measured and discussed in chapter eight using MR measurements. The electrical resistance of these assemblages of wires was compared with the theoretical calculations and accordingly both the gold leads and the contact resistance were estimated. The technical difficulties associated with the electrical connection and measurements of isolated nanowires were also presented in this chapter. The angular dependent MR data was in good agreement with the theoretical predictions for anisotropic magnetoresistance. The anisotropic magnetoresistance ratio for both assemblages of nanowires was in agreement with the bulk value reported in literature. These measurements indicated, in contrast to MOKE measurements, that high percentages of magnetic moments aligned away from the easy axis of magnetisation upon removing the field at transverse measurements. This behaviour was attributed to the effect of magnetostatic intraction among these wires or due to the nanowires surface regularities or the difference between surface and bulk magnetisation behaviour.

The MR measurments at all angles investigated showed a combination of small and large features in the resistance profiles. The angular dependence of the switching field obtained from the field at large features were compared with the theoretical calculations of curling model. Agreement was observed at small angles and disagreement at higher angles indicated that the magnetisation reversal in these wires changed from curling to S-W model. This was in agreement with other results reported in the literature using other composition of wires and similar dimensions.

For both assemblages of wires, the switching fields obtained from the small and large features in the MR profiles were compared with each other and with the switching field obtained from MOKE measurments on the same nanowires. A slight difference in the switching field were obtained between the two assemblages of wires and was attributed to the difference in the nanowire length or the complicated magnetostatic intractions in these small assemblages of wires. The switching fields obtained from the small features in MR data were found to be comparable to the switching fields of the large reversal in the MOKE measurements, whilst the switching fields obtained from the large features were found to be much less than their counterpart results obtained from MOKE measurements. Since, this was the first study to combine the MR and MOKE measurements on the same wires, the switching fields obtained here were compared and discussed with the switching fields of their counterparts nanowire reported in literature that used the same investigative techniques. Good agreement was obtained from these comparisons and it is pointed out here that the magnetisation process at the surface of such isolated nanowires differs from the bulk. This result was in agreement with the other results reported elsewhere on thin films and amorphous microwires.

Chapter nine presented an investigation of the magnetic and magnetisation reversal behaviour of cylindrical and planar cross-section nanowires using micromagnetic modelling (OOMMF software). These measurements were performed on $Ni_{81}Fe_{19}$ nanowires with a range of diameters/thicknesses between 10 to 200 nm with the same length of 1 μm. The effect of nanowire cross-sectional geometry and dimensions on the magnetic behaviour were discussed and compared with each other and with the experimental results obtained from MOKE and MR measurements.

In both circular and square cross-section geometries, the switching field was found to increase with decreasing diameter or thickness. This was attributed to the formation of single domain structures or due to the increase of the shape anisotropy as the diameter and thickness of the nanowires became smaller. The cylindrical nanowires, showed slightly higher switching fields than their counterparts planar nanowires. This was attributed to the discretisation effect of the cylindrical nanowire that may aid complexity to the domain structure and hence slightly increasing the magnetic field required to switch the magnetisation from one state to another. Furthermore, the existence of sharp corners in the planar nanowires may prevent the occurrence of the vortex state easily at the edges of the wires.

Nanowires with diameters and thicknesses up to 100 nm showed highest squareness ratio (~1) than thicker nanowires. This was attributed to the effect of the demagnetising field which decreases with decreasing the nanowires diameter. There was no noticeable difference in the remanent magnetisation between the two geometries of nanowires with diameters/ thickness up to 150 nm. The planar nanowires with diameters more than 150 nm showed slightly higher squareness ratio than their counterpart cylindrical nanowires. This again was attributed to the complicated domain structure.

The switching fields obtained from simulation of thick nanowires were compared and discussed with their counterpart nanowires studied experimentally by MOKE and MR measurements. There was an agreement between these measurements which further supports the idea that the surface magnetic moments within the thick nanowires reverse differently from the bulk. The magnetic moment distributions at different field strengths showed the complicated domain and domain wall structures within these wires but relatively simple axial magnetisation at the surface of the nanowires.

The angular dependence of the remanent magnetisation and switching field on a range of diameters and thicknesses of individual wires were also investigated in chapter nine. This was carried out using a series of micromagnetic simulations by applying the magnetic fields along and perpendicular to the nanowires long axis. The remanent magnetisation was found to decrease with increasing the nanowires long axis angle away from the field. This was found to be in agreement with the theoretical calculations indicating the dominate shape anisotropy on the behaviour. The angular dependence of the switching field showed that nanowires with less than 30 nm diameter reverse differently from the nanowires with diameters greater than 50 nm. This behaviour was in agreement with other results reported in literature using other compositions of wires and investigative techniques. The simulated wire showed higher switching field than their counterpart experimental wire. This was attributed to the difference in the nanowire diameter and composition in addition to the variation of temperature during the simulation and measurements. The normalised angular dependence showed a good agreement with the classical curling model of reversal at all angles, indicated that the curling model of reversal was a reasonable analytical representation of the magnetisation reversal process in such nanowires, although the micromagnetic structure was actually more complex and not simple curling-like behaviour.

10.2 Suggestions for further work

In order to develop the present work and to gain more understanding on the surface and bulk magnetisation behaviour in such isolated nanowires, the following are possible suggestions for further work:

The magnetoresistance measurements could be repeated again on template released isolated ferromagnetic nanowires using multiprobe electrical connections to eliminate both effects of contact and gold lead resistance. This configuration of electrical connections could allow also magnetisation measurements to be performed on different parts on the same wire and to determine the homogeneity of the magnetisation reversal within a nanowire.

The MOKE and MR measurements could be undertaken on similar isolated nanowires with different diameters, lengths and compositions. This will provide a more generalised understanding of the surface and bulk magnetic and magnetisation reversal behaviour.

As seen in chapters four and eight, a wide range of nanowire samples were electrically connected to the contact pads, but the magnetoresistance measurements showed that the connections were often non-ohmic and highly resistive or an open circuit. One of the most important reasons was that the gold electrodes were not thick enough to adequately connect these circular cross-section nanowires with the electrodes. Therefore, this needs more work by increasing the thickness of the deposited electrodes; this may allow the measurements to be performed easily on a wide range of isolated nanowires. This would require improvements to the lithography.

To understand in more details the effect of nanowire geometry on the magnetisation reversal process in thick nanowires, the results of this study needs to be compared with the planar cross-section nanowires created by ion beam milling or EBL or LCVD using the same investigative techniques.

Finally, a detailed comparison of the magnetisation behaviour between individual and small bundles of ferromagnetic nanowires needs to be studied using micromagnetic simulations to gain more insight into the effect of magnetostatic interactions among such small bundles of nanowires.